Terms and Conditions of Use of Digitised Theses from Trinity College Library Dublin

Copyright statement

All material supplied by Trinity College Library is protected by copyright (under the Copyright and Related Rights Act, 2000 as amended) and other relevant Intellectual Property Rights. By accessing and using a Digitised Thesis from Trinity College Library you acknowledge that all Intellectual Property Rights in any Works supplied are the sole and exclusive property of the copyright and/or other IPR holder. Specific copyright holders may not be explicitly identified. Use of materials from other sources within a thesis should not be construed as a claim over them.

A non-exclusive, non-transferable licence is hereby granted to those using or reproducing, in whole or in part, the material for valid purposes, providing the copyright owners are acknowledged using the normal conventions. Where specific permission to use material is required, this is identified and such permission must be sought from the copyright holder or agency cited.

Liability statement

By using a Digitised Thesis, I accept that Trinity College Dublin bears no legal responsibility for the accuracy, legality or comprehensiveness of materials contained within the thesis, and that Trinity College Dublin accepts no liability for indirect, consequential, or incidental, damages or losses arising from use of the thesis for whatever reason. Information located in a thesis may be subject to specific use constraints, details of which may not be explicitly described. It is the responsibility of potential and actual users to be aware of such constraints and to abide by them. By making use of material from a digitised thesis, you accept these copyright and disclaimer provisions. Where it is brought to the attention of Trinity College Library that there may be a breach of copyright or other restraint, it is the policy to withdraw or take down access to a thesis while the issue is being resolved.

Access Agreement

By using a Digitised Thesis from Trinity College Library you are bound by the following Terms & Conditions. Please read them carefully.

I have read and I understand the following statement: All material supplied via a Digitised Thesis from Trinity College Library is protected by copyright and other intellectual property rights, and duplication or sale of all or part of any of a thesis is not permitted, except that material may be duplicated by you for your research use or for educational purposes in electronic or print form providing the copyright owners are acknowledged using the normal conventions. You must obtain permission for any other use. Electronic or print copies may not be offered, whether for sale or otherwise to anyone. This copy has been supplied on the understanding that it is copyright material and that no quotation from the thesis may be published without proper acknowledgement.

An Ultrafast IR Study of Cytosine-Rich Nucleic Acids

and

A Photophysical Study of Porphyrin-Nucleic Acid Systems

A thesis submitted to the University of Dublin for the degree of Doctor of Philosophy

by

Páraic M. Keane B.A.(Mod.), M.Sc.

Under the supervision of
Prof. John M. Kelly

School of Chemistry
Trinity College Dublin

January 2011

Declaration

I declare that

this thesis has not been submitted as an exercise for a degree at this or any other University.

the work is entirely that of the author except where otherwise indicated and acknowledged

the Library is granted permission to lend or copy this thesis

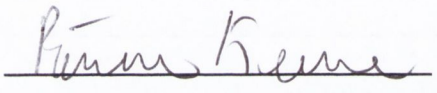

Summary

Work is presented in this thesis on two separate but complementary topics in the photochemistry of nucleic acids.

Part one addresses the effect of direct UV excitation on the cytosine derivatives. Cytosine can form mutagenic dimers on exposure to sunlight, and this section examines the photophysical processes that occur in cytosine derivatives a few picoseconds after UV excitation. The experimental data is gathered primarily from the method of picosecond time-resolved infrared spectroscopy (ps-TRIR), with a particular interest in a non-emissive, relatively long-lived singlet $n\pi^*$ excited state previously observed in some cytosine systems.

In Chapter Three, monomeric cytosine derivatives are studied using both transient spectroscopy and computational methods. Data is obtained on the new ULTRA ps-TRIR apparatus, including the first successful recording of the TRIR spectrum of a nucleic acid in H_2O, and extended spectral characterisation of the long-lived $^1n\pi^*$ state. It is also confirmed that the formation of this state is very sensitive to the presence of the ribose group at the N1-position. A number of theories are suggested to explain this phenomenon. The excited-state IR spectra are calculated using HF-CIS methods and the transient assigned as a $^1n_O\pi^*$ excited state, pending further calculations to model the effect of solvent.

In Chapter Four the study is extended to dinucleotide (d(CpC)) and polynucleotide (poly(rC)) sequences where bases are linked and may be stacked, but not base-paired. It is found that the long-lived $^1n\pi^*$ state is still produced in these sequences, and in similar yields to the monomer, though the lifetime is increased. The $^1n\pi^*$ decay route remains the dominant decay pathway in the dinucleotide/polynucleotide systems, and only tentative evidence is found for commonly cited excimer species.

In Chapter Five the effect of protonation of biologically significant C-polymers is studied, with specific focus on the formation of hemi-protonated i-motif and duplex structures. The formation of these higher order structures is readily observed by distinctive features in the TRIR spectra. The $^1n\pi^*$ state is shown to be present in the base-paired sequences, with lifetimes similar to that of poly(rC). Apparently longer bleach recovery lifetimes suggest that additional excimer species may be present.

The study on the C system reveals the power of TRIR for studying non-emissive states in nucleic acids, and shows that the long-lived $^1n\pi^*$ state is an important decay pathway in C-rich sequences in a variety of structural forms.

The second part examines a photosensitiser molecule that can mediate the photo-oxidation of DNA by the absorption of visible light. The chosen photosensitiser is a Pt(II) metalloporphyrin (PtTMPyP4) that displays room-temperature phosphorescence, allowing for ready monitoring of the long-lived triplet state.

In Chapter Seven the ground-state binding interactions of PtTMPyP4 with a range of nucleic acids are studied by UV/vis and circular dichroism spectroscopy. PtTMPyP4 forms π-stacked complexes with mononucleotides, intercalates into GC-rich polymers, and interacts by mixed groove-binding modes with AT-rich DNA. The interactions of PtTMPyP4 with the special G-rich quadruplex are also compared to those of the 5-coordinate Zn(II) analogue.

In Chapter Eight the phosphorescence properties of PtTMPyP4 are studied in mono- and polynucleotides using steady-state and time-resolved emission techniques. The triplet state is shown to be dynamically quenched by chloride ions in solution. Significant enhancements in emission are observed in the presence of adenine-rich sequences, which is attributed primarily to the effect of shielding from dissolved oxygen quencher. The emission of PtTMPyP4 is quenched by guanosine 5′-monophosphate (GMP) due to a photo-induced electron transfer from the PtTMPyP4 triplet state to guanine, which occurs *via* both dynamic and static mechanisms. Phosphorescence is not quenched in G-containing polymer sequences, However it is not enhanced to the same degree as in corresponding A-rich sequences, implying that a relatively inefficient electron transfer contributes to non-radiative decay.

In Chapter Nine the excited singlet and triplet states of PtTMPyP4 and the parent free base (H_2TMPyP4) molecule are studied by transient UV/vis/near-IR and IR absorption spectroscopy. The triplet state of PtTMPyP4 is characterised from the UV/vis to near-IR region. The presence of nucleotides results in shifts in the spectra and changes in triplet lifetime matching those recorded by time-resolved emission. No photoproducts are observed in the presence of GMP suggesting that the reverse electron transfer is very efficient. TRIR reveals distinctive spectral characteristics of both PtTMPyP4 and non-metallated H_2TMPyP4. A tentative estimate is thus made on the rate of singlet to triplet intersystem crossing in PtTMPyP4.

The results suggest that, although photoinduced electron transfer occurs from guanine to PtTMPyP4, the porphyrin probably does not photo-oxidise DNA by the type 1 electron transfer mechanism, but rather by a type 2 singlet oxygen mechanism.

Acknowledgements

Many thanks to Prof. John M. Kelly for welcoming me back into the chemistry community and providing a comprehensive scientific apprenticeship.

Much of the work in this thesis was performed in collaboration. For the project on direct excitation, I thank project leader Dr. Susan Quinn, and Drs. Ger Doorley and Michal Wojdyla, who I worked with on the experimental runs in the Rutherford Appleton Laboratories (RAL) and during the post-run data analysis. Thanks also to Prof. Graeme Watson (TCD), who performed all the calculations reported in Chapter Three. I also acknowledge our collaborators in the RAL, namely Prof. Tony Parker, Prof. Mike Towrie, Dr. Ian Clark and Dr. Greg Greetham. I also specifically acknowledge Dr. Wojdyla and Prof. Kelly for recording the transient spectra of the porphyrins on the ULTRA apparatus (in Chapter Ten).

Thanks to Prof Christine Cardin and Dr. Abeer Naseer for their help with the crystallography trials, with a special mention to the Cardins for the wonderful hospitality they showed me during my trips to the University of Reading.

I shall also recall with nostalgic fondness the evolving and revolving incarnations of the Kelly group that coincided with my residency; Dave, Deirdre, Ger, Sibu, Damian, Kyra, Gemma, Marie-Hélène, Suni, Michal, Jayden, Matthew, Swagata, Michael and numerous undergraduate and summer students, for providing an environment that was never dull...

Thanks to all the staff in the School of Chemistry, including Dr. Martin Feeney and Patsy Greene in the Phys. Chem. lab, Dr. John O'Brien, Dr. Manuel Ruether, Brendan Mulvany, Fred Cowzer and the administrative staff.

For financial support I acknowledge Science Foundation Ireland, the Trinity College Postgraduate Award, EU programme for RAL access and the RIA/RSC exchange programme, as well as the Trinity Trust travel grant, the Centre for Synthesis and Chemical Biology, and IRCSET, for occasional funding

Finally, thanks to my parents for their substantial support, and for my father's help with typesetting in LaTeX.

In memory of my two grandmothers

Abbreviations

1-MeCyt	1-methylcytosine
Φ_{isc}	quantum yield of $S_1 \rightarrow T_1$ intersystem crossing
A	adenine
AIMS	*ab initio* multiple spawning
AMP	adenosine 5′–monophosphate
B3LYP	Becke three-parameter Lee-Yang-Parr
C	cytosine
CAS-PT2	complete active space perturbation theory
CAS-SCF	complete active space self consistent field
CD	circular dichroism
CI	conical intersection
CIS	configuration interaction singles
CPD	cyclobutane pyrimidine dimer
CT	charge transfer
Cyd	cytidine
CMP	cytidine 5′–monophosphate
d(CpC)	deoxy(cytidyl 3′→5′ cytidine)
DFT	density functional theory
DNA	deoxyribonucleic acid
ET	electron transfer
FTIR	Fourier transform infrared
G	guanine
GMP	guanosine 5′–monophosphate
HF	Hartree-Fock
ICD	induced circular dichroism
k_{nr}	unimolecular non-radiative decay constant
k_r	unimolecular radiative decay constant
k_q	bimolecular quenching constant
LD	linear dichroism

MPD	2-methyl-2,4-pentanediol
NIR	near-infrared
NMR	nuclear magnetic resonance
PCM	polarisable continuum model
PET	photoinduced electron transfer
PIRATE	Picosecond Infrared Absorption and Transient Excitation
poly(rA)	poly(adenylic acid)
poly(rC)	poly(cytidylic acid)
poly(rG)	poly(guanylic acid)
$[poly(dA\text{-}dT)]_2$	poly(deoxyadenylic acid-thymidylic acid)
$[poly(dG\text{-}dC)]_2$	poly(deoxyguanylic acid-deoxycytidylic acid)
r	binding ratio
RAL	Rutherford Appleton Laboratories
RNA	ribonucleic acid
S_0	ground state
SHE	standard hydrogen electrode
S_n	n^{th} singlet excited state
SPC	single photon counting
T	thymine
TA	transient absorption
TCSPC	time-correlated single photon counting
TD	time-dependent
TMPy	(tetra-*N*-methyl-pyridyl)porphyrin
T_n	n^{th} triplet excited state
TRIR	time-resolved infrared
ULTRA	Ultra-sensitive Life science Time-Resolved Analysis
W-C	Watson-Crick

Contents

List of Figures

List of Tables

Chapter 1

General Introduction

1.1 Overview

Nucleic acids, such as DNA, are the carriers of genetic information in living systems. The biological, chemical and physical properties of nucleic acids have been exploited in areas as diverse as genetics, forensics, nanotechnology and medicine. In this thesis nucleic acids are studied primarily through the lens of photochemistry. Photochemical reactions are of major biological significance and can give rise to mutations and cancer in tissue that has been over-exposed to UV radiation. DNA can also act as a host for small drug molecules, and photoactive molecules can indirectly induce the photo-oxidation of DNA in a process known as photosensitisation. Both these fundamental modes of DNA photochemistry, direct excitation and photosensitised oxidation (Fig. 1.1), are examined in this thesis.

In part one, picosecond time-resolved IR spectroscopy is used to probe the response of a range of cytosine derivatives to UV light, while some of the experimental results have been augmented with calculations. These studies aim to find a connection between DNA structure and the deactivation pathways that lead to DNA damage or repair.

In part two a metalloporphyrin photosensitiser is studied in a variety of nucleic acid systems from mononucleotides to polynucleotides. Absorption techniques are used to model binding interactions, while excited-state processes such as guanine photo-oxidation are monitored using photophysical techniques over orders of timescales from microseconds down to femtoseconds.

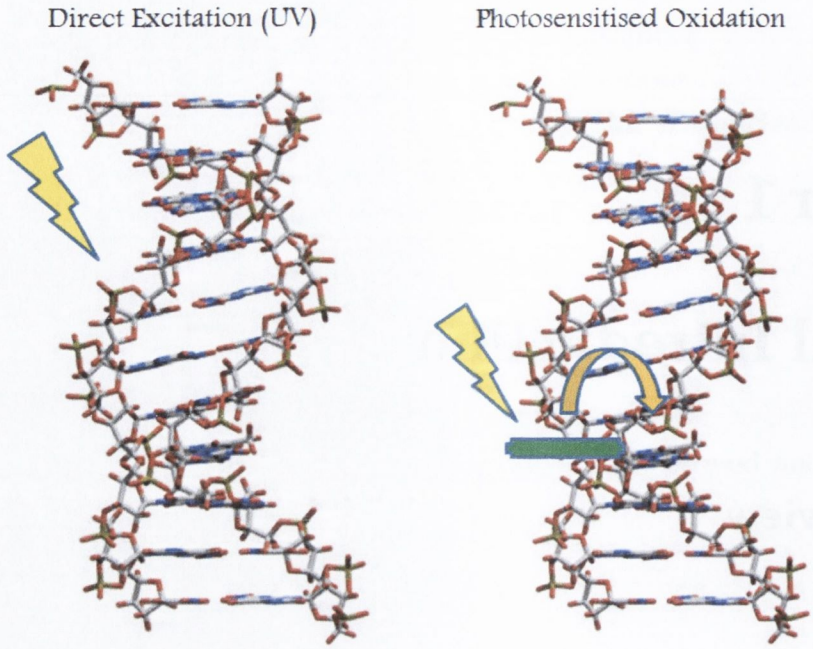

Figure 1.1: Comparison of two fields of DNA photochemistry. (DNA structure from Middleton et al[1]

1.2 Introduction to Nucleic Acids

The fundamental units of DNA and RNA are the nucleobases (Fig. 1.2), of which there are two purines (adenine and guanine) and three pyrimidines (cytosine, thymine and uracil). Thymine is present in DNA, but is replaced by uracil in RNA.

The nucleobases can be further substituted at the N1 (pyrimidines) or N9 (purines)

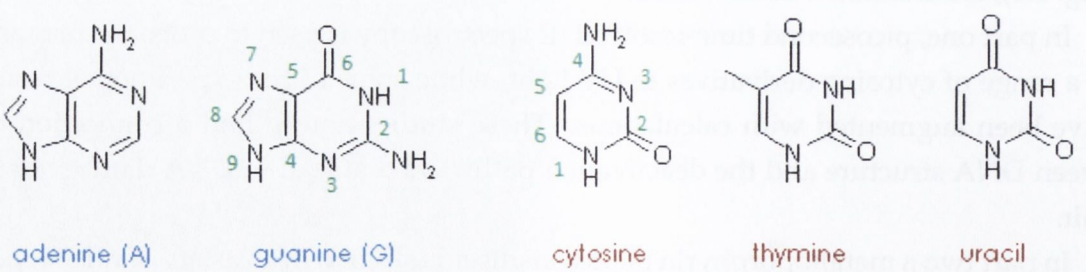

Figure 1.2: The nucleobases, with purines in blue and pyrimidines in red. Ring numbering scheme is shown

position to form a nucleoside or a nucleotide (Fig. 1.4), with the distinction between RNA and DNA arising with the absence or presence of the 2′-hydroxy substituent on the sugar.

These basic units are linked together by a phosphodiester backbone to form the characteristic DNA polymer. RNA usually exists as a single strand, while the double-stranded DNA structure arises from selective base complementarity (A-T and G-C) formed by hydrogen bonding (Fig 1.5). However many different base-pairing combinations are possible following tautomeristation or protonation of the bases.

Double-stranded and single-stranded DNA and RNA can exist in a number of helical conformations, namely A,B and Z DNA (Fig. 1.6 on page 5). The preferred structure is sensitive to properties such as ionic strength, hydration and base-sequence and composition. The difference in higher order structure is usually reflected in the stereochemistry of the ribose group, with RNA preferring the C3′ endo conformation (Fig. 1.3).

DNA can also interact with smaller molecules, either covalently or non-covalently. For the latter case, which is most relevant to this thesis, there are three principal modes of association (see Fig. 1.7 on page 5)[3].

- outside binding - non-specific electrostatic interactions with phosphate groups (e.g. metal cations, spermine)
- intercalation - planar aromatic/heteroaromatic molecules insert between steps in DNA forming hydrophobic stacking contacts (e.g. daunomycin)
- groove binding - molecules bind in either minor or major groove by specific contacts with DNA functional groups (typically curved cationic molecules such as netropsin)

Many spectroscopic techniques can be used to characterise DNA and drug-DNA interactions, including NMR, IR, resonance Raman, circular and linear dichroism, fluorescence and transient techniques.

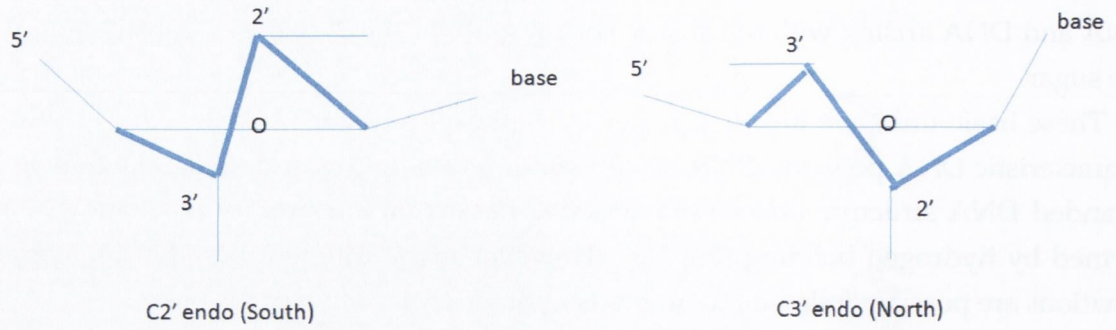

Figure 1.3: The C2′endo and C3′endo sugar conformations

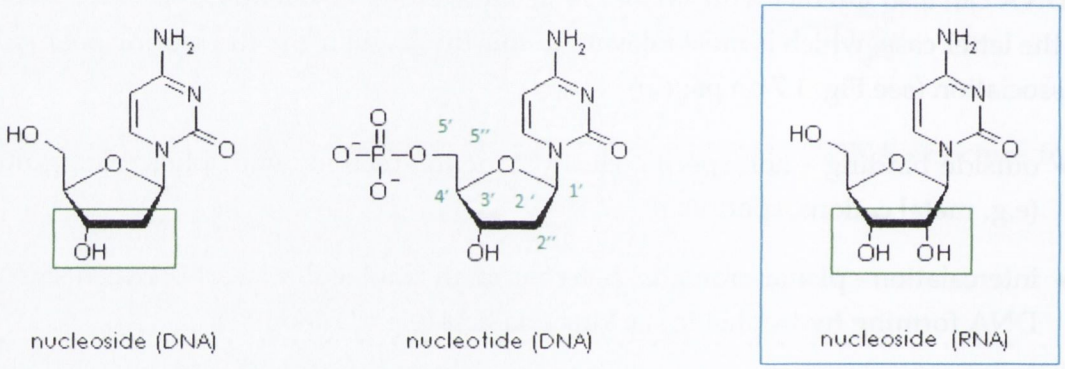

Figure 1.4: Nucleosides and nucleotides. Ribose numbering scheme is shown

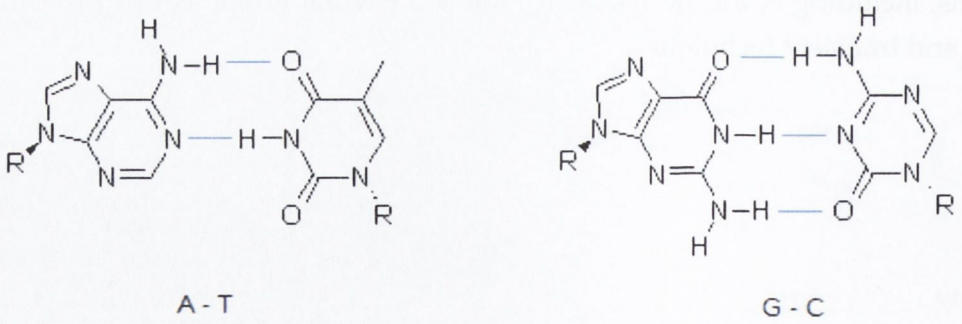

Figure 1.5: The Watson-Crick base pairs of double-stranded DNA

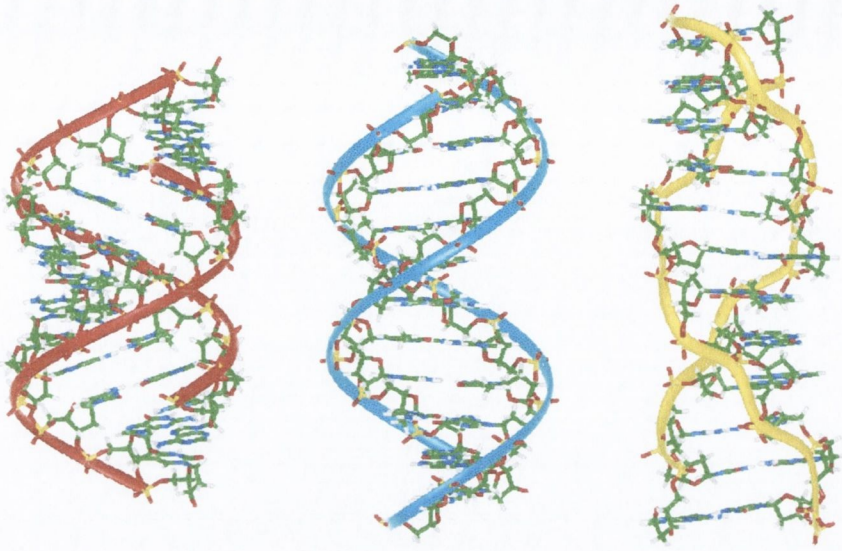

Figure 1.6: Structures of (left to right) A, B and Z DNA[2].

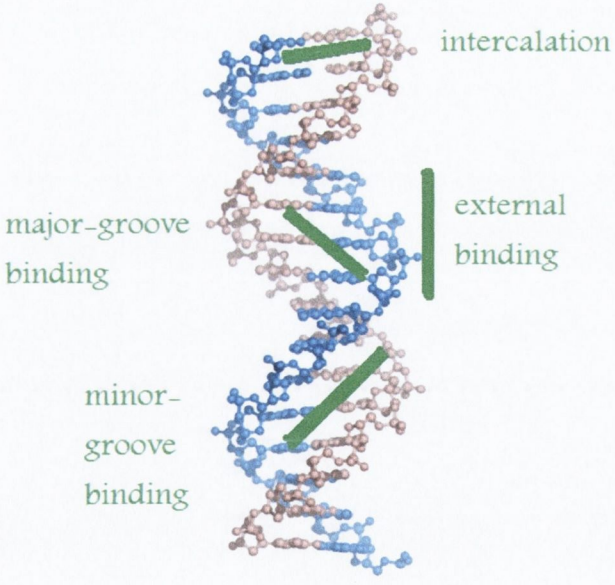

Figure 1.7: Modes of non-covalent binding of small molecules to DNA. (DNA image derived[4].)

Chapter 2

Direct Excitation of Cytosine-rich DNA: Introduction

2.1 Photochemistry and Photophysics of Nucleic Acids

The chromophores of DNA are the nucleobases, which absorb in the UVB and UVC regions below 300 nm (Fig. 8.15). Extinction coefficients are around $10^4\,\mathrm{dm^3\,mol^{-1}\,cm^{-1}}$, which decreases in base-stacked polymers due to exciton coupling. The bright state is the $^1\pi\pi^*$ state, which has been known for some time to have a low fluorescence quantum yield and short lifetime[5].

The ability of DNA to cope with incident UV radiation is crucial for the protection of genetic code, and the ultrafast decay helps to inhibit photochemical damage due to rapid removal of the energetic excited state (Fig. 2.2 on the following page). This is often cited as an evolutionary adaptation of the four nucleobases, which presumably

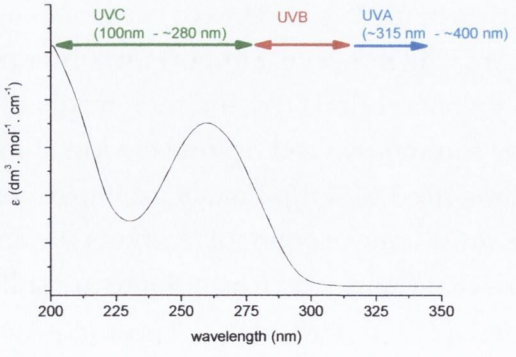

Figure 2.1: UV absorption spectrum of DNA with regions of the UV

evolved out of the necessity to survive strong fluxes of solar UV radiation in archaic times[6,7]. The ozone layer has developed since then, which effectively absorbs sunlight below 295 nm. More atmospheric penetration is thus achieved by UVB (290 -320 nm), which, although a small portion of the solar spectrum, is predominantly responsible for skin cancer.

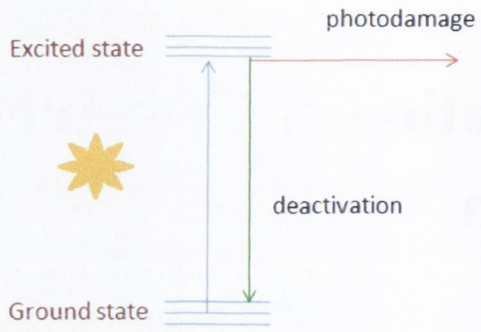

Figure 2.2: Fate of a UV-excited photon in DNA

The photochemistry of DNA has been studied extensively. However, the primary photophysical processes that occur immediately after UV absorption are not understood in the same detail. Although the lifetimes of the isolated chromophores are short, long-lived excited states can be formed on chemical modification of the nucleobases or on the formation of higher-order structure such as double-stranded DNA. Longer-lived states have greater potential to initiate harmful photochemistry, so there is much interest in long-lived excited states in nucleic acids.

2.2 Techniques for Studying Excited States of DNA

Studies of the photophysics of nucleic acids have been facilitated by recent advances in femtosecond spectroscopy. The three most important solution-phase methods are fluorescence, transient UV/vis absorption (TA) and time-resolved mid-infared (TRIR). Fluorescence techniques are commonly used despite the low fluorescence quantum yields of the nucleobases, and the need to scrupulously exclude fluorescent impurities. However, the sensitivity and short time response of methods such as single photon counting and upconversion means that fluorescence techniques are still used widely to probe ultrafast radiative decay in DNA. In particular, the group of Gustavsson and Markovitsi has made extensive use of fluorescence techniques[8].

TA allows for monitoring of both excited-state absorption and ground-state recovery. It also offers some spectral information on emissive and non-emissive excited states

and other transient species. Bern Kohler and his group have presented data predominantly recorded by TA[1].

TRIR offers all the features of TA plus far superior structural detail and information on specific vibrational modes, particularly the in–plane aromatic and carbonyl stretches in the 1400–1750 cm^{-1} region. The main disadvantage of TRIR is that strong water absorption in this region necessitates the use of D_2O instead of H_2O.

2.3 Ground-State Properties of Cytosine Derivatives

There are six tautomers of cytosine (Fig. 2.3), though substitution at N1 means that three of these (4-6) are inaccessible in the nucleoside or nucleotide. The amino-oxo tautomer (1) is the most biologically prevalent tautomer, and it forms the Watson-Crick (W-C) base-pair with guanine. It is stabilised in solution due to a high dipole moment and good hydrogen-bonding affinity. Other rare tautomers can allow for alternative base-pairing motifs with non-trivial consequences, such as the point mutation that can form between adenine and the imino-oxo tautomer (3) of Cyt[9,10].

A number of computational studies have shown the influence of solvent effects on the structure of the cytosine nucleobase[11–16]. In particular, the carbonyl bond is

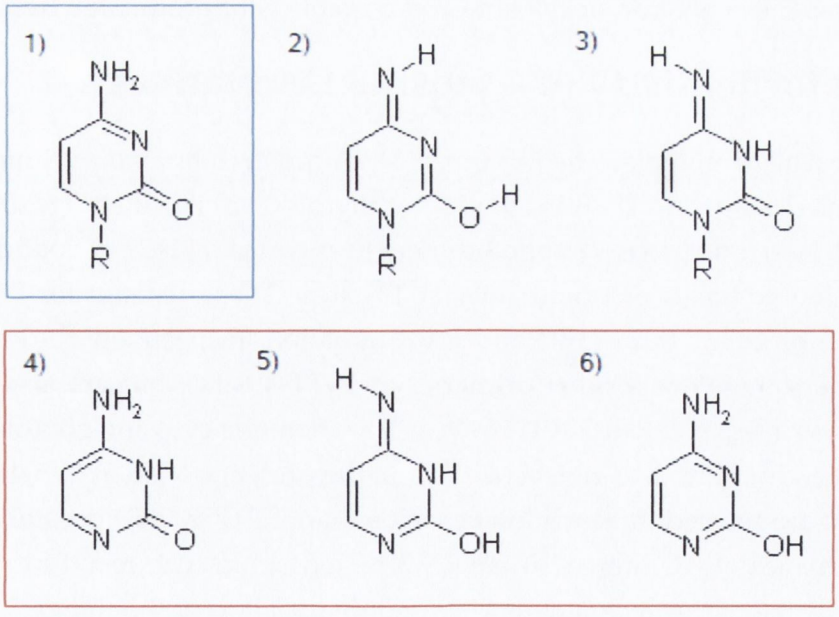

Figure 2.3: Tautomers of cytosine and derivatives. (1) canonical amino-oxo (2) imino-hydroxy (3) imino-oxo. Red panel shows tautomers (4-6) accessible only to the isolated nucleobase. All imino tautomers can exist as either E- or Z- rotamers

strengthened and the ring partially deformed due to H-bonding to the solvent[14], resulting in significant differences between the gas-phase and solution-phase IR spectra[9].

Cytosine derivatives can be protonated at N3 (pKa = 4.2), while deprotonation occurs on the sugar (pKa′ = 12.24)[17] The protonation of C opens additional routes to self-complementary base-pairs, as the protonated N3 can form a new H-binding site. These hemi-protonated base-pairs (Fig. 2.4) do not form in isolated systems, but play a central role in the structural chemistry of cytosine-rich polymer sequences, as shall be discussed later (Section 2.6.1.3).

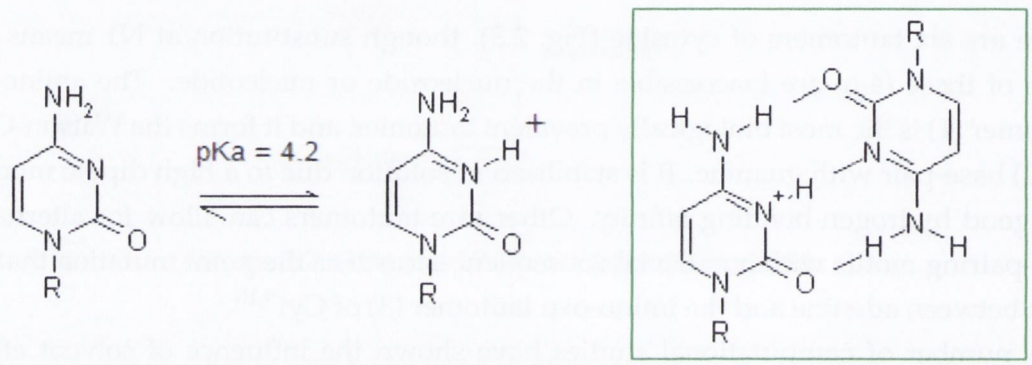

Figure 2.4: Protonation of cytosine and possible hemiprotonated base-pairs

2.4 Photochemistry of Cytosine Derivatives

The most prevalent photolesions in human DNA are cyclobutane pyrimidine dimers (CPDs), formed following UVB irradiation of thymine or cytosine (Fig.2.5). The most abundant of these are the *cis-syn* photodimers formed via a [2+2] cycloaddition across the C5=C6 double bond, predominantly at TT sites. These account for 77% and 78% of total photoproducts from UVC and UVB radiation, respectively[18]. Pyrimidine(6-4)pyrimidone dimers are formed primarily at 5′-TT-3′ sites, but are also induced at 5′-TC-3′ and to a lesser extent 5′-CC-3′ sites[19]. Monomeric cytosine photohydrates can be formed directly from the singlet state[3], or in the presence of an external sensitiser[20].

CC CPDs are formed in much lower yields than TT (Fig. 2.6), possibly due to the higher absorbance of CC dimers in the UVB region, which can result in rapid photochemical cleavage of the cyclobutane ring and dissociation of the dimer[18]. CC dimers have been studied much less than the TT counterparts, yet are more mutagenic. This is due to hydrolysis of CC dimers to UU lesions. The uracil bases subsequently base-pair with adenine, and the repair processes ultimately replace UU with TT. Such C-T and CC-TT transformations have been observed in skin cancer cells[20].

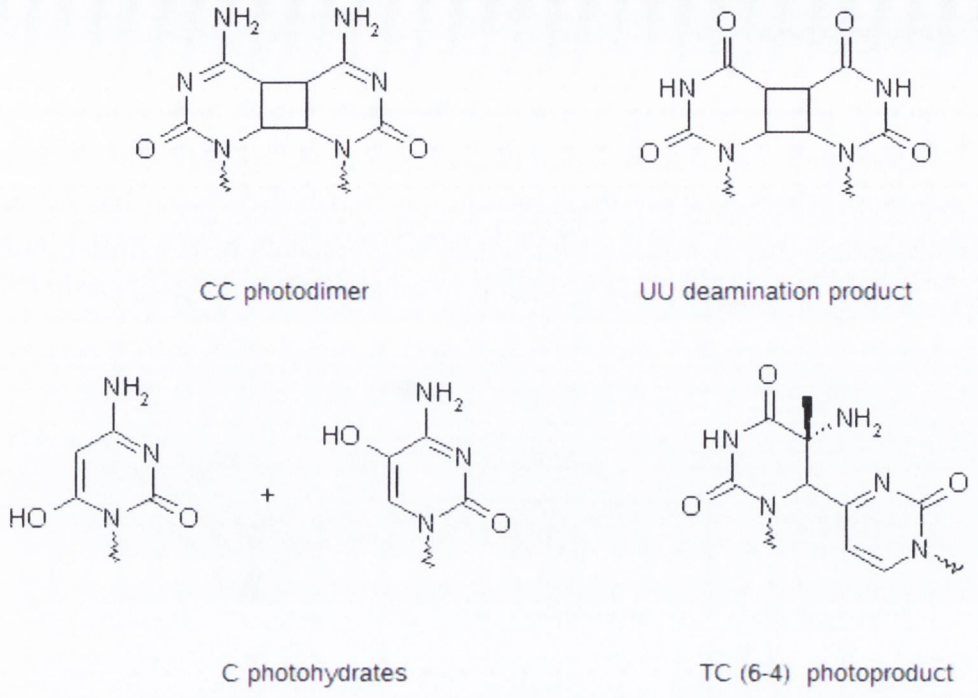

Figure 2.5: Various photoproducts of cytosine formed by UV irradiation

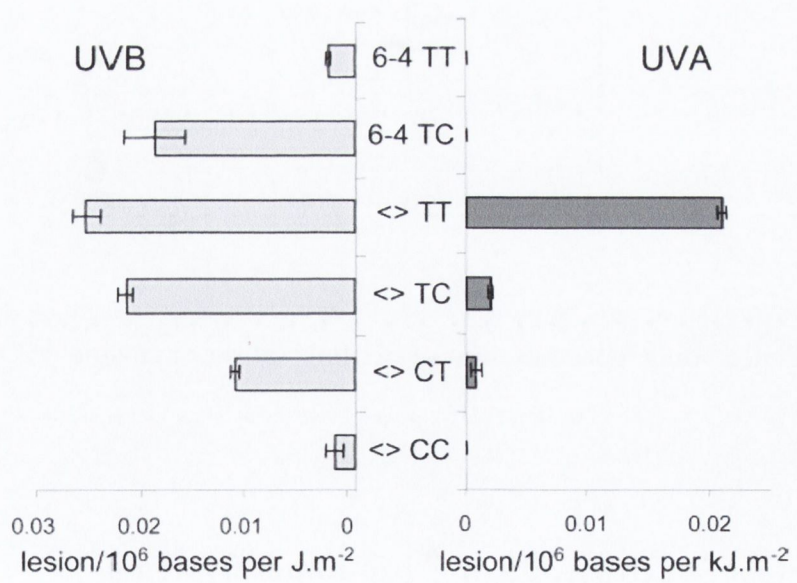

Figure 2.6: Chart comparing photochemical yields of common CPDs[21]

2.5 Photophysics of Cytosine and Monomeric Derivatives

The three lowest lying excited singlet states are the $^1\pi\pi^*$, $^1n_N\pi^*$ and $^1n_O\pi^*$ (Fig. 2.7). The $^1\pi\pi^*$ is actually the second singlet excited state (S_2) in C according to some calculations[22], while it is the S_1 state in thymine and uracil. The $^1\pi\pi^*$ state has by far the highest oscillator strength, so this is populated with UV excitation. The triplet state has a lifetime of around 250 ns and is formed with a very low quantum yield (<0.01)[23].

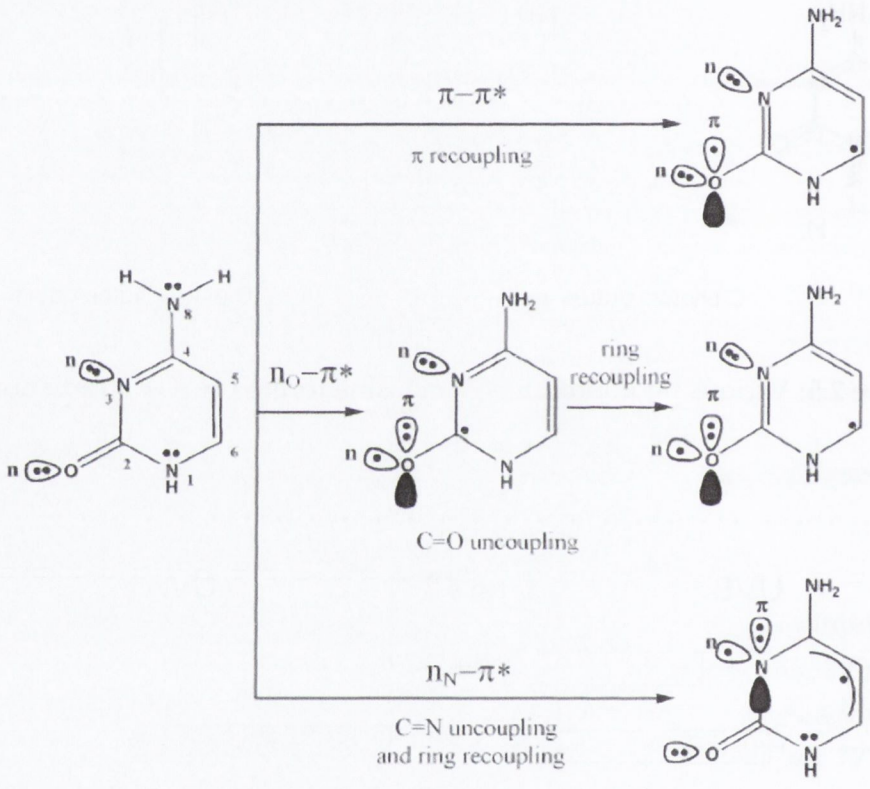

Figure 2.7: Valence bond representation of excited states of cytosine[24,25] (from Quinn et al[25])

2.5.1 Ultrafast Spectroscopy of C Monomer Systems

The singlet-state photophysics of cytosine and its monomeric derivatives (see for example Fig. 2.8 on the facing page) have been the subject of extensive experimental study over the past decade, with some variations reported in singlet excited-state lifetimes

(see Table 2.1). These disagreements may often be attributed to the limitations of the technique employed, the time resolution, or how data is fitted and interpreted.

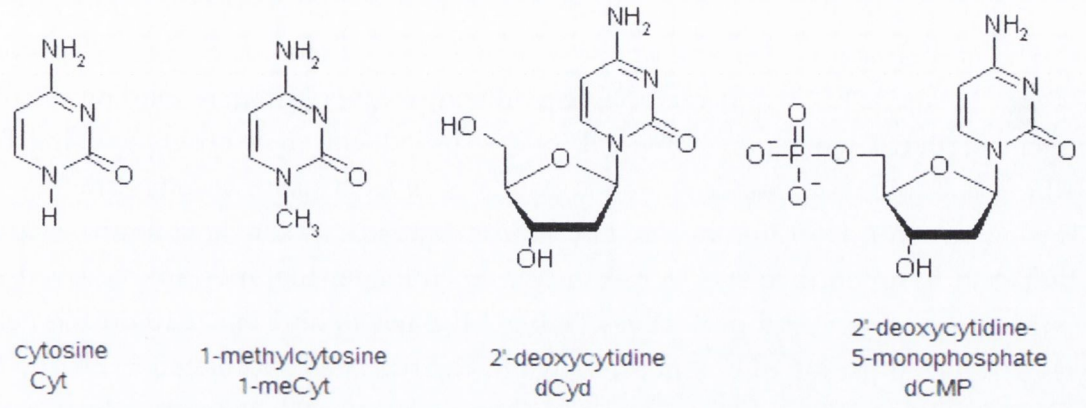

Figure 2.8: Structures of C-monomers with standard abbreviations

Table 2.1: Summary of data from aqueous-phase ultrafast studies on Cyt and monomeric derivatives

Species[ref]	Lifetimes	Technique	Species[ref]	Lifetime	Technique
Cyt[26]	1.1 ps	TA	Cyt^-[17]	13.3 ps	TA
	200 fs, 1 ps	upconversion	Cyd^+[17]	630 fs	TA
Cyt[17]	1 ps	TA	5-meCyt[17]	7.2 ps	TA
Cyt[27]	2.9 ps†, 12 ps	TA 250 nm (bleach)	5-meCyt^+[17]	2.57 ps	TA
	0.7 ps, 12 ps	TA 340 nm (trans.)	5-meCyt^-[17]	250 ps	TA
Cyt[25]	4.4 ps†	TRIR	5-meCyd[17]	7.2 ps	TA
dCyd[28]	180 fs, 920 fs	fluor	5-FCyt[17]	88 ps	TA
dCyd[25]	2.6 ps†, 37 ps	TRIR	4N-AcCyd[17]	250 ps	TA
Cyd[5,29]	720 fs	TA	5-meCyd[17]	7.2 ps	TA
Cyd[30]	720 fs	fluor	5-meCyt[31]	1.1 ps, 5.9 ps	fluor
Cyd[17]	1 ps	TA	5-FCyt[32]	73 ps	TA
dCMP[28]	270 fs, 1.38 ps	fluor	$dCMP^+$[25]	4.0 ps	TRIR
dCMP[25]	33 ps	TRIR			
dCMP[27]	3.7 ps†, 34 ps	TA 250			
	0.7 ps 34 ps	TA 340			

†vibrational cooling of S_0.

2.5.1.1 Cytosine

The aqueous-phase $^1\pi\pi^*$ lifetime of cytosine has been measured as <1 ps[17,26]. Ultrafast internal conversion in cytosine and C derivatives is believed to occur due to a near-barrierless conical intersection between the singlet excited state(s) and the ground state. The ground state is hence formed with an excess vibrational energy of approx. 34,000 cm^{-1} (Fig. 2.9)[5]. In aqueous solution, solvent-solute hydrogen bonding results in rapid vibrational cooling on a timescale of 2 – 4 ps, which can be observed using TA or TRIR[25,29]. Cooling is retarded in non H-bonding solvents such as acetonitrile[33].

The key structural features involved in the ultrafast internal conversion can be studied by substituting on the ring. For example, much longer lifetimes are observed in the 5-fluoro and 4-N-acetyl derivatives (Table 2.1, page 13 and Fig. 2.10 on the next page)[17]. The lengthening of lifetimes relative to Cyt has been speculated to be due to stabilisation of the excited state structures, with an increase in the barriers to the conical intersections with the ground-state[17,32].

Incidentally, cytosine has been reported to have multiexponential decay kinetics in the gas-phase[34–37]. However in these cases the tautomer populations, and ordering of the excited states, are expected to be differ from those in solution[38,39].

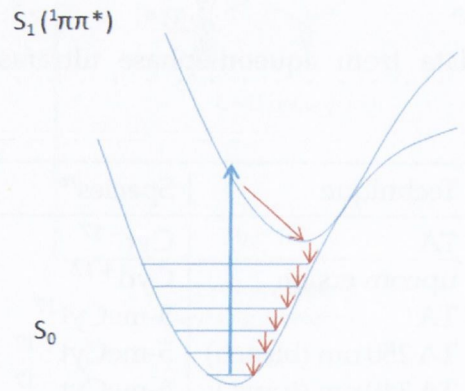

Figure 2.9: Excitation into Frank-Condon (FC) region followed by decay via conical intersection and vibrational cooling of ground state

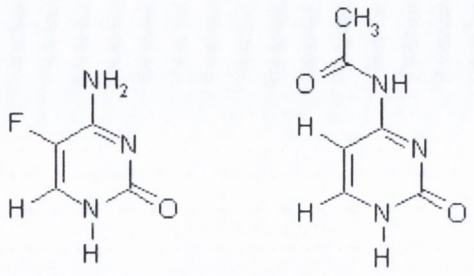

Figure 2.10: Structures of 5-FCyt and 4N-AcCyt[17]

2.5.1.2 N1 substitution - (2′-deoxy)cytidine and (2′-deoxy)cytidine monophosphate

The most important modification on the cytosine ring is the addition of the ribose substituent to the N1-position. Initial ultrafast experiments showed the $^1\pi\pi^*$ lifetimes of cytidine in H_2O (720 fs[5,29] and 760 fs[30]) to be similar to that of cytosine, with a small increase observed for dCMP (960 fs). Markovitsi and co-workers later argued that fluorescence decays in dCyd and dCMP must be described as biexponential, and reported that the lifetime of both components was sensitive to the presence of the phosphate group[28]. Malone et al observed a more intense transient absorption signal for cytidine than cytosine, suggesting to them that vibronic coupling between sugar and base in cytidine increases the S_1-S_N absorption cross section relative to cytosine[17].

Subsequent fs TA measurements from the Kohler group show that bleach recoveries at 250 nm for cytosine and CMP are both biexponential[27]. However the magnitude and relative amplitude of the longer-lived component is larger for CMP. This was suggested to be due to population trapping on the $^1n\pi^*$ surface, whereby H-bonding of solvent to the sugar group induces rapid cooling of the $^1n\pi^*$ to its energy minimum. This $^1n\pi^*$ excited state is observed in each of the pyrimidine mononucleotides, and is suggested to provide a route to the triplet state, which is a known precursor to CPD formation. Similar kinetics observed in uracil, 1-cyclohexyluracil and 1,3-dimethyluracil lead the authors to suggest that the long-lived state is sensitive specifically to the presence of the ribose at the N1 position[27,40].

Sensitivity to N1-ribose/deoxyribose substitution is also revealed by ps-TRIR in D_2O solution[25]. Lifetimes of 2-4 ps are observed for Cyt, dCyd and dCMP due to vibrational cooling of hot ground states, while a second component is present for dCyd (37 ps) and dCMP (33 ps), but not for Cyt (Fig. 2.11 on the following page). Moreover, the long-lived decay is accompanied by a transient feature at 1574 cm^{-1}. The two $^1n\pi^*$ states ($^1n_N\pi^*$ and $^1n_O\pi^*$) were considered, and the $^1n_N\pi^*$ state was favoured on the

assumptions that the transient was a carbonyl stretch, and that the carbonyl stretch in the $^1n_O\pi^*$ state would be shifted to much lower frequency.

The similar kinetics recorded for cytosine nucleotides in H_2O and D_2O suggests that there is no solvent isotope effect in the decay of the $^1n\pi^*$ state. Similar observations have been made with uracil[40].

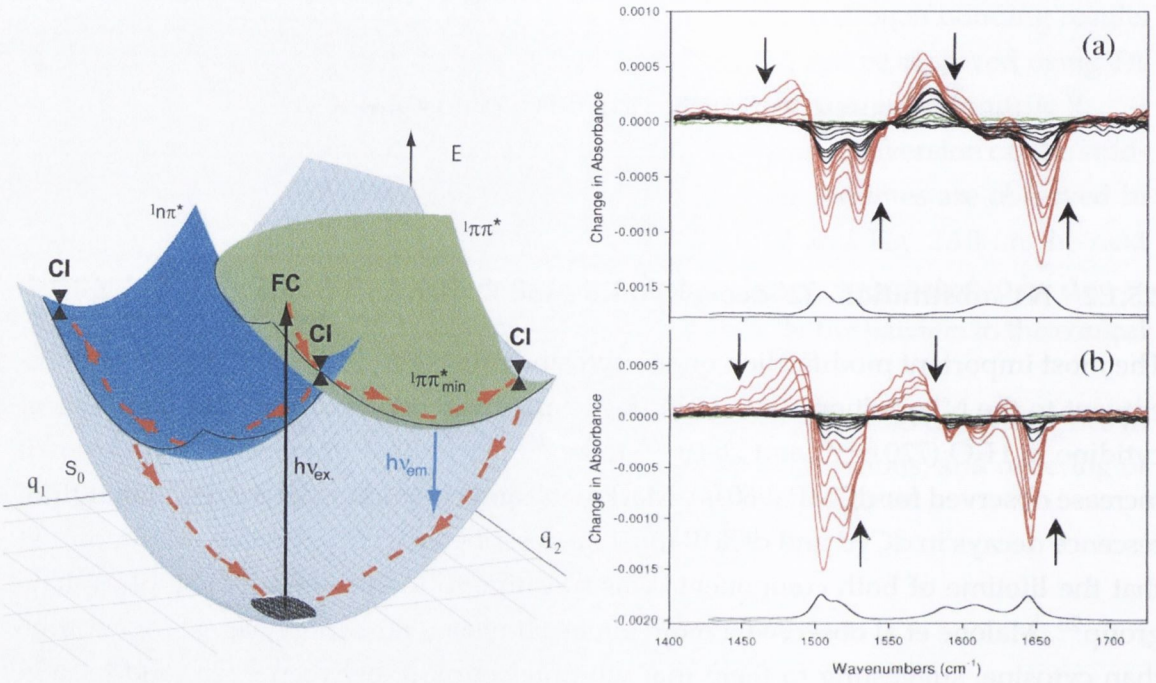

Figure 2.11: LEFT: Model of the $S_0/S_1/S_2$ surface in pyrimidines[27]. RIGHT: TRIR spectra of (a) dCyd and (b) Cyt[25]. Decays from 2-10 ps in (red), 15-1000 ps (black). The $^1n\pi^*$ absorption is evident in dCyd at 1574 cm^{-1}

2.5.2 Computational Studies on C Monomers

Important contributions have been made to DNA photophysics by computational chemistry. In the case of cytosine, a particular focus of work has been on the role of the $^1\pi\pi^*$, $^1n_N\pi^*$ and $^1n_O\pi^*$ states in ultrafast decay in the gas phase.

2.5.2.1 Cytosine in the Gas Phase

Complete active space self consistent field (CAS-SCF) and time-dependent Becke three-parameter Lee-Yang-Parr (TD-B3LYP) calculations by Ismail et al[24] suggest that the primary path to the ground state in photoexcited cytosine is via a state switch from the close-lying $^1\pi\pi^*$ to $^1n_O\pi^*$ followed by a $^1n_O\pi^*/S_0$ conical intersection. Access to the

$^1n_N\pi^*$ is blocked by a 0.42 eV energy barrier due to considerable distortion around N3 (Fig. 2.12a).

Merchan and Serrano-Andrés[41] added dynamic correlation energy with the complete active space perturbation theory (CAS-PT2) method, and, in contrast to Ismail et al, propose a direct $(^1\pi\pi^*/S_0)_{CI}$ as the primary mechanism of radiationless deactivation. They propose that the $^1n_O\pi^*$ and $^1n_N\pi^*$ states have only a minor role in the photophysics due to significant energy barriers from the $^1\pi\pi^*$ state of 0.42 eV and 0.5 eV, respectively (Fig. 2.12b).

The contrasting models proposed by Ismail and Merchan reveal a strong dependence on the chosen level of theory in the calculation. Blancafort and Robb[42] attempted to reconcile some of the disagreement by combining both CAS-SCF and CAS-PT2 methods. This more advanced treatment yielded a three-state degeneracy between the $^1\pi\pi^*$, $^1n_O\pi^*$ and ground states. This conical intersection occurs along two seams of degeneracy - the S_1/S_0 and S_2/S_1 (Fig. 2.13 on the next page). Because of the S_2/S_1 crossing, excitation into the Franck-Condon (FC) region results in an excited state that is neither a pure $^1\pi\pi^*$ nor $^1n_O\pi^*$, but a vibronically coupled mixture of both. The authors therefore comment that the excited state becomes progressively darker, and that recrossing from S_1/S_0 to S_2/S_1 may result in a longer-lived decay pathway. They correlate this with the (relatively) long 3.2 ps gas-phase lifetime recorded for cytosine by photoelectron spectroscopy[35], though this lifetime has since been re-evaluated as a 1.82 ps component[36].

There have been several studies on an $(S_1/S_0)_{CI}$ for pyrimidines that involves an ethene-like out-of-plane distortion of the 6-membered ring (Fig. 2.14 on the following page), with little input from $^1n\pi^*$ states. This is proposed to occur in uracil[43] and G-C base pairs[44], as well as in cytosine[39,45,46]. The conical intersection with the ground state

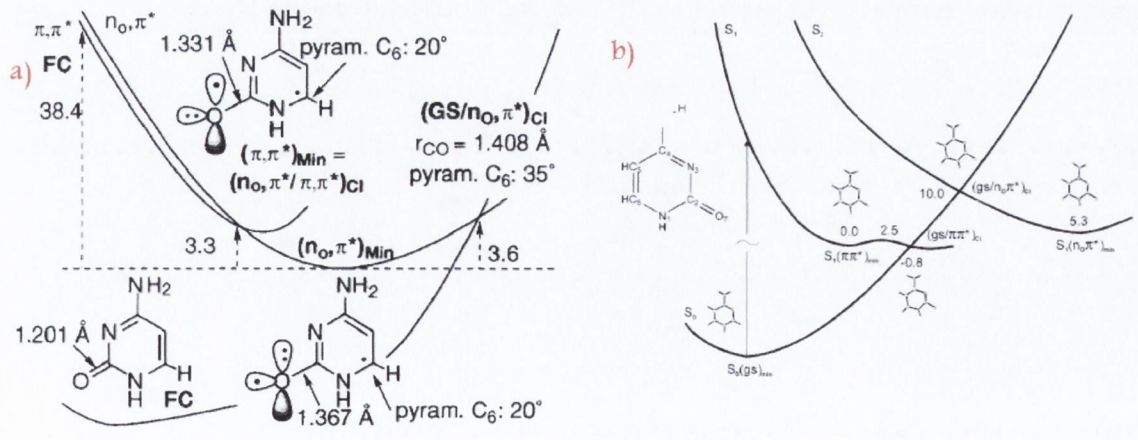

Figure 2.12: Primary decay pathways in cytosine as predicted by (a) Ismail et al[24] and (b) Merchan and Serrano-Andrés[41]. Energies in kcal mol^{-1}

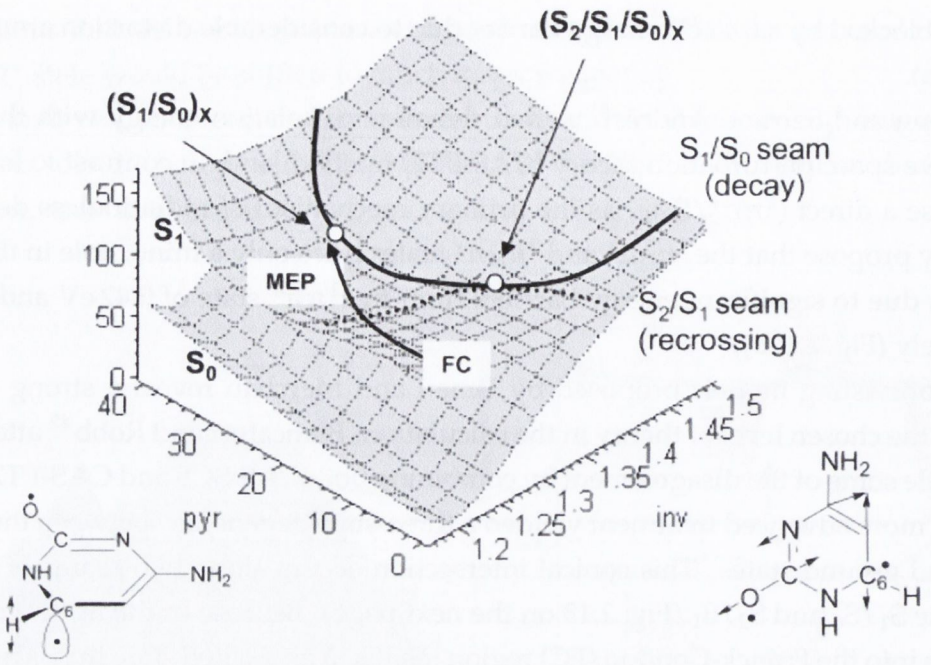

Figure 2.13: Theoretical three state model of Blancafort and Robb[42]

involves a twisting of the C5=C6 bond. The hydrogens of C5 and C6 become displaced in opposite directions, and singly occupied p_z orbitals are decoupled from ring plane, creating a biradical state. Zgierski et al claim that 5-fluoro substitution stabilises the $^1\pi\pi^*$ state resulting in a longer lifetime, and add that this result cannot be explained by the models of Ismail or Merchan[45]. A significant observation is that in biradical decay the ring distortion occurs away from the C2N3C4 plane. This implies that the ultrafast decay channel is preserved in W-C-paired double-stranded DNA.

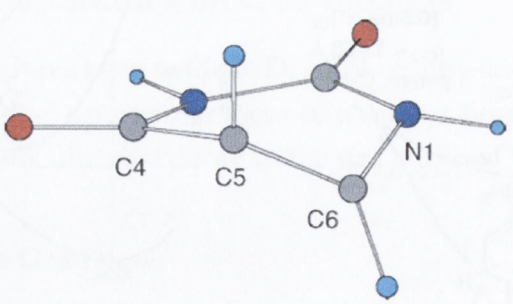

Figure 2.14: Biradical structure of cytosine $^1\pi\pi^*$ excited state showing displaced C5 and C6 protons[46]

Merchan et al[47] revisited their previous studies with a CAS-PT2//CAS-SCF study on the pyrimidine bases (C,T,U). The barrierless $(^1\pi\pi^*/S_0)_{CI}$ is described as an ethene-like structure and is implicated in the 160 fs decay recorded by Canuel et al[36] However, the authors stress the need for dynamic correlation to optimise the calculations due to the effect of very small energy changes on the decay mechanisms.

Blancafort[48] proposes a more complete model for cytosine by recalculating energy barriers using a consistent high level of theory, namely optimisation at the CAS-SCF level and recalculation at the CAS-PT2 level, with a focus on the contribution of the $^1n\pi^*$ states. These calculations show that the most favourable route is along ethylene C5-C6 lengthening and N1-C6 shortening (Fig. 2.15a). The barrier to the CI along the $^1n_O\pi^*$ bond inversion pathway is quite high (>1.4 eV). The barrier to $^1n_N\pi^*$ is 0.2 eV with respect to $(^1\pi\pi^*)_{min}$ (Fig. 2.15b). The $^1n_O\pi^*$ is suggested to contribute to excited-state decay as its energy minimum lies below the vertical excitation energy of cytosine (0.8 eV)[48].

A number of other studies have been published on conical intersections in cytosine[22,49,50], though Hudock and Martinez claim that molecular dynamics calculations are needed to accurately describe the photophysics of cytosine[51], considering the number of apparent potential decay routes (i.e. conical intersections between the ground state and the $^1\pi\pi^*$, $^1n_N\pi^*$ or $^1n_O\pi^*$ states). For this problem they used *ab initio* multiple spawning (AIMS). The electronic structure was solved using state averaged (SA) CAS-SCF and the SA-5-CA5(12/9)-MSPT2 method. They show that many of the decay pathways are accessed simultaneously in under 1 ps, and that exited-state quenching occurs by all three CIs: the $^1n_N\pi^*/S_0$ (65%), $^1n_O\pi^*/S_0$ (15%) and $^1\pi\pi^*/S_0$ (5%). 62% of the $^1n_N\pi^*$ population pass though the $^1n_O\pi^*$ state first. There is also cross-talk between these three trajectories so they do not act independently (see Fig. 2.16). Significantly, the

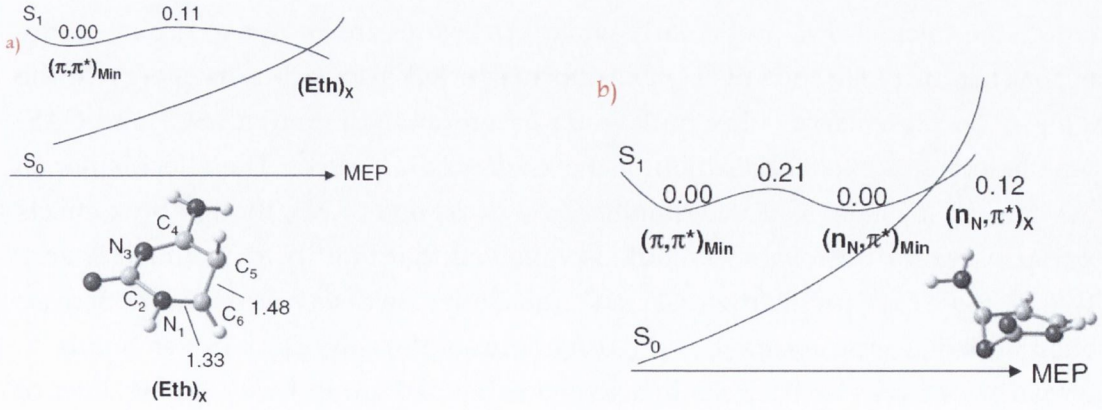

Figure 2.15: (a) Decay via ethene-like CI (b) Decay via $(^1n_N\pi^*/S_0)_{CI}$ from Blancafort[48]

authors observe population trapping on the $^1n_O\pi^*$ state surface, which they note to be consistent with the long-lived dark states observed in solution by Hare et al[27].

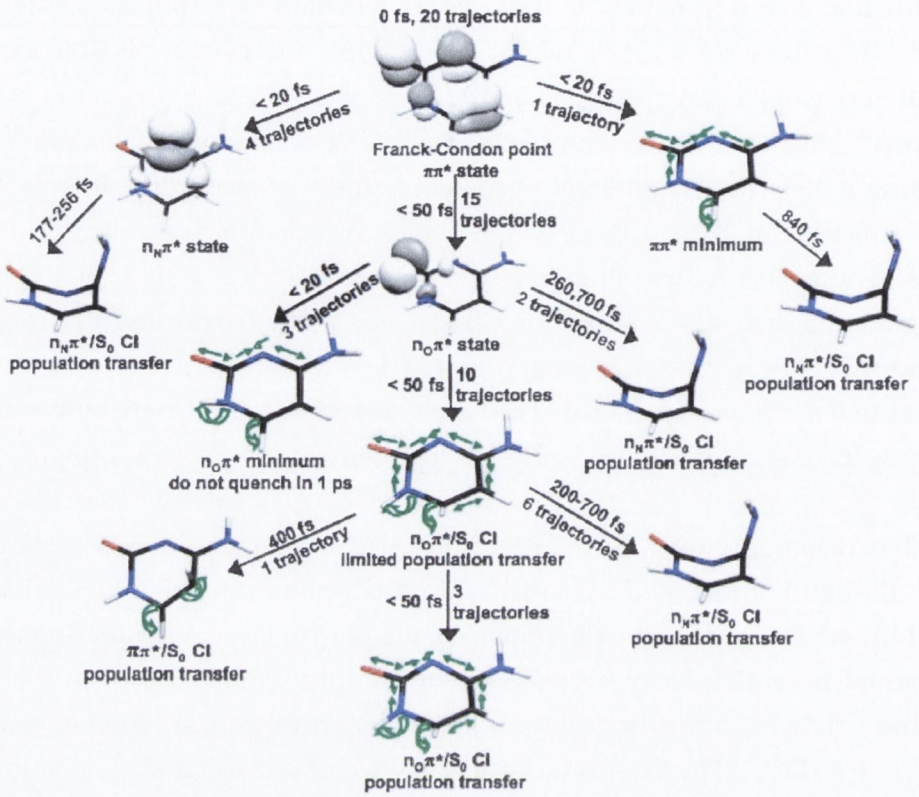

Figure 2.16: Multiple decay pathways of photoexcited cytosine as calculated by Hudock and Martinez[51]

2.5.2.2 Effects of Solvent

In order to approximate biological conditions it is essential to mimic an aqueous environment in the calculations, particularly when $^1n\pi^*$ states are known to rise in energy in the presence of polar solvent[48]. Blancafort reported a lowering in energy of the $(S_1/S_0)_{CI}$ in the presence of either bulk water or a monohydrate (CAS-SCF and CAS-PT2 calculations), due to stabilisation of the zwitterionic state[52]. The effect is not so clear for the $^1n_N\pi^*$ state, as it is destabilised by hydration of N3, though bulk effects may compensate for this. Santoro et al also showed that the $^1n_N\pi^*$ in uracil is very sensitive to hydration, predicting that $^1n\pi^*$ transitions are disfavoured by an increase of solvent bulk dielectric constant, and particularly solute/solvent hydrogen bonds[53].

Comparisons have also been made between H-bonded ground and excited states of cytosine using Hartree-Fock/CIS theory. Differences in H-bonding pattern have been calculated between ground state and the excited $^1n_N\pi^*$ states (Fig. 2.17)[16].

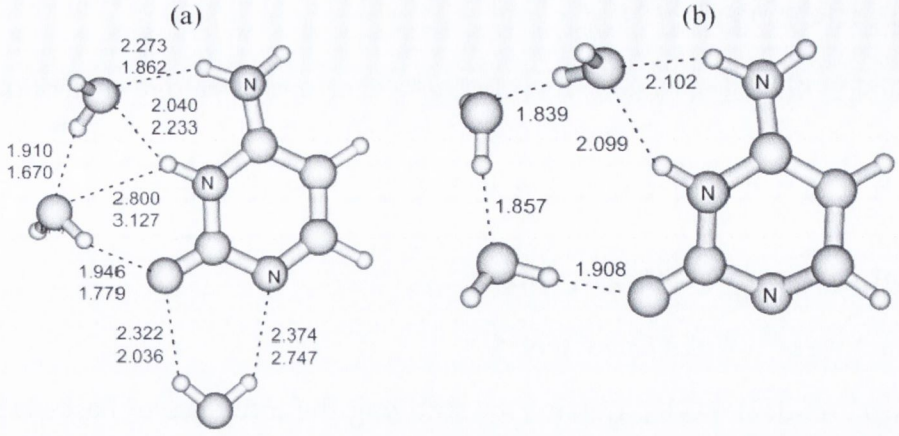

Figure 2.17: Optimised structures of (a) ground state and (b) $^1n_N\pi^*$ excited state of cytosine with three H-bonded H_2O molecules[16]. Bond distances in Å

2.5.2.3 Effects of Substitution at N1

The papers discussed so far have not considered 1-substituted pyrimidine derivatives. Experiments have proven this to be a significant oversight, as it is now known that sugar substitution has an influential role in excited-state decay in pyrimidines[25,27]. So et al calculated that sugar substitution results in an increase in the oscillator strength of the $^1\pi\pi^*$ state by about 50% in pyrimidines in the gas-phase[54]. The $^1\pi\pi^*(S_1)$ - $^1n\pi^*(S_2)$ gap is also increased slightly on progressing from cytosine to cytidine or deoxycytidine, though the authors do not expect these shifts to result in qualitative changes in excited-state decay. However, they note that the S_3 ($^1n\pi^*$) and S_4 ($^1\sigma\pi^*$) states have substantial contributions from ribose states.

The only systematic report of a family of pyrimidine monomers has been for thymine (Thy) by Improta and Barone[55]. They have studied 1-MeThy, Thy and TMP[55] using DFT and TD-DFT for ground and excited states, respectively, while also applying a polarisable continuum model (PCM) to account for bulk solvent effects. In 1-MeThy, the methyl at N1 does not affect significantly the n and π^* orbitals, whereas the π orbital is slightly destabilised due to anti-bonding interactions with the methyl CH groups. As a result the $S_0 \rightarrow S_1$ transition is red-shifted by approx. 0.1 eV with respect to T. Replacement with sugar does not alter π and π^*, but the n orbital is now mixed with orbitals on the sugar. The calculated result is an increase in oscillator strength of $^1n\pi^*$ transitions, which the authors mention may have implications for excited-state decay in nucleosides and nucleotides.

2.6 Polymer Systems

In natural DNA, the bases exists as a polymer consisting of linked nucleotides. The higher-order structure introduces additional structural features such as base-pairing and base-stacking, which are known to affect excited-state properties.

2.6.1 Structure of C-rich Polymers

2.6.1.1 Structure of d(CpC) Dinucleotide

Dinucleotides are ideal model systems for studying the influence of base-stacking in the absence of base-pairing. Free rotation around seven bonds, and variable pucker of the sugar groups, allows for diverse conformations[56]. However, the 'two-state' model is generally adopted, where the structure is considered as a rapid equilibrium between the stacked and unstacked forms[57](Fig. 2.18). The stacked form exists in a right-handed conformation, while the extended form adopts a left-handed structure[58]. The equilibrium is known to shift toward the unstacked form as temperature increases, and the degree of stacking has been monitored quantitatively using NMR[58–62] and CD spectroscopy[56,63]. r(CpC) has been determined to be 35% and 55% stacked at 20 ^{0}C by NMR[58] and CD[63], respectively. However the latter value was recorded in 4.7 M KF solution (to lower the freezing point). d(CpC) has been found to be quite poorly stacked compared to r(CpC), as shown from CD[64,65] and calculations[66–69], although no values for percentage stacking have been reported. The lowest energy sugar pucker conformation is unstacked[68], and the B-form structure has little overlap although bases are parallel (Fig. 2.19 on the next page)[67].

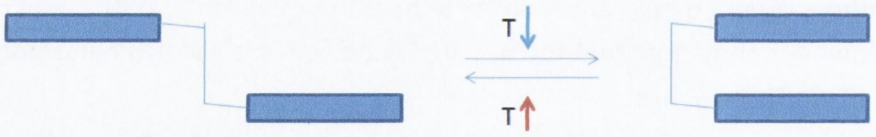

Figure 2.18: Schematic of the temperature-dependent equilibrium between stacked and extended forms of dinucleotides

2.6.1.2 Structure of Poly(rC) Polynucleotide

The absence of Watson-Crick base-pairing in RNA homopolymers means that such species exhibit more structural heterogeneity than either double-stranded DNA or dinucleotides. Poly(rC) is a simple sequence but is suspected to have biological significance, as long rC tracts have been observed in a number of viruses[70]. The structural

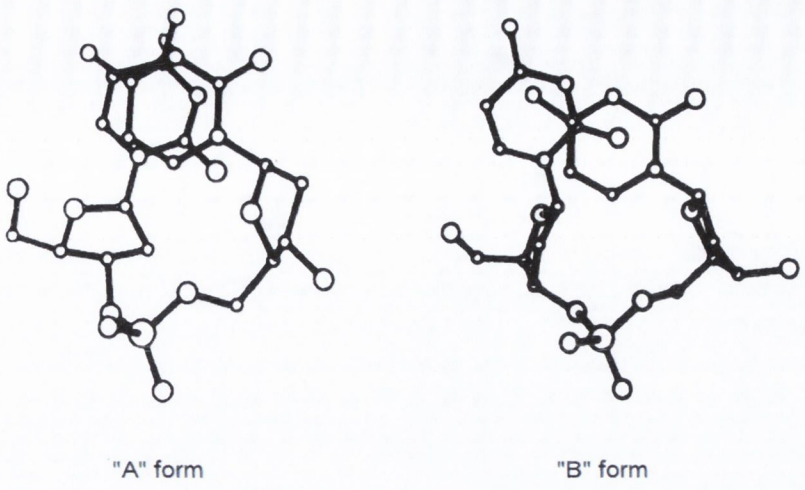

Figure 2.19: Calculated lowest energy structures of d(CpC) in 'A' and 'B' form[67]

properties of the poly(rC) polynucleotide have been discussed in detail in the literature, though these studies have been complicated by the ability of cytosine to form hemi-protonated base-pairs at low pH (see Section 2.3). Early X-ray crystal structures show poly(rC) in a right-handed helical form with another closely wrapped poly(rC) molecule, stabilised by hemi-protonated C and hydrogen bonds[71].

IR and UV studies at variable pH imply that poly(rC) exists as a single strand in neutral conditions. At pH 5.7 it undergoes a transition from single-stranded to double-stranded, due to the formation of hemi-protonated C-CH^+ base pairs. At pH 5 it is hemi-protonated. At pH 3 and below, electrostatic repulsion forces the structure to separate into two single strands[72]. Similar transition pHs of 3.7 and 5.5 have been determined from Raman spectroscopy[73]. It is also reported that at temperatures <40°C, neutral poly(rC) is in the A-form with stacked cytosine bases, gradually lost on heating to 90°C. The hemi-protonated double strand cooperatively melts into two identical single strands of alternating positive charge at 80°C. This denatured structure is ordered, but is not stacked and not in the A form.

Broido and Kearns, using a variety of 1D and 2D NMR methods, constructed a model for poly(rC) (at pH 7.1) that is left-handed, and possibly stabilised by hydrogen bonds between carbonyl and amino groups of adjacent bases (Fig 2.21 on the following page)[74]. Significantly, the bases are not stacked in their model, but are tilted at 45° to each other. Some support for this structure is found from vibrational Raman optical activity measurements[75].

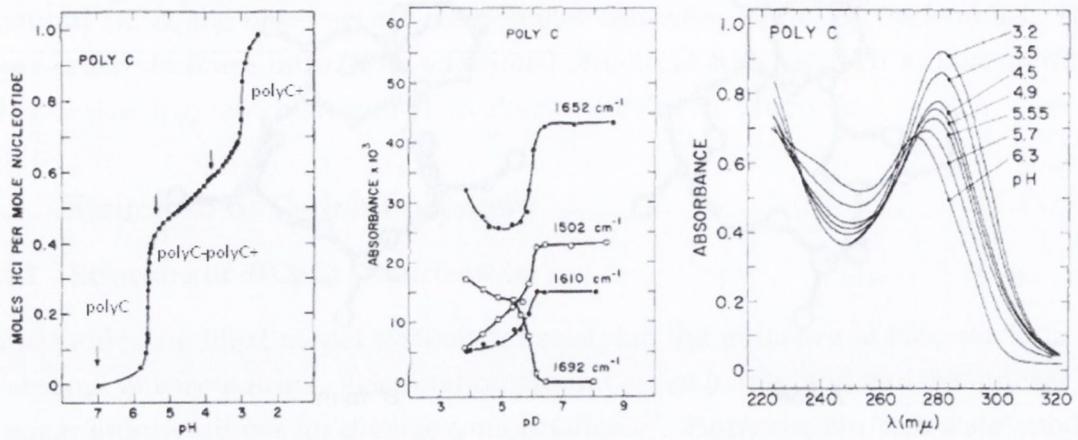

Figure 2.20: Spectroscopic properties associated with the pH-dependent structure of poly(rC). LEFT: pH curve MIDDLE: IR intensities RIGHT: UV spectra[72]

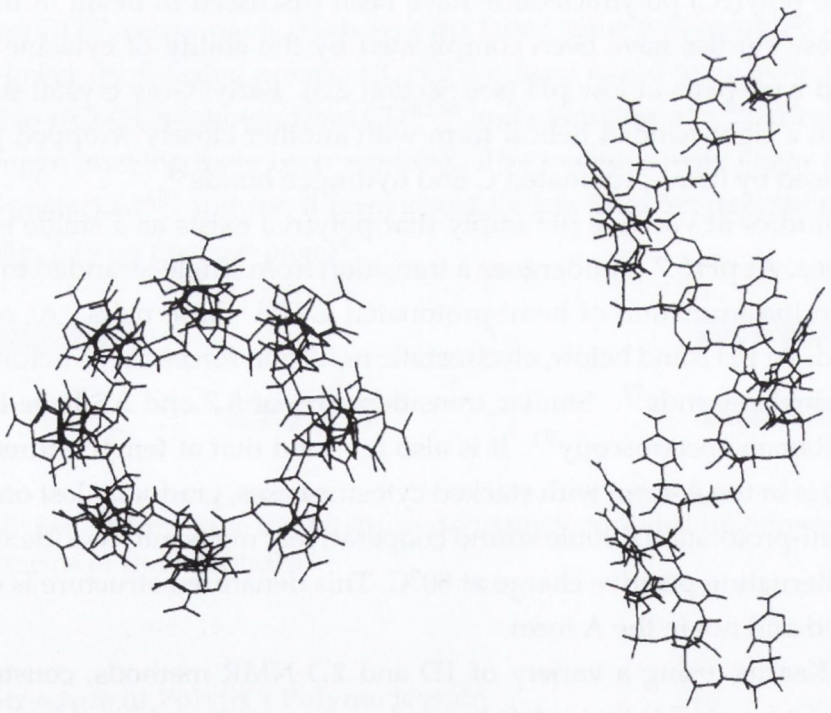

Figure 2.21: Structure of poly(rC) at pH 7.1 from Broido and Kearns[74]. Note that the bases are not stacked in this model

2.6.1.3 Structure of the i-motif

The loss of the ribose 2′-hydroxyl group in dC-rich sequences results in different structural morphologies to those seen in rC systems. Hemi-protonated deoxycytidilates can form the tetrameric i-motif structure, consisting of interdigitated C–CH^+ base pairs (Fig. 2.22). This structure is unique for C and it is believed to play a biological role as dC-rich sequences exist in telomeres and centromeres in chromosomes. I-motifs in promoter regions of certain oncogenes show promise as targets for cancer therapy[76], while the formation of i-motifs is also linked to the onset of insulin-dependent diabetes mellitus[77].

The structure of the i-motif was first recognised from NMR[78] and X-Ray crystallography[79,80] in the 1990s. Four strands of at least two consecutive Cs are required for i-motif formation[81]. The structure exists as parallel strands in antiparallel orientation, with sugars present in both C2′ endo and C3′ endo conformations. There is no direct vertical stacking of the C-rings due to electrostatic repulsion, though the exocyclic amino and carbonyl stack on top of each other. In some sequences (e.g. C_3T), hemi-protonation can oocur at physiological pH[79]. It is claimed that the stability of dC over rC for these structures is due to sugar-sugar contacts and the energetic penalty for desolvating the 2′-hydroxy group in rC[82,83]. The interdigitating structure gives rise to a characteristic CD spectrum which can be used to monitor the pH-dependent formation of the i-motif (Fig 2.23 on the next page).

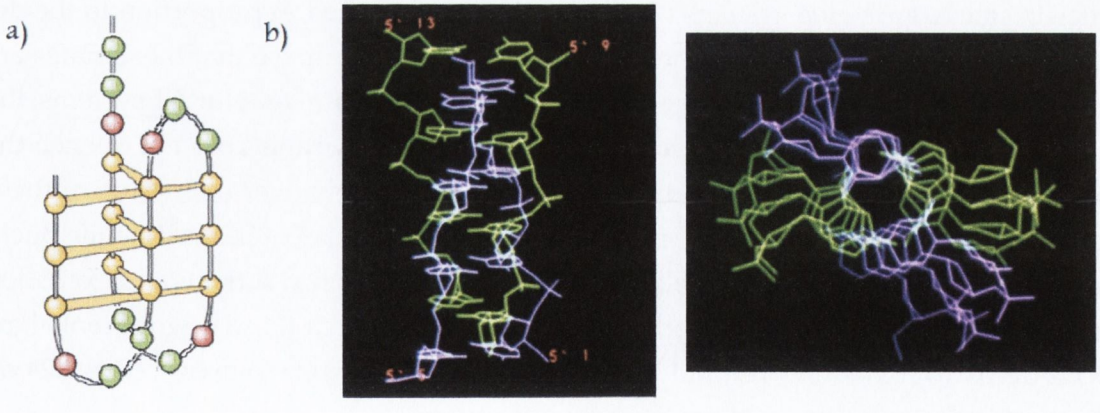

Figure 2.22: (a) Schematic of the intramolecular i-motif of $d(C_3TA_2)_4$[76] (b) Crystal structure of C_4 intermolecular i-motif[80]

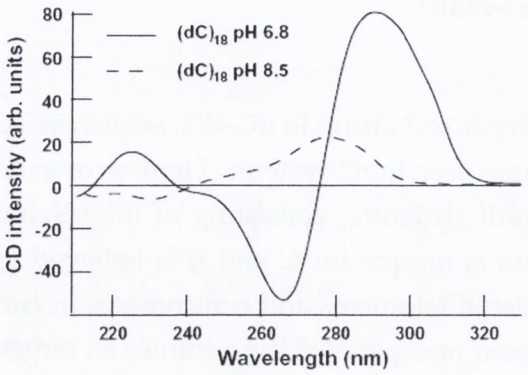

Figure 2.23: Comparison of CD spectra for dC_{18} at pH 6.8 (i-motif) and pH 8.5 (random coil)[84]

2.6.2 Photophysics of DNA Polymers

2.6.2.1 Base-Pairing and Base-Stacking

Studies on the photophysical properties of DNA and RNA polymers are dominated by discussion on base-stacking and base-pairing, and the roles they play in either long- or short-lived excited states. Before reviewing the specific literature on C-systems, the general features of DNA polymer photophysics are addressed.

Red-shifted emission has been known to occur in DNA for many years, and has often been attributed to excimers or exciplexes formed between vertically stacked bases as the 3.4 Å vertical base stacking distance is similar to that seen in organic excimer crystals[85]. TA measurements by the Kohler group demonstrate that long-lived excited states in stacked adenine systems (ApA, poly(rA)) are formed in proportion to the degree of vertical base stacking in the oligomer[86], and they propose that these states are localised on just two successive stacked bases[87] They also claim that for AT systems, the excitation is localised on one (A) strand and that AT base-pairing does not quench the long-lived states[88]. There has been considerable controversy over the nature of these excited states. Markovitsi et al believed that these were Frenkel excitons[89], while Buchvarov et al have also shown a correlation between chain length in A tracts and excitation deactivation[90]. By contrast, Kohler and co-workers claim that these bright Frenkel excitons decay to non-emissive (and longer-lived) excimers or exciplexes[87] (Fig. 2.24 on the facing page)

Similar discussion surrounds GC systems. Theoreticians have predicted rapid proton transfer in the WC base pair that may mediate ultrafast decay[44,91], and ultrafast decay has since been observed by fluorescence upconversion[92]. However, longer-lived

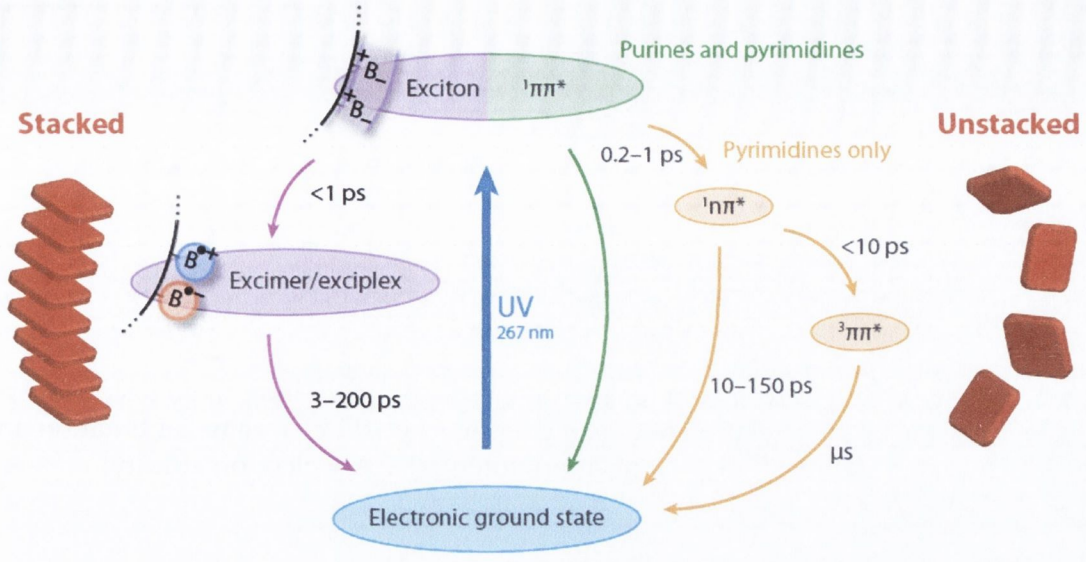

Figure 2.24: General scheme for stacked and unstacked bases proposed by Kohler and co-workers[1] showing a distinction in decay mechanism between stacked and unstacked systems. A noteworthy observation is the lack of localised excited states for stacked systems

dark electronic states have also been detected in [poly(dG-dC)]$_2$ by TRIR[93] and in GC oligonucleotides by TA[94]. A kinetic isotope effect is seen for the transient lifetime, and Kohler and co-workers hence infer that the exciplex lifetime is sensitive to the Watson-Crick base pairing[95].

The charge transfer nature of excited states in stacked systems has been studied in a series of dinucleotides (ApA, ApG, ApC, ApU and CpG)[87]. A tentative correlation is made between the lifetime of the long-lived states, and the driving force for charge recombination (see Fig. 2.25 on the next page, page 28). Charge transfer is suggested to originate from the asymmetric stacking of bases, which causes electron-rich and electron-poor regions of the chromophore to overlap. This theory eschews any arguments about the likelihood of charge transfer between almost identical chemical species, such as occurs in ApA (or CpC).

2.6.2.2 Photophysics of C Polymers

Base stacking is also a common theme in the photophysics of C homoplymers, as is the ability of C to form the hemi-protonated H bonds[84,96–100]. In low temperature EG:H_2O solutions, red-shifted fluorescence has been recorded for r(CpC) and poly(rC), and assigned as excimer emission[99]. Shoulders in the absorption spectra are said to correspond to exciton splitting, and the exciton is believed to be localised on just one stacked pair.

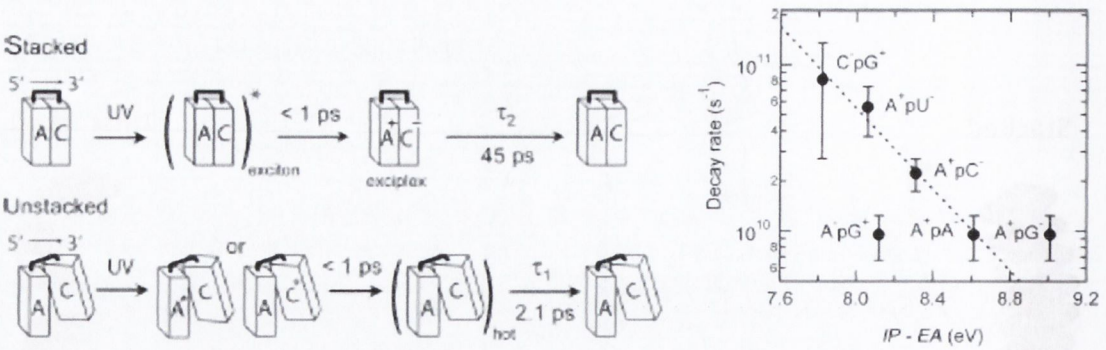

Figure 2.25: LEFT: Proposed model for exciplex formation and long-lived decay in ApC dinucleotide. RIGHT: Correlation between driving force for charge recombination and exciplex/excimer lifetimes[87]. IP = ionisation potential, EA = electron affinity

However, excimer emission in r(CpC) and poly(rC) is much less evident at room temperature. Vigny and Favre recorded very similar yields of "monomer" fluorescence from rCMP, r(CpC) and poly(rC)[97]. Red-shifted 'excimer' emission was detected for r(CppC), triplex polyI.poly(rC).poly(rC+), and the hemi-protonated poly(rC-rCH$^+$) duplex (pH 4)[97,98], which they say is due to favourable base overlap in these systems. It was also claimed that photoproduct absorption is observed from 300 nm to 400 nm when excimer emission occurs, suggesting a connection between longer-lived excited states and photochemical reactions.

Plessow et al studied rCMP, d(CpC) and dC_{15} using ps time-resolved emission spectroscopy[100]. Red-shifted fluorescence in d(CpC) and dC_{15} (Fig. 2.26 on the facing page) were assigned as excimer states, with lifetimes varying from 500 ps in CMP to 1200 ps in dC_{15}. Lifetimes were dependent on emission wavelength, and increased to 2 ns when recorded into the blue region at 460 nm. They also recorded an 80 ps decay for dC_{15}, which they claim is lengthened fluorescence due to lower solvent accessibility in the polymer. However, Cohen et al believe this should be reassigned as a hemi-protonated structure, which is formed at neutral pH for some polydeoxycytidilates[84].

Transient absorption measurements by Cohen et al show an additional 12 ps decay in poly(rC) that is not present in rCMP (Table 2.2 on the next page)[84]. Significantly, they claim not to see any evidence for locally excited $^1n\pi^*$ states in poly(rC). An i-motif structure is formed in dC_{18} at neutral pH, and for both acidic poly(rC) and neutral dC_{18}, long-lived decays of > 1 ns lifetime were recorded. The long-lived decay is assigned to excimers formed by very close overlap between interdigitating C-CH+ base pairs. In poly(rC), this decay disappears when the duplex is denatured at high temperature. They propose that, because of their similar kinetics, both acidic poly(rC) and neutral dC_{18} share a common structural feature, namely a matching base-overlap geometry.

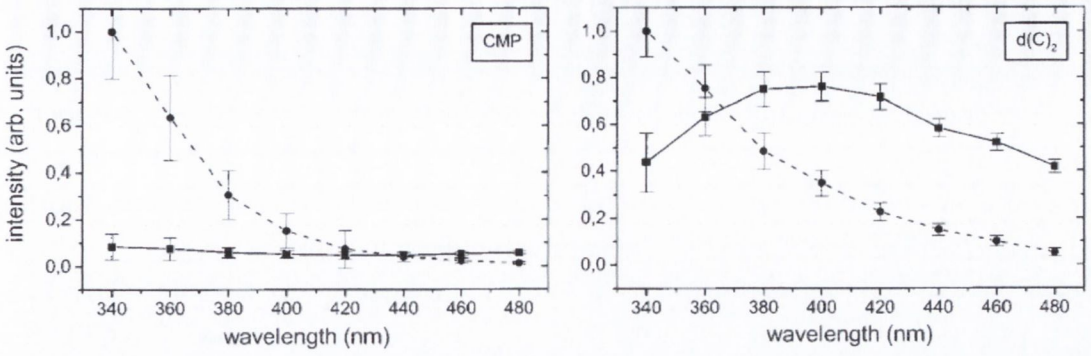

Figure 2.26: Comparison of time-resolved fluorescence spectra of CMP and d(CpC). Dashed line = short component, full line = long component[100]

Table 2.2: Kinetic data on C-polymer systems recorded by Cohen et al[84] using fs-TA with 263 nm excitation

species	pH	τ_1	τ_2
rCMP	6.8	750 ± 80 fs	
poly(rC)	6.8	2.5 ± 0.4 ps (71%)	12 ± 4 (29%)
poly(rC)	4	a few ps	c. 1 ns
dC_{18}	6.8	a few ps	c. 1 ns
dC_{18}	8.5†		
poly(rC) 70^{O}C	4	1.33 ± 0.15 ps	
poly(rC) 70^{O}C	6.8	c. 1 ps	

† no values quoted but said to be very similar to poly(rC) at pH 6.8

The connection between cytosine dark/excimer states and CPD formation has not been firmly established. Thymine dimers are an interesting comparison, as they are formed in high yields despite the inability of thymine to form stable excimers. To date there have been a number of ultrafast studies on CPD formation in TT systems[101–105]. The most significant conclusion is that the formation of *cis-syn* TT dimers is determined by the mutual orientation of bases at the instant of excitation, and that these CPDs can form within 1 ps directly from the $^1\pi\pi^*$ state[102,103]. This suggests that long-lived $^1n\pi^*$ states are not implicated in CPD formation. Interestingly, Hare et al also claim that the thymine triplet state is fully formed within 10 ps, and therefore suggest that the triplet is not populated from the long-lived $^1n\pi^*$ state[101]. These reports cast some doubt on the importance of $^1n\pi^*$ states in pyrimidine photochemistry.

2.6.2.3 Computational Studies on C Polymers

The role of stacked C excimers in CPD formation has been addressed in a number of recent computational studies. CAS-PT2 calculations by Merchan and co-workers[106] show agreement between the vertical emission energy of the bound excimer, and the red-shifted emission in dC_2 and dC_{15} observed by Plessow et al[100].

From the $^1\pi\pi^*$ state, the locally excited (LE) state decays to a stable relaxed excimer, which must then overcome a 0.2 eV energy barrier to reach the CI to CPD formation (Fig. 2.27). At the $(S_1/S_0)_{CI}$ there is elongation of C5-C6 and decrease of C5-C5′ and C6-C6′ separation, corresponding to 2+2 cycloaddition. A local minimum on the hyper-surface is suggested as an explanation for fluorescence in C-polymers. It also hints as to why T forms higher yields of CPD, as the Me group prevents formation of stable excimers, and as a result there is no competitive deactivation via direct excimer decay to S_0[85]. However this conclusion would need to be investigated considering the very low yields of fluorescence observed in C polymers in ambient conditions. A route also occurs along the triplet manifold in the presence of photosensitisers, and it is noted that diffusion-controlled excimer formation between C-monomers would also progress via the long-lived triplet state. The triplet excimer decays in a barrierless fashion to the CPD (Fig. 2.27), explaining the observed photoproducts in C following exogenous triplet sensitisation. Merchan and co-workers also calculated that an S_2 excimer is stable at larger interatomic distances[106]. This suggests a possible role for $^1n\pi^*$ states in excimer formation, although other workers have calculated that there is no coupling between $^1n\pi^*$ states in stacked cytosine[107].

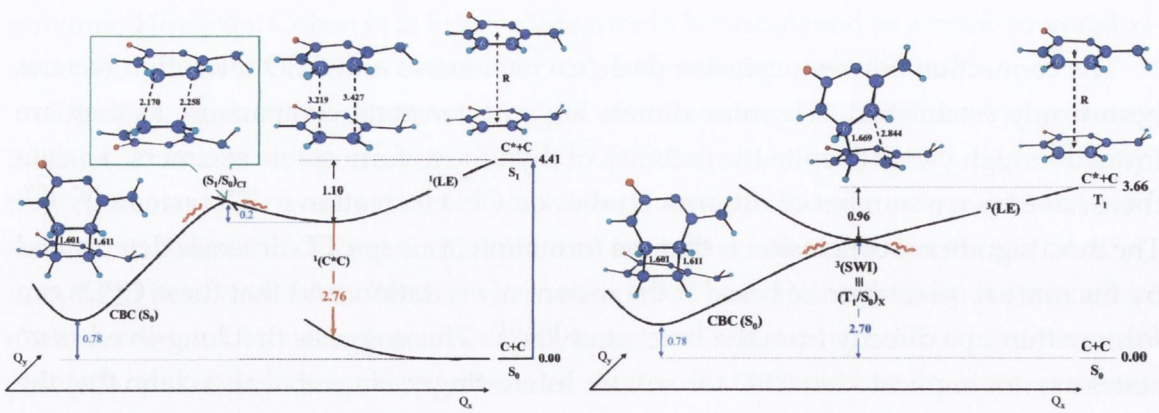

Figure 2.27: Calculated energetics for C-C excimer formed from LEFT: singlet state RIGHT: triplet state[85]

2.7 Aims

The work in this thesis builds on the C-monomer study of Quinn et al[25] and follows two general aims: further investigation of the dark $^1n\pi^*$ state in monomer systems, and the extension of the C study to large polymeric systems. The overarching objective is to unravel the connection between the structure of DNA, and the excited-state processes that result in deactivation or DNA damage. The specific goals are listed under the relevant chapter headings below.

2.7.1 Monomer Systems - Chapter 3

Monomeric C derivatives are studied in order to answer the following questions:

- How do the spectral and kinetic properties of the dCMP $^1n\pi^*$ state differ in H_2O and D_2O?
- What is the role of the N1 substitution in the formation and decay of the $^1n\pi^*$ state, and is the dark state present in 1-methylcytosine where the ribose is absent?
- Can a direct assignment be made for the dark state by calculating IR spectra of the excited states?

2.7.2 Dinucleotides and Polynucleotides - Chapter 4

The study is extended to model multimer sequences, where bases are linked and may be stacked.

- Is the locally excited dark $^1n\pi^*$ state present in extended systems, contrary to the results of Cohen et al[84]? If so, are its properties influenced by the structure of the dinucleotide or polynucleotide?
- Is there evidence for additional excited-state decay pathways such as an excimer?

2.7.3 Higher Order Systems - Chapter 5

Biological sequences, particularly higher order hemi-protonated C systems are studied here.

- Is the locally excited $^1n\pi^*$ state present in the base-stacked and base-paired i-motif structure?
- Is there evidence for additional excited-state decay pathways such as an excimer?

Chapter 3

Monomer Systems

The dark excited state in monomeric cytosine derivatives is studied using time-resolved infrared spectroscopy. Direct assignment of the transient state is attempted using computational methods.

3.1 Ps-TRIR Spectroscopy

The principle of the TRIR experiment is to excite the sample with a 267 nm laser pulse, and record an IR spectrum at a fixed delay after excitation with a broadband IR probe pulse (Fig. 3.1). Full technical specifications are listed in Chapter 13.

All previous work on the DNA direct excitation was reported on the PIRATE apparatus[25,93,108–111], so this is one of the first reports of data from the next generation ULTRA system. ULTRA features a number of improvements over PIRATE, as shown in Table 3.1 on the following page.

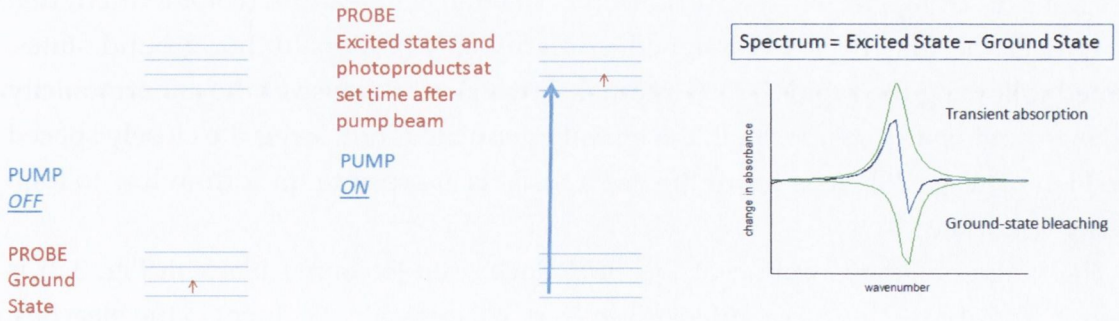

Figure 3.1: Schematic of the TRIR experiment showing LEFT: relevant electronic and vibrational transitions RIGHT: Generation of the [excited state - ground state] difference spectrum and separation into its components

Table 3.1: Comparison of the PIRATE and ULTRA systems

	repetition rate	spectral range	max. sensitivity	time-range
PIRATE	0.5 kHz	150 cm^{-1}	2 x 10^{-5} in 60 s	2-2000 ps
ULTRA	10 kHz	400 cm^{-1}	1 x 10^{-6} in 1 sec	0.5-3800 ps

These include increased laser repetition rates, faster data acquisition times, and the facility to monitor a wider spectral region in a single experiment. Due to faster acquisitions, more time delays could be recorded to improve kinetics, and the improved instrument response parameters allowed decays to be measured below 2 ps.

Samples for TRIR measurements were typically made to a concentration of 10 mM in buffered D_2O (25 mM NaH_2PO_4, 25 mM Na_2HPO_4, pH 7 $\pm$ 0.2, pD 7.4 $\pm$ 0.2). The usual sample volume was 40 μl, which was dropped between two CaF_2 windows with a spacer pathlength of 56 μm. This yielded an absorbance at 266 nm of approx. 0.5.

The primary method for obtaining kinetic data was by fitting the difference signal at single wavenumbers. Where biexponential kinetics were observed, the long component was sometimes refitted separately by omitting early delays. In certain cases kinetics were obtained by fitting the spectrum at each delay to a sum of overlapping Lorentzian curves, and calculating lifetimes from the areas of the fitted peaks.

3.1.1 Expanded Spectral Window–dCMP in D_2O

The TRIR spectrum of dCMP in D_2O (1450 - 1700 cm^{-1}) has been well characterised on the PIRATE system[25], However dCMP was revisited on ULTRA in order to study an extended spectral region from 1300 $^{-1}$ - 1450 cm^{-1}, and to compare data from the two TRIR systems.

In the TRIR spectra (Fig. 3.2 on the next page), bleaching and recovery is evident in regions of strong ground-state absorption. The transient features (coloured red) that decay over the first 10 ps are assigned primarily as vibrationally hot ground states, formed following the rapid $S_1 \rightarrow S_0$ internal conversion. Because of the anharmonicity of the ground-state potential well, the initially populated 'hot' levels are closely spaced (see Fig. 3.3, page 36). As a result the hot transients are seen to track from low to high energy with time[108] .

The longer-lived absorption of the $^1n\pi^*$ dark state (coloured black in Fig. 3.2) is present at 1574 cm^{-1}, and ground-state recovery via this state is evident in the bleaches. In the region below 1450 cm^{-1} there are previously unrecorded transient absorptions at 1360 cm^{-1} and 1440 cm^{-1}.

Kinetics for the main bleaches and transients were calculated using single-point methods (Fig. 3.4, page 36). Similar biexponential decay was observed for the tran-

sients at 1360 cm^{-1} and 1574 cm^{-1} (38 ± 3 ps), and the bleach recoveries (see Table 3.2, page 37). This implies that the new transient feature has the same origin as the 1574 cm^{-1} transient. Noticeably shorter lifetimes (30 ± 5 ps) were recorded for the 'long' component when monoexponential fitting was used over the long delays. It is also notable from the spectrum that the decay does not return to the baseline in certain places.

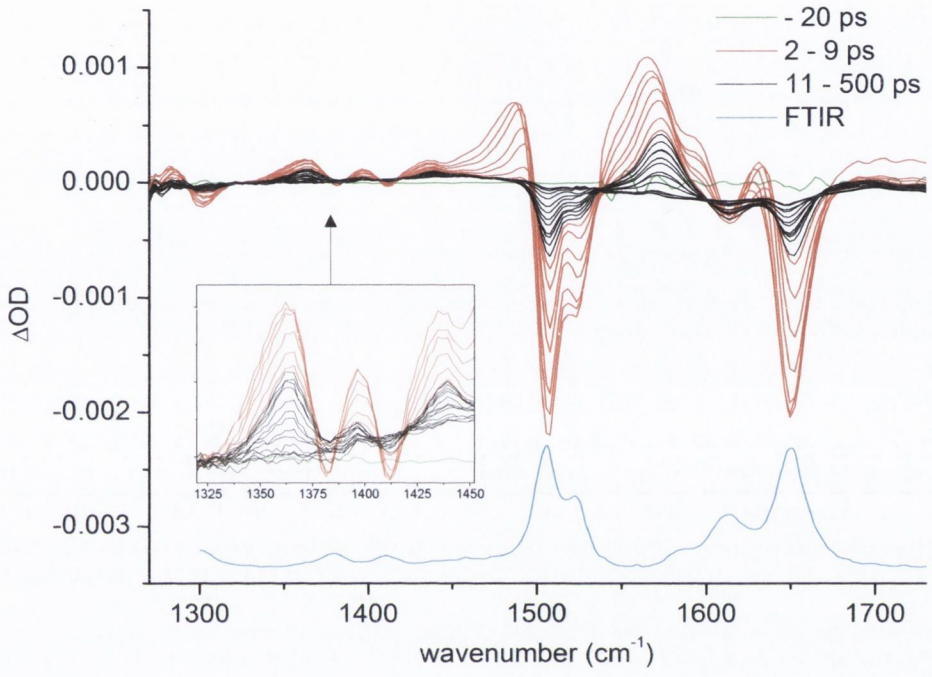

Figure 3.2: ps-TRIR of extended spectral region of dCMP in D_2O (50 mM phosphate, pH 7). Recorded on ULTRA apparatus in a flow cell. Delays (ps):-0.5, 1, 1.5, 2, 2.5, 3, 4, 5, 7, 9, 11, 14, 17, 20, 25, 30, 40, 50, 70, 100, 150, 250, 350, 500. Inset: Enlarged view of new transient feature

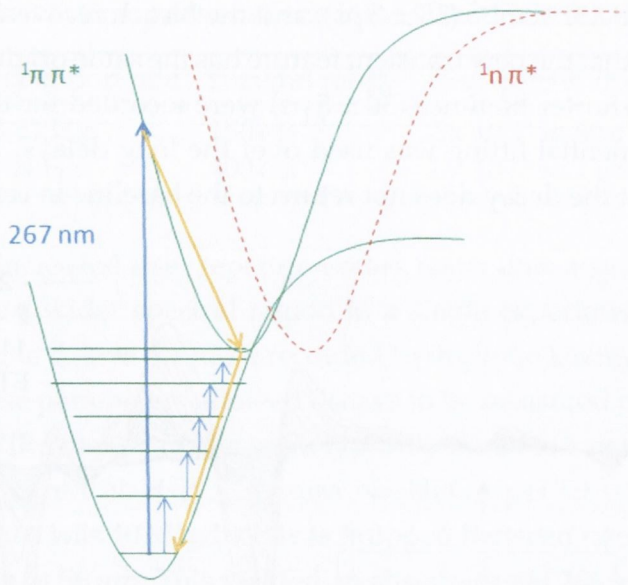

Figure 3.3: Processes observed in ps-TRIR experiment on dCMP. Pump excitation into the Frank-Condon region, followed by rapid cooling of the $^1\pi\pi^*$, and conical intersection with g.s. Absorptions ($\Delta n = 1$) are then observed between the higher vibrational levels in the ground state as the molecule thermally equilibrates with the solvent. Possible mechanism for the alternative decay via the $^1n\pi^*$ state will be discussed in Section 3.2.3

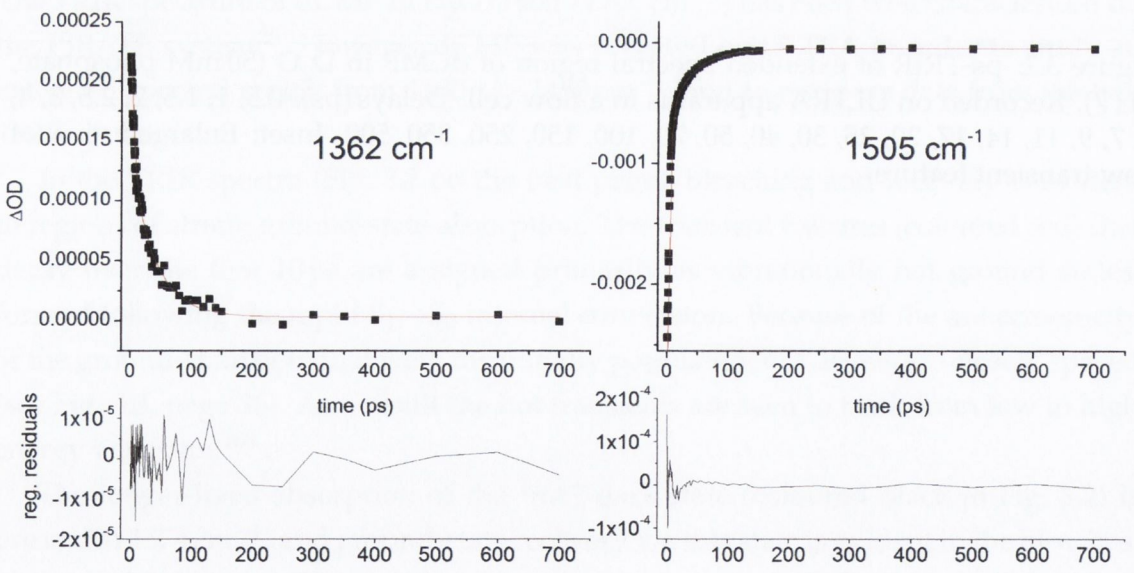

Figure 3.4: Biexponential single-point kinetic fits and residuals for dCMP in D_2O over extended spectral range (ULTRA). 50 mM phosphate, pH 7

Table 3.2: Kinetic parameters and fitting errors for dCMP in D_2O over extended window. Biexponential and monoexponential (t>10 ps) models (ULTRA). 50 mM phosphate, pH 7

$\tilde{\nu}/cm^{-1}$	τ_1 (ps)	A_1	τ_2 (ps)	A_2	R^2	τ (ps)	R^2
1360(Tr)	3.5 ± 0.7	43	35 ± 4	57	0.99476	33 ± 3	0.9869
1362(Tr)	4.8 ± 1.0	45	39 ± 6	55	0.99494	34 ± 3	0.98868
1364(Tr)	5.9 ± 1.5	40	40 ± 7	60	0.99455	35 ± 2	0.9928
1503(B)	2.6 ± 0.2	84	46 ± 13	15	0.99381	35 ± 1	0.9982
1505(B)	3.6 ± 0.3	81	44 ± 13	17	0.99549	30 ± 2	0.9954
1508(B)	4.4 ± 0.4	81	44 ± 13	17	0.99625	27 ± 2	0.99251
1571(Tr)	4.5 ± 0.5	66	39 ± 4	42	0.99754	32 ± 2	0.9935
1574(Tr)	5.6 ± 0.9	59	40 ± 5	51	0.99708	32 ± 2	0.9942
1577(Tr)	7.2 ± 1.7	53	41 ± 6	61	0.99657	33 ± 2	0.99458
1646(B)	2.6 ± 0.1	91	47 ± 10	9	0.99705	37 ± 4	0.98241
1649(B)	3.5 ± 0.2	90	46 ± 11	10	0.99706	29 ± 3	0.97106
1652(B)	4.4 ± 0.3	85	49 ± 19	10	0.99604	23 ± 3	0.96346

3.1.2 Isotope Effects–dCMP in H_2O

Obtaining IR spectra in H_2O in the 1400-1700 cm^{-1} region is clearly desirable but is a technical challenge due to the strong background absorption from the ν_2 bending mode of H_2O at 1643 cm^{-1}. A sensitive transient absorption system can, in principle, successfully eliminate the water absorption through subtraction. This was attempted previously on PIRATE, and was eventually recorded successfully on ULTRA. The effect of H_2O absorption was minimised by using the shortest available pathlength (6 μm), and increasing the dCMP concentration from 10 mM to 50 mM, after it was confirmed that appreciable intermolecular interactions were not introduced at the higher concentration.

The resulting TRIR spectrum (Fig. 3.5 on the following page) has a number of notable features. The region around 1650 cm^{-1} shows a feature attributed to the 'temperature jump' phenomenon. This is caused by efficient absorption of the probe beam by the H_2O absorption at 1643 cm^{-1}. This results in energy dumping into the higher vibrational modes and rapid heating of the solution. It is noteworthy that the resultant transient does not decay in the timescale of the experiment, unlike the hot ground states of the nucleobase.

Despite the presence of the T-jump feature, the spectrum still reveals significant structural and kinetic information about dCMP. Primary peaks were compared to those in D_2O (Fig. 3.6, page 39), and the respective peaks are assigned in Table 3.3, page 39. Many of the bleaches are shifted, the most notable being the amino group scissoring

mode $\delta(NH_2)$ which is the most sensitive to deuteration. There is also a long-lived transient feature at 1545 cm^{-1}, which appears at slightly lower frequency than the $^1n\pi^*$ state in D_2O. There is also a region of apparent long-lived decay in the 1450 cm^{-1} region.

Single-point kinetic fitting was performed to a biexponential model. The only bleach that could be fitted was the band at 1495 cm^{-1} (Table 3.4, page 40), and this yielded similar vibrational cooling lifetimes (2.5 – 4 ps) to those recorded in D_2O. However, when the transient regions were fitted, significantly faster cooling dynamics were obtained (c. 1 ps, Table 3.5, page 40). There were variations in the lifetime of the long-lived state, depending on whether it was measured from the bleach or transient, or using bi- or monoexponentials. The relative percentage of the long-lived component in H_2O was calculated from the bleach recovery, and fits in the range 10-14%, depending on whether a constant baseline offset was included (Table 3.4).

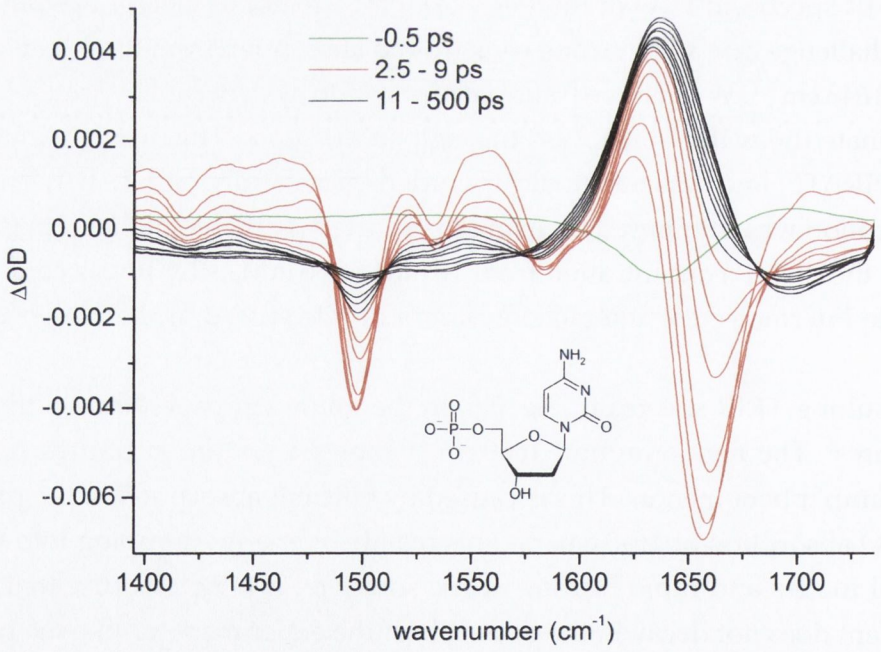

Figure 3.5: ps-TRIR spectrum of 50 mM dCMP in H_2O. Recorded on ULTRA in a 6μm pathlength in a flow cell. Delays (ps) -0.5, 2.5, 3, 4, 5, 7, 9, 11, 17, 25, 40, 70, 150, 250, 500. 50 mM phosphate, pH 7

Table 3.3: Comparison of bleach and transient spectral features (in cm^{-1}) for dCMP in H_2O and D_2O (ULTRA)

assign.	ν(C=O)	ν(ring)	$\delta(NH_2)$	ν(ring)	ν(ring)	ν(ring)		
peak type	B	B	B	B	B	B	Tr	Tr
H_2O	1654	1601	1581	1533	1498	1417	1545	1633
D_2O	1649	1613	-	1523	1505	1412	1574	

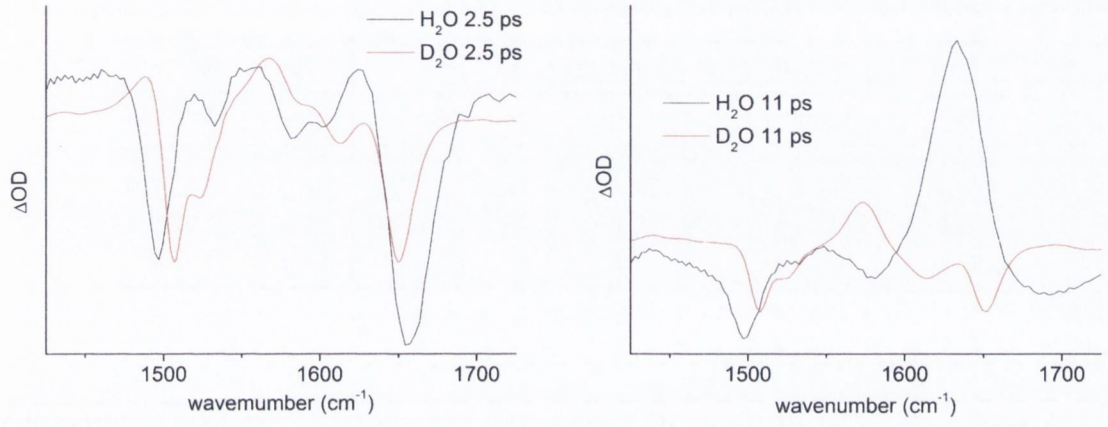

Figure 3.6: Comparison of dCMP in H_2O and D_2O - scaled to equal ΔOD in ring (band approx. 1500 cm^{-1}) at 2.5 ps (ULTRA)

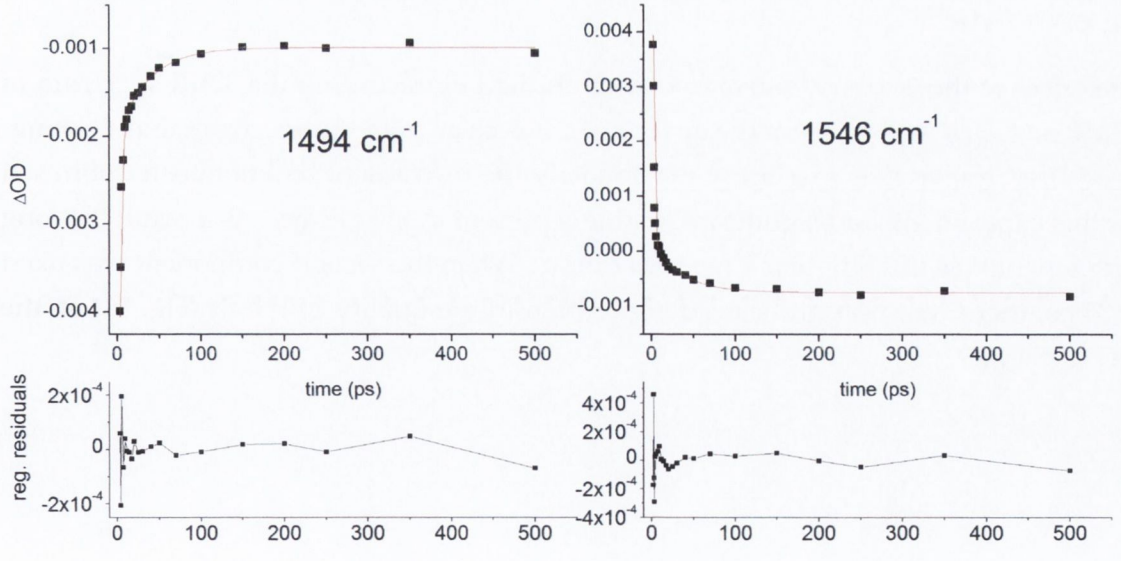

Figure 3.7: Biexponential single-point kinetic fits and residuals of dCMP in H_2O in 50 mM phosphate, pH 7 (ULTRA)

Table 3.4: Bleach recovery kinetics for dCMP in H_2O by biexponential and monoexponential (t>10 ps) models (ULTRA). 50 mM phosphate, pH 7

$\tilde{\nu}$ (cm^{-1})	A_0	τ_1 (ps)	A_1	τ_2 (ps)	A_2	R^2	τ (ps)	R^2
1494	10	2.4 ± 0.3	79 (88)	37 ± 8	10 (12)	0.9904	33 ± 3	0.9865
1497	12	3.1 ± 0.4	76 (87)	39 ± 11	12 (13)	0.99117	30 ± 3	0.98658
1499	15	4.0 ± 0.5	73 (86)	40 ± 14	12 (14)	0.99153	25 ± 3	0.9801

Table 3.5: Transient kinetics for dCMP in H_2O by biexponential and monoexponential (t>10 ps) models (ULTRA). 50 mM phosphate, pH 7

$\tilde{\nu}$ (cm^{-1})	τ_1 (ps)	A_1	τ_2 (ps)	A_2	R^2	τ (ps)	R^2
1541	0.4 ± 0.1	74	33 ± 3	26	0.9892	36 ± 5	0.96833
1543	0.6 ± 0.1	80	28 ± 3	20	0.98983	38 ± 5	0.97146
1546	0.8 ± 0.1	74	26 ± 4	26	0.9875	38 ± 5	0.97339
1549	1.0 ± 0.1	78	26 ± 4	22	0.98749	38 ± 5	0.97274
1551	1.1 ± 0.2	80	26 ± 5	20	0.98691	38 ± 6	0.9559

3.1.3 Substituent Effects

One of the most significant observations regarding the dark $^1n\pi^*$ state in C derivatives was that it was absent in nucleobase cytosine[25]. As the N1 substituent was clearly important in the excited-state decay, spectra were recorded on rCMP and 1-methylcytosine (1-MeCyt)

3.1.3.1 rCMP

The effect of the 2′-ribose substituent was studied by recording the TRIR spectrum of rCMP on ULTRA (Fig. 3.8 on the next page). It is clear from the spectrum that the long-lived $^1n\pi^*$ transient is present. Unfortunately the instrument had not been optimised for this experiment, and significant scatter is present in the decays. As a result the long component was fitted with a large uncertainty. When the second component was fixed at 35 ps, there was no significant deterioration in the quality of the fit (Fig. 3.9 on the facing page).

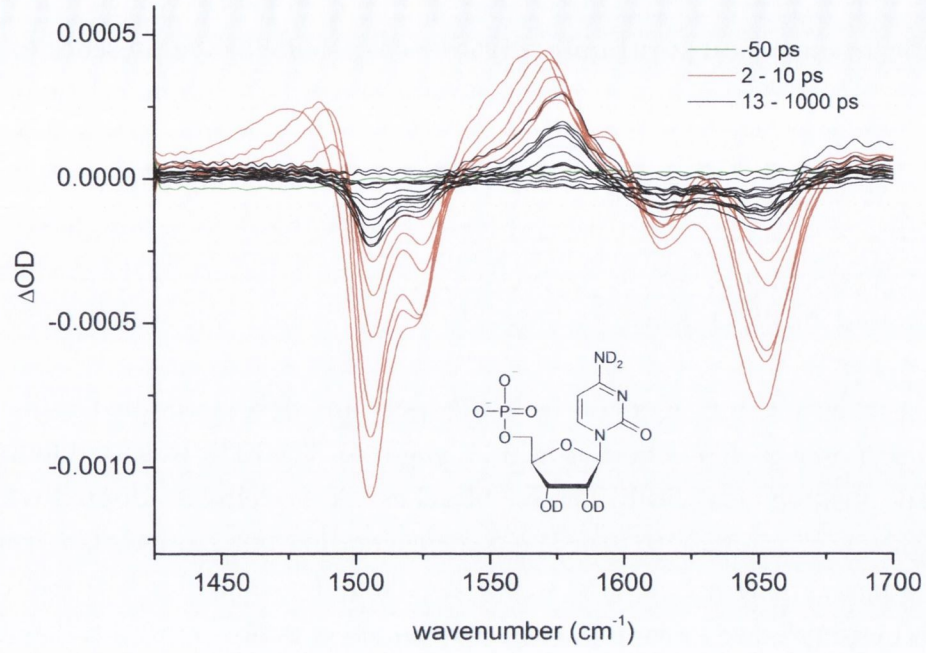

Figure 3.8: ps-TRIR spectra of rCMP recorded on ULTRA. Delays (ps): -50, 1, 2, 3, 4, 6, 8, 10, 13, 17, 20, 25, 30, 40, 55, 80, 100, 150, 200, 400, 700, 1000. In 50 mM phosphate (pH 7) in D_2O

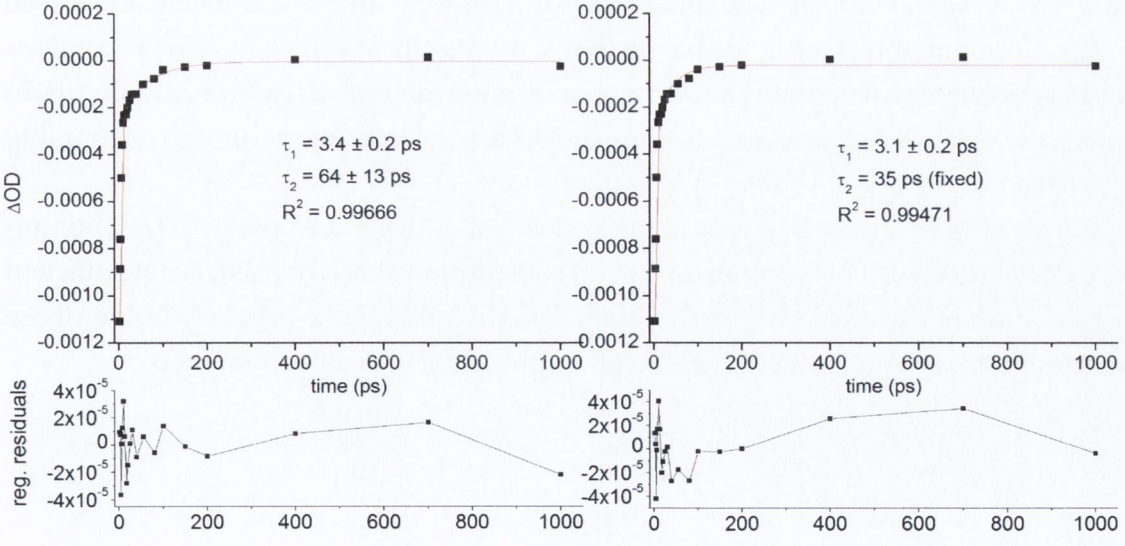

Figure 3.9: Biexponential single-point kinetics for rCMP in D_2O (ULTRA). 50 mM phosphate, pH 7

3.1.3.2 1-MeCyt

1-MeCyt is an important structural derivative of cytosine as the presence of the simple methyl group blocks prototropism between N1 and O7, reducing the number of possible tautomeric forms (see Fig. 2.3 on page 9). The ps-TRIR spectrum of 1-MeCyt was recorded on the PIRATE apparatus (Fig. 3.10 on the facing page). The spectrum is mostly recovered by about 10 ps, and there is no evidence for a long-lived transient feature in the spectrum. The transient absorptions are assigned solely as vibrationally excited ground states, and the 'tracking' of the hot bands is especially evident in this system.

The bleaches and transients in the TRIR spectrum were decoupled using sums of overlapping Lorentzian functions (Fig. 3.11, page 44). The FTIR was used to fix parameters (peak position and width) for five bleaches. A model was adopted where each ground state was assumed to generate a corresponding hot ground-state transient at lower frequency. With this model it was noticed that the small bleach at 1580 cm^{-1} appeared to be coupled to a disproportionately large hot band at 1570 cm^{-1} (Fit A). The fitting model was reassessed and the spectrum was then refit where this transient was coupled with the 1612 cm^{-1} mode, and a hot transient was not fitted for the 1580 cm^{-1} band (Fit B).

The spectra were fitted at every delay, and the kinetics calculated from the areas under the Lorentzian curves (by Dr. Michal Wojdyla). Lifetimes were also calculated by single-point methods and the two methods compared (see Fig. 3.12, page 45 and Table 3.6 on the next page). The lifetime is 4.0 ± 0.4 ps, with good agreement between the two fitting methods, even for bands that show significant tracking. The exceptions are those instances where one of the fits is of poor quality. This typically occurs in regions of very low net absorption, where peaks are revealed only through decoupling (e.g peaks 1 and 7 in Fit A in Fig. 3.11).

The absence of a long-lived transient means that 1-MeCyt behaves like Cyt, but unlike dCMP and Cyd. This demonstrates that substitution at N1, of itself, is not sufficient for formation of the dark state in C. Rather it is clear that some property of the ribose substituent has a large influence on the photophysics of cytosine monomers.

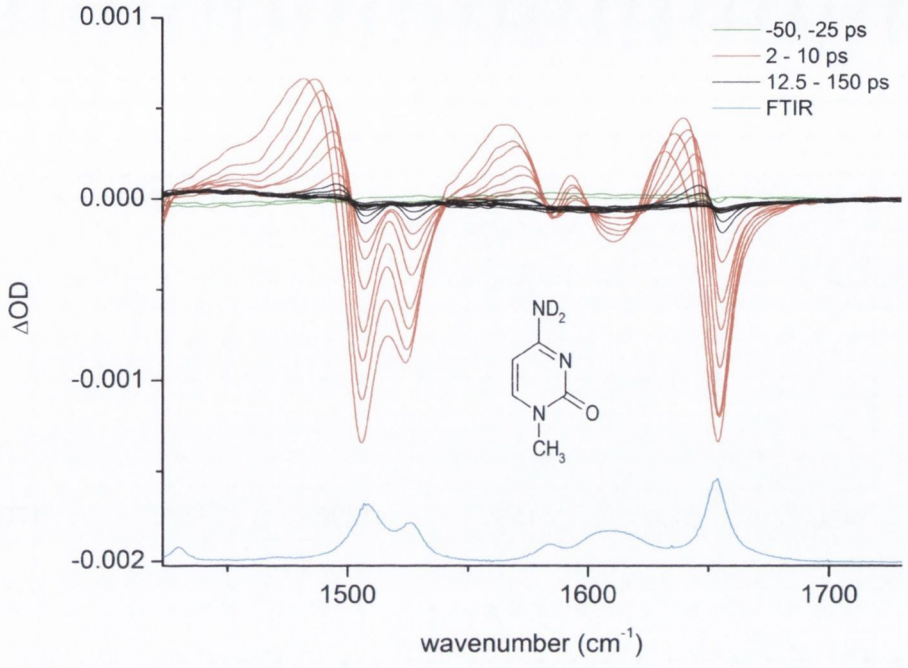

Figure 3.10: ps-TRIR spectra of 10 mM 1-MeCyt recorded on PIRATE. Delays (ps): -50, -25, 2, 3, 4, 5, 6.5, 8, 10, 12.5, 15, 20, 25, 35, 40, 50, 100, 130, 150. In 50 mM phosphate in D_2O

Table 3.6: Comparison of single-point and Lorentzian fitting for 1-MeCyt in buffered D_2O pH 7 (PIRATE)

band	assign.	τ (ps) fitting	R^2	τ (ps) single point†	R^2
1(T)	ν(N3C4,C4N$_{am}$)$_{hot}$	6.4 ± 2.7	0.71009	2.3 ± 0.2	0.97528
2(T)	ν(N3C4,C4C5)$_{hot}$	4.6 ± 0.2	0.99533	4.1 ± 0.4	0.97921
3(B)	ν(N3C4,C4N$_{am}$)	4.0 ± 0.1	0.99837	4.3 ± 0.1	0.99727
4(B)	ν(N3C4,C4C5)	4.7 ± 0.3	0.99016	4.0 ± 0.3	0.98615
5(T)	‡	3.3 ± 0.1	0.9946	3.3 ± 0.1	0.99448
6(B)	‡	5.0 ± 0.3	0.89374	5.5 ± 2.1	0.74996
7(T)	ν(C5C6)$_{hot}$	6.6 ± 13.4	0.1079	3.1 ± 0.3	0.97803
8(B)	ν(C5C6)	4.0 ± 0.8	0.89997	3.7 ± 0.3	0.97858
9(T)	ν(CO)$_{hot}$	4.9 ± 0.2	0.99713	4.9 ± 0.7	0.94759
10(B)	ν(CO)	5.2 ± 0.2	0.99529	6.0 ± 0.6	0.97773

†from band maxima ‡vibration not assigned

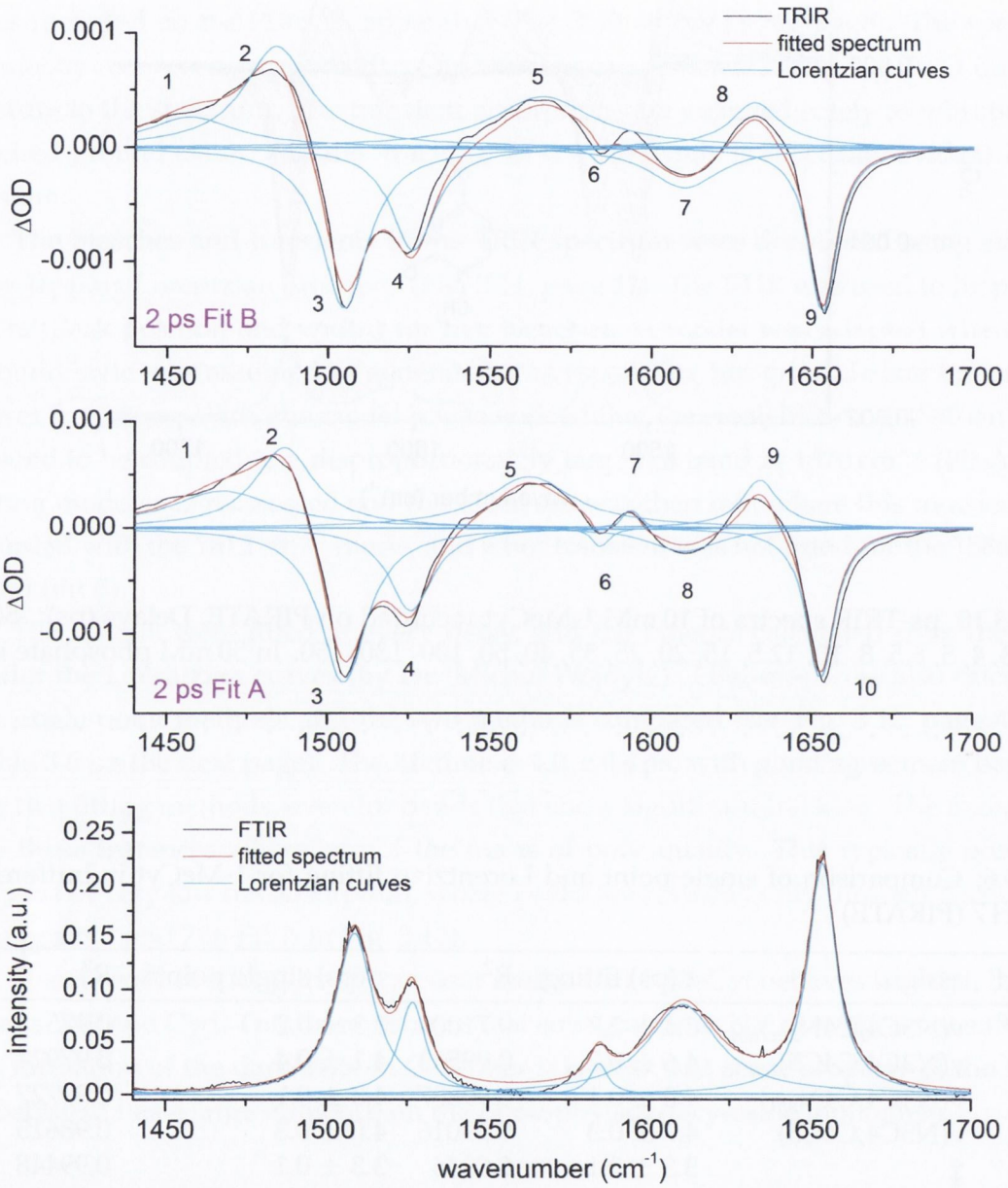

Figure 3.11: FTIR and TRIR (2 ps) of 10 mM 1-MeCyt fitted to a sum of overlapping Lorentzian functions. (from PIRATE data)

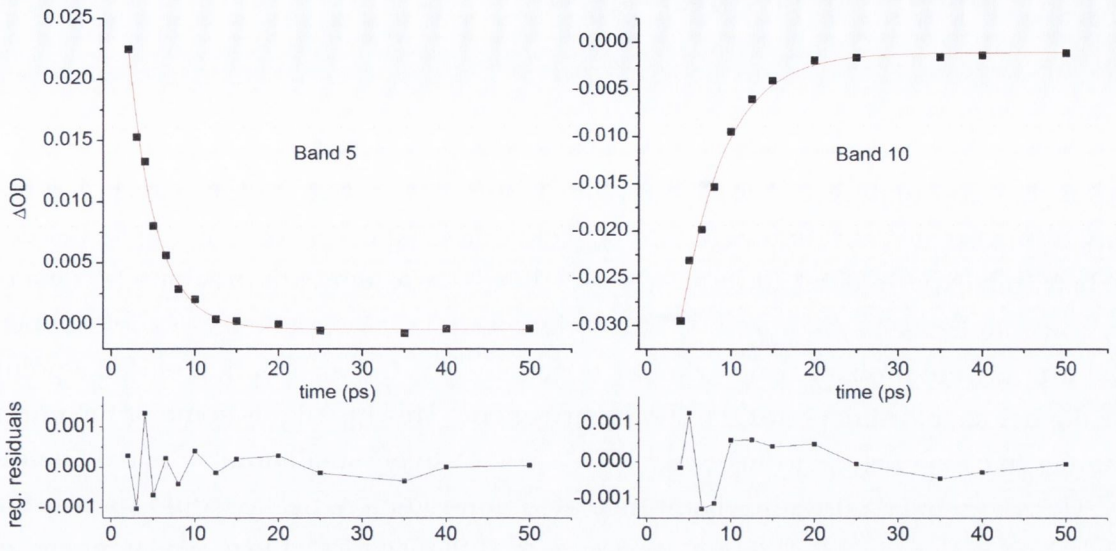

Figure 3.12: Monoexponential fitting to bleach and transient bands of 1-MeCyt obtained from Lorentzian fitting (PIRATE)

3.2 Discussion on ps-TRIR

3.2.1 Comparison between ULTRA and PIRATE - dCMP

It was noticed during analysis of the data from ULTRA that slightly longer lifetimes were recorded for the dCMP $^1n\pi^*$ state, than those recorded on PIRATE. Given that more data points were generally recorded on ULTRA than PIRATE, the former data may be deemed more reliable, However, we found that photodecomposition of samples was often a problem on ULTRA. We believe this was because the repetition rate of the pump beam was so high that the sample wasn't sufficiently rastered between pulses, and that the same region was receiving large fluxes of UV radiation.

In many cases this resulted in slight lengthening of the lifetime of the $^1n\pi^*$ state, although the data was still within 10–15% of what was recorded on PIRATE. Non-recovery and deviations in the baseline were also observed on ULTRA. This was improved by sacrificing some spectral bandwidth and having a dedicated reference detector, as it was noticed that the probe beam showed large fluctuations across the spectrum during experiments. It should be stressed that some of the data presented here was recorded before the system was fully optimised for TRIR, Nevertheless, sufficient corrections in the spectra still allowed for extremely rapid TRIR run-times, such that the limiting step in the experiment was the preparation of samples.

3.2.2 Solvent Isotope Effect - dCMP

After rigorous analysis of the kinetics for dCMP in H_2O and D_2O we concluded that any difference in $^1n\pi^*$ lifetime, or in the yield of formation, is too slight to be discernable within experimental and fitting error. This is consistent with previous TA data on cytosine and uracil systems[25,27,40] The variations in mono-exponential vs. biexponential fitting were probably due to subtle effects such as the distribution of delay points or the degree of influence of the short component. This highlights some of the uncertainties in biexponential fitting when there are a relatively small number of data points.

Conventional theory on solvent-mediated non-radiative decay would predict that the decay of the $^1n\pi^*$ state would be slower in D_2O than H_2O due to the larger energy difference between vibrational modes in D_2O, and consequent smaller overlap integrals with excited-state modes on dCMP - an excellent example of this phenomenon is the approx. 10-fold increase in singlet oxygen lifetime in D_2O relative to H_2O. The absence of a solvent isotope effect in the lifetime of the $^1n\pi^*$ state in dCMP suggests that the solvent does not have a primary role in the deactivation. In particular, the deactivation probably does not have any involvement from H/D-bonds, and the excited state may instead deactivate through intramolecular processes, or by coupling with modes that are not isotope dependent. Isotopic substitution also occurs on the nucleotide (amino and 2′-OH), so there may be a compensating effect if these modes are involved in vibrational relaxation.

Interestingly there is a discrepancy between the contributions of the $^1n\pi^*$ state to the bleaching kinetics for this work and the transient UV work of Hare et al[27]. They report bleach contributions of 30% compared to 15% by TRIR. One possibility is that there was significant bleach and transient overlap in the UV, and that the kinetics were obtained in a region where there was an overlapping short-lived transient.

Although the dark state shows no kinetic solvent isotope effect, we may expect the vibrational cooling kinetics to be affected, as previously reported for 9-methyladenine[33]. The cooling kinetics are very similar in both solvents when recorded at the bleach, but in the transient region, much shorter cooling lifetimes are recorded in H_2O than in D_2O. This may reflect stronger coupling of specific vibrational modes with H_2O, although it should be noted that the resolution of such short lifetimes may require deconvolution from the instrument response. The effect of the temperature jump phenomenon on the cooling kinetics is also not known, but it seems reasonable that the presence of vibrationally excited solvent would affect how readily it accepted excess energy from the nucleobase.

3.2.3 Effect of N1-Substituent on Dark State

As discussed previously, cytosine can form more tautomers than 1-substituted derivatives such as 1-MeCyt (Section 2.3), and does not form the long lived $^1n\pi^*$ state. The fact that there is also no long-lived state in 1-MeCyt proves that the absence of a dark state is not related to these additional tautomers.

The profound influence of the N1 substituent on the excited state decay pathways is counterintuitive as the sugar is electronically isolated from the chromophore, and would not be expected to be so important[112]. The differences between 1-MeCyt and dCMP also demonstrate that N1(N9)-methylated nucleobases should not necessarily be treated as simplified analogues of higher order systems, contrary to what has previously been suggested by some theoreticians[55,113]

There are a number of possible ways that the ribose/deoxyribose group could influence the deactivation of the excited state(s), although before a discussion on mechanism it is worth stressing that TRIR data can be interpreted in two ways. Firstly, a long-lived component may exist in very low yields in cytosine, but occur in higher yields with 1-substituent. In the second case, the dark state may be populated in comparable yields in either system, but may show lengthening of lifetime with 1-substitution. Kohler and co-workers favour the latter argument (see Section 2.5.1.2). The IR data could also be interpreted either way, as shown from the Lorentzian fits of the 1570 cm^{-1} transient of 1-MeCyt (Fig. 3.11 on page 44). However, the spectra for dCyd and dCMP are quite different to 1-MeCyt in this region, thus slightly favouring the hypothesis that the dark state is not significantly populated in 1-MeCyt.

The first possible role considered for the ribose group is mass. The presence of a large 'anchor' may affect the vibrations of the excited state, perhaps impeding some access to the excited state/ground state conical intersections, or allowing a vibration to occur that carries the excitation onto the $^1n\pi^*$ surface. However it is noteworthy that 1-cyclohexyluracil has been reported to have very similar kinetics to uracil, which shows that mass is not a factor in that case[27,40].

Another possibility is for coupling between sugar and chromophore by intramolecular H-bonding. Any coupling that stabilises an excited-state conformation should then be expected to influence the lifetime, such as that observed for the N4Ac molecule[17]. There is possible H-bonding between the 5'OH and C6 in dCyd (Fig. 3.13 on the next page). However this does not explain the presence of the dark state in dCMP. There may also be H bonding between the 2'OH and C=O in rCMP, but this is not possible in dCMP.

We have seen no evidence for intermolecular processes such as stacking at the 10 mM concentrations used in the TRIR. Also, any influence from collisional processes is likely

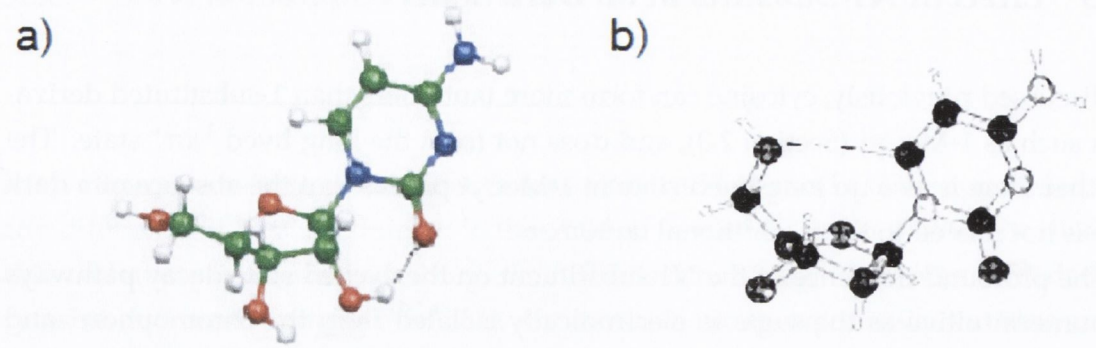

Figure 3.13: Possible intramolecular association in some cytosine derivatives a) 2′OH + C=O in Cyd[54] b) 5′OH and C6H in dCyd[114]

to be minimal as the excited states are too short-lived for diffusion-controlled processes to be significant.

Another possibility is an electrostatic effect due to the phosphate group in dCMP. This theory follows from the work of Markovitsi and co-workers, who claim that ionic strength and the phosphate group have an influence on pyrimidine excited state decay[7,26]. Their calculations on the $^1\pi\pi^*$ state demonstrate how the excited states are polarised relative to the ground state, and presumably to each other (Fig. 3.14). The presence of a proximate negative charge may alter the relative stabilities of the excited states and perhaps stabilise the $^1n\pi^*$ states. However, the similarities between dark state dynamics in dCMP and dCyd (no phosphate) argues against this theory somewhat.

There is also the suggestion, arriving from computational studies, that there is mixing between the orbitals on the ribose group and the non-bonding orbitals on the nucle-

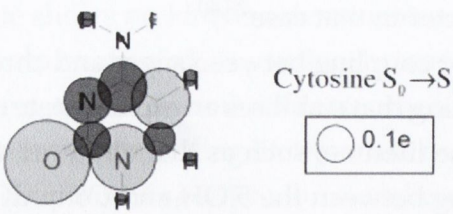

Figure 3.14: Change in charge distribution of the $^1\pi\pi^*$ state relative to the ground-state, black = negative, grey = positive. Area of disk is proportional to absolute change in charge[115].

obase[54,55]. This may result in an increase in oscillator strength of the $^1n\pi^*$ transitions or a change in the relative energies of the $^1n\pi^*$ and $^1n\pi^*$ states, with subsequent impact on the excited-state decay.

The final mechanism to be considered is that the presence of the sugar influences the local water structure around the nucleobase. Different excited states may show different H-bonding preferences, so it is possible that the relative energies of these states are altered. This may then alter the conical intersection between the $^1n\pi^*$ states and the ground state, or affect how efficiently the $^1n\pi^*$ state is populated. Some support comes from the work of Shukla and Leszczynski, who show a difference in solvent H-bonding structure between the ground and excited ($^1n_N\pi^*$) states[16].

3.3 Calculations of IR Spectra of Cytosine Derivatives

The goal of simulating the IR spectra was ultimately to assign the dark state in dCyd and dCMP as either the $^1n_N\pi^*$ or $^1n_O\pi^*$ state. IR spectra in the ground state can be calculated by either Hartree-Fock (HF) or density functional theory (DFT) methods. HF considers each electron as seeing an average field from each other electron, wherein each electron is treated as an independent entity. Correlation, the influence of one electron on another, is thus absent from HF calculations. DFT treats the wavefunction as a probability density. Correlation is also under-represented in DFT, but this method is often regarded as a superior method to HF for structural determination and computational efficiency, and marginally better IR data for Cyt has been reported by DFT than by HF[15].

Ground state DFT (B3LYP and MP2) calculations were used previously to consider whether the long-lived transient was a cytosine tautomer[25]. However, in the current work ground-states were optimised at the HF level so that the excited states ($^1\pi\pi^*$, $^1n_N\pi^*$, $^1n_O\pi^*$) could be calculated using the analogous CIS method. Difference spectra (CIS excited state - HF ground state) could then be plotted and compared to the experimental TRIR spectra.

Attempts were also made to model the effect of solvent by incorporating a default Polarisable Continuum Method (PCM), which introduces a dielectric component but neglects specific effects such as H-bonding, surface effects, or local ordering of solvent molecules.

Calculations were initially performed with a 6-31G(d,p) basis set. Some calculations, including the addition of a dielectric, were performed with a 6-311++G(d,p) basis set. A range of cytosine derivatives of increasing structural complexity were chosen (Fig. 3.15 on the following page). These molecules differ in the nature of the N1 substituent.

In order to account for H/D exchange in deuterated solvent conditions, the calcula-

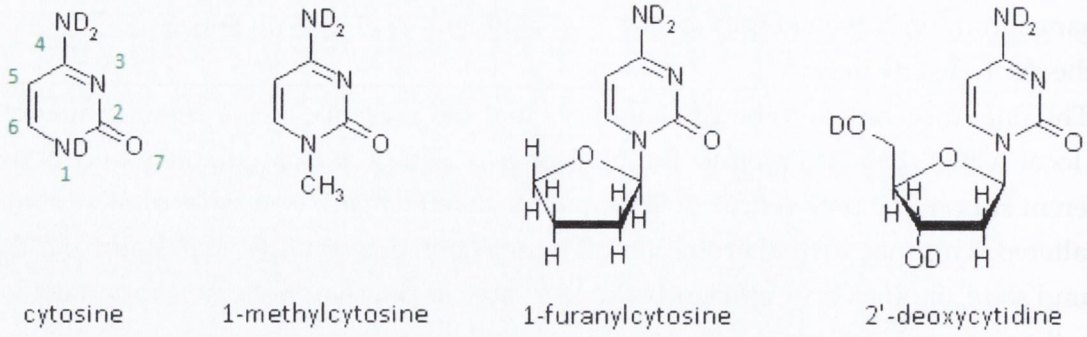

Figure 3.15: C structures used in calculations. Structures shown with labile protons substituted with deuterons

tions were performed with either H or D at labile sites. These were the C4 amino group, the N1 position of cytosine and the sugar hydroxyl protons on dCyd. All calculated frequencies were scaled by 0.9 to account for anharmonicity and correlation[15]. A standard Gaussian function of 10 cm^{-1} width was applied to all peaks to mimic the broadening expected in solution. All calculations were performed by Prof. Graeme Watson (TCD) on Gaussian 09[116].

3.3.1 Ground-State Calculations

The main ring stretches, carbonyl stretches and CH_3, CH rocking modes appear in the region from 1000 cm^{-1} to 1800 cm^{-1}. The low frequencies modes are the NH_2 wagging and twisting, some out-of-plane distortions, and the non-specific modes (torsion, breathing). The C-H and N-H stretches are at high frequencies (>3000 cm^{-1}). The spectrum of dCyd is supplemented with a range of ribose modes in the region 1380 cm^{-1} to 1480 cm^{-1}

The IR spectra of the four molecules are very similar in the ring region (Fig. 3.16a), with a slight shift to low wavenumbers for the larger molecules. The H-substituted ground states were compared to the available literature and gas-phase FTIR data (Tables 3.7, page 52 and 3.8, page 53) for Cyt[15] and 1-MeCyt[9]. Our data is generally in agreement with literature values, although the HF calculations tend to overestimate the frequency of the carbonyl stretch in particular. There is no significant improvement on progressing from the 6-31G(d,p) to 6-311++G(d,p) basis sets, as it can be seen from Tables 3.7 and 3.8 that better agreement with experimental data for some vibrations is actually found with the smaller basis set. Calculated IR data was available from the literature for Cyd[117] but not dCyd, so the dCyd data were not compared as rigorously.

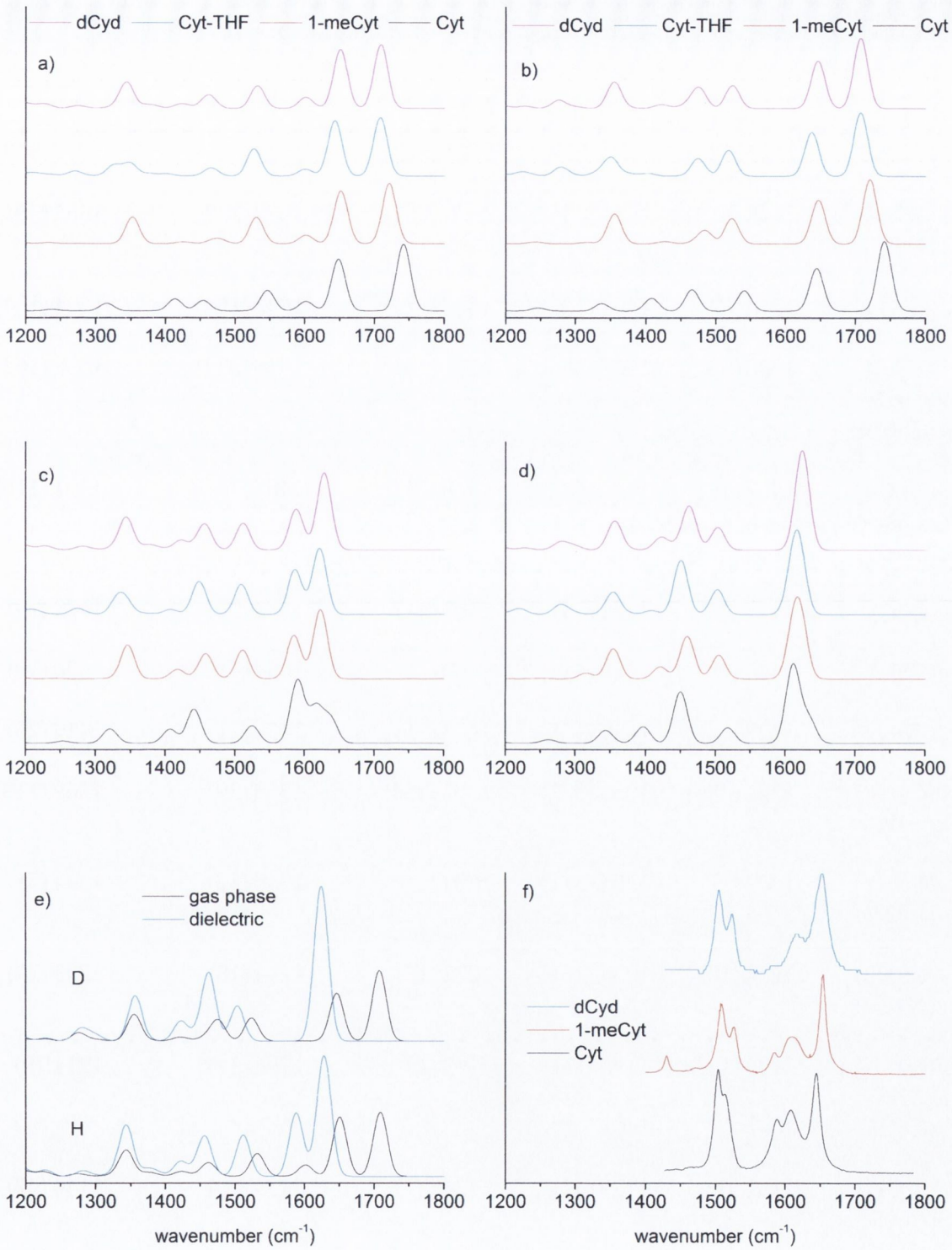

Figure 3.16: Calculated IR spectra of cytosine, 1-methylcytosine, 1-furanylcytosine and 2′-deoxycytidine by HF method with a 6-311++G(d,p) basis set. a) gas-phase b) gas-phase with deuteration c) with dielectric d) with dielectric and deuteration e) direct comparison of the effect of dielectric on IR spectra of dCyd in hydrogenated and deuterated states f) FTIR spectra in D_2O

Table 3.7: Calculated IR frequencies and intensities (in parentheses) for 1-MeCyt by HF, compared to literature values from Smets et al[9]. Scaling factor = 0.9 (HF)

assignment	6-31G(d,p)	6-31G(d,p)[9]	6-311++G(d,p)	6-311++G(d,p)[9]	FTIR[9]
ν(C=O)	1744 (735)	1743 (774)	1721 (895)	1729 (886)	1717 (340)
ν(C5C6) ν(N3C4)	1665 (670)	1656 (735)	1652 (781)	1659 (778)	1662 (361)
δ(scNH_2)	1613 (83)	1608 (109)	1602 (125)	1607 (154)	1594 (154)
ν(N3C4) ν(C4C5) ν(C5C6)	1538 (357)	1528 (365)	1531 (391)	1536 (382)	1532 (162)
ν(N3C4) ν(C6N1) δ(C5H)	1487 (46)	1482 (50)	1478 (52)	1485 (76)	1491 (118)
$\delta(CH_3)$	1473 (31)	1472 (38)	1467 (41)	1472 (22)	1472 (19)
$\delta(CH_3)$	1440 (5)	1446 (4)	1433 (7)	1439 (7)	1430 (10)
$\delta(CH_3)$	1428 (12)	1429 (15)	1423 (21)	1430 (21)	1419 (26)
ν(C6N1) ν(C4N)	1361 (355)	1353 (377)	1352 (394)	1358 (391)	1369 (113)
ν(C6H) ν(C4N)	1309 (1)	1305 (3)	1303 (1)	1310 (1)	1324 (5)
ν(C2N3) ν(N1C2)	1234 (10)	1234 (16)	1232 (15)	1244 (18)	1235 (19)
$\nu(N1C_{Me})$ δ(C5H) ν(C5C6)	1196 (12)	1190 (11)	1193 (13)	1196 (12)	1214*(9)
δ(C5H) δ(C6H) $\rho_1(CH_3)$	1132 (69)	1129 (67)	1128 (73)	1134 (70)	1144 (47)
$\rho_2(CH_3)$	1131 (2)	1123 (2)	1124 (1)	1127 (2)	1127 (3)

ν = stretch, δ = in-plane deformation, ρ = rocking, sc = scissoring

Table 3.8: Calculated IR frequencies and intensities (in parentheses) of cytosine compared to literature values. DFT and experimental data from Kwiatkowski et al[15] and references therein. Scaling factors = 0.9 (HF), 0.97 (DFT)

assignment[15]	DFT $\tilde{\nu}\,cm^{-1}$	HF 6-31G(d,p) $\tilde{\nu}\,cm^{-1}$	HF 6-311++G(d,p) $\tilde{\nu}\,cm^{-1}$	Exp† Ne matrix	Exp† Ar matrix
ν(C2O7)	1763 (623)	1784 (872)	1742 (989)	1730 (685)	1733 (782)
ν(C5C6) ν(N3C4)	1654 (438)	1670 (676)	1648 (770)	1659 (437)	1656 (384)
δ(scNH_2)	1592 (124)	1610 (178)	1602 (139)	1602 (367)	1598 (312)
ν(N3C4) ν(C4C5)	1530 (163)	1557 (303)	1547 (303)	1540 (88)	1539 (139)
ν(N3C4) ν(C4N_{am}) δ(C6H) δ(N1C6)	1471 (98)	1472 (128)	1454 (154)	1475 (164)	1475 (242)
δ(N1H)	1403 (85)	1419 (162)	1414 (177)	1423 (191)	1423 (30)
δ(C6H) ν(C4N_{am}) δ(C5H)	1322 (35)	1331 (83)	1316 (110)	1340 (39)	1337 (66)
ν(C2N3)	1225 (26)	1252 (24)	1237 (22)	1237 (53)	1244 (28)

† exp IR intensities scaled with integral absorbance.
ν = stretch, δ = in-plane deformation, sc = scissoring

Changes in the spectra are seen when the exchangeable protons are substituted with deuterons (Fig. 3.16b). The main effect is that the NH_2 scissors mode is shifted from approx. $1600\,cm^{-1}$ to approx. $1100\,cm^{-1}$ in ND_2 as previously observed[118,119]. The carbonyl is not covalently linked to the amino group and is perturbed only slightly, as previously reported[119].

The addition of the PCM dielectric results in a shift of most frequencies to lower frequencies, and an increase in intensities (Fig. 3.16c,d). Addition of the dielectric causes a shift of the carbonyl, as would be expected given the polarity of the C=O bond. Notably the PCM over-estimates the CO shift (peak 2 in Fig. 3.17 and Table 3.9 on the next page), but very accurately predicts the nearby ring vibration (peak 3). This suggests

that specific effects such as H-bonding etc. are having a greater effect on the carbonyl than on some of the ring vibrations.

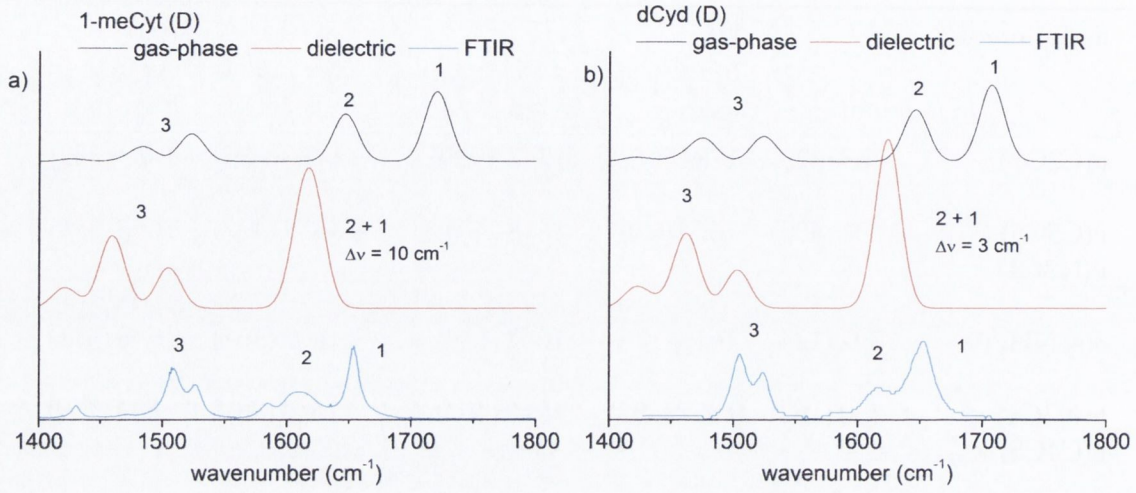

Figure 3.17: Direct comparisons of the main IR peaks in (a) 1-MeCyt (b) dCyd in gas-phase, dielectric and solution (FTIR). Band 1 = ν(C=O) Band 2 = ν(C5C6),ν(N3C4) Band 3 = ν(N3C4),ν(C4C5) and ν(C6N1),ν(N3C4). HF 6-311++G(d,p)

Table 3.9: Frequencies (in cm^{-1}) of ν(C=O) band in 1-MeCyt and dCyd

	gas-phase	dielectric	FTIR
1-MeCyt	1721	1622	1654
dCyd	1708	1625	1652

3.3.2 Excited-State Calculations

Our calculated lowest energy configurations of the singlet excited states of 1-MeCyt show substantial distortions of ring planarity in each case (Fig 3.18 on the following page). In the $^1\pi\pi^*$, the reduction of C5C6 bond order results in distortion of the ring plane. The singly occupied p orbitals on C5 and C6 protons point away from each other, consistent with the previously calculated structures of the biradical $(S_1/S_0)_{CI}$[45,46]. The main distortion occurs away from the three sites (O7,N3,NH_2) that form the W-C base pair with guanine, consistent with the facile formation of the $^1\pi\pi^*$ state in double-stranded DNA.

The $^1n_N\pi^*$ state shows distortion into a boat conformation, as predicted by repulsion between the doubly occupied N3 p orbital and the C4 p orbital[16,24]. Less distortion of planarity is seen in the $^1n_O\pi^*$ state, although the carbonyl shifts out-of-plane, as predicted from its single-bond character and change of the C3 carbon from sp3 to less rigid sp2 hybridisation. There is a slight difference between the 6-31G(d,p) and 6-311++G(d,p) calculations in the bond angle, and hence bond order, of the carbonyl. This results in a slight shift in frequency for the carbonyl stretch at the two basis sets. Both $^1n\pi^*$ states show deformation of the W-C bonding plane, although this appears to be much more exaggerated in the $^1n_N\pi^*$ state than the $^1n_O\pi^*$ state.

In the $^1n\pi^*$ states, the stable sugar conformation in 2′–deoxycytosine is the 2′–endo position, as in the ground state (Fig. 3.19 on the next page). It is interesting to note that the glycosidic bond angle is different in the two lowest energy $^1n\pi^*$ states. It is plausible that this could result in a change in relative stabilities of the excited states in polymeric systems, where there is steric restriction on the rotation of the N-glycosidic bond. It also suggests that there is some connection between the $^1n\pi^*$ state stability and the presence of an N1-deoxyribose group.

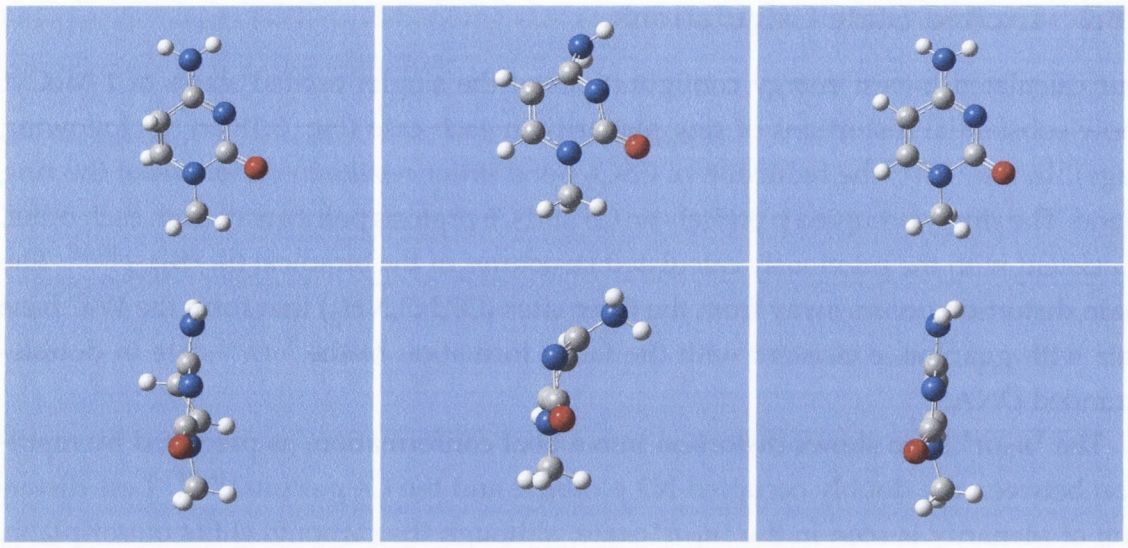

Figure 3.18: Lowest energy structure of 1-methylcytosine excited states by CIS method with 6-31G(d,p) basis set. LEFT: $^1\pi\pi^*$ MIDDLE: $^1n_N\pi^*$ RIGHT: $^1n_O\pi^*$. The edge-on view looks along the W-C base-pairing axis

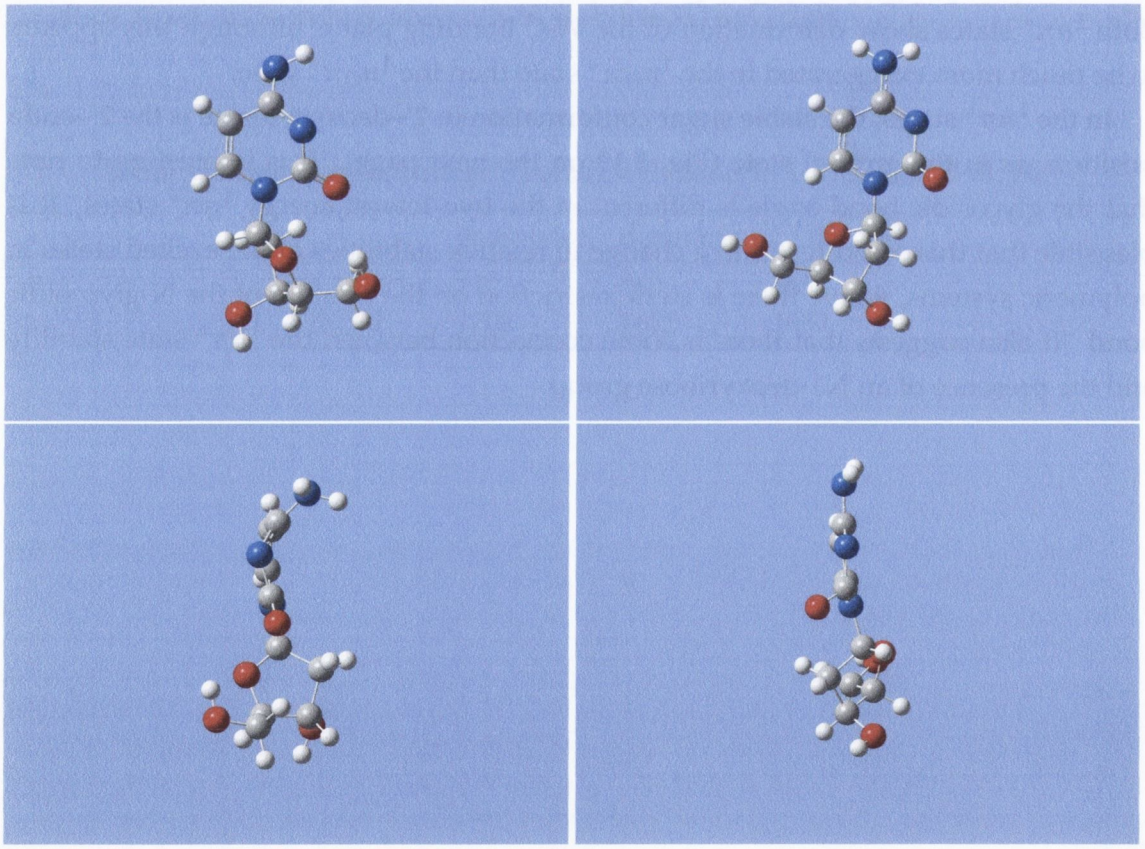

Figure 3.19: Lowest energy structures of 2′-dCyd excited states from CIS method with 6-31G(d,p) basis set. LEFT: $^1n_N\pi^*$ RIGHT: $^1n_O\pi^*$

Calculated IR spectra are shown for the $^1n\pi^*$ states of 1-MeCyt in Fig. 3.20 on the following page, while assignments are tabulated in Tables 3.11 and 3.12 (page 60). In the spectra of the three excited states there is a notable distinction between the $^1n_N\pi^*$ and $^1n_O\pi^*$ states in the high wavenumber (>1700 cm^{-1}) region. The high frequency vibration (1734 cm^{-1}) in the $^1n_N\pi^*$ state arises from the carbonyl stretching. As the carbonyl bond is weakened in the $^1n_O\pi^*$ state, this peak is shifted to 1359 cm^{-1}.

Difference spectra (CIS excited state - HF ground state) are presented for the $^1n\pi^*$ states in Fig. 3.20. In the $^1n_N\pi^*$ state, an absorption is expected at higher energy to the ground-state carbonyl bleach. This is absent in the experimental TRIR, supporting a provisional assignment of the dark state as the $^1n_O\pi^*$, and the 1574 cm^{-1} transient as an out-of-phase ring stretch vibration (see Table 3.12). Both the $^1n_O\pi^*$ and $^1n_N\pi^*$ states have a number of absorption bands at lower wavenumber. It is therefore difficult to unambiguously match any of these to the 1362 cm^{-1} transient observed on the ULTRA apparatus, though it nevertheless confirms that $^1n\pi^*$ absorptions are expected in that region.

An assignment for the $^1n\pi^*$ state in H_2O is complicated slightly by the water absorption feature, though it is clear that there is a broad transient overlapping the ground-state ring vibrations. The calculations also show that an excited-state NH_2 vibration is expected in H_2O in the same region. Inspection of the vibrations with the Gaussview program shows that both these modes (1617 cm^{-1}, 1593 cm^{-1}) have contributions from the NH_2 scissoring. An apparent transient feature below 1494 cm^{-1} in H_2O might correspond to this absorption.

Data was available with the 6-311++G(d,p) basis set for the $^1n_O\pi^*$ state of the three other systems, and there is very little change in the spectra (see Fig. 3.21 on the next page) from one molecule to the next, as also observed in the ground state. The effect of the N1-substituent on the excited state vibrational spectroscopy of the nucleobase itself appears minimal.

The $^1\pi\pi^*$ state is similar to the $^1n_N\pi^*$ in that it features a carbonyl absorption shifted to higher energy relative to the ground state. The isotopic substitution affects those vibrations that are coupled to the NH_2/ND_2 group. The most notable of these is in the $^1\pi\pi^*$, state, where the NH_2 scissoring (1600cm^{-1}) is a more intense band than in the other states. Otherwise the main peaks are similar under both conditions (Fig. 3.22, page 59).

Unfortunately the dielectric could not be applied to the excited state using the CIS method, due to the interconversion of the close-lying $^1\pi\pi^*$ and $^1n_N\pi^*$ states during the calculations.

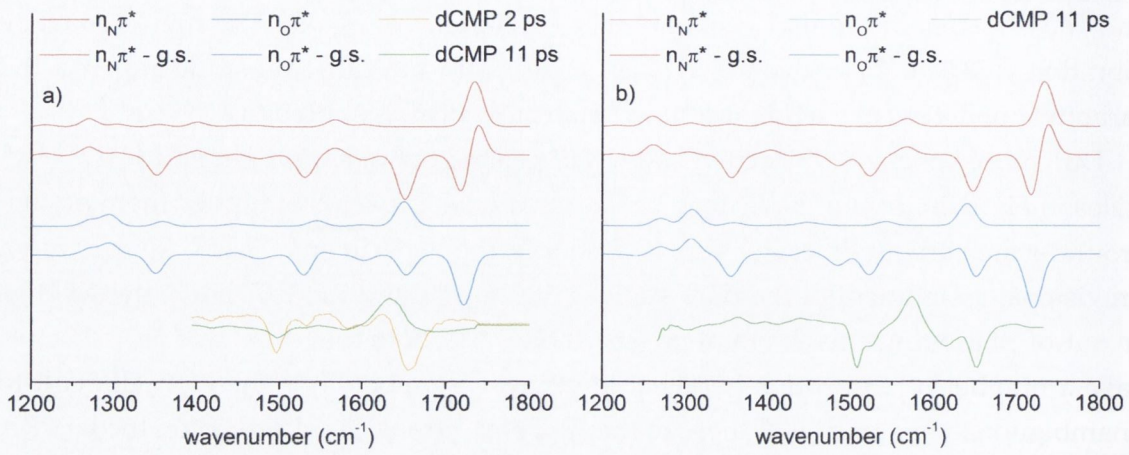

Figure 3.20: Calculated $^1n_N\pi^*$ and $^1n_O\pi^*$ excited states and difference spectra for (a) 1-MeCyt (b) deuterated 1-MeCyt. Experimental TRIR spectra of dCMP in H_2O and D_2O are shown for comparison. [HF-CIS] 6311++G(d,p) basis set

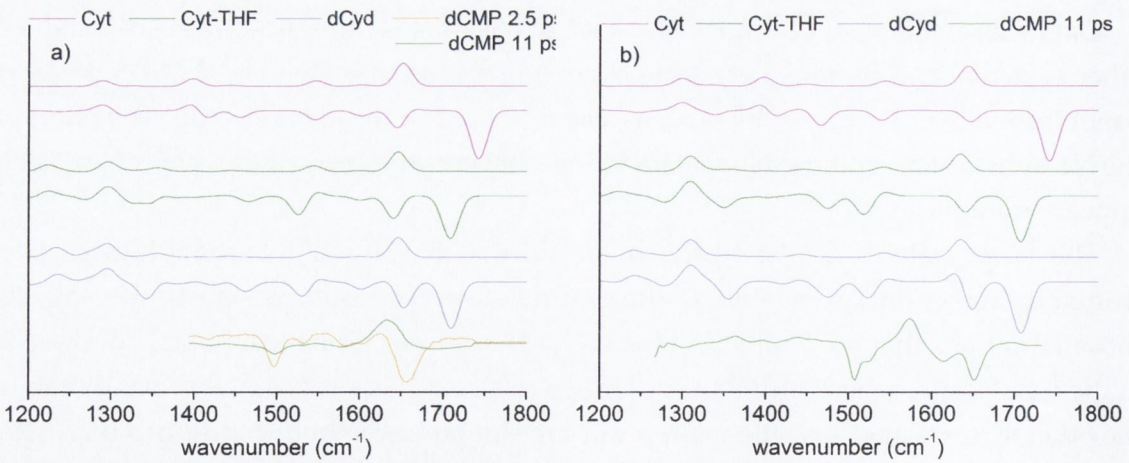

Figure 3.21: Calculated $^1n_O\pi^*$ excited states and difference spectra for (a) Cyt, Cyt-THF, dCyd (b) deuterated Cyt, Cyt-THF, dCyd. Experimental TRIR spectra of dCMP in H_2O and D_2O are shown for comparison. [HF-CIS] 6311++G(d,p) basis set

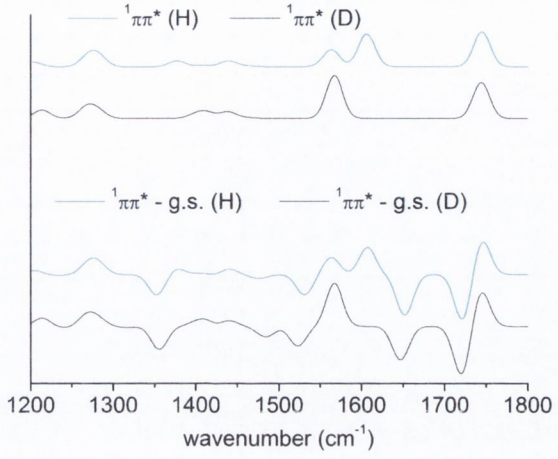

Figure 3.22: Calculated $^1\pi\pi^*$ excited states and difference spectra of 1-MeCyt in deuterated and non-deuterated conditions. [HF-CIS] 6311++G(d,p) basis set

Table 3.10: Calculated IR frequencies and intensities of $^1\pi\pi^*$ 1-MeCyt. CIS method 6-311++G(d,p) basis set, 0.9 scaling factor

assignment	$\tilde{\nu}$/cm^{-1} (intensity)
ν(C2O7)	1745 (668)
δ(scNH$_2$)	1606 (628)
ν(N3C4)	1563 (326)
δ(CH$_3$)	1464 (12)
δ(CH$_3$)	1455 (5)
ν(C5C6), δ(CH$_3$)	1439 (112)
δ(CH$_3$), ν(C5C6)	1408 (29)
ν(C4N14), ν(C4C5)	1376 (115)
ν(C6N1), δ(C5H)	1283 (183)

ν = stretch, δ = in-plane deformation, sc = scissoring

Table 3.11: Calculated IR frequencies and intensities of $^1n_N\pi^*$ in 1-MeCyt CIS method 6-311++G(d,p) basis set, 0.9 scaling factor

assignment	$\tilde{\nu}/\mathrm{cm}^{-1}$ (intensity)
$\nu(C_2O_7)$	1734 (796)
$\delta(\mathrm{scNH_2})$	1602 (36)
ν(C5C6), ν(N1C6)	1507 (122)
$\delta(CH_3)$	1471 (19)
$\delta(CH_3)$	1450 (23)
$\delta(CH_3)$	1428 (7)
ν(N3C4)	1401 (81)
ν(C4C5), δ(C5H), δ(C6H)	1355 (44)
δ(C6H), ν(N1C2), ν(N3C4)	1303 (48)
ν(N1C6), ν(C4C5)	1270 (144)
δ(C5H), δ(C6H), ν(C4C5)	1217 (35)

ν = stretch, δ = in-plane deformation, sc = scissoring

Table 3.12: Calculated IR frequencies and intensities of $^1n_O\pi^*$ in 1-MeCyt.CIS method 6-311++G(d,p) basis set, 0.9 scaling factor

assignment	$\tilde{\nu}/\mathrm{cm}^{-1}$ (intensity)
ν(N3C4), ν(C5C6), $\delta(\mathrm{NH_2})$	1650 (430)
$\delta(\mathrm{scNH_2})$	1601 (20)
ν(C5C6), $\nu(C_4C_5)$, $\nu(C_4N_3)$	1545 (97)
$\delta(CH_3)$	1465 (13)
$\delta(CH_3)$, δ(C5H), δ(C6H)	1446 (7)
ν(N1C6), ν(C4C5), $\delta(CH_3)$	1444 (30)
$\delta(CH_3)$	1415 (7)
ν(C2O7), ν(C2N3), δ(C6H), $\delta(CH_3)$	1359 (85)
ν(C4N14), δ(C5H), δ(C6H)	1295 (203)
δ(C6H), $\delta(CH_3)$	1271 (112)

ν = stretch, δ = in-plane deformation, sc = scissoring

3.4 Discussion on Calculated IR Spectra

3.4.1 Ground-State Calculations

In order to arrive at acceptable descriptions of the excited states, it was necessary to ascertain the validity of the ground state calculations, for which reliable literature comparisons are available. The agreement of the IR data of cytosine and 1-MeCyt with previous calculation and experiment shows that the HF calculations are sufficiently accurate.

Applying the polarisable continuum model (PCM) neglects the specific H-bonding effects that are accounted for in discrete methods[11,12], although discrete methods require a large number of interacting water molecules to approximate a dilute solution and can be computationally expensive. However, Sambrano et al claim that bulk effects are more significant than H-bonding, especially when the solvent has a high dielectric constant[120].

In the ground-state the accuracy of the dielectric component can be assessed as there is experimental data available for comparison (FTIRs). The overestimation of the shift in the carbonyl compared to the ring bands is possibly because specific effects influence the carbonyl more than the ring. This highlights the difficulty in properly accounting for the solvent, and hints as to why few studies have appeared of solvated nucleobases[121].

3.4.2 Excited-State Calculations

The previous assignment of the long-lived IR transient at $1574\,\mathrm{cm}^{-1}$ as a $^1n_N\pi^*$ state was made tentatively, on the basis that the carbonyl bond in the $^1n_O\pi^*$ should be weakened and would not appear in the spectral window[25]. However, there was no direct evidence that the transient was indeed associated with a carbonyl stretch, and little experimental evidence to favour an assignment of one excited state over the other.

As well as neglecting solvent effects, gas-phase calculations may also arrive at incorrect relative stabilities of the excited states. The chosen CIS technique may also mis-represent the relative energies if different electronic correlation is present in each excited state. Despite this, relative stabilities should not be a factor here as our calculations only show the IR spectra of the relevant excited-state structure, not the probability that the excited state is actually formed, nor how rapidly it will decay.

The accuracy of the ground-state gas-phase calculations leads to the tentative con-

clusion that the gas-phase excited-state spectra are also correct, and that the difference spectra are correct in the gas-phase. The possible extension of the assignment from the gas phase to solution rests on whether the presence of the solvent will have a significantly different effect on the excited states than the ground state, and on one excited state over another. The specific question to be answered is whether solvation will shift the carbonyl band of the $^1n_N\pi^*$ state more than the ground state, or whether the carbonyl stretch in the $^1n_N\pi^*$ state would still occur at higher wavenumber than the ground state.

There is limited data available to answer this question, the most important being the study by Shukla and Leszczynski, where they calculate ground state and $^1n_N\pi^*$ geometries in the presence of three H-bonded H_2O molecules[16]. They show an increase in C=O bond length from 1.191Å to 1.206Å in the ground state, and 1.182Å to 1.202Å for the $^1n_N\pi^*$. The carbonyl bond is therefore still stronger in the $^1n_N\pi^*$ state than the ground state, even in the presence of H-bonded water.

There is considerable data available on the dipole moments and orientations of the excited states, both from this work and the literature. Excited-state dipole moments are not necessarily larger than the ground-states, although the dipole moments are global figures that describe the whole molecule and do not offer predictions on how specific vibrations will be affected by solvent.

Despite the limitations of the gas-phase calculations there is little to suggest that the assignment of the $^1n_O\pi^*$ state would be reversed. Ideally, the excited-state spectrum of the solvated excited state would be calculated. This has not been achieved to date, and represents a considerable challenge for computational methods. Additionally, the multideterminate calculations on the cytosine nucleobase need to be extended to dCyd, wherein the additional electrons of the sugar moiety would have enormous effects on computation time.

The assignment of the $^1n_O\pi^*$ state needs to be considered in light of previous excited-state calculations. In studies with CAS-SCF and CAS-PT2 methods the $^1n_N\pi^*$ is calculated to be at considerably higher energy that the $^1\pi\pi^*$ state in the gas phase[24,41,42]. As the solvent is expected to raise the energy on $^1n\pi^*$ states, the $^1n_N\pi^*$ state may be even less accessible from the $^1\pi\pi^*$ state in solution. Meanwhile the $^1n_O\pi^*$ has been predicted to be close to the $^1\pi\pi^*$ and to participate in excited-state decay[42,48]. Of particular interest is the work of Hudock and Martinez who predict population trapping for 15% of excitations on the $^1n_O\pi^*$ surface after 1 ps[51]. The 15% probability is strikingly similar to the % contributions recorded by TRIR, though this similarity is probably coincidental as the two values refer to different conditions. However, a trend may be extracted from the literature that the $^1n_O\pi^*$ may have local minima that result in longer deactivation times. Our assignment of the dark state as the $^1n_O\pi^*$ is therefore physically reasonable.

3.5 Conclusions

The dark $^1n\pi^*$ state has been further characterised by recording its IR spectrum between 1300 and 1450 cm^{-1}. A TRIR spectrum of dCMP has been successfully recorded in H_2O, revealing that the relaxation of the dark $^1n\pi^*$ state is similar in both H_2O and D_2O. The absence of the long-lived state in 1-MeCyt confirms that the formation of the $^1n\pi^*$ is influenced by the ribose group. A number of theories have been proposed, favouring a model in which the relative energies of the singlet excited states are influenced by the local solvent environment, which is in turn affected by the ribose group. An assignment of the dark state has been provisionally made as a $^1n_O\pi^*$ state, but it is necessary to incorporate solvent effects in order to strengthen this assignment.

Chapter 4

Dinucleotides and Polynucleotides

Having characterised dark excited states in the monomer systems, the study now extends to dinucleotide (d(CpC)) and polynucleotide (poly(rC)) sequences, in order to ascertain the effect that linked nucleotides and base-base interactions have on the excited state. All TRIR data reported here were recorded in D_2O on the PIRATE system.

4.1 UV and CD Spectra

The electronic spectra of d(CpC) and poly(rC) are compared to dCMP in Fig. 4.1 on the following page, and the relative spectral shifts listed in Table 4.1. The UV and CD spectrum of d(CpC) are in agreement with published results[64]. The maximum absorbance (270 nm) is very slightly blue-shifted from that of dCMP (272 nm). In the CD spectrum of d(CpC), the positive absorbance is characteristic of the stacking conformation. More substantial blue shifting is seen for poly(rC), with a large positive CD that has been assigned to base-tilting, though base-stacking may also be expected to have a similar effect[75].

Table 4.1: λ_{max} of absorption for d(CpC) and poly(rC) and shifts relative to dCMP (in D_2O 50 mM phosphate pH 7)

species	λ (nm)	$\tilde{\nu}$ (cm^{-1})	$\Delta\tilde{\nu}$ (cm^{-1})
dCMP	271	36900	-
d(CpC)	270	37037	137
poly(rC)	268	37313	413

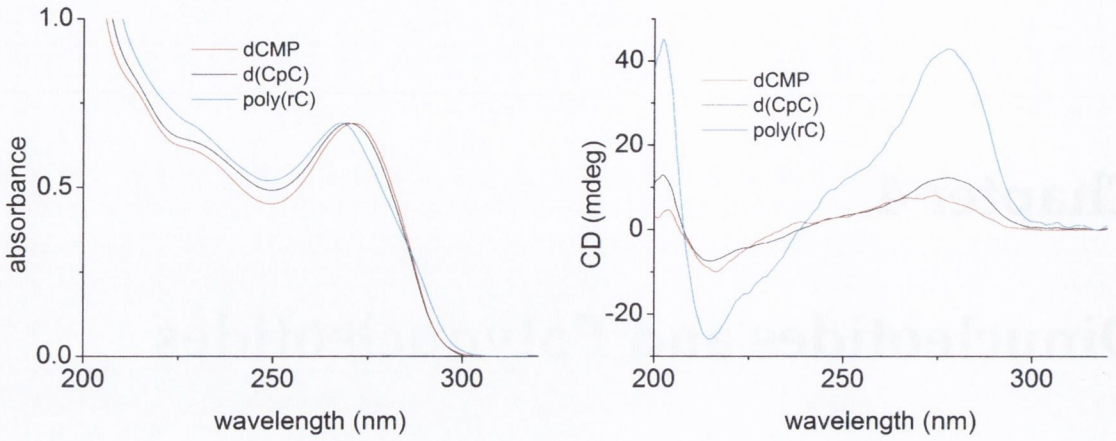

Figure 4.1: LEFT: Normalised UV spectra and RIGHT CD spectra of 10 mM dCMP, d(CpC) and poly(rC) in D_2O (50 mM phosphate, pH 7)

4.2 TRIR spectra

4.2.1 d(CpC)

The ps-TRIR and FTIR spectra of d(CpC) are shown (Fig. 4.2 on the next page). There are strong similarities between this spectrum and that of dCMP. Fast transient decay occurs over the first 10 ps, with some evidence for tracking in the 1500 cm^{-1} region. A long-lived transient feature is present at 1574 cm^{-1}.

The d(CpC) spectrum at two different delays was separated into discrete Lorentzian components, yielding similar features to dCMP (Figs 4.3 on page 68 and A.1, page 209). A single Lorentzian band was used to fit the region around 1570 cm^{-1}, and this is the only long-lived feature present in the region from 1450 - 1750 cm^{-1}.

4.2.2 Poly(rC)

The TRIR spectrum of poly(rC) (Fig. 4.2) differs from that of dCMP or d(CpC). There is a reversal of intensity of the low frequency ring bands, with considerable sharpening of the 1505 cm^{-1} band. A comparison of the ground-state IR of the three systems is given in Table 4.2.

Vibrational cooling is evident over the first 10 ps after excitation, with evidence for tracking, especially in the lower frequency ring modes (around 1500 cm^{-1}.) A long-lived transient is again present at 1574 cm^{-1}. No transient features are present in the high frequency region from 1650 to 1750 cm^{-1}. The TRIR spectra at 2 ps and 21 ps were fit using overlapping Lorentzian functions (Fig. 4.4, page 69). After 20 ps the 1574 cm^{-1} bands persists, and an additional transient feature remains at 1635 cm^{-1}.

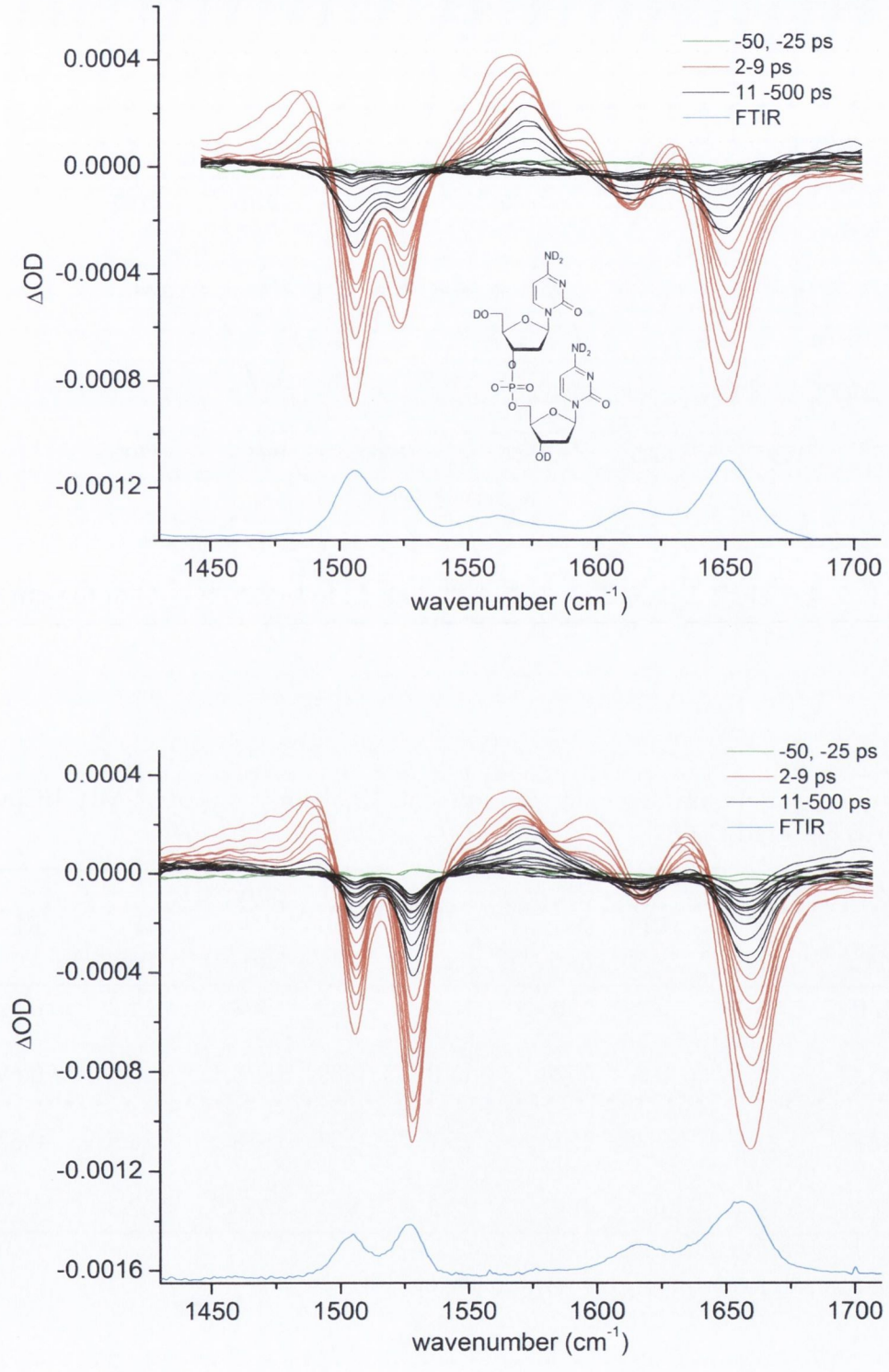

Figure 4.2: FTIR and TRIR spectra of TOP: d(CpC) Delays (ps):-50, -25, 2, 3, 4, 5, 6, 7, 9, 11, 15, 21, 34, 51, 79, 89, 110, 134, 160, 192, 234, 400, 500 BOTTOM: poly(rC) Delays (ps): -50, -25, 2, 3, 4, 5, 6, 7, 9, 11, 15, 21, 34, 51, 70, 89, 110, 134, 160, 192, 234, 306, 400, 500. Both 10 mM recorded on PIRATE in D_2O in 50 mM phosphate buffer (pH 7)

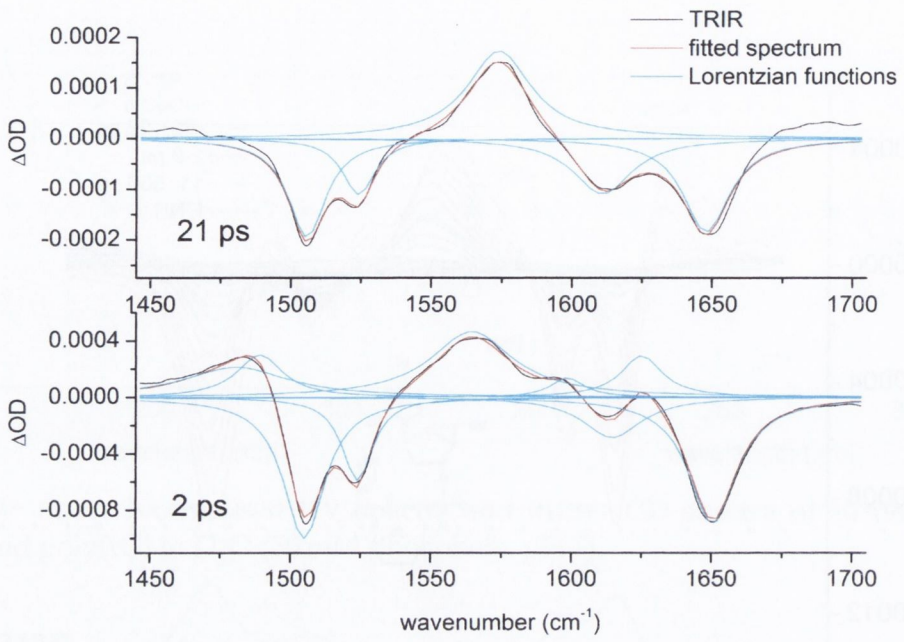

Figure 4.3: FTIR and TRIR (2 ps, 21 ps) of 10 mM d(CpC) in buffered D_2O fit to sum of overlapping Lorentzian peaks. Data from PIRATE

Table 4.2: Fitted spectral parameters for ground state IR absorptions of dCMP, d(CpC) and poly(rC) in buffered D_2O

vib.	dCMP $\tilde{\nu}$ (cm^{-1})	w (cm^{-1})	RI	d(CpC) $\tilde{\nu}$ (cm^{-1})	w (cm^{-1})	RI	poly(rC) $\tilde{\nu}$ (cm^{-1})	w (cm^{-1})	RI
$\nu(N_3C_4)$ $\nu(C_6N_1)$	1505	16	0.99	1505.5	16.5	0.82	1504	11.7	0.52
$\nu(N_3C_4)$ $\nu(C_4C_5)$	1525	11.1	0.6	1524	14.0	0.52	1526.5	10.9	0.69
$\nu(C_5C_6)$ $\nu(N_3C_4)$	1612	24.4	0.36	1614.5	25.7	0.33	1616	24.5	0.33
$\nu(C_2O_7)$	1649	19.4	1	1651	20.2	1	1655.5	22.3	1

w = full width at half maximum,
RI = relative intensity calculated from intensity of C=O stretch

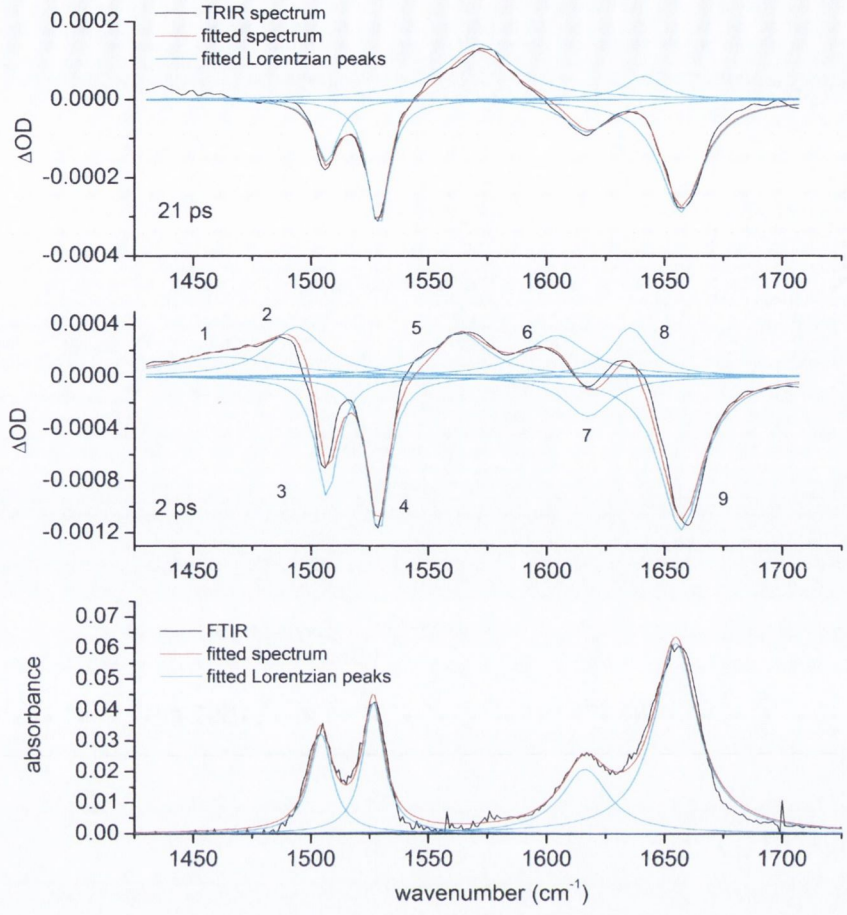

Figure 4.4: TRIR (2 ps, 21 ps) of 10 mM poly(rC) fit to a sum of overlapping Lorentzian functions. Data from PIRATE

4.3 Kinetics

4.3.1 d(CpC)

Results from single-point kinetic analysis are shown in Table 4.3 on page 71 with the main fitted decays in Fig. 4.5 on the following page. Kinetics were fitted to biexponential model, with a short 'cooling' component and one longer-lived decay. In the bleaching kinetics there is some dependence of the short component lifetime on wavenumber (above 1649 cm^{-1}). This is probably a consequence of overlapping hot transients, as has been reported previously for GMP[109]. This should not have a large effect on the lifetime of the second component, as any overlapping hot transient will have decayed by about 10 ps. The transient and bleach recovery have similar lifetimes of 53 ± 6 ps, implying that ground-state recovery occurs through the the dark $^1n\pi^*$ state.

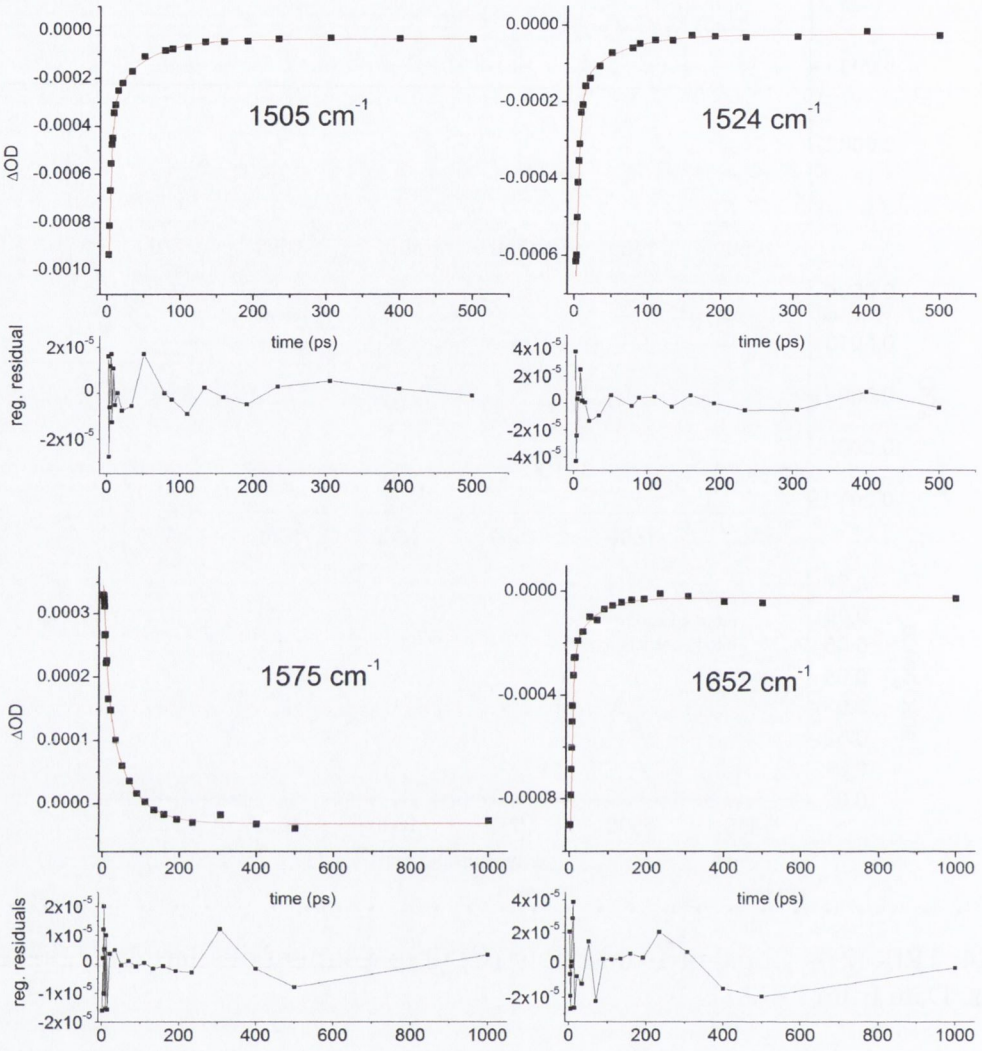

Figure 4.5: Biexponential single point fits and residuals for main bleach and transient bands of 10 mM d(CpC) in D_2O in 50 mM phosphate pH 7 (PIRATE)

Table 4.3: Kinetic parameters and fitting errors for d(CpC) in D_2O in 50 mM phosphate pH 7. Calculated from single-point method

$\tilde{\nu}$ (cm^{-1})	τ_1 (ps)	A_1	τ_2 (ps)	A_2	R^2
1502 (B)	2.3 ± 0.1	82	48 ± 6	17	0.99688
1505 (B)	3.6 ± 0.2	79	46 ± 6	19	0.99818
1508 (B)	4.1 ± 0.2	77	48 ± 5	21	0.99873
1521 (B)	3.4 ± 0.3	83	51 ± 15	14	0.99237
1524 (B)	4.8 ± 0.5	83	50 ± 22	15	0.99215
1649 (B)	3.6 ± 0.2	82	56 ± 16	18	0.99818
1652 (B)	4.5 ± 0.4	82	58 ± 15	16	0.99503
1655 (B)	4.7 ± 0.4	84	63 ± 19	15	0.99396
1572 (Tr)	6.8 ± 1.1		55 ± 7		0.99689
1575 (Tr)	10.1 ± 2.7		59 ± 12		0.99689
1577 (Tr)	12.8 ± 5.6		57 ± 13		0.99503

4.3.2 Poly(rC)

In poly(rC), bleach decays fit in the range 85 ± 15 ps (see Table 4.4 on page 73 and Fig. 4.6 on the following page). As was observed for d(CpC), the lifetimes of bleach and transient agree within error. The contribution of long-lived decay was compared for dCMP, d(CpC) and poly(rC) by examining suitable bleach kinetics. The ν(CO) band at 1656 cm^{-1} was chosen as it gave the largest signal, and fitting models showed it to have the fewest overlapping transients (see Fig. 3.11, page 44). In order to correct for the overlap, kinetics were recalculated from fitted Lorentzian curves of the ν(CO) bleach (Fig 4.7 on page 73). Fitting was performed on the assumption that the zero-time on the delay line was accurate, as variations here could affect the relative contributions of long and short components.

The percentage contributions of the long component is similar in all systems, with apparently only slight increases in the order dCMP<d(CpC)<poly(rC). As expected, the contribution of long-lived species is greater by curve fitting in dCMP and d(CpC), as single-point fitting understates the short component (Table 4.5, page 73). The similarity in amplitudes in poly(rC) is possibly because the overlapping transient at 1635 cm^{-1} ($\tau = 9 \pm 1$ ps, fit not shown) is longer-lived than the other hot bands.

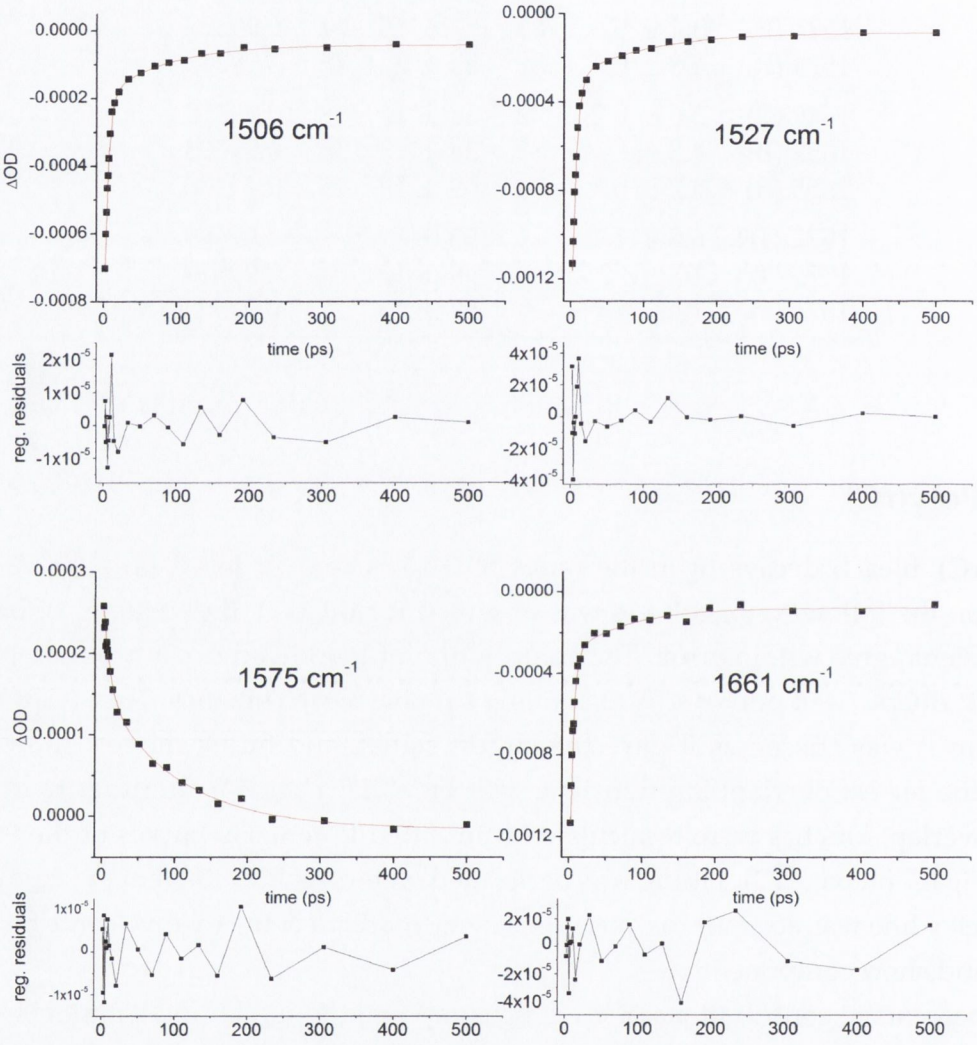

Figure 4.6: Biexponential single-point fits and residuals for main bleach and transient bands of poly(rC) in D_2O in 50 mM phosphate pH 7 (PIRATE)

Table 4.4: Kinetic parameters and fitting errors for poly(rC) in D_2O in 50 mM phosphate pH 7. Fit by single-point method

$\tilde{\nu}$ (cm^{-1})	τ_1 (ps)	A_1 (%)	τ_2 (ps)	A_2 (%)	R^2
1503(B)	3.6 ± 0.1	83	94 ± 11	14	0.99832
1506(B)	5.0 ± 0.2	82	83 ± 12	13	0.99857
1509(B)	5.3 ± 0.3	78	88 ± 13	18	0.99789
1525(B)	4.0 ± 0.2	83	85 ± 10	11	0.9985
1527(B)	5.8 ± 0.3	85	101 ± 25	9	0.99741
1530(B)	6.9 ± 0.5	86	117 ± 45	7	0.99563
1533(B)	7.9 ± 0.9	86	112 ± 73	6	0.99113
1654(B)	3.2 ± 0.3	81	65 ± 13	13	0.99401
1657(B)	3.8 ± 0.3	83	70 ± 15	12	0.99497
1661(B)	4.3 ± 0.3	84	77 ± 18	11	0.99516
1664(B)	5 ± 0.3	85	90 ± 26	10	0.99551
1572(Tr)	7 ± 1		93 ± 11		0.99601
1575(Tr)	10 ± 2		104 ± 15		0.99497

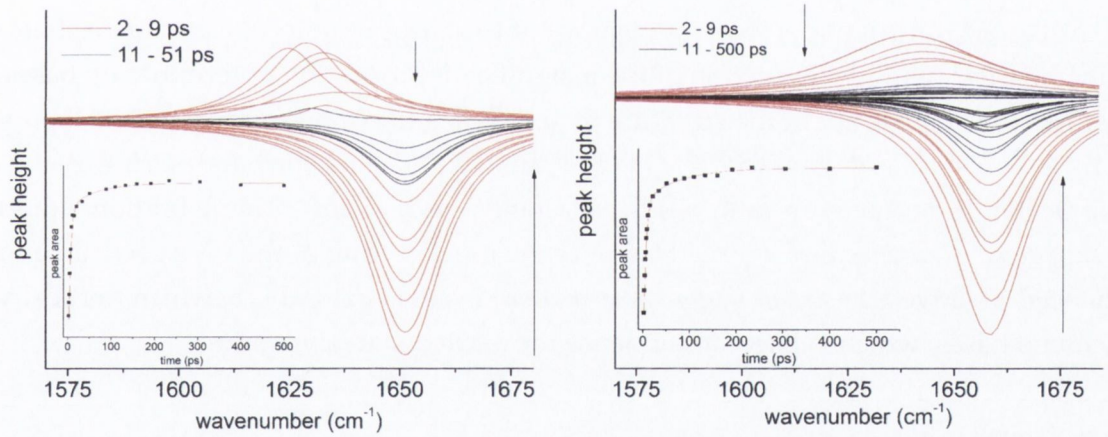

Figure 4.7: Lorentzian curve fitting and (inset) biexponential fits for carbonyl bleach in LEFT: d(CpC) and RIGHT: poly(rC), in buffered D_2O (PIRATE)

Table 4.5: Relative amplitudes of short and long components for biexponential kinetic fitting to carbonyl bleach in d(CpC) and poly(rC) in D_2O. Calculated from single-point (sp) fitting and Lorentzian curve-fitting (L)

	dCMP		d(CpC)		poly(rC)	
	sp	L	sp	L	sp	L
short (%)	84	89	83	87	83	83
long (%)	16	11	17	13	17	17

4.4 Discussion

4.4.1 Structures of d(CpC) and Poly(rC)

Linking two nucleotides to form the d(CpC) dinucleotide introduces some notable secondary features. Firstly, the two cytosine moieties are structurally distinct species, as one is 3′dCp and the other 5′pdC. Secondly, the dinucleotide may exist as an equilibrium mixture of stacked and unstacked conformations.

This study of polymeric C systems was motivated, to some extent, by recent studies on the effect of base-stacking on DNA/RNA photophysics[84,87,88]. It was originally intended to study the r(CpC) dinucleotide, which is known to be 34% stacked in solution[58]. However, subsequent examination of the synthesised compound by NMR revealed that the deoxy-(CpC) dinucleotide had been supplied. Although this structure is considerably less stacked than the ribose analogue, there is clearly an appreciable electronic interaction between the vertically displaced bases. For example, the slight blue shift in the absorption λ_{max} (137 cm^{-1} relative to dCMP) could be ascribed to the Frenkel excitons characteristic of "H"–type aggregation[122], while the positive CD is indicative of vertical base-stacking[64].

Unlike the dinucleotide, the vast majority of the bases in poly(rC) should be chemically identical, with the exception of the insignificant proportion of terminating bases. There is some debate about the structure of poly(rC), and strong support for the theory that the bases are not stacked[74,75]. Large-scale base-stacking or base-pairing is contraindicated from the IR spectra, as suppression of the 1525 cm^{-1} ring vibration would be expected in either case[93,123,124]. However the blue-shifting of the UV spectrum and enhanced positive CD signal suggests that there is some coupling between vertically separated bases, which is likely to influence the excited state dynamics.

4.4.2 Vibrational Cooling

In both d(CpC) and poly(rC) there is evidence for 'tracking' of hot transient bands from low to high wavenumber, as seen in the monomer systems. This contrasts with TRIR experiments on [poly(dG-dC)]$_2$, where the absence of tracking is suggested to be due to rapid distribution of the vibrational energy caused by delocalisation of the Frank-Condon excited state over stacked bases, or efficient phonon coupling between same[93]. However it is also conceivable that vibrational redistribution in that case is facilitated to a greater extent by base-pairing. For example, dA_{18} and ApA are stacked but not base-paired, and have similar cooling kinetics to dAMP[125]. TMP and the poorly stacked dT_{18} oligomer are also reported to have similar cooling kinetics[88,125] (although this is contradicted in a later report[102]). The tracking of the cooling bands in d(CpC) and

poly(rC) suggests that vibrational energy remains localised on the excited nucleobase. The very modest lengthening of the cooling lifetime (relative to dCMP monomer) may be due to partial shielding from the solvent, which would decrease the efficiency of intermolecular vibrational relaxation.

4.4.3 Dark-State Dynamics

The presence of the 1574 cm^{-1} transient in the TRIR of d(CpC) and poly(rC) proves that the $^1n\pi^*$ state is populated in linked nucleotide systems. $S_1 \rightarrow S_0$ internal conversion still dominates in these systems, though the agreement between transient and bleach kinetics for both systems shows that the dark state is the primary 'long-lived' decay pathway. The similarity in relative decay amplitudes between dCMP and d(CpC) or poly(rC) shows that no significant additional deactivation route is accessible in the multimer systems.

TRIR reveals that the principal effect of progressing from dCMP to d(CpC) is the lengthening of the $^1n\pi^*$ lifetime by approx 50%. The precise meaning of the 53 ± 6 ps lifetime is ambiguous at this stage. It may be a weighted average lifetime of the stacked and unstacked forms, in which case the unstacked form retains a 34 ps lifetime. It could otherwise be purely representative of the dinucleotide, in which case the lifetime is increased by linking the two bases, and is not dependent on base stacking. To answer this question fully it would be necessary to study the r(CpC) derivative, with its increased stacked populations. An alternative explanation is that the 53 ps lifetime is an average of two separate lifetimes from the 3′dCp and 5′pdC moieties, but any difference in kinetics would likely be very slight, and impossible to resolve from our data.

As the bases in poly(rC) are essentially identical, the long (85 ± 15 ps) lifetime may be taken as the true $^1n\pi^*$ state lifetime. A possible reason for the longer lifetime relative to dCMP (33 ± 4 ps) is protection from solvent. Deactivation may also be impeded if the nucleobase structure is more rigid in the polymer than the monomer, thereby inhibiting vibrations in the $^1n\pi^*$ state. Alternatively the barrier to the $(^1n\pi^*/S_0)$ conical intersection (CI) may rise in energy. The $(^1\pi\pi^*/^1n\pi^*)_{CI}$ appears not be affected as the dark state is still formed, and in the same yields as in the monomer. The likelihood then would be that the $(^1n\pi^*/S_0)_{CI}$ is destabilised in the polymer.

The assignment of the long-lived state as an $^1n_O\pi^*$ state in the previous chapter may also be discussed in the context of the polymer results. There is significant deformation of ring-planarity in the $^1n_N\pi^*$ state, though ring planarity is preserved in the $^1n_O\pi^*$ state. Steric issues in the polymer could destabilise the $^1n_N\pi^*$ more than the $^1n_O\pi^*$ state. The experimental data thus supports, albeit very tentatively, the assignment of the dark state as a $^1n_O\pi^*$ state.

4.4.4 Additional Decay Pathways

The possible presence of excimers in polymeric C systems has been a dominant theme in the literature and needs to be addressed with reference to the TRIR data[84,96,99,100]. Time-resolved emission spectra clearly show a difference between CMP and d(CpC), with the latter showing evidence for additional long-lived fluorescence in the near-UV[100]. The above study exemplifies that fluorescence measurements are very sensitive to radiative decay. In contrast the TRIR bleach kinetics constitute all radiative and non-radiative decay pathways, so the effect of a slight increase in the weak emission yield is not likely to be observed. However, it has been suggested that excimers are mainly charge-transfer in nature, and that they have low radiative character[84]. Higher yields of long-lived states would then be observed in the bleach recovery.

In principle, excimer formation may be confirmed by a distinctive IR spectrum. However, these may be effectively obscured if the excimer yield is low, or if there is overlap with the existing bleach and transient bands. In this context, it is worth stressing that there is no IR excimer band in ApA[125] in the 1450 - 1750 cm^{-1} region, despite the strong evidence that ApA forms an excimer[87]. The presence of an excimer, therefore, cannot be ruled out. Interpretation of the kinetics is also complicated by the possibility that a C-C excimer would have a similar lifetime (c. 50 ps) to that recorded for the $^1n\pi^*$ state, based on the lifetimes for other dinucleotides reported by Takaya et al[87]. It is noteworthy that in the related r(CpC) compound, excimer properties have only been recorded at low temperature, despite appreciable stacking in ambient conditions.

In order to assess the previous literature on poly(rC) photophysics, only room temperature studies were considered. Accordingly, poly(rC) has similar "monomer" fluorescence to dCMP with a low quantum yield ($\Phi_f = 1.4 \times 10^{-4}$)[97]. This is fully consistent with our TRIR data as the increase in long-lived decay is very slight.

By contrast, the transient UV/vis results of Cohen et al are more difficult to reconcile with the TRIR data[84]. In that paper they do not probe at 340 nm, so can not observe the signature UV absorbance of the $^1n\pi^*$ state[27]. Instead they observe a species absorbing at 570 nm, with a 12 ps lifetime. However, they also observe similar kinetics for the bleach at 280 nm, implying that this transient species repopulates the ground state. By extension, they do not observe the $^1n\pi^*$ state in the bleach. Unfortunately they monitor a different bleach wavelength (280 nm) than that used for their study on $^1n\pi^*$ states in pyrimidine monomers (250 nm)[27], so a direct comparison is impossible.

A possible reason why they do not observe $^1n\pi^*$ kinetics in the bleach is that there is overlap with a transient species, which decreases the percentage contribution of the $^1n\pi^*$ state to the measured kinetics. Another possibility is that there is a large solvent isotope effect in the photophysics of the polymer. The latter is unlikely given the

absence of an isotope effect for the $^1n\pi^*$ state in monomer systems, and the modest isotope effects seen for long-lived decay in polymers[88,126].

It is not clear to us what the 12 ps component in Cohen et al's TA study is, although the authors assign it as an excimer. It constitutes 30% of the signal at 570 nm, and from the authors claims of 'mirror symmetry' with bleach kinetics, we can infer that a similar contribution is observed in the bleaching. In principle, these bleach kinetics should also be observed by TRIR. Although we do not observe such a species, it is possible that the bleach recoveries in the TRIR are actually tri-exponential, and that the 12 ps component is subsumed into the vibrational cooling kinetics. This is beyond what we can confidently extract from our kinetic data.

It is also worth considering that the fitting discrepancies in the poly(rC) carbonyl region (Fig. 4.4) are related to this 12 ps species. The persistence of the hot carbonyl transient contrasts with the dCMP and d(CpC) systems when fitted with a similar method. The fitted lifetime (9 ± 1 ps) is also similar to that reported by Kohler et al, and an excimer species has previously been observed close to the carbonyl band of guanine in stacked G-tetrad systems[109]. The fact that this feature only reveals itself through subtraction puts faith in the fitting model and the assumptions made. For example, the presence of transient bands can be affected if the peak width for the bleaches is not fixed. However, important features in TRIR spectra can be revealed through subtraction alone[127], once the fitting model is correct.

Despite some disagreement with the Kohler work, TRIR should be considered the authoritative data on the dark state dynamics, as TRIR is a superior spectral technique to transient UV/vis. Although the presence of excimer species in poly(rC) may still be an open question, the evidence for the presence of the locally excited $^1n\pi^*$ state in poly(rC) is compelling.

4.5 Conclusions

The locally excited $^1n\pi^*$ state has been shown to be present in the linked nucleotide sequences, d(CpC) and poly(rC). The yields of formation are similar to the monomer but the lifetimes increase. This state is still the dominant long-lived decay route, with only tentative evidence for additional decay channels such as an excimer.

Chapter 5

Higher Order Systems

In this section the excited-state properties of oligonucleotide sequences and poly(rC) are studied as a function of pH, where acid conditions promote the formation of higher-order structures. These include the tetrameric 'i-motif' structure, the formation of which is believed to have biological relevance, and double-stranded poly(rC-rCH$^+$). These hemi-protonated structures are known to exhibit long-lived excited states, but have never been studied by TRIR. The results presented in this chapter were recorded in D_2O on both PIRATE and ULTRA.

5.1 DNA - $d(C_3TA_2)_4$

The aim of the studies on the oligonucleotides was to separately observe the i-motif and single-stranded forms. Experiments were performed at pH 5.5, where i-motif formation is induced, and pH 8.5 where the sequence is expected to be a single-stranded random coil. The oligonucleotide sequence chosen was $d(C_3TA_2)_4$, as $(CCCTAA)_n$ repeat sequences appear as complementary strands to the telomeric $(TTAGGG)_n$ repeats found in human chromosomes.

5.1.1 UV and CD Spectra

The absorption spectrum of the sequence at pH 5.5 is substantially red-shifted relative to that recorded at pH 8.5 (Fig. 5.1 on the following page). In the CD spectra, the sequence at pH 8.5 shows positive absorption at 270 nm and negative absorption at 250 nm, indicative of a normal single-stranded structure. At pH 5.5 the positive maximum is red-shifted to 289 nm, and there is absorption as far out as 310 nm. These features are characteristic of the i-motif structure, and agree with the published CD spectrum of $(C_3TA_2)_3C_3$ [128,129].

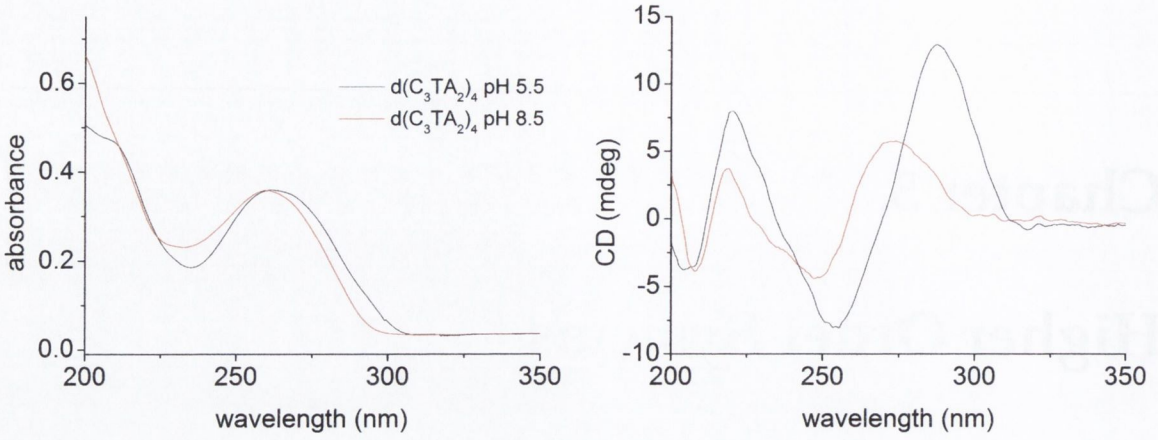

Figure 5.1: LEFT: UV and RIGHT: CD spectra of $d(C_3TA_2)_4$ at pH 5.5 (50 mM NaH_2PO_4) and pH 8.5 (50 mM Na_2HPO_4) in D_2O

5.1.2 TRIR Spectra

The FTIR and TRIR spectra of the oligonucleotides feature overlapping bands from cytosine, adenine and thymine. Assignments for the depletion bands at both pHs are listed in Table 5.1.

Table 5.1: Assignments (in cm^{-1}) of bleach bands in TRIR spectra of $d(C_3TA_2)_4$ at pH 5.5 and pH 8.5. Specific assignments in Banyay et al[123]

pH	A ν(ring)	C ν(ring)	C ν(ring)	A ν(ring)	T ν(C4O4)	C ν(C2O)	T ν(C2O2)
8.5	1483	1506	1524	1626	1647(sh)	1654	1696
5.5	1482	1508	1525	1626	obs	1666, 1699	obs

obs = obscured

The TRIR of $d(C_3TA_2)_4$ at pH 8.5 (Fig. 5.2 on the facing page) exhibits a long-lived transient absorption around 1570 cm^{-1}, and there is also non-recovery of the bleaches in the region above 1600 cm^{-1}. Vibrational cooling is evident at short times with some tracking of the transient bands.

At pH 5.5 the sequence (Fig. 5.3, page 82) shows significant spectral changes above 1600 cm^{-1}. Hemiprotonation and C-CH^+ base-pairing in the i-motif increases the localisation of π electrons on the carbonyl groups resulting in higher C=O force constants than in unprotonated cytosine[130]. As there are two distinct cytosine species in a base-pair, there are two ν(CO) bands in the i-motif (1666 cm^{-1} and 1669 cm^{-1}).

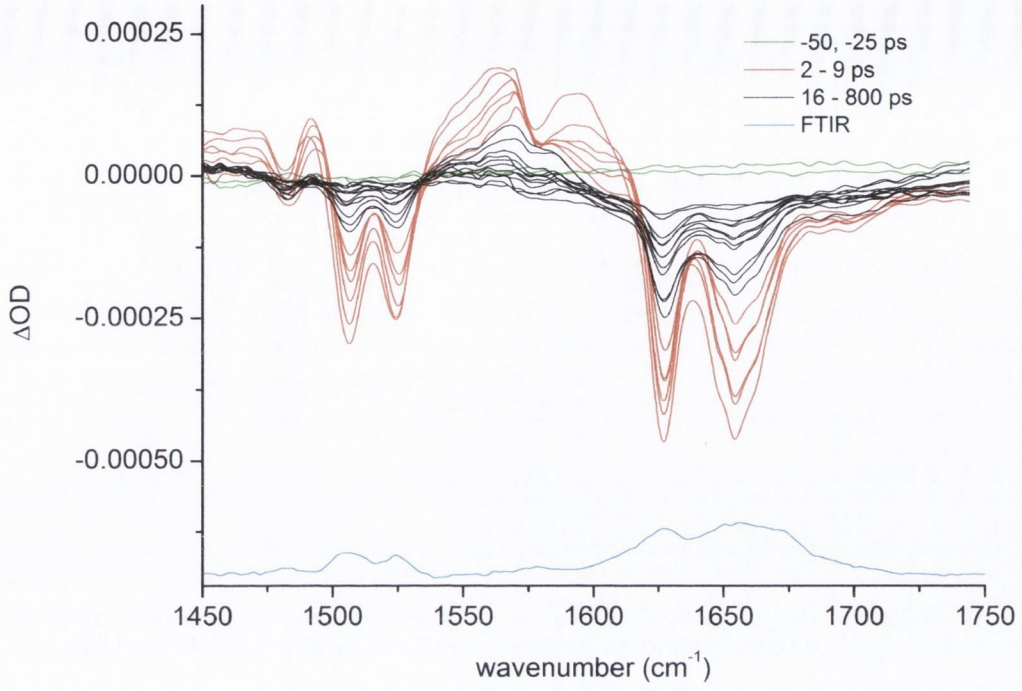

Figure 5.2: ps-TRIR and FTIR spectra of $d(C_3TA_2)_4$ in D_2O at pH 8.5 (50 mM Na_2HPO_4) recorded on PIRATE. Delays (ps): -50, -25, 2, 3, 4, 5, 6, 9, 16, 31, 49, 68, 88, 111, 136, 169, 209, 267, 394, 600, 800

The TRIR spectra gives sharper resolution of these bands than the FTIR, presumably due to overlapping transient bands. This observation prompted us to attempt a separation of the excited state from the difference spectrum. Difficulties were encountered fitting the ground state to a satisfactory model, given the large number of contributing modes. Instead, the excited-state spectrum was determined by adding back a scaled FTIR spectrum to the TRIR trace (Fig. 5.4 on the next page). This analysis reveals considerable transient absorption features in the 1700 cm^{-1} region. These are clearly not 'hot' bands, as they persist at long times. The narrowing of the bleach bands is far more pronounced here than in any other systems studied, suggesting that the fitted transients are indeed real, and not an artefact from fitting different peak widths in the ground and excited states.

The FTIR shows substantial suppression of the ring stretches at 1505 cm^{-1} and 1525 cm^{-1}. This is consistent with the lower population of unassociated and unprotonated C residues[130], although bleaches are still observed in the TRIR. This has previously been reported for other oligonucleotide sequences[125]. As in the random coil, a long-lived transient is present around 1570 cm^{-1}, and there is non-recovery of depletions from 1600-1750 cm^{-1}.

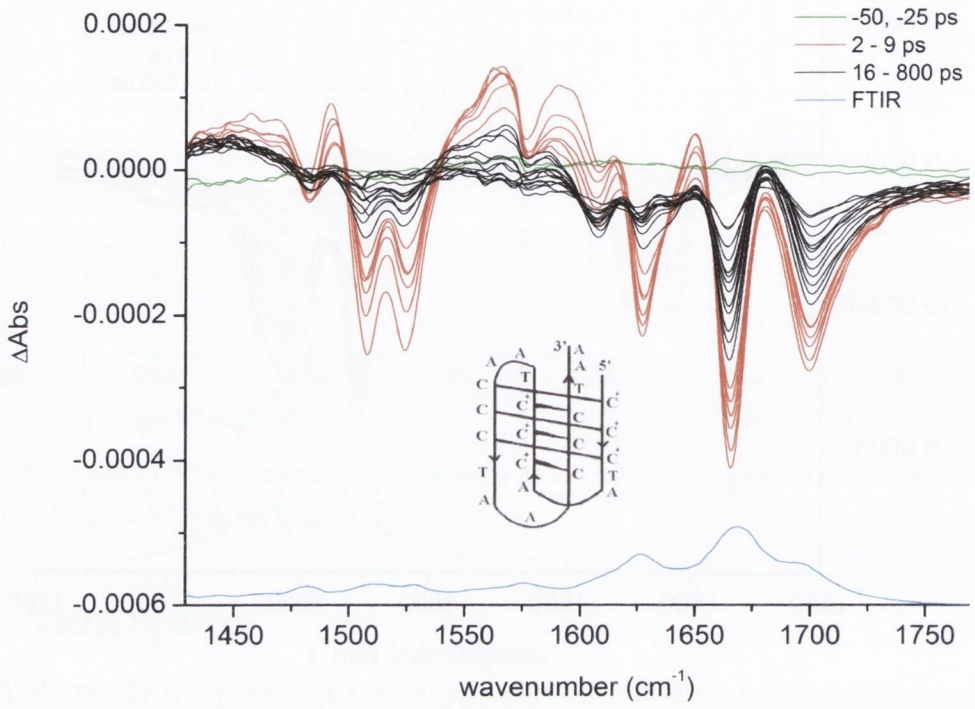

Figure 5.3: FTIR and TRIR spectra of $d(C_3TA_2)_4$ in D_2O at pH 5.5 (50 mM NaH_2PO_4) recorded on PIRATE. Delays at (ps) -50, -25, 2, 3, 4, 5, 6, 9, 16, 31, 49, 68, 88, 111, 136, 169, 209, 267, 394, 600, 800

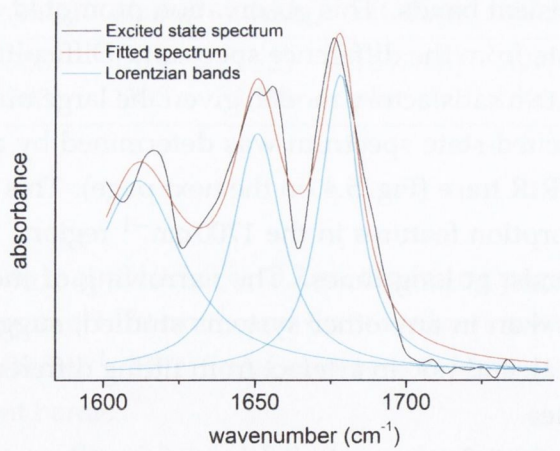

Figure 5.4: Excited state and fitted Lorentzian peaks for $d(C_3TA_2)_4$ (pH 5.5) for 2 ps delay

As non-recovery was confined to one spectral area we suspected that it was due to formation of thymine photoproducts. The first and last experiment runs were thus extracted from the cumulative spectra (Fig. 5.5), and it is evident that the spectrum changes shape with increasing exposure to the UV pump beam. This is noticeable in the decreased bleach intensity, corresponding to a decreased ground-state absorbance.

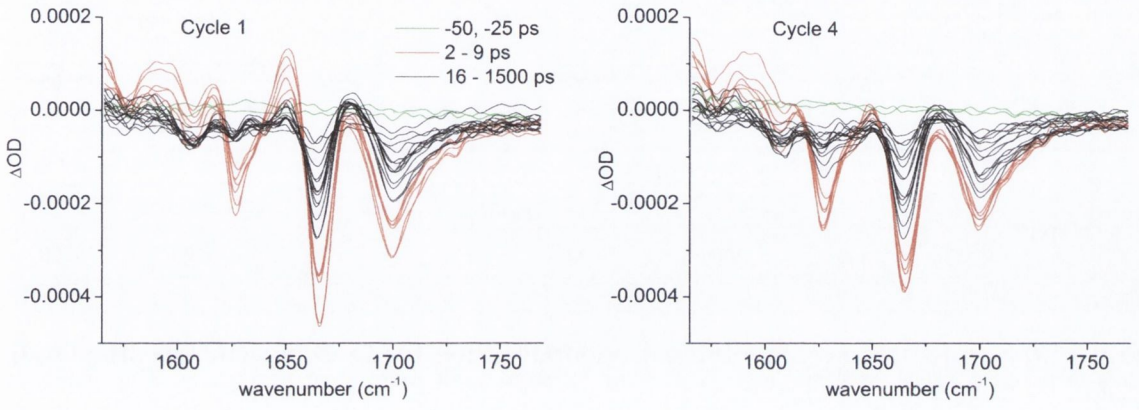

Figure 5.5: First and fourth cycles of TRIR measurement of $d(C_3TA_2)_4$ at pH 5.5 in D_2O on PIRATE

The TRIR of $d(C_3TA_2)_4$ in neutral conditions was also recorded, and resembles that at pH 8.5, confirming that this sequence does not form the i-motif at neutral pH (Fig. A.2, page 210). Spectra were also recorded of $d(C_5T_3)_3C_5$, which is known to form an i-motif[81,131], at pH 5.5 and pH 8.5 (Figs. A.4 on page 211). Similar to $d(C_3TA_2)_4$, $d(C_5T_3)_3C_5$ shows two carbonyl bleaches at pH 5.5, and evidence for a long-lived transient in the 1570 cm^{-1} region.

5.1.3 Kinetics

Kinetic analysis was performed using single-point analysis only. Test fits were also performed using three exponentials, in order to assess if the non-recovery could be assigned to a long-lived decay or a permanent photoproduct (Fig. 5.6 on the next page). Both fits give approximately equal y_0 (A_0) values, showing that even with a third exponential the fit does not naturally recover to the baseline.

Data were subsequently fit to biexponential kinetics. Where non-recovery was present the residual absorbance was factored into kinetics by calculating the percentage contribution of the constant amplitude component, A_0.

At pH 8.5 (Fig. 5.7 on page 85 and Table 5.2 on page 86), the longest lifetimes were recorded for the adenine ring bleach region (1625 cm^{-1}). The kinetics of the other

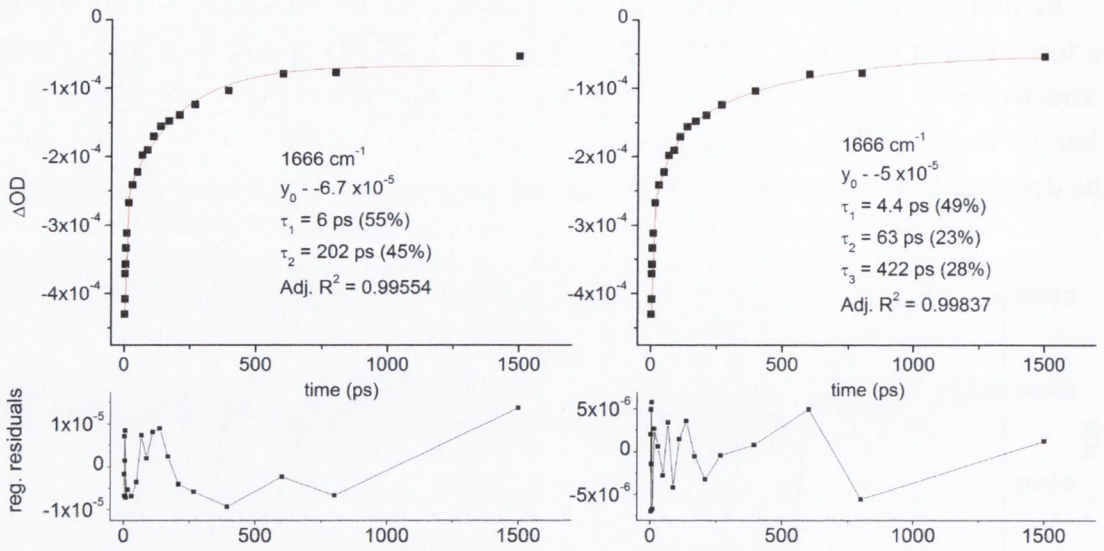

Figure 5.6: Comparison of 2- and 3-exponential fitting for C=O bleaches in $d(C_3TA_2)_4$ at pH 5.5 (50 mM NaH_2PO_4) in D_2O

bleaches, and the transient band, showed similar lifetimes to poly(rC) (90 ± 15 ps). The bleach recoveries in the "T" region (>1650 cm^{-1}) are slightly longer than those recorded at the C ring region (1505 - 1525 cm^{-1}).

At pH 5.5 (Fig. 5.8 on page 87 and Table 5.3 on page 88) the longest lifetimes of over 150 ps were recorded for the carbonyl bleach recoveries at 1666 cm^{-1} and 1700 cm^{-1}. It can also be seen that the long-lived channel constitutes approx. 50% of the recovery in these regions, whereas it is only approx. 20% in the C ring region.

The lifetime of the transient around 1570 cm^{-1} were shorter than the 90 ps values recorded at pH 8.5, though there are large fitting errors at pH 5.5. In fact it is notable, from data at both pH 5.5 and pH 8.5, that there are significant variations between lifetimes obtained at adjacent wavenumber points.

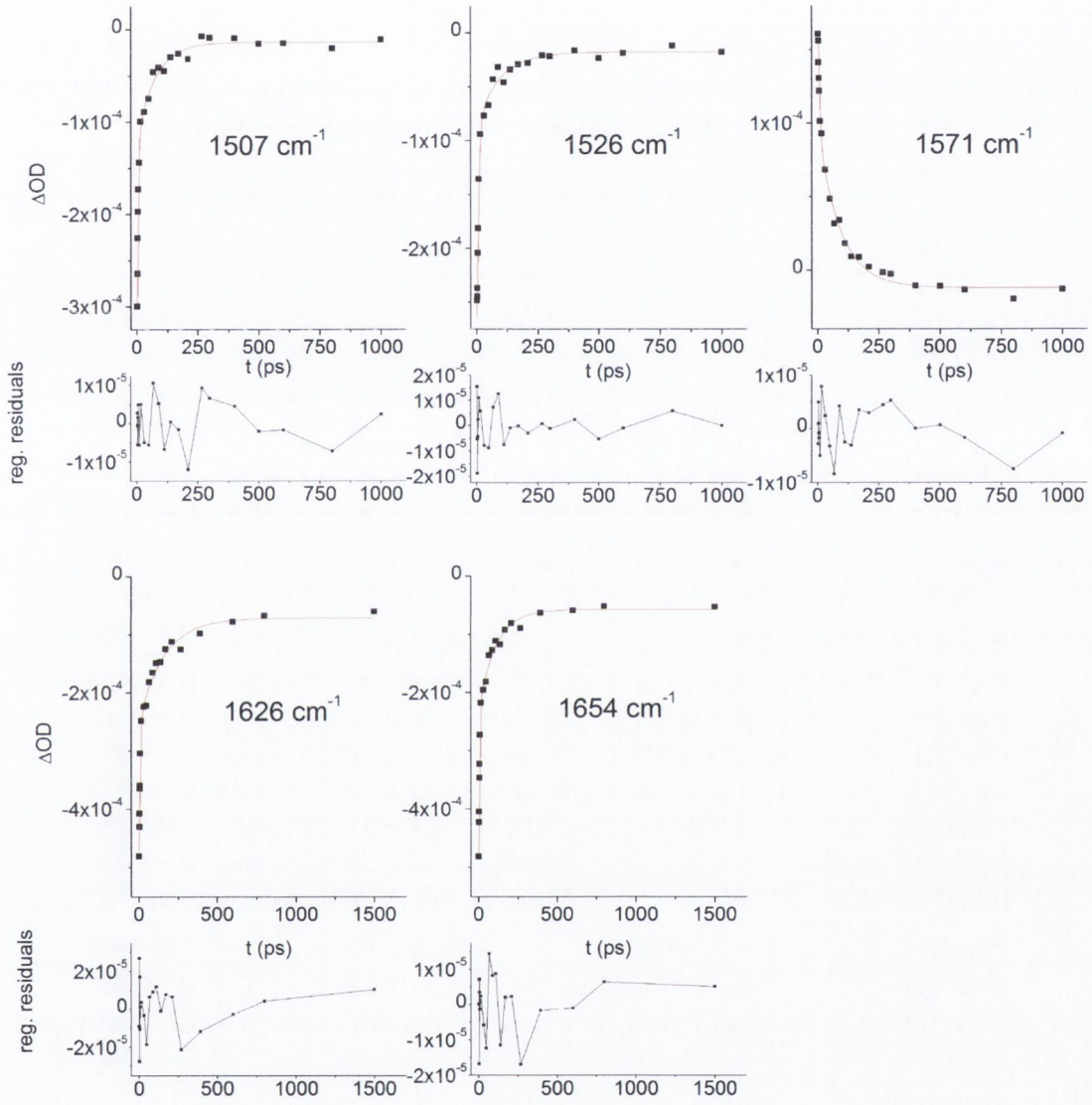

Figure 5.7: Biexponential fits and residuals for main transients and bleaches in $d(C_3TA_2)_4$ at pH 8.5 (50 mM Na_2HPO_4) in D_2O

Table 5.2: Biexponential single-point fitting parameters and fitting errors for $d(C_3TA_2)_4$ at pH 8.5 (50 mM Na_2HPO_4) in D_2O. Values in parenthesis are for $A_0 = 0$

$\tilde{\nu}$ (cm^{-1})	A_0 (%)	τ_1 (ps)	A_1 (%)	τ_2 (ps)	A_2 (%)	R^2
1502(B)	3	1.7 ± 0.2	84 (87)	83 ± 12	13 (13)	0.99112
1505(B)	5	3.3 ± 0.3	74 (78)	73 ± 12	21 (22)	0.99417
1507(B)	3	4.0 ± 0.4	72 (74)	75 ± 11	25 (26)	0.99484
1510(B)	5	3.0 ± 0.3	71 (75)	59 ± 8	24 (25)	0.99476
1521(B)	5	3.6 ± 0.4	75 (79)	96 ± 20	20 (21)	0.99009
1524(B)	5	4.8 ± 0.7	75 (79)	80 ± 19	20 (21)	0.98975
1526(B)	6	7 ± 1	74 (78)	94 ± 33	21 (22)	0.98929
1529(B)	9	9 ± 2	70 (77)	79 ± 39	21 (23)	0.98608
1623(B)	13	3.0 ± 0.6	60 (69)	168 ± 37	27 (31)	0.97596
1626(B)	13	5.6 ± 1	56 (64)	157 ± 32	32 (36)	0.9866
1628(B)	14	6.7 ± 1.5	51 (59)	130 ± 27	29 (41)	0.98733
1647(B)	9	2.5 ± 0.4	67 (74)	96 ± 14	24 (26)	0.98922
1651(B)	10	3.2 ± 0.6	65 (72)	103 ± 20	26 (28)	0.98516
1654(B)	10	4.5 ± 0.9	62 (68)	107 ± 14	29 (32)	0.99489
1657(B)	9	4.2 ± 0.6	62 (69)	100 ± 16	28 (31)	0.99211
1660(B)	10	4.5 ± 0.6	63 (70)	113 ± 19	23 (30)	0.99185
1663(B)	10	5.3 ± 0.7	62 (69)	120 ± 20	28 (31)	0.99327
1667(B)	13	5.7 ± 1.1	59 (68)	118 ± 30	28 (32)	0.98481
1565(Tr)	-	4.7 ± 0.7		103 ± 17		0.99332
1568(Tr)	-	6.7 ± 1.5		130 ± 27		0.98733
1571(Tr)	-	6.2 ± 1.2		92 ± 10		0.99436
1574(Tr)	-	11.13 ± 8.7		99 ± 23		0.98096

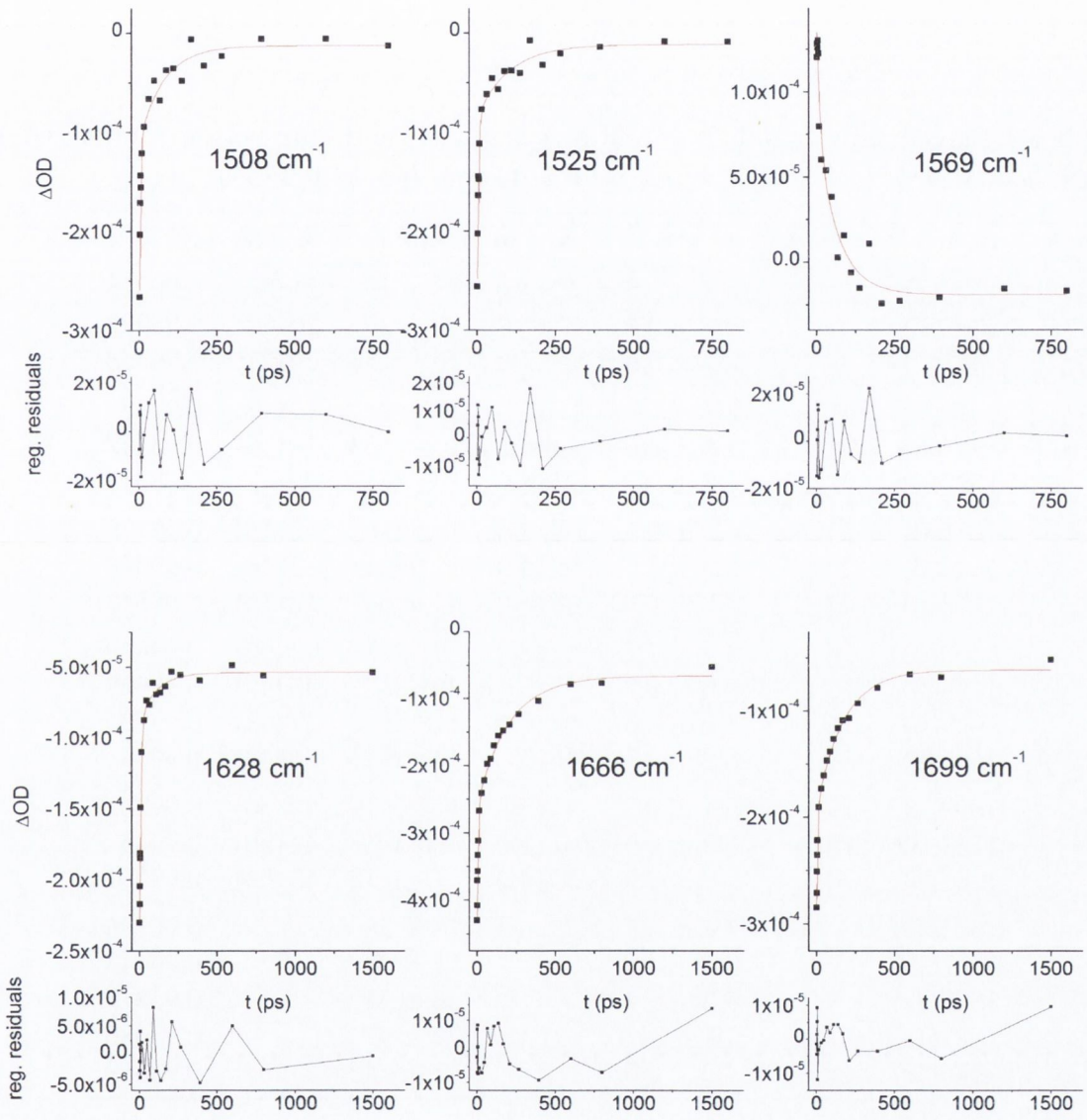

Figure 5.8: Biexponential fits and residuals for main transients and bleaches in $d(C_3TA_2)_4$ at pH 5.5 (50 mM NaH_2PO_4) in D_2O

Table 5.3: Biexponential single-point fitting parameters and fitting errors for $d(C_3TA_2)_4$ at pH 5.5 (50 mM NaH_2PO_4) in D_2O. Values in parenthesis are for $A_0 = 0$

$\tilde{\nu}$ (cm^{-1})	A_0 (%)	τ_1 (ps)	A_1 (%)	τ_2 (ps)	A_2 (%)	R^2
1506(B)	17	3.8 ± 0.5	62 (75)	78 ± 13	21 (25)	0.99335
1508(B)	9	2.7 ± 0.6	71 (78)	79 ± 25	20 (22)	0.96992
1511(B)	6	2.7 ± 0.6	74 (79)	101 ± 35	20 (21)	0.96358
1522(B)	9	2.5 ± 0.5	75 (83)	86 ± 29	16 (17)	0.9702
1525(B)	9	3.6 ± 0.6	74 (82)	101 ± 33	16 (18)	0.98167
1527(B)	9	4.8 ± 0.3	75 (83)	109 ± 42	15 (17)	0.98514
1625(B)	23	6.4 ± 0.9	65 (84)	132 ± 6	12 (16)	0.99138
1628(B)	20	8.8 ± 0.8	68 (84)	114 ± 41	12 (16)	0.99548
1632(B)	23	12.3 ± 3.3	65 (84)	84 ± 64	12 (16)	0.99548
1663(B)	17	4.4 ± 0.7	42 (50)	181 ± 17	42 (50)	0.99419
1666(B)	14	6.0 ± 0.7	46 (53)	201 ± 21	40 (47)	0.99523
1669(B)	14	5.8 ± 0.6	49 (57)	148 ± 12	37 (43)	0.9973
1696(B)	18	5.2 ± 0.7	46 (57)	148 ± 15	36 (43)	0.9954
1699(B)	19	5.1 ± 0.9	41 (50)	172 ± 19	40 (50)	0.99267
1702(B)	18	5.2 ± 0.9	41 (50)	186 ± 17	41 (50)	0.9945
1705(B)	20	3.8 ± 0.9	35 (44)	173 ± 18	45 (56)	0.99051
1564(Tr)		7.4 ± 3.6		78 ± 38		0.96186
1567(Tr)		7.6 ± 4.7		71 ± 30		0.96443
1570(Tr)		9.3 ± 9.4		66 ± 34		0.95317
1572(Tr)		19 ± 24		79 ± 97		0.93486
1575(Tr)		4.3 ± 8.5		124 ± 45		0.92669

5.2 RNA - Poly(rC)

TRIR experiments were performed on poly(rC) at low pH (pH 4.5/5), under conditions where hemi-protonated $[poly(rC\text{-}rC^+)]_2$ duplexes are believed to form[72,73].

5.2.1 pH 5.5

Experiments were performed at pH 5.5 using 50 mM NaH_2PO_4. At pH 5.5 hemiprotonated poly(rC) exists and undergoes a structural change to $[poly(rC\text{-}rCH^+)]_2$ as shown by the CD spectrum (Fig. 5.9, page 90). The shift in the UV spectrum, and the presence of the CD signal at 285 nm, are similar to those observed earlier in the formation of the i-motif (see Fig. 5.1 on page 80).

The drop in pH results in a red shift and hyperchromism of the absorption spectrum, as expected (Fig. 2.20, page 24)[72]. In the FTIR and TRIR (Fig 5.10 on the next page) a new band emerges at 1698 cm^{-1} associated with the higher energy carbonyl in the hemi-protonated base pair[72]. This is very similar to what was observed in the i-motif structure of $d(C_3TA_2)_4$ (and $(C_5T_3)_3C_5$). There is also a transient feature in the 1570 cm^{-1} region, which is most obvious in the spectrum recorded on PIRATE (Fig. 5.12, page 91).

The kinetic plots (Fig. 5.11 on page 91) reveal the substantial scatter at long delays in the ULTRA plots. Lifetimes for a long component of > 100 ps were obtained from the bleaches, albeit with a large uncertainty in the values. However these lifetimes were corroborated by fits to PIRATE data, where similar bleach recovery lifetimes were obtained (Fig. 5.13, page 92). Interestingly, shorter lifetimes were obtained for the transient at 1574 cm^{-1} than the bleach recovery, suggesting in this case that the dark $^1n\pi^*$ state was not the sole long-lived decay channel.

5.2.2 pH <5.5

A solution pH of less than 5.5 was achieved using phosphoric acid in the absence of buffer. Regulation of pH proved challenging in these systems due to the known tendency of the polymer to form turbid solutions at low pH and precipitate at around pH 3. By implication the single-stranded fully protonated species ($poly(rCH^+)$) cannot be observed by solution IR[72]. The adjustment of pH in these experiments was done in a 'trial and error' manner without knowledge of the phosphoric acid concentration. The pH of the resulting small volumes was recorded using pH indicator strips to a pH value $\pm$ 0.2. Particular attention was paid to the opacity of the solution as more acid was added.

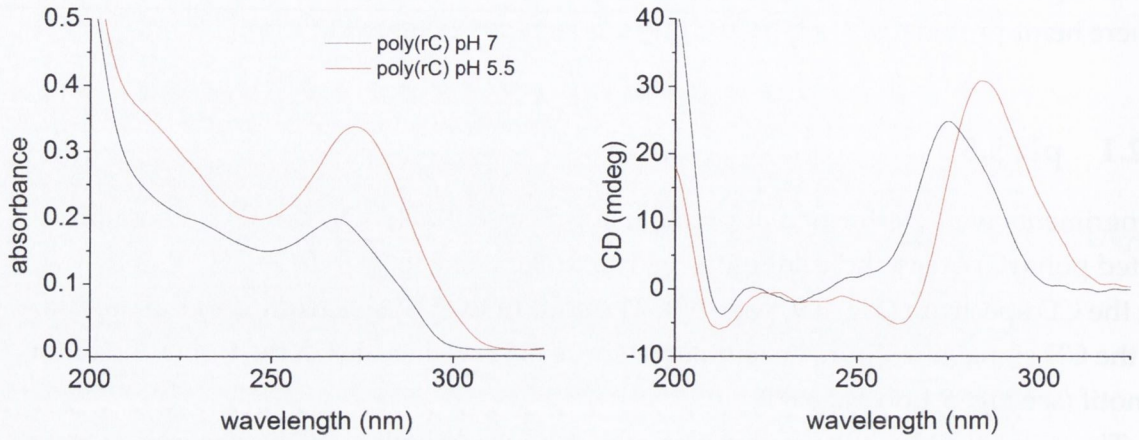

Figure 5.9: LEFT: UV/vis and RIGHT: CD spectra of 10 mM poly(rC) at pH 5.5 and pH 7

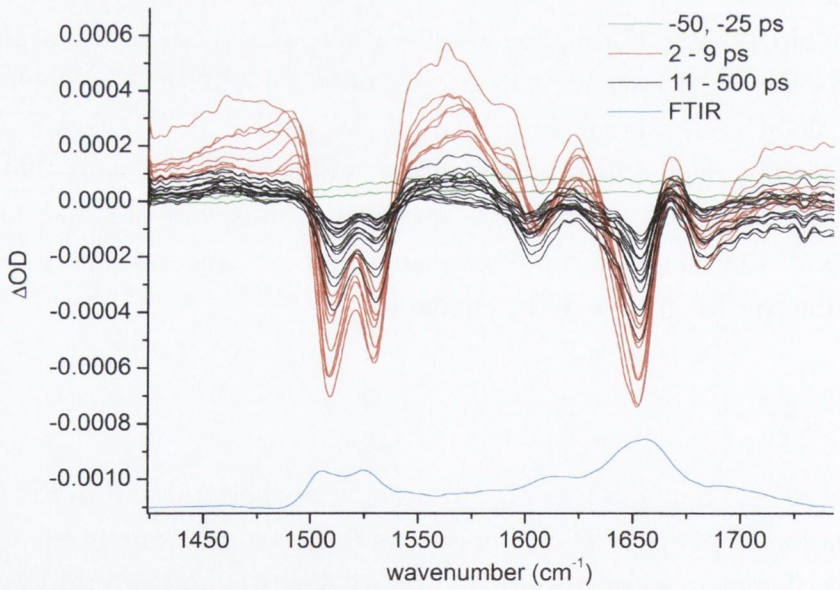

Figure 5.10: TRIR of 10 mM poly(rC) in 50 mM NaH_2PO_4 pH 5.5 in D_2O recorded on ULTRA. Delays (ps): -50, -25, 1.75, 2, 3, 4, 5, 6, 7, 9, 11, 15, 21, 34, 51, 70, 89, 110, 134, 160, 192, 234, 306, 400, 500

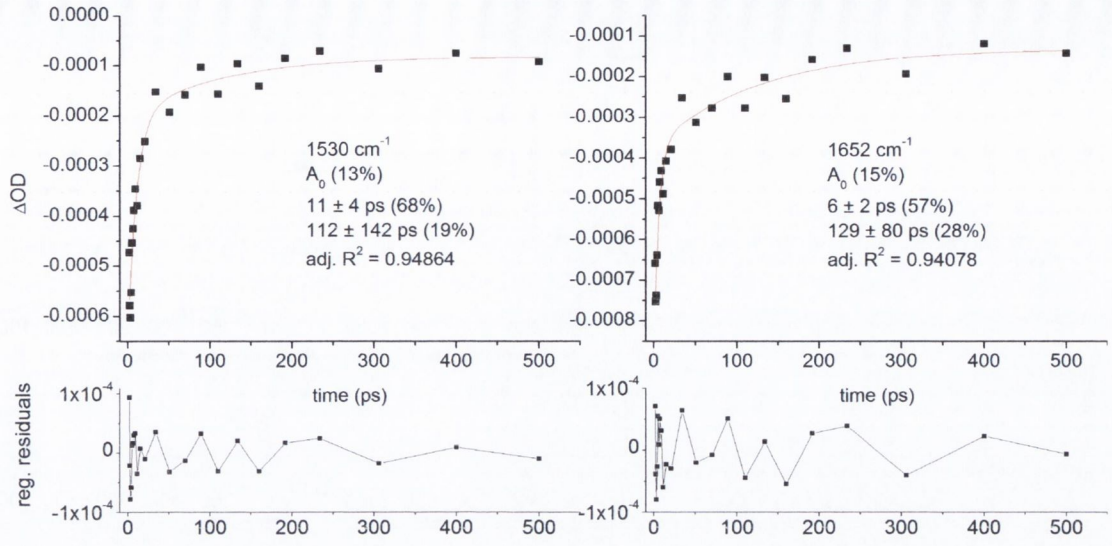

Figure 5.11: Biexponential fits and residuals for 10 mM poly(rC) at pH 5.5 (50 mM Na_2HPO_4) in D_2O on ULTRA

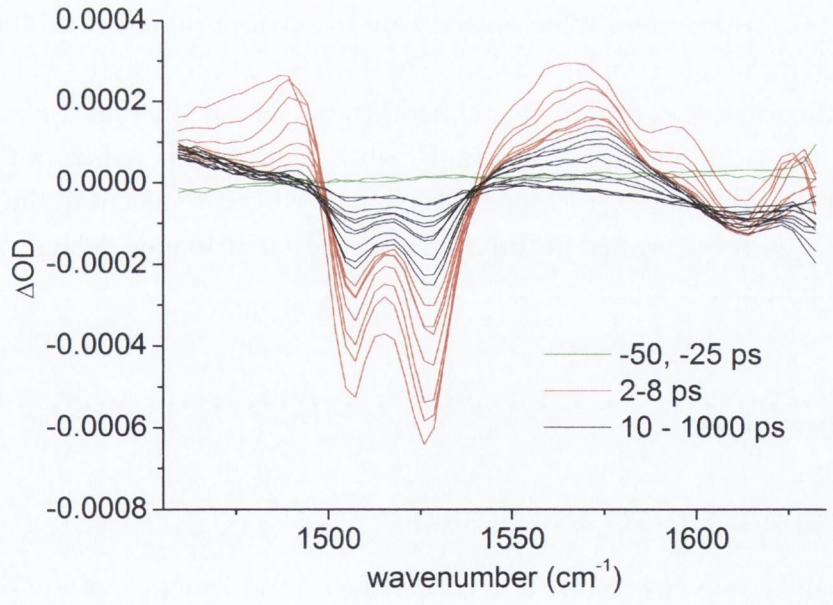

Figure 5.12: TRIR of 10 mM poly(rC) in 50 mM NaH_2PO_4 pH 5.5 recorded on PIRATE. Delays (ps): -50, -25, 1, 2, 3, 4, 5, 6, 8, 10, 15, 20, 35, 50, 100, 150, 250, 500, 1000

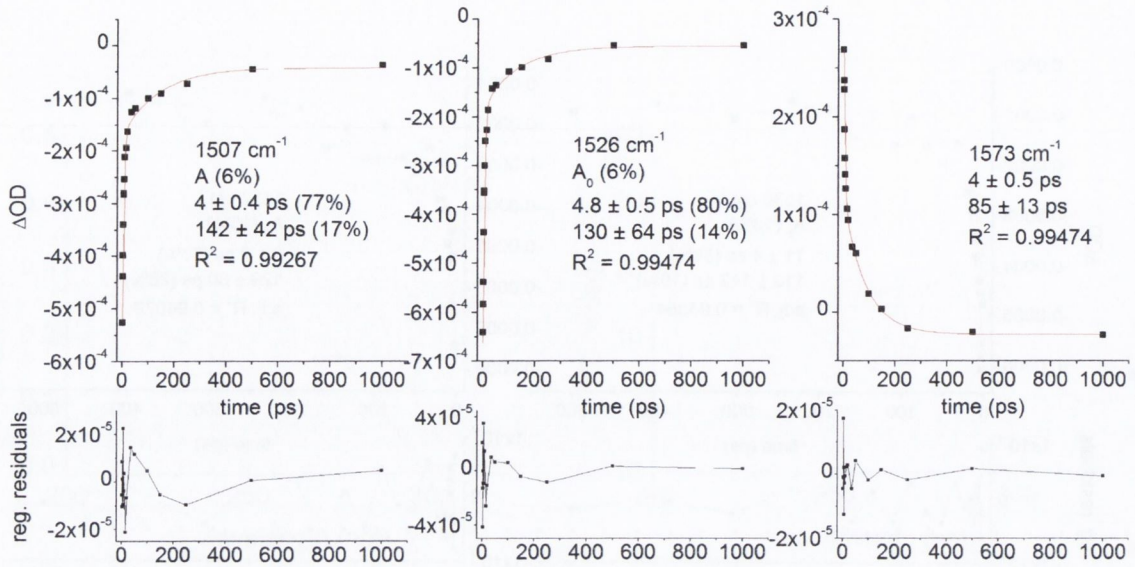

Figure 5.13: Biexponential fits and residuals for 10 mM poly(rC) at pH 5.5 (50 mM Na_2HPO_4) in D_2O

The FTIR and TRIR showed increased suppression of the ring bands at 1505 cm^{-1} and 1525 cm^{-1}, relative to the pH 5.5 samples (Figs 5.14 on the next page and 5.16 on page 94). This is consistent with the higher proportion of protonated residues, and the transition from the single-stranded poly(rC) to the base-paired poly(rC-rCH$^+$) duplex. Accordingly the intensity of the carbonyl band from CH$^+$ at 1700 cm^{-1} also increases. The changes in relative intensities of the IR bands are as predicted from the work of Hartman and Rich[72]. There also appears to be a long-lived transient in the 1570 cm^{-1} region, though with the scatter in the difference signal at longer delays, a definitive assignment is tenuous.

5.3 Discussion

5.3.1 Electronic Spectra and Structure

Interestingly, there appears to be more consensus on the structure of the i-motif than on 'simpler' structures such as poly(rC). This is perhaps due to the conformational restriction imposed by base-pairing in the i-motif, compared to the unrestricted random coil structures of some polynucleotides.

The large red-shift in the absorption λ_{max} of the i-motif relative to the random coil is similar to the spectral changes in a J-aggregate, which has previously been suggested

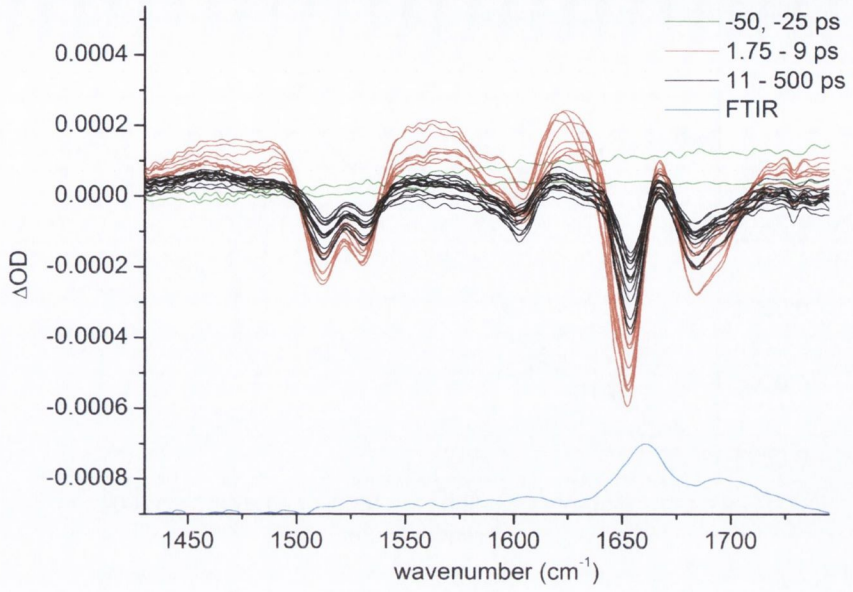

Figure 5.14: ps-TRIR of 10 mM poly(rC) (+H_3PO_4 pH 4.5) in D_2O recorded on ULTRA. Delays (ps): -50, -25, 1.75, 2, 3, 4, 5, 6, 7, 9, 11, 15, 21, 34, 51, 70, 89, 110, 134, 160, 192, 234, 306, 400, 500

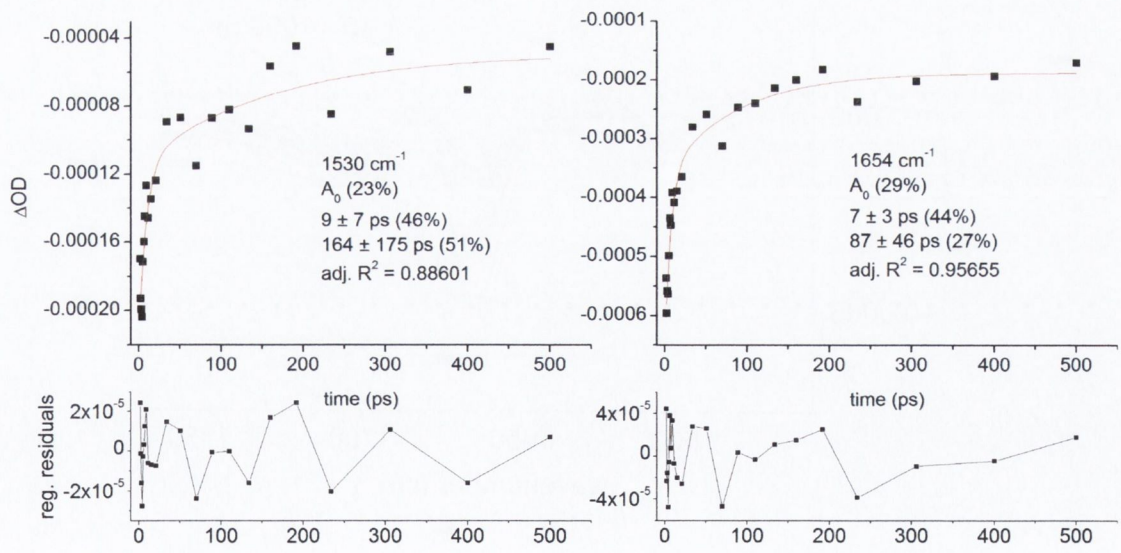

Figure 5.15: Biexponential fits and residuals for 10 mM poly(rC) at pH 4.5 (ULTRA)

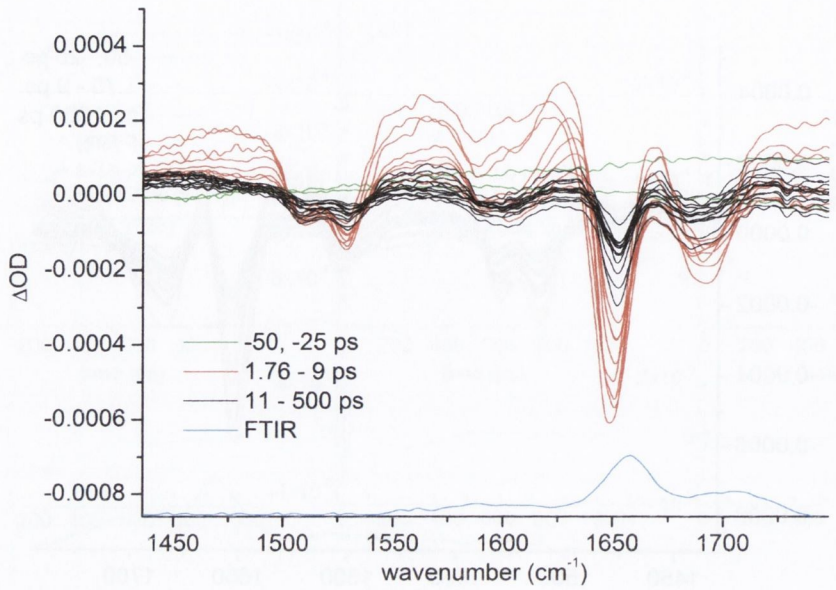

Figure 5.16: ps-TRIR of 10 mM poly(rC) (H_3PO_4 pH 4.0) in D_2O recorded on ULTRA. Delays (ps): -50, -25, 1.8, 2, 3, 4, 5, 6, 7, 9, 11, 15, 21, 34, 51, 70, 89, 110, 134, 160, 192, 234, 306, 400, 500

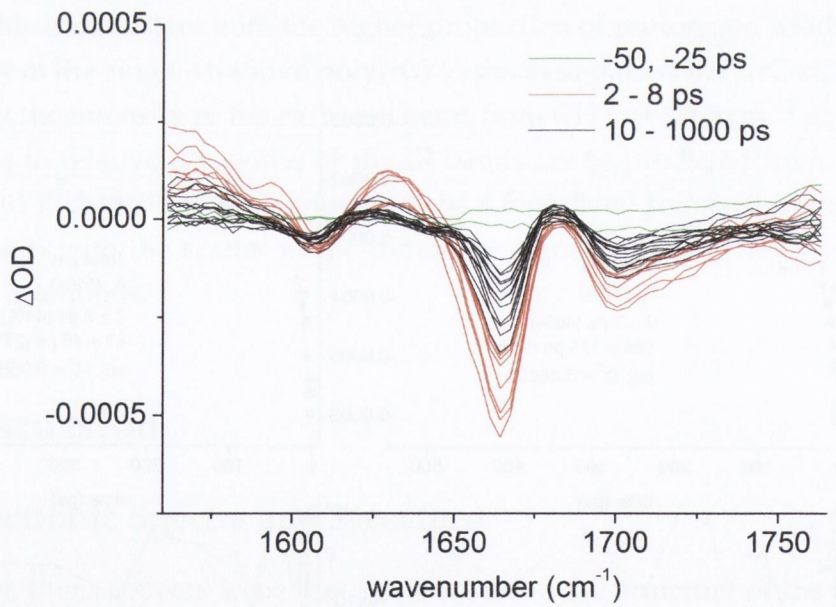

Figure 5.17: ps-TRIR of 10 mM poly(rC) in H_3PO_4 (pH 4.0) in D_2O recorded on PIRATE. Delays (ps): -50, -25, 2, 3, 3.5, 4.5, 6, 7, 8, 10, 13, 18.5, 32.5, 53, 75, 103, 135, 177, 240, 390, 750, 1000

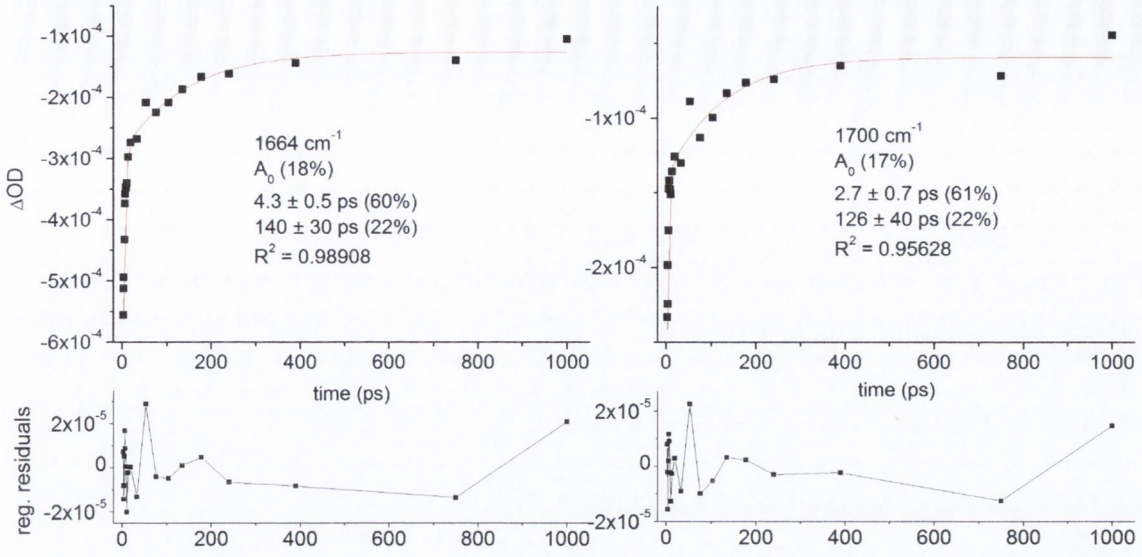

Figure 5.18: Biexponential fits and residuals for 10 M poly(rC) in H_3PO_4 (pH 4.0) on PIRATE

as the origin of the UV spectrum of the guanine quadruplex (the G-quadruplex will be discussed in chapter 7)[122]. In the i-motif, this model can be rationalised by the offset stacking patterns of the C units. Strong absorption out to 320 nm shows that the i-motif structure can be preferentially excited in this region, which has also been noted for the G-quadruplex[132]. This has implications for biological systems as the flux of incident solar UV radiation increases significantly above 300 nm.

5.3.2 Vibrational Cooling

The cooling lifetimes of the oligonucleotide sequences are slightly longer than those recorded in monomer systems. The i-motif is believed to be stabilised by desolvation of the deoxyribose group[83], so there may be less solvent accessible to the cytosine bases in the i-motif than in an isolated nucleobase. Tracking of the hot bands is not as pronounced as previous examples. This suggests some delocalisation of vibrational energy over a number of bases. Base-pairing might facilitates the rapid redistribution of vibrational energy. For example, obvious tracking is present in dA_{18} or poly(dA), but is less clear in double-stranded $dA_{18}.dT_{18}$, or poly(dA).poly(dT)[125].

5.3.3 Dark-State Dynamics

A long-lived transient is present at around 1570 cm^{-1} for both i-motif (pH 5.5) and random coil (pH 8.5) forms of $d(C_3TA_2)_4$ and $d(C_5T_3)_3C_5$. We believe that this is the

locally excited $^1n\pi^*$ state. This shows that the $^1n\pi^*$ state is formed in biological mixed-base sequences, and not just in monomeric and homo-polymeric sequences. This result implies that the structural features of the i-motif (base-pairing and stacking) do not quench the $^1n\pi^*$ state. Similar conclusions may be drawn about the hemi-protonated poly(rC-rCH$^+$).

The presence of the $^1n\pi^*$ absorption in the base-paired i-motif can inform the assignment of the excited state. The $^1n_N\pi^*$ is destabilised by protonation of N3[24], yet the dark state is still populated in the i-motif. $^1n\pi^*$ states are also destabilised in H-bonded base-pairs[133], which we expect to be more important in the $^1n_N\pi^*$ than the $^1n_O\pi^*$ due to the large distortion of the C2N3C4 plane and removal of an electron from N3. The presence of the dark state in the hemi-protonated systems may hence be interpreted as additional support for the $^1n_O\pi^*$ assignment.

5.3.4 Additional Decay Pathways

The oligonucleotides show longer bleach lifetimes than the monomer or model systems, though unambiguous kinetic analyses of the oligonucleotide data is complicated by the non-recovery seen in many spectra, for both random coil and i-motif. This has been a frequently encountered problem when studying thymine-containing systems by TRIR[125]. Different recovery kinetics were recorded in the "T" region than the ring region, with notably longer lifetimes in the former. This may be a real effect as the recovery kinetics of the A,T and C bases might not be coupled, so need not recover at the same rate. However this would imply that the ring and carbonyl vibrations in C are not coupled in these systems.

Interestingly, Kohler and co-workers reported non-recovery in C-only sequences such as the dC_{18} i-motif[84], despite the low quantum yield of C-C photoproduct formation. Even accounting for non-recovery, the bleach decays in $d(C_3TA_2)_4$ show a larger contribution from long-lived states in the i-motif than the random coil. The hemi-protonated structure clearly has a significant impact on the excited state of poly(rC-rC+) as these are longer than those in single-stranded poly(rC).

The i-motif and hemi-protonated poly(rC) are known to have greatly enhanced fluorescence relative to the C-monomer[84,98,100], suggesting that an appreciable radiative decay channel exists in competition with non-radiative $^1n\pi^*$ deactivation. The lifetimes are of the order 1–2 ns[84,98,100], although it is notable that the quantum yields of fluorescence are still very low $\sim 10^{-3}$[98].

An excimer has been proposed by Cohen et al for hemi-protonated C systems, that arises from stacking of the exocyclic carbonyl and amino groups[79,80]. In such systems, the excimer model may indeed be valid, as our preliminary analysis of the transient

spectra suggests that there may be a long-lived transient species present. However the origins of the long-lived decay and transient features in the i-motif structure are difficult to extract with certainty, due to the number of structural changes involved in the transition from random coil to i-motif (e.g. Fig. 5.19 on the next page). These include hemi-protonation, C–CH+ base-pairing and the base-pair interdigitation. Previous groups have attempted to observe C-C+ base-pairing in isolation from base-stacking by using short sequences with non-consecutive C-residues[134]. However they failed to eliminate stacking without also losing the base-pairing. This may be due to the strict conditions for formation of the i-motif[81], though isolated C–CH+ base pairs might potentially be observed using modified "locked" nucleic-acid sequences[103,134,135].

The work of Cohen et al draws attention to some lingering uncertainties about the structures of poly(rC-rCH$^+$) and the i-motif. It is generally believed that the four-stranded structure is not formed in poly(rC-rCH$^+$)[136], and that differences in base-stacking structures occur as depicted in Fig. 5.19. There is a reported example of four-stranded RNA structures[137], and Cohen et al suggest that, as the kinetics are similar, both the RNA and DNA sequences are four-stranded.

However the use of kinetics alone is probably insufficient for structural determination. The main support they summon is that the UV and CD spectra are similar for hemi-protonated poly(rC) and dC_{18} (absorption red shift, positive CD). However they neglect to mention that protonation of poly(rC) causes an increase in absorption that is not observed in the formation of the i-motif. Interestingly, they claim that the similar kinetics are not related to base pairing, even though the base-pair is the only structural feature that both duplex and quadruplex are known to share. Recently it has been proposed that G-C base-pairing is more likely to induce fast decay due to proton transfer[44,92]. Detailed study on the C-C+ base-pair remains to be done, so its possible role in slow decay should not yet be dismissed.

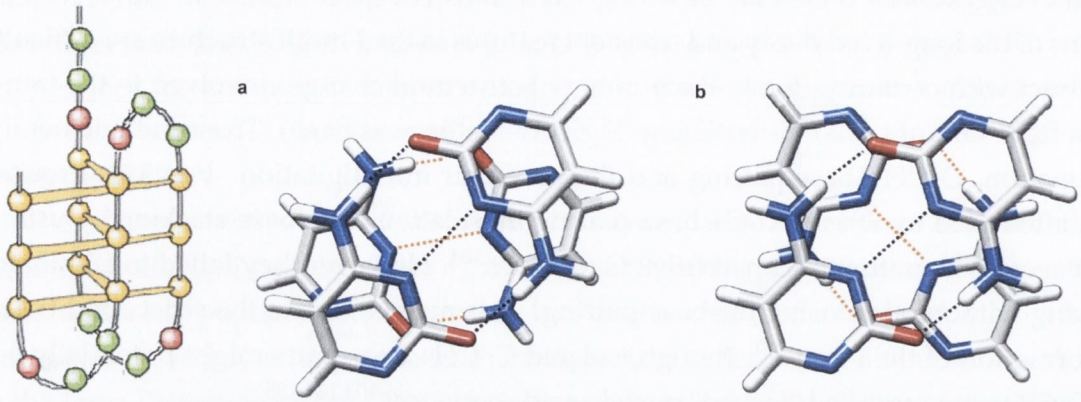

Figure 5.19: LEFT: The i-motif structure of $d(C_3TA_2)_4$ (after Guo et al[76]) RIGHT: Base stacking structures of (a) locked d(CpC) dinucleotide analogue[138] (b) i-motif[80] as presented by Cohen et al[84]

5.4 Conclusions

Hemi-protonated DNA and RNA sequences have been characterised, and are notable for distinctive carbonyl bleaching bands in the TRIR spectra. The localised $^1n\pi^*$ state appears to be present in both DNA and RNA sequences at varying pH, suggesting that this dark state is present in biological sequences and not quenched by C-CH^+ base-pairing. Longer bleach kinetics were recorded for these sequences than for poly(rC), though kinetic analysis is compromised by apparent photo-damage in T-containing sequences.

Chapter 6

Direct Excitation - Conclusions and Future Work

6.1 Conclusions

TRIR spectroscopy is shown to be a powerful technique for studying nucleic acids, particularly for the C systems where non-fluorescent states can be readily identified, and without the ambiguities inherent in TA. The advantages of TRIR over TA are demonstrated most vividly in the study of poly(rC), where there is clear spectroscopic evidence for a $^1n\pi^*$ that the Kohler group do not observe.

One of the key disadvantages of TRIR, the need to use D_2O in the 1450-1700 cm^{-1} region, has been partially circumvented, although the temperature jump 'artefact' is unavoidable and means that reliable data cannot be obtained in the carbonyl region.

Some weaknesses of the ps-TRIR method are revealed. In particular, processes shorter than 1 ps could not be measured. As a result the $^1\pi\pi^*$ state of nucleic acid systems cannot be observed. If the $^1\pi\pi^*$ state could be observed, it would be hugely informative as we may be able to observe $^1\pi\pi^*$-$^1n\pi^*$ transitions, and hence get a richer understanding of the excited state landscape. It could also verify the calculated IR spectrum of the $^1\pi\pi^*$ state. As an absorption technique, TRIR proportionately represents all decay mechanisms, thus is insensitive to weakly emissive excimer states that can may be better observed by fluorescence techniques.

By performing experiments on both PIRATE and ULTRA we have been able to directly compare the two TRIR systems. Some of the main benefits of the ULTRA system have been in experiment run time. As shown, a full spectrum can be recorded in one scan, eliminating the need to reconfigure the apparatus, and stitch spectral windows post-experiment. Ironically, we did not derive full benefit from the increased repetition rates, as photodecomposition became a problem due to the inability to raster the sam-

ple out of the pump beam fast enough. This may be alleviated by an optional pulse selection system, whereby some pulses could be dumped before reaching the sample, or by reducing the repetition rate.

In the preceding chapters the role of the $^1n\pi^*$ state in cytosine has been examined. Key findings include the importance of N1 ribose substitution in the dark state and the absence of a kinetic isotope effect in the dynamics of the dark state. Improved spectral characterisation has been achieved, and a preliminary assignment of a $^1n_O\pi^*$ state made. Our results could not infer the precise role of the N1 state in the formation of the long-lived state, though a number of theories were proposed.

The dark $^1n\pi^*$ state is shown to be an important excited-state feature in polymeric as well as monomeric systems. In particular it remains the dominant long-lived decay pathway in d(CpC) and poly(rC), where evidence of an excimer species is minimal. In linked systems, the state seems to remain locally excited on the nucleobase, with modulation of lifetime by the local environment of the excited state. This is a significant observation for linked C systems, where discussion has previously been framed almost exclusively around excimer states[84,96,98–100]. Our results also affirm that localised excited states need to be considered in the photophysics of nucleic acid polymers, and not just of pyrimidine monomers.

This dark state is also evident in higher order C-systems where considerable base-pairing and base-stacking exists, showing that formation of the state occurs independently of other non-localised excited-states. However it is not yet clear what role, if any, the $^1n\pi^*$ state has in the photochemistry of cytosine. While T-T dimerisation is believed to proceed directly from the $^1\pi\pi^*$ state[102], the $^1n\pi^*$ state in C may be an intermediate to the triplet state, which is a known photoproduct precursor[23].

In the hemi-protonated systems, additional excited state decay channels are available, with evidence for a transient species in the TRIR, which may tentatively be assigned as an excimer.

The photophysical processes in cytosine derivatives, as as implied from our results, are summarised graphically in Fig. 6.1.

6.2 Future Work

The gas-phase calculations cannot give a definitive assignment of the excited state, due to the large shifts in band positions that is likely to occur in solution. Incorporating solvent into the calculation is a necessity, but would require multideterminant methods to avoid mixing of the close-lying excited states, and would be computationally very expensive if individual H_2O molecules, rather than a bulk dielectric, were incorporated. The latter case would be important, considering the significance of specific effects on

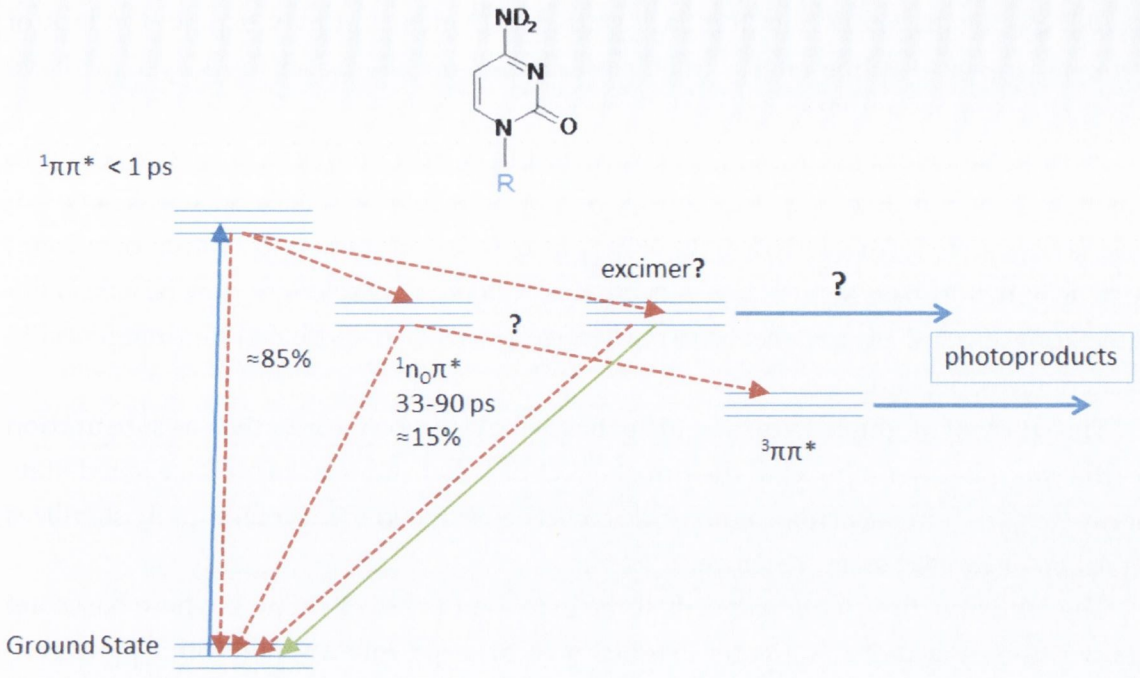

Figure 6.1: Summary of the main conclusions from the ps-TRIR study of the direct excitation of cytosine-rich nucleic acids

the IR spectrum of the ground-state. If however, the aim is solely to distinguish between only two excited states, the complexity of solvent calculation may conceivably be relaxed. However the solution to the question may alternatively be found through experiment, namely by recording TRIR and FTIR spectra of ^{18}O substituted dCMP or dCyd[25]. This would tell if the 1574 cm^{-1} transient was a carbonyl, and the secondary effect of $_{18}O$ isotopic substitution on other modes could be easily modelled using the computational methods reported in this work.

The role of the sugar group in the long-lived decay is unresolved. This represents a considerable challenge to computational chemists, as it requires both the incorporation of solvent into the calculation, and the use of large systems (nucleosides rather than nucleobases). The role of the N1 substituent has largely been ignored in the computation literature, although this may represent a limit in computational power, rather than a lack of desire to study such systems. With this in mind the question may be better addressed experimentally. The synthesis of a variety of 1-substituted derivatives, such as the 1-furanylcytosine molecule, would allow for systematic examination of each functional group on the sugar. Alternatively, the role of the dark state may be probed in detail using 2D-IR, and Time-dependent 2D-IR[139,140]. These experiments provide rich detail on the coupling between vibrational modes, even in the excited states. These

would specifically show how the dark state deactivates, and may explain the lack of a kinetic solvent isotope effect. Such experiments on DNA and RNA systems have commenced on the ULTRA system.

It may also be interesting to pump the sample at a different excitation wavelength, other than 266 nm. Exciting at longer wavelength may show if excess excited state energy is needed to form the dark state. It may also excite different populations of species, such as in mixed-base sequences. Varying the excitation wavelength may be especially interesting if hemi-protonated base-pairs were present, as these can be preferentially excited above 300 nm.

The study of modified cytosine nucleobases may also be informative, as substitution on the ring can often hint as to the direct effect of structural factors on the excited-state decay[17,32,49,111]. In particular, a molecule could be designed that preferentially stabilises a particular excited-state structure.

The study of dinucleotides needs to be extended to cover r(CpC), where bases are known to be stacked to a greater extent. Such an experiment would offer more conclusive evidence on excimer formation in these systems, as it would likely occur in reasonably high yields. It would also clarify the origin of the 50 ps lifetime we observe for d(CpC), in particular the contribution of base-stacking. We have also studied GpC and CpG by TRIR, and other C-containing dinucleotides such as ApC would be worth studying, as data is already available on this system[87].

The studies on the i-motif were hampered slightly due to photodegradation, and the complexity of analysing mixed-base sequence. This could be simplified by studying a homopolymer such dC_{18}, which has already been studied by UV/vis by Kohler and co-workers[84]. These experiments are important in light of the transient absorptions extracted from the TRIR of $d(C_3TA_2)_4$. It is a demonstration of the power of TRIR to record spectral information on transient species, but needs to be repeated given the nature of the fitting performed. Similarly, the study of poly(rC-rCH$^+$) may also be revisited with the aim of obtained high quality kinetic data, as this is an ideal system to compare with neutral poly(rC)

The model proposed by Kohler and co-workers, based on locally excited states in unstacked systems and delocalised excited states in stacked systems, has been shown not to be applicable generally. Results in this thesis shows that both types of long-lived excited state can coexist in polypyrimidine systems.

Chapter 7

Photosensitised Oxidation – Introduction

In the previous chapters the effects of direct excitation of DNA were examined. In the following chapters, photo-excitation is not of the DNA itself, but of a bound chromophore that can mediate photochemical reactions on its host.

7.1 Mechanisms of Photosensitised Oxidation of Nucleic Acids

Photosensitised oxidation of DNA can occur when a nearby organic molecule absorbs light to form reactive excited states. Photosensitised oxidation in DNA is usually specific to guanine, as it is the most readily oxidised nucleobase. Guanine photo-oxidation is often separated into two distinct mechanisms, type 2 and type 1. The reactive intermediate in type 2 photo-oxidation is singlet oxygen, which is generated by an energy transfer from the excited triplet state of the sensitiser to ground-state triplet oxygen (Fig. 7.1 on the following page). Singlet oxygen generation is accompanied by quenching of the triplet state of the photosensitiser, and singlet oxygen can be detected directly by its weak luminescence at 1270 nm.

Singlet oxygen can be generated by a sensitiser that is not bound to DNA, and diffuse within its excited state lifetime, or be generated from a sensitiser bound to DNA. However it should be noted that there is often low accessibility of oxygen to molecules bound to DNA, and that target cancer cells are also known to be hypoxic.

Type 1 photo-oxidation is caused by electron transfer (ET), which may be direct or photoinduced, the latter of which is discussed in the next section. Generally, type 1 oxidation is favoured in anaerobic environments, where re-oxidation of the sensitiser is inhibited. The oxygen-dependence of these reactions is therefore the opposite to that in

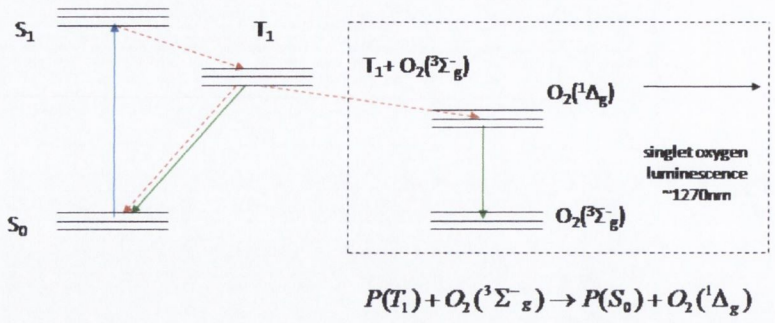

Figure 7.1: Generation of singlet oxygen via the sensitiser triplet state

type 2, and this fact can be used to experimentally distinguish one mechanism from the other. A selection of type 1 and type 2 photo-oxidation products is shown in Fig. 7.2 on the next page. Both paths lead to formation of 8-oxodG, which is up to two orders of magnitude more susceptible to further oxidation than the G precursor[141,142]. This can ultimately lead to DNA strand-breaks, which can be detected by techniques such as electrospray mass-spectrometry, HPLC and gel eleoctrophoresis[142,143]. Type 1 photo-oxidation generally affects guanine residues in sequences containing consecutive guanine residues, whereas type 2 oxidation can affect any guanine without specificity[142]. Type 1 oxidations are of particular interest as they allow for photosensitised reactions in DNA without the need for an intermediary (i.e. molecular oxygen).

7.2 Photoinduced Electron Transfer

Photoinduced electron transfer (PET) reactions are fundamental to energy conversion processes in biological (e.g. photosynthesis) and synthetic (e.g. photovoltaics) systems. PET is predicated on the fact that excited states are both better oxidising agents and reducing agents than their corresponding ground states (Fig. 7.3, page 106). The likelihood of a PET event can be predicted from a knowledge of the thermodynamic redox potentials of the donor (D) and acceptor (A) in their relevant electronic states. This is expressed below as the Gibbs energy for a reductive PET (Eq. 10.1)[144,145]. A negative ΔG^0 term implies that electron transfer is favourable. The ΔE_{00} term accounts for the excited state energy of the acceptor. The last term accounts for the Coulombic interaction between the redox pair, but is usually negligible in polar solvent such as water.

$$\Delta G^0 = F[E^0(D^+/D) - E^0(A/A^-)] - \Delta E_{00} - N_A \frac{e^2}{4\pi\epsilon_0 \epsilon r} \tag{7.1}$$

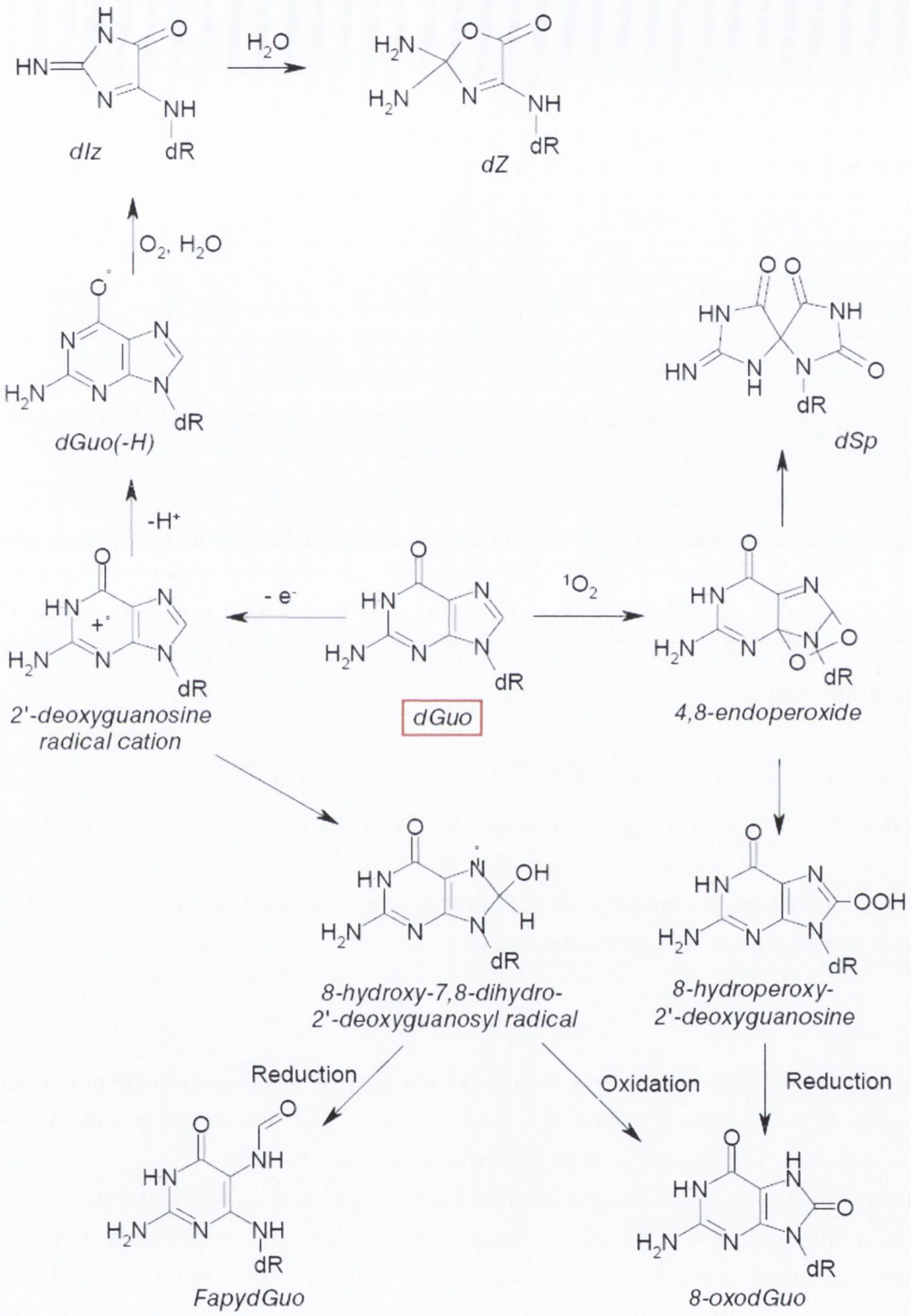

Figure 7.2: Guanine products formed following type 1 ($-e^-$) and type 2 ($^1O_2$) photo-oxidations of the deoxy-guanosine residue (dGuo), as drawn by Cadet et al[141]

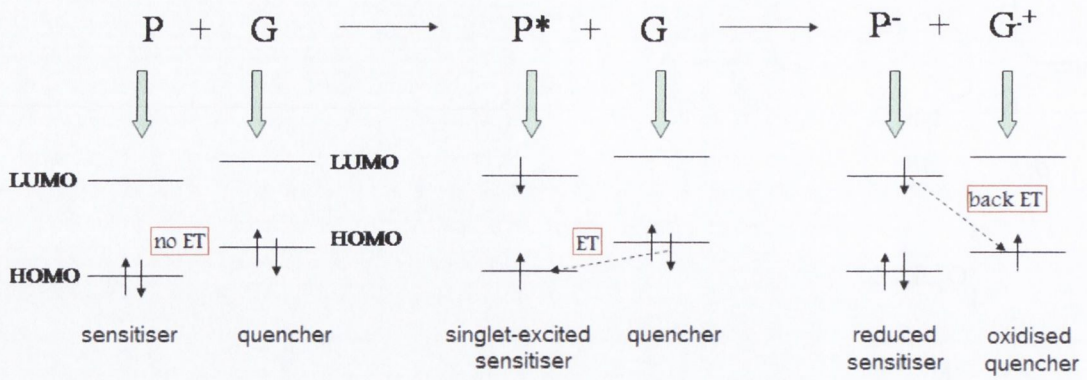

Figure 7.3: A thermodynamically favourable photoinduced electron transfer from guanine (G) to a singlet-excited photosensitiser (P). Derived from Valeur[146]

The relationship between the thermodynamic driving force and the kinetic efficiency of electron transfer is often discussed in terms of Marcus theory[147]. Marcus theory is an expansion of the classic Arrhenius equation, and has been very successful in predicting electron transfer rates in many systems, including those involving photo-oxidation of guanine[148].

$$k = \frac{4\pi^2}{h\sqrt{4\pi\lambda k_B T}}|V|^2 \exp\left(-\frac{(\Delta G^0 + \lambda)^2}{4\lambda k_B T}\right) \tag{7.2}$$

In the Marcus equation (Eq. 7.2) V is the electronic coupling between the initial and final states, and λ is the reorganisation energy (i.e. the energy difference between the initially formed charge-transfer pair, and its stable minimum). For a perfect parabolic system ΔG and ΔG^* are related as follows (Eq. 7.3)

$$\Delta G^* = \frac{\lambda}{4}\left(1 + \frac{\Delta G^0}{\lambda}\right)^2 \tag{7.3}$$

A notable implication of Marcus kinetics is that the rate increases with driving force only up to $\Delta G = -\lambda$. Thereafter the rate decreases with increasing exorgenicity due to poor electronic coupling (the so-called 'Marcus inverted region').

PET results in luminescence quenching of a fluorophore due to radiationless deactivation of the excited state. Steady-state and time-resolved fluorescence spectroscopy are therefore valuable techniques for detection and characterisation of the forward electron transfer. The use of fluorescence measurements can also allude to the mechanism of quenching, namely whether it is dynamic (deactivation of fluorophore due to diffusion-controlled collisions with quencher), or static (formation of a non-emissive complex between fluorophore and quencher). The former results in a decrease in both

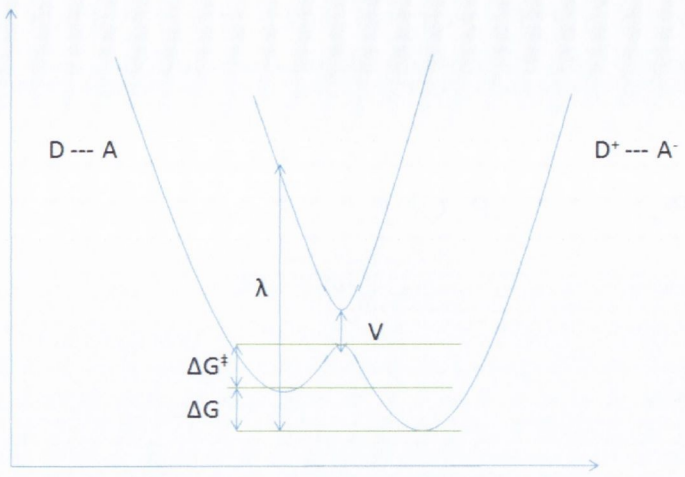

Figure 7.4: Energetics of electron transfer in the Marcus 'normal' region

lifetime and intensity, while the latter causes quenching of intensity only. This distinction relies on the assumption that the bound complex is not fluorescent, and therefore does not contribute to the measured lifetime. In reality this is a simplification. In most cases static simply means too short-lived to be detected, and any fluorescence that is too fast to be resolved from a measurement will be interpreted as being static quenching[149].

For simple systems the bimolecular quenching constant (k_q) or the ground-state association constant (K_a) can be calculated from the Stern-Volmer equations for pure dynamic (Eq. 7.4) or static (Eq. 7.5) quenching, respectively. Q is the quencher, Φ is the emission quantum yield and subscript '0' denotes the absence of quencher. Deviations from linear Stern-Volmer kinetics are found in complex systems, such as in the formation of a fluorescent ground-state complex, or when mixed mechanisms are occurring.

$$\frac{\tau_0}{\tau} = \frac{\Phi_0}{\Phi} = 1 + k_q \tau_0 [Q] \tag{7.4}$$

$$\frac{\Phi_0}{\Phi} = 1 + K_a [Q] \tag{7.5}$$

Emission measurements probe the forward electron transfer but reveal little about what happens next. Once the excitation has disappeared the electron and 'hole' can either recombine, or diffuse into charge-separated species, depending on the relative efficiencies of the competing processes of reverse electron transfer and cage escape (Fig. 7.5 on the following page). In the photo-oxidation of DNA, efficient reverse electron transfer results in instant repair or prevention of DNA damage, so is an important feature to consider with type 1 photosensitisers. Photoproducts (radical anions and cations) have

their own distinctive absorption spectra, so can be effectively studied using transient absorption spectroscopy with the appropriate time-resolution.

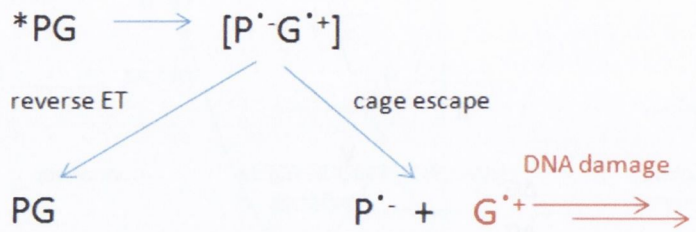

Figure 7.5: Competition between charge recombination and charge separation

7.3 Porphyrins – H_2TMPyP4

The photosensitiser molecules studied in this thesis are porphyrins (Fig. 7.6 on the next page). Porphyrin derivatives, such as haemoglobin and chlorophyll, are involved in biological processes such as light harvesting, oxygen transport and storage, electron transport and energy transfer[150].

The central protons in the porphyrin macrocycle are very weakly acidic and can be readily substituted by most metals. Depending on the coordination number, metals can acquire axial ligands to change the shape from planar to square pyramidal or octahedral. The porphyrin macrocycle itself is generally planar, although the presence of large metals or bulky substituents can distort the structure out-of-plane[151,152].

Porphyrins are brightly coloured due to the conjugated system of 18 π electrons giving rise to highly allowed $\pi^* \leftarrow \pi$ transitions ($\epsilon_{max} > 100{,}000$ dm^3 mol^{-1} cm^{-1}) in the visible region. The primary absorptions arise from transitions between two HOMOs and two LUMOs on the macrocycle (Fig. 7.7 on the facing page). Single $e_g \leftarrow a_u$ transitions generate the Q-bands, while a double ($2\,e_g \leftarrow a_{2u}$) transition results in the characteristic Soret band. The presence of the metal increases the symmetry of the porphyrin and results in fewer Q-bands than the free base.

The dominant deactivation mechanisms of the $\pi\pi^*$ excited states are also altered depending on the chosen metal[150]. Examples include fluorescence (e.g. free base, Zn(II)), room temperature phosphorescence (Pt(II), Pd(II)), non-radiative decay through low-lying d-d states (Ni(II)), and structural changes such as photoinduced axial ligand release (Ni(II))[153] or exciplex formation (Cu(II))[154].

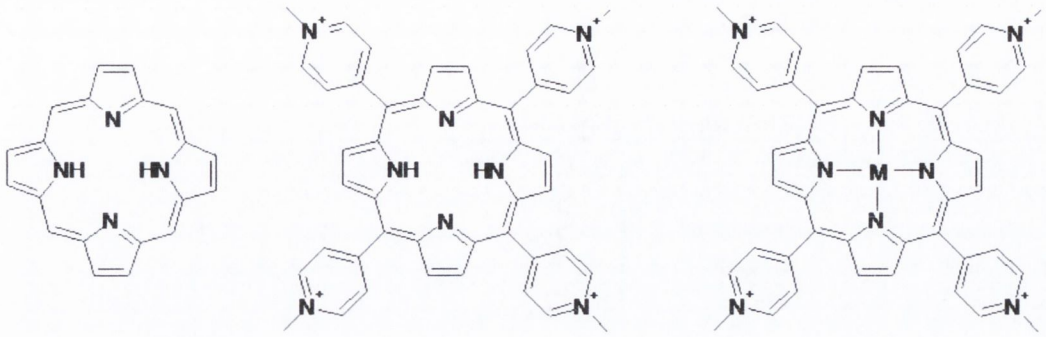

Figure 7.6: Porphyrin structures. From left to right: The free base porphine macrocycle, free base H_2TMPyP4, metalloporphyrin MTMPyP4

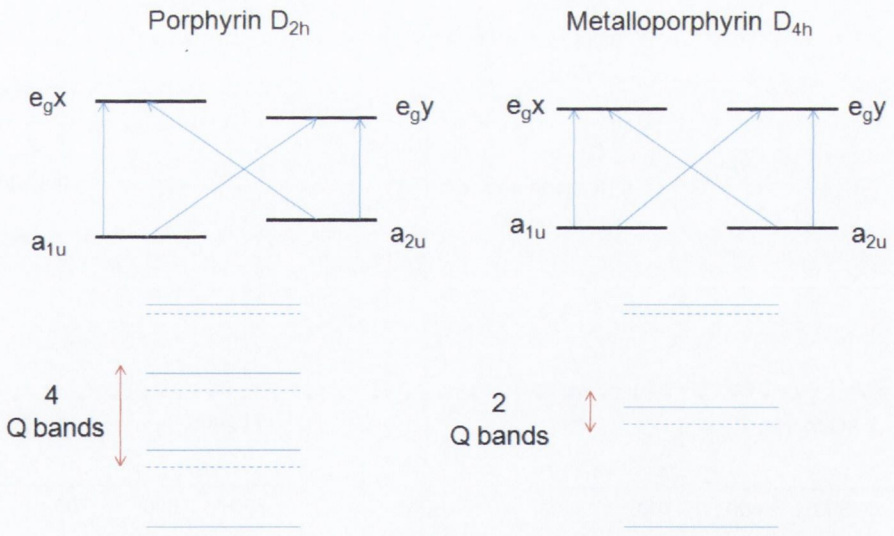

Figure 7.7: $\pi* \leftarrow \pi$ transitions in LEFT: free base porphyrin and RIGHT: metalloporphyrin, based on Gouterman four-orbital model. Solid lines are electronic states and dashed lines are vibronic components. Adapted from Murphy[155]

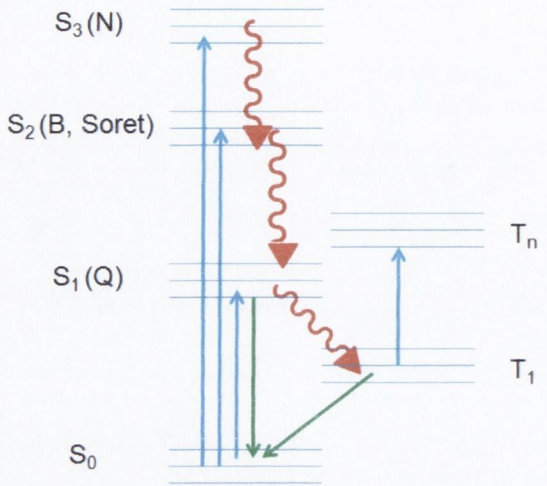

Figure 7.8: Generalised Jablonski diagram for common transitions in porphyrins

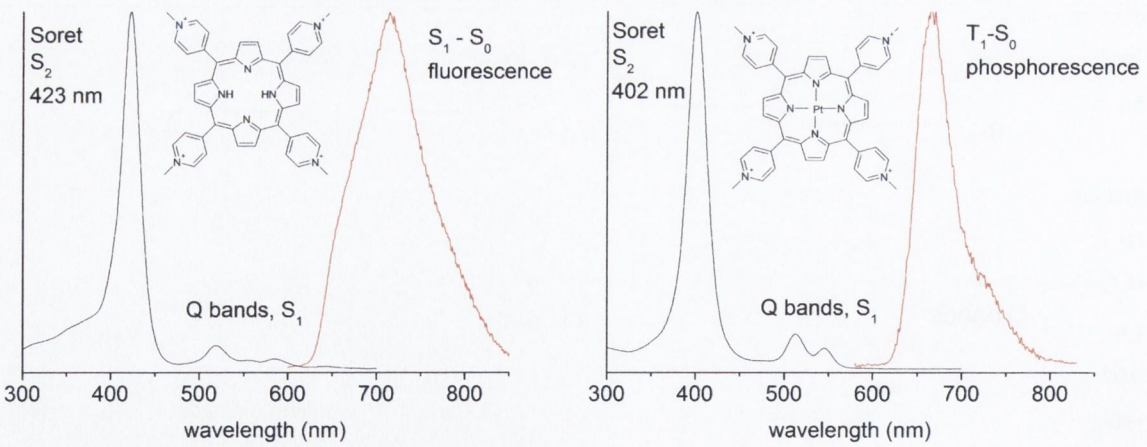

Figure 7.9: Normalised absorption and emission spectra of LEFT: H_2TMPyP4 and RIGHT: PtTMPyP4

Due to high yields of singlet-triplet intersystem crossing, porphyrins are very effective type 2 sensitisers and have found application in photodynamic therapy. Generally, free base porphyins and metalloporphyrins with diamagnetic (but not paramagnetic) metals are effective generators of singlet oxygen[156]. The possibility of both PET and singlet oxygen generation means that porphyrins can interact with DNA by a dual mechanism[143], so they are very interesting molecules to study from a photophysical and photochemical perspective.

The porphyrins studied in this work are derivatives of tetracationic 5,10,15,20 *meso*-tetrakis(4-*N*-methylypyridyl)porphyrin (TMPy), shown in Fig 7.6 on page 109. Most porphyrins, even charged porphyrins, tend to aggregate readily in solution due to π–stacking interactions. However TMPy porphyrins have been shown to be remarkably stubborn to aggregation even at high salt concentrations[157,158]. This is believed to be due to a combination of the 4+ charge and an intramolecular charge transfer that confers substantial positive charge character on the macrocycle itself (Fig. 7.13, page 115)[157,159]. Predominance of the monomeric form facilitates spectroscopic measurements on the porphyrin, but also improves the photosensitising ability as aggregated porphyrins tend to show quenched excited states[160–162].

TMPy porphyrins interact with a variety of nucleic acid systems due to electrostatic attraction with the phosphate groups and stacking interactions with the nucleobases. They are also potent photo-oxidisers, with the ability to efficiently photo-oxidise single- and double-stranded DNA[155,163,164].

7.4 Platinum Porphyrins – PtTMPyP4

The work in this thesis is focussed on Pt(II)TMPyP4. Pt(II) (d8) porphyrins are known as irregular-hypso porphyrins of the phosphorescent type[150]. These are so called because the Soret band maximum is blue-shifted relative to the free base, due to metal to ligand π backbonding ($d_\pi(d_{xz},d_{yz})$ to $e_g(\pi^*)$).

PtTMPyP4 is formally square planar with D_{4h} symmetry. The presence of the heavy Pt atom in the porphyrin macrocycle results in very efficient intersystem crossing to the triplet state ($\Phi_{isc} = 1$) following photo-excitation. As a result, PtTMPyP4 is non-fluorescent, but instead displays room temperature phosphorescence (Fig. 7.9) with a lifetime of c. 7μs in degassed aqueous solution[165]. Long-lived triplet states are susceptible to quenching by species in solution, especially oxygen. As a result they are convenient luminescence probes, and oxygen sensors have been developed from PtTMPyP4 immobilised in media such as mesoporous silica[166] and Nafion®[167–169].

The biological activity of PtTMPyP4 has also been investigated, and it is shown to deactivate the λ-phage virus under 528 nm irradiation, but apparently by a different

mechanism to H_2TMPyP4[170]. Recently, PtTMPyP4 has also shown promise as an agent in brachytherapy (internal radiotherapy), where release of Auger electrons in Pt(II) is shown to treat tumours in mice[171].

Miscellaneous papers have also been published on the photochemistry[172] and non-aqueous electrochemistry[173] of PtTMPyP4. Significantly, PtTMPyP4 has been reported to undergo emission quenching in the presence of chloride. This has been assigned as self-quenching attributed to aggregation at high ionic strength[165,174], but these claims are inconsistent with the reluctance of TMPy porphyrins to aggregate[157,158]. Although the effect of halide atoms on excited triplet states of aromatic hydrocarbons has been studied extensively[175–178], there appears not to be any such studies on porphyrins. Given the ubiquity of Cl^- in biological solutions, and the scarcity of published work on halide quenching of porphyrins, this result beckons further investigation.

7.5 TMPy and Nucleic Acids – Binding Interactions

7.5.1 TMPy and Mononucleotides

H_2TMPyP4 and some of its metal derivatives have been shown to form face-to-face π-stacked complexes ($K_a \sim 10^3\,M^{-1}$) with the nucleotides of adenine, guanine, cytosine and thymine[179–183] (see Fig. 7.10).

The stability of the complex arises mainly from hydrophobic interactions (>75% contribution) rather than the Coulombic attraction between porphyrin and nucleotide (<25% contribution)[179,180]. Given the importance of π–stacking interactions, larger as-

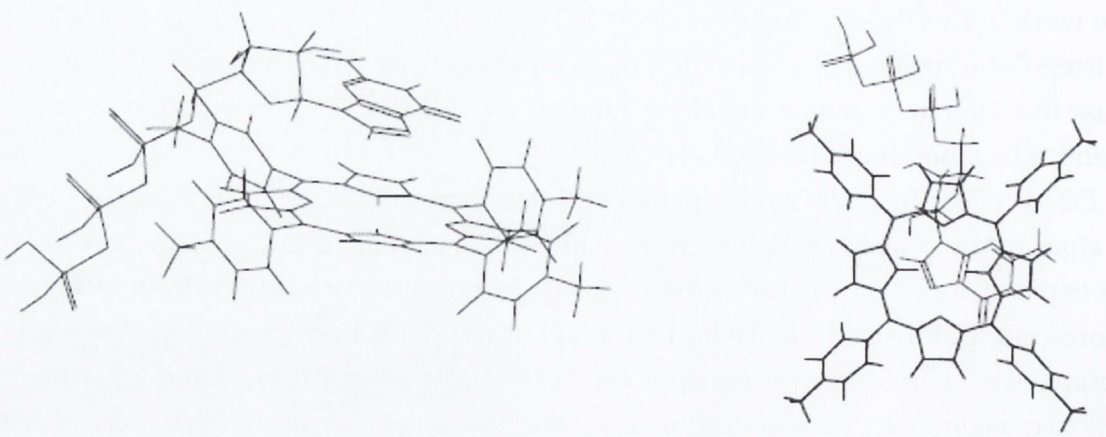

Figure 7.10: Geometry-optimised complex of H_2TMPyP4 with guanosine triphosphate (GTP)[184]

sociation constants are observed with purines than pyrimidines, and it has also been suggested that the presence of the hydrophilic 2′OH group in ribonucleotides may reduce binding affinities relative to deoxy- nucleotides[185]. A strong dependence on buffer conditions has been reported[183], though there are some apparent inconsistencies in the values quoted in the literature. For example, the association constant for the H_2TMPyP4-dCMP complex is quoted as 198 M^{-1} in 100 mM phosphate buffer by Jasuja et al, but 43,180 M^{-1} by Sirish and Schneider, also in 100 mM phosphate[183]. The stoichiometry of the complex is commonly reported as 1:1, although Pasternack et al have shown evidence for a small contribution of 1:2 complexes[179].

7.5.2 TMPy and Polynucleotides

The binding of TMPyP4 and its derivatives to DNA and polynucleotides has been studied extensively using techniques such as UV/vis absorption[186], circular and linear dichroism[187], fluorescence[188], transient absorption[189], resonance Raman[190], NMR[191], resonance light scattering[192] and X-ray crystallography[193]. As shown in Fig. 7.11, there are three generally accepted binding modes for TMPy to duplex DNA: intercalation (dominant at GC sites), groove binding (dominant at AT sites) and outside-binding[194,195].

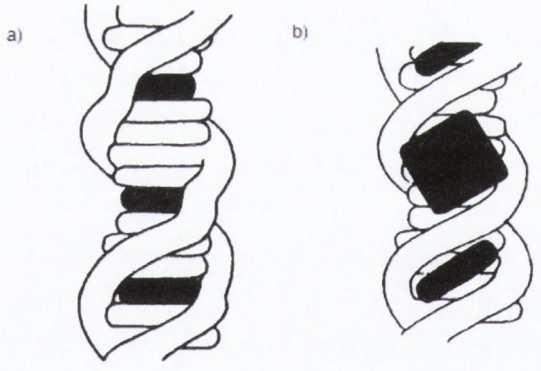

Figure 7.11: Proposed binding modes for a porphyrin (CuTMPyP4) in DNA a) intercalation b) minor and major groove binding, the latter with self-stacking[196]

H_2TMPyP4 intercalates into GC sites in DNA and synthetic [poly(dG-dC)]$_2$ with an affinity $\sim 10^6$ M^{-1})[197]. It was claimed originally from NMR experiments that the interaction is specifically at 5′-CG-3′ sites[191,198], though recent reports claim little variation in affinity for 5′-CG and 5′-GC sites[190]. TMPy has been described as a "threading", rather than a classical intercalator, due to the large size of the molecule and the necessity to accommodate the *meso* groups in the intercalation site[3]. The *meso* groups must

overcome a 15 kcal mol^{-1} energy barrier to achieve co-planarity with the porphyrin ring[197], so it has been proposed that intercalated TMPy induces some structural distortion in [poly(dG-dC)]$_2$ and DNA[196,199]. H_2TMPyP4 has been also reported to induce Z-B transitions in DNA under certain conditions[200,201].

H_2TMPyP4 binds to AT sites with a similar affinity to GC sites[202]. Due to steric hindrance from the thymine methyl group that blocks intercalation[203], H_2TMPyP4 tends to groove bind at these sites. The binding of H_2TMPyP4 to AT systems, in particular, has been studied in detail by the group of Seog Kim using CD and LD[187,199,204–209]. They propose that H_2TMPy binds in the minor groove, and stacks in the major groove, depending on the [porphyrin]/[DNA] ratio[187].

In native DNA, H_2TMPyP4 has a number of distinct binding sites available. High ionic strength favours AT outside binding, while GC intercalation occurs at low ionic strength[210–212]. It has been claimed that the base composition decides the dominant binding mode in mixed sequences, as GC–rich duplexes afford greater H-bonding stabilisation and inhibit the structural distortion required for good AT binding[213].

Various metal derivatives have also been studied in the presence of polynucleotides (e.g. Zn[214], Pd[215], Pt[216], Co[217], Cu[218], Ni[153], Mn[164], Fe[219]). Porphyrins with axial ligands (e.g. 5-coordinate ZnTMPyP4, 6-coordinate Mn, Fe, Co) present too wide a profile for intercalation, and prefer to groove bind in natural DNA[186,202]. In [poly(dG-dC)]$_2$, axially ligated metalloporphyrins are believed to groove bind but by a different mechanism than they do in [poly(dA-dT)]$_2$[199]. Facile axial ligand release can alter the mode of binding. Chirvony et al claim that ZnTMPyP4 can become a 4–coordinate intercalator at low ionic strength[214]. Meanwhile 6–coordinate Ni(II)TMPyP4 can undergo photoinduced ligand release[153], while CuTMPyP4 is believed to form an emissive exciplex with the adenine and thymine residues in DNA[154,220].

Square-planar d8 metalloporphyrins such as PdTMPyP4 and PtTMPyP4 show evidence of intercalation into native DNA[174,215,216,221] and poly(dA)[216]. However, metals with large atom radii may form non-planar metalloporphyrins[151], which would be expected to impede intercalation or impose a structural change on the DNA polymer.

7.6 TMPy and Nucleic Acids – Excited-State Processes

7.6.1 Emission

The effect of DNA on excited singlet and triplet states can be used as a probe for the immediate environment of the porphyrin. The formation of a complex between H_2TMPyP4 and 2′-deoxy-AMP (dAMP) causes an increase in fluorescence lifetime and quantum yield, as well as resolution of a featureless fluorescence spectrum into two

bands[181,182,222]. Similar effects have been noted in DNA[188](Fig. 7.12).

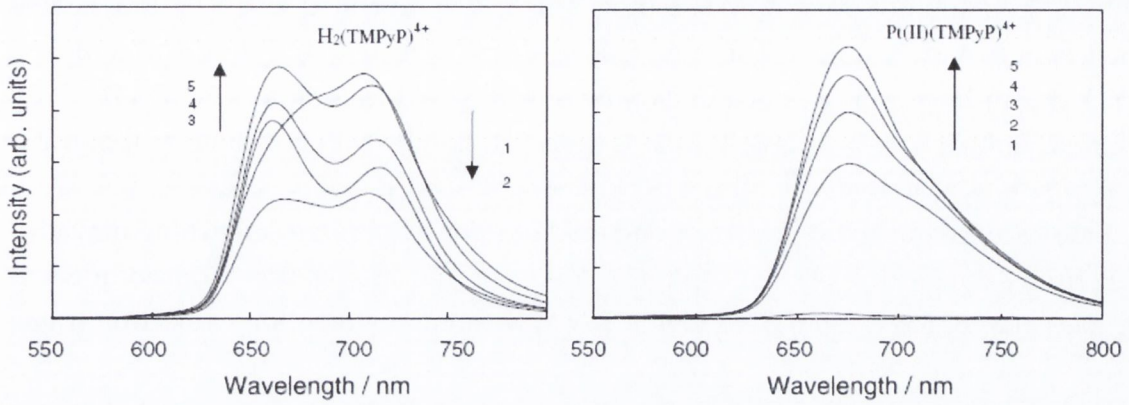

Figure 7.12: Effect of increasing DNA concentrations on the emission spectra of H_2TMPyP4 and PtTMPyP4[174]

This effect is proposed to be due to the intramolecular charge transfer state between the peripheral groups and the porphyrin macrocycle (Fig. 7.13). This state is believed to lie very close in energy to S_1 in H_2O, but is raised in energy in apolar media, such as that provided in a hydrophobic stacking environment[159,222]. The energy of the ICT state might also be affected by the presence of the negatively charged phosphate groups of DNA[223]. The net result is the removal of a radiationless deactivation pathway, and a change in the spectrum shape due to elimination of vibronic coupling between S_1 and the ICT state[159,222].

Figure 7.13: The proposed resonance forms of TMPy. After Blinova and Vasil'ev[165]

By contrast, fluorescence lifetime and quantum yield is quenched when H_2TMPyP4 is complexed with dGMP[181,182,222], or intercalated between GC base pairs[188,223]. This has been attributed to a thermodynamically favourable photoinduced electron transfer from guanine to the H_2TMPyP4 S_1 state, with a forward rate constant of c. $10^9\ s^{-1}$ in the polymer[223,224]. Quenching is primarily via the singlet state, though can also occur

via the triplet in H_2TMPyP4-GMP complexes[224]. It has been claimed that not all intercalated porphyrins are quenched by G[190], suggesting that the PET is sensitive to the mutual orientation of donor and acceptor. This is demonstrated in the multiple emission lifetimes and lifetime distribution (100 ps – 6 ns) in the H_2TMPyP4-GMP complex, which the authors propose to be due to the flexibility of the complex (Fig. 7.14)[222]. By contrast, a much narrower distribution is observed for H_2TMPyP4 bound to [poly(dG-dC)]$_2$

Fluorescence quenching offers strong evidence for ET, though quenching may also arise from self-stacking of the porphyrin. For example, aggregation-induced quenching has been reported for H_2TMPyP4 in DNA, without any mention of electron trans-

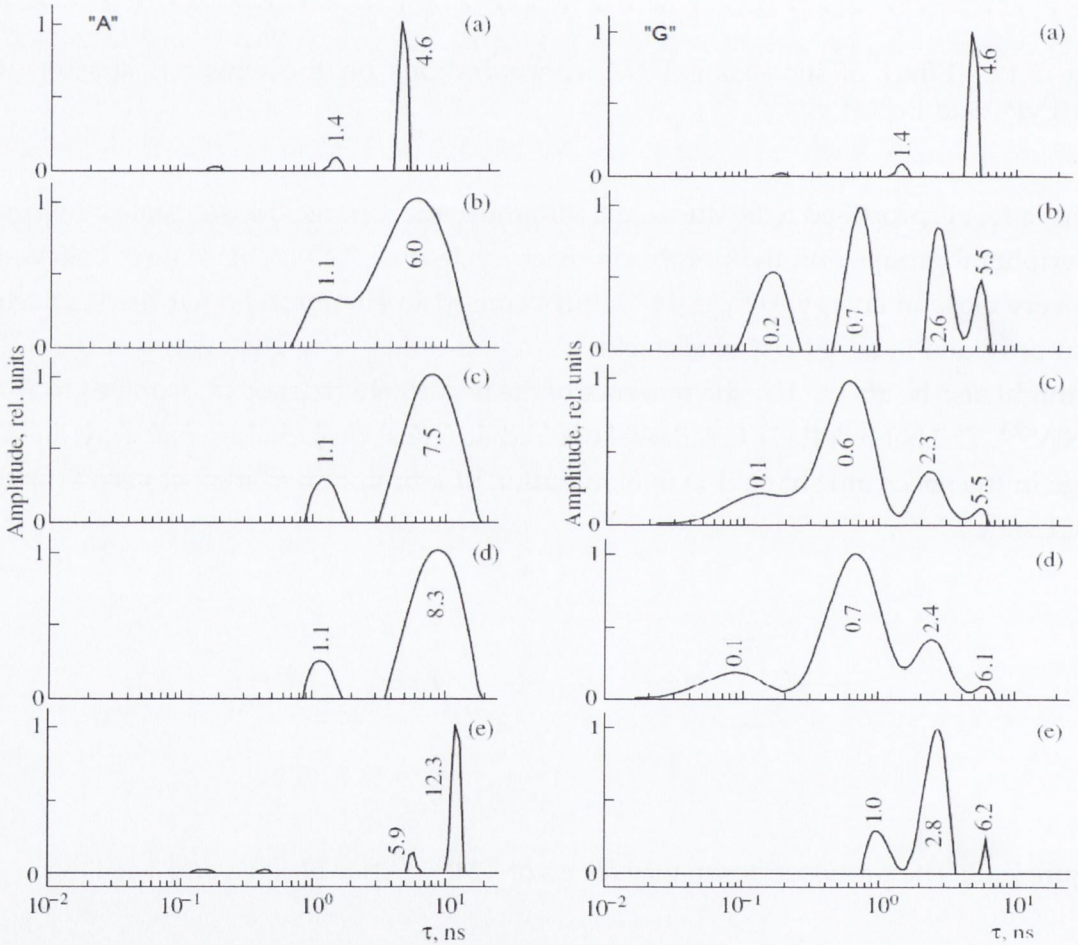

Figure 7.14: Fluorescence lifetime distributions in H_2TMPyP4-nucleic acid systems recorded by Sazanovich et al[222] showing LEFT: (a) H_2TMPyP4 only (b) + 0.001 M AMP (c) + 0.01 M AMP (d) + 0.1 M AMP, (e) + [poly(dA-dT)]$_2$ RIGHT: (a) H_2TMPyP4 only (b) + 0.001 M GMP (c) + 0.01 M GMP (d) + 0.1 M GMP (e) + [poly(dG-dC)]$_2$

fer[219,225]. PtTMPyP4 and PdTMPyP4 have been shown to exhibit luminescence enhancement in the presence of DNA (see Fig. 7.12 on page 115)[174,215,221]. For PdTMPyP4, this has been attributed to shielding of the intercalated porphyrin from dissolved oxygen quencher, while for PtTMPyP4 it was rationalised as destacking of the aggregated porphyrin on contact with DNA[174]. Interestingly, photo-induced electron transfer has not been reported for any of the TMP metalloporphyrins in the presence of DNA.

7.6.2 Transient Absorption

Nanosecond transient spectroscopy (ns-TA) has been used to calculate triplet lifetimes of H_2TMPyP4[190,223] and ZnTMPyP4[214] in polynucleotides, and hence infer binding modes from the degree of shielding afforded from dissolved oxygen.

Significantly, no electron-transfer photoproducts for the H_2TMPyP4-guanine system have been observed by ns-TA, implying that if electron transfer occurs, the reverse transfer is very efficient and occurs within the instrument response time (< c. 20 ns)[223]. It must also be stressed that the porphyrin radical anion absorbs above 750 nm[226–229], a spectral region where standard photomultipliers have low sensitivity. The guanine radical cation is also weakly absorbing and may overlap with the porphyrin T-T spectrum. Despite the lack of spectroscopic evidence from TA, support for a photoinduced electron transfer between H_2TMPyP4 and guanine is available from other techniques[170,230]. Kalyanasundaram characterised the near-IR transient absorption of the TMPy porphyrins in the early 1980s (Fig. 7.15), but this spectral region has been ignored since[231].

A small number of ultrafast TA reports have appeared on the PET of porphyrins, with mixed success in identifying photo-products of electron transfer. Using fem-

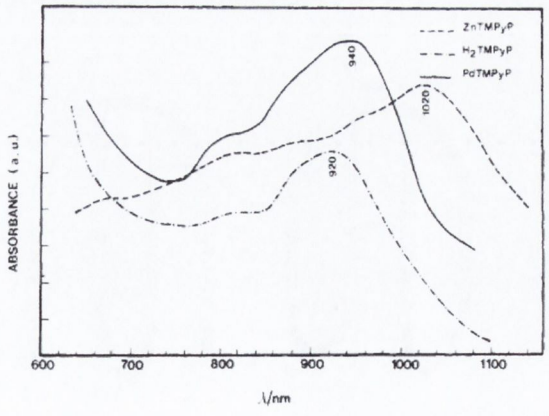

Figure 7.15: Triplet-triplet absorption spectra of H_2TMPyP4, ZnTMPyP4 and PdTMPyP4 in the near-IR region[231]

tosecond techniques, Steenkeste et al recorded a reverse rate constant of 8.3 x 10^{12} s^{-1} for the reduction of a bis-arignyl derivative of H_2TMPyP4[232], though in a recent paper on an acridine derivative they claim that recombination is too fast for them to detect (<200 fs)[233]. Wei et al showed the first guanine photo-oxidation by a metallophthalocyanine, and were able to observe what they believe is the guanine radical cation using ESR spectroscopy[234].

Apart from a study on a porphyrin-Re(II) dyad[235], there have been no reported ps-TRIR studies on porphyrins. This suggests a whole new avenue of investigation for porphyrin systems.

7.7 Quadruplex DNA

7.7.1 Structure

Much of the current interest in TMPy porphyrins arises from their ability to bind to and stabilise quadruplex DNA, a secondary structure characteristic of G-rich DNA. The basis of the G-quadruplex is the G-tetrad, which is formed by Hoogsteen-bonded coplanar guanine residues in the presence of a chelating metal cation such as Na^+, K^+ or Sr^{2+} (Fig. 7.16a). G-tetrads can be formed with high concentrations (>500 mM) of the free nucleotide guanosine 5′monophosphate (GMP)[236], and where consecutive guanines appear in a DNA polymer, these can stack vertically to form quadruplex DNA (Fig. 7.16b). There are many possible structures of the quadruplex, including intramolecular (e.g. $AG_3(T_2AG_3)_3$) or intermolecular association ($(G_4T_4G_4)_2$ or $(TG_4T)_4$), and the structures have been well characterised by X-Ray, NMR and CD spectroscopy[237].

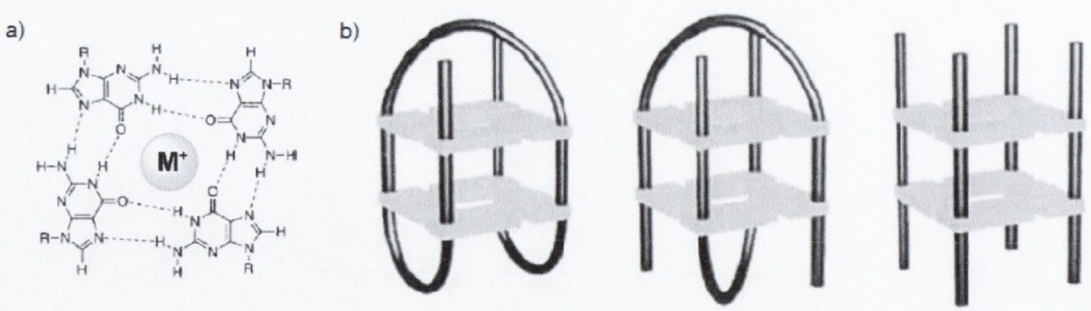

Figure 7.16: (a) The structure of the G-tetrad[109] (b) G-quadruplexes formed from 1, 2 and 4 strands. The G-tetrad is coloured grey[238]

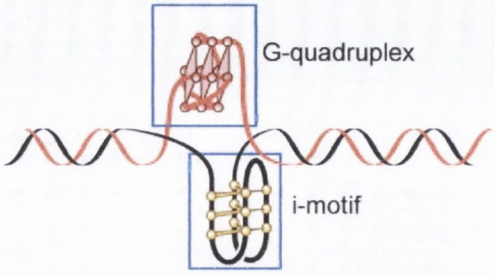

Figure 7.17: G-quadruplex and i-motif in telomeric DNA[239]

7.7.2 TMPy and Quadruplex

G-quadruplex sequences are complementary to C-rich sequences, and G-quadruplexes may form in tandem with the i-motif in certain conditions (Fig. 7.17). The single-stranded overhangs present at the end of chromosomes, known as telomeres, consist of guanine-rich repeat units of $(TTAGGG)_n$ up to 200 bases long[240]. Cell replication results in shortening of the telomere, inducing the eventual cell death. The telomerase enzyme, which is present in approx. 90% of tumours, maintains telomere length resulting in the 'immortality' characteristic of a cancer cell. However telomerase can not replicate the telomere when it is in the folded quadruplex structure. As a result, there is great interest in drug molecules that can stabilise the quadruplex form, as this offers a potential route to chemotherapy.

Cationic porphyrins, especially H_2TMPyP4, have similar dimensions to the G-tetrad, and have proven to be effective 'telomerase inhibitors'. There has been significant work done on the binding interactions of H_2TMPyP4 with quadruplexes, with specific interest in whether the porphyrin stacks onto the G-tetrad, outside binds, or interacts with the loops[241–252]. It is generally not believed that the porphyrin can intercalate between successive tetrads, but may stack onto the end or have electrostatic interactions with the phosphate-rich grooves. Examples are shown for the simple $[d(TGGGGT)]_4$ system in Fig. 7.18 on the following page. However, porphyrins with large central metal atoms (2nd and 3rd row transition metals including PtTMPyP4) show reduced activity against telomerase when bound to quadruplex DNA, possibly due to their inability to incorporate into sterically constrained quadruplex structures[241].

Despite the wealth of solution studies, there is only one example of a definitive TMPy-quadruplex structure from X-ray crystallography[254]. However the quadruplexes themselves have been successfully crystallised[255–261] so an X-ray structure of the bound complex would be a valuable contribution to the evolving understanding of TMPy-quadruplex binding interactions.

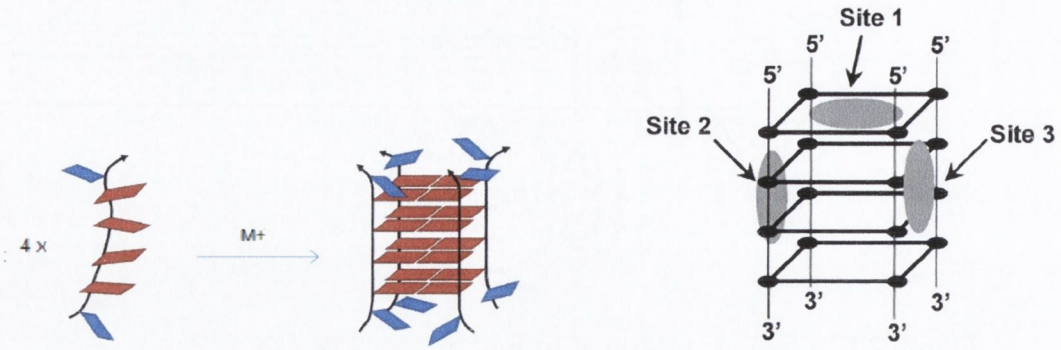

Figure 7.18: Formation of $[d(TGGGGT)]_4$ quadruplex and possible porphyrin binding modes[253]

7.8 Aims

TMPy porphyrins, like ruthenium polypyridyl complexes, have become classic photoprobes. Despite the extensive literature on H_2TMPyP4, Pt(II)TMPyP4 has not been studied in the same detail. This is despite the ease of studying the triplet state, the excited state implicated in type 2 photo-oxidation of DNA. This thesis therefore aims to fill some of these gaps by addressing the following specific questions.

7.8.1 Binding Studies – Chapter 8

- How does PtTMPyP4 interact in the ground-state with mononucleotides?
- What are the modes of binding of PtTMPyP4 to polynucleotides and how do these compare to H_2TMPyP4?
- How does PtTMPyP4 interact with the guanine-quadruplex structure compared to 5-coordinate ZnTMPyP4?

7.8.2 Emission Studies – Chapter 9

- How is the PtTMPyP4 triplet state quenched by chloride ions in solution?
- How does PtTMPyP4 interact in the excited state with mono and polynucleotides?
- Do phosphorescence studies show evidence for photo-oxidation of guanine?

7.8.3 Transient Absorption Spectroscopy – Chapter 10

- Can the excited-state parameters of PtTMPyP4 (triplet state and singlet-triplet intersystem crossing) be characterised?
- Is there spectroscopic evidence for photo-induced electron transfer from guanine to Pt(II)TMPyP4?
- How can time-resolved infrared spectroscopy be used for photophysical studies of porphyrins?

Chapter 8

Binding Studies

In this chapter the ground-state interactions of PtTMPyP4 with mono- and polynucleotides are studied using UV/vis absorption and circular dichroism (CD) spectroscopy. Quantitative data is calculated for binding affinities and possible modes of binding are discussed compared to free base H_2TMPyP4. Attempts are also made to deduce the structure of the PtTMPyP4- and ZnTMPyP4-quadruplex complex by solution and crystallographic methods.

Samples of PtTMPyP4 for spectroscopic measurement were prepared to a concentration of approx. 6 μM ($A_{max} \cong 1$ in a 1 cm cuvette) in buffered (25 mM NaH_2PO_4, 25 mM Na_2HPO_4, pH 7) H_2O solution. PtTMPyP4 and nucleic acid concentrations were determined spectrophotometrically using published extinction coefficients (Table 13.1 on page 208). Spectra were sometimes recorded in acrylic cuvettes, as TMPy porphyrins have been known to adhere to quartz cuvettes[155]. We observed little difference in data obtained in either quartz or acrylic cuvettes, though CD measurements were recorded exclusively in quartz due to spurious signals recorded in acrylic cuvettes.

8.1 PtTMPyP4 and Mononucleotides

The ground-state interactions of PtTMPyP4 with the purine RNA mononucleotides, AMP and GMP (overleaf), were studied using UV/vis spectroscopy. The addition of AMP or GMP to 6 μM PtTMPyP4 results in a bathochromic shift (shift to longer wavelength) and hypochromism (decrease in absorbance) of absorption bands in the Soret and Q-band regions (Fig. 8.1 on the following page, Table 8.1, page 127). This is characteristic of a face-to-face π-stacked complex formed between porphyrin and nucleotide[179,180,182,183]. Isosbestic points are observed at 411 nm for the initial additions of mononucleotide up to approx 0.2–0.5 mM. The isosbestic point then disappears as more nucleotide is added (Fig. 8.2 on the next page).

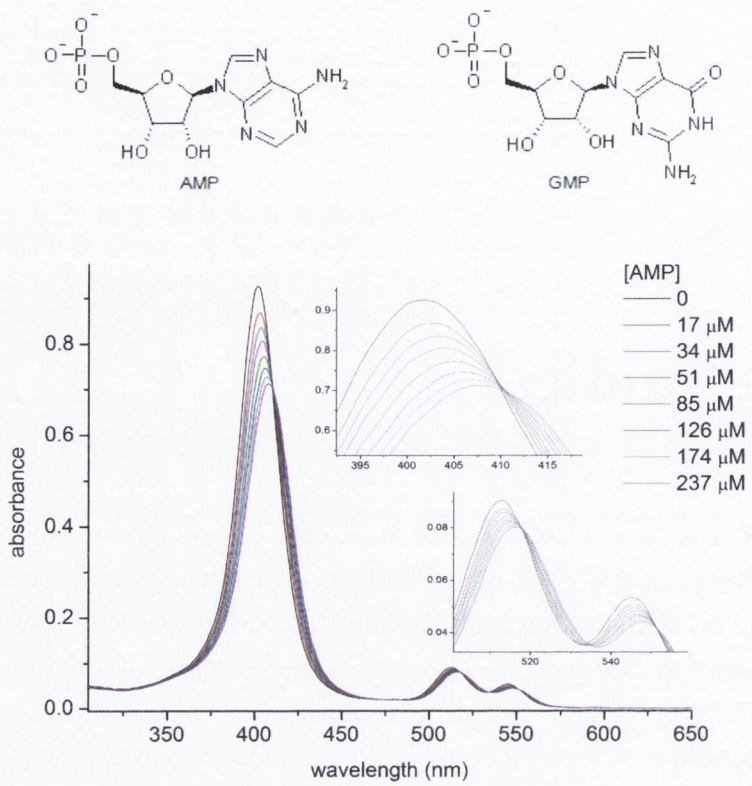

Figure 8.1: UV/vis spectra of PtTMPyP4 in presence of low concentrations of AMP (50 mM Na-phosphate buffer pH 7)

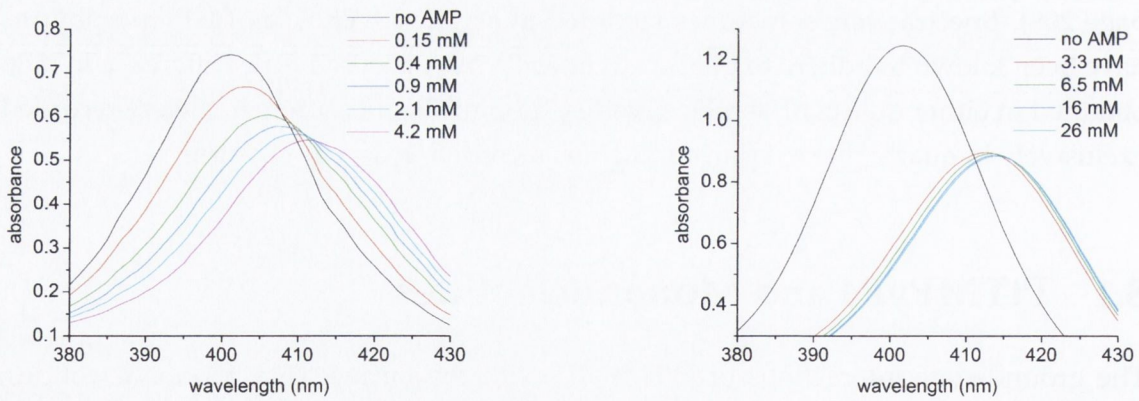

Figure 8.2: UV/vis spectra of PtTMPyP4 Soret region in presence of higher concentrations of AMP (50 mM Na-phosphate buffer pH 7)

For a 1:1 complex between a porphyrin P and a nucleotide N, the ground-state association constant (K_{g1}) is described by Eq. 8.1

$$K_{g1} = \frac{[PN]}{[P]_{free}[N]_{free}} \tag{8.1}$$

K_g was calculated from the changes in the PtTMPyP4 absorption spectra using Benesi-Hildebrand (Eq. 8.2)[262] and Scott-type equations (Eq. 8.3)[263], where ΔAbs is the change in absorbance at Soret max (401 nm), [N] is nucleotide concentration, and ΔAbs_i is the extrapolated change in absorbance at saturated binding.

$$\frac{1}{\Delta Abs} = \frac{1}{[N]K_{g1}\Delta Abs_i} + \frac{1}{\Delta Abs_i} \tag{8.2}$$

$$\frac{\Delta Abs}{[N]} = -K_{g1}\Delta Abs + K_{g1}\Delta Abs_i \tag{8.3}$$

Although widely used, the inverse relationships in the Benesi-Hildebrand fit results in unequal weighting of data points, so the Scott equation is a more suitable test for the linearity of the binding plot[264]. Titrations were performed under two conditions: constant porphyrin concentration (a PtTMPyP4-N solution was added to PtTMPyP4), and a diluted porphyrin concentration (N solution added to PtTMPyP4) (Fig. 8.3). In the latter case, corrections were made for dilution. However, we noticed that some of these binding plots (Fig. 8.4 on the following page) showed greater deviations from linearity than in the undiluted solutions (Fig. 8.3).

Curvature and the loss of isosbestic points suggested that there were multiple associated species formed. Calculation of binding constants was then performed using the generalised equation for multiple association (Eq. 8.4).

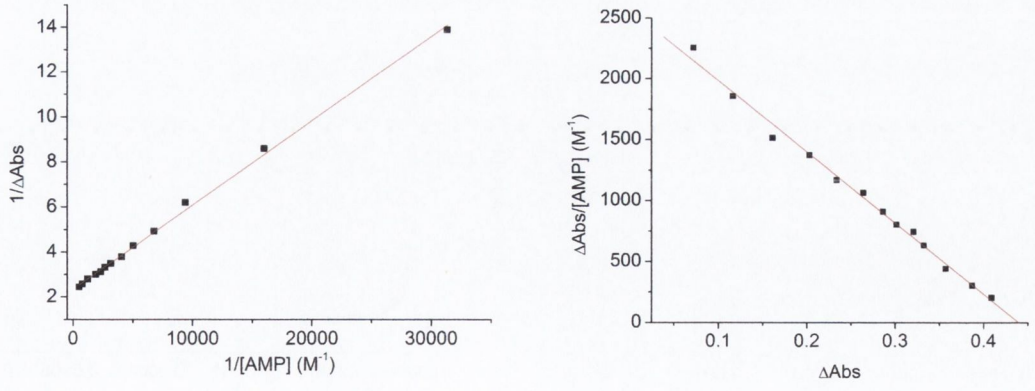

Figure 8.3: LEFT: Benesi-Hildebrand and RIGHT: Scott binding plots for PtTMPyP4-AMP complexes up to 2 mM AMP in constant PtTMPyP4 concentration (6 μM). In 50 mM Na-phosphate buffer pH 7

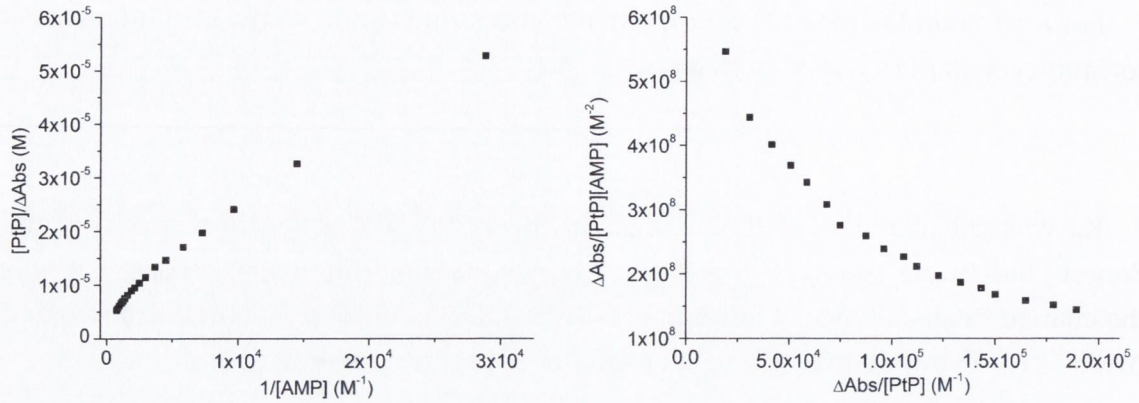

Figure 8.4: LEFT: Benesi-Hildebrand and RIGHT Scott binding plots for PtTMPyP4-AMP complexes up to 2 mM AMP with dilution of PtTMPy4. In 50 mM Na-phosphate buffer pH 7

$$\frac{[PtP]}{\Delta Abs} = \frac{1 + K_{g1}[N] + K_{g1}K_2[N]^2}{K_{g1}\Delta\epsilon_1[N] + K_{g1}K_{g2}\Delta\epsilon_2[N]^2} \tag{8.4}$$

where $\Delta\epsilon$ denotes the change in extinction coefficient of the bound porphyrin relative to free. Eq. 8.4 reduces to a form of the simple Benesi-Hildebrand equation when $K_{g2} = 0$ (Eq. 8.5).

$$\frac{[PtP]}{\Delta Abs} = \frac{1 + K_1[N]}{K_1\Delta\epsilon_1[N]} \tag{8.5}$$

Fitting to Eq. 8.5 returned similar values to the Benesi-Hildebrand and Scott equations (Fig. 8.5), and converged at physically unrealistic values of both $\Delta\epsilon_2$ and K_{g2}. The fitting data thus support a 1:1 association model.

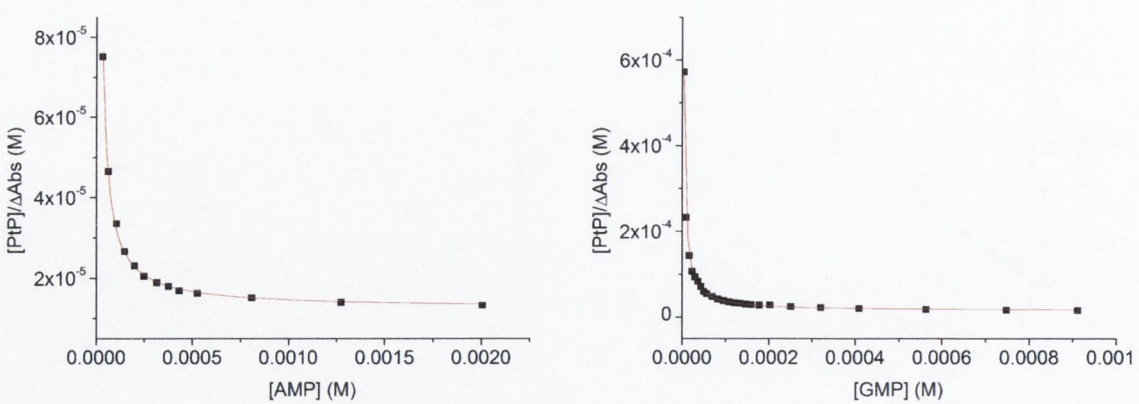

Figure 8.5: Non-linear fitting for LEFT: PtTMPyP4-AMP and RIGHT: PtTMPyP4-GMP to Eq. 8.4

8.1.1 Discussion on Mononucleotides

The calculated binding constants are slightly higher than those reported for H_2TMPyP4-purine systems, although the literature data were recorded at higher ionic strength[181,182]. There is no significant specificity in binding between AMP and GMP despite the fact that they have different (*syn/anti*) favoured conformations. This may be due to the large and flexible binding site available, unlike those observed in systems such as dinuclear metal complexes[265].

Table 8.1: Calculated ground-state binding parameters for 1:1 PtTMPyP4-nucleotide complexes in 50 mM Na-phosphate buffer pH 7. $H = (A_{free\,max} - A_{bound})/A_{free\,max} \times 100$

	$\Delta\lambda$ (nm)	H(%)	K_{g1} (M^{-1})
AMP	10	35	6200
GMP	9	29	5300

Although non-linear curve fitting suggests that the 1:1 porphyrin:nucleotide complex dominates under the conditions studied, it is rational to believe that a 1:2 complex (Fig. 8.6) could be formed at high nucleotide concentrations or low ionic strength (Fig.8.6). The porphyrin is achiral with two very similar binding sites on either face, and there is ample electrostatic attraction due to the 4+ charge on the porphyrin. Also, the largest K_2 values (130–150 M^{-1}) recorded by Pasternack et al were for metalloporphyrins (CuTMPyP4 and NiTMPyP4)[179].

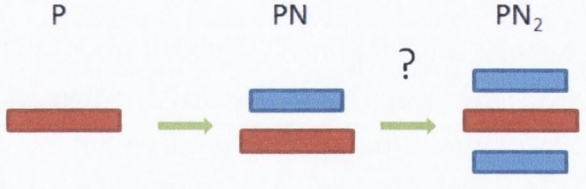

Figure 8.6: Stacked porphyrin-nucleotide complexes

The curvature of the binding plots is a common signal of higher order association, though the appropriate use of spectroscopic data in such cases has attracted critical discussion by Deranleau[266,267]. He shows that at least 75% of the saturation range should be plotted, and that under these conditions, some non-linearity is inevitable in the binding plots. It is therefore interesting to note that Jasuja et al show excellent Benesi-Hildebrand fits of the H_2TMPyP4-GMP complex to 1:1 stoichiometry. However, they only present the data up to 0.47 mM GMP, even though they report fluorescence

quenching data up to 16 mM[182]. It is also noteworthy that the Bensi-Hildebrand equation assumes that [N]»[P], which does not hold along the entire saturation range. While curvature usually signifies higher order complexes, it does not necessarily mean that the higher order complex is a major form. For example K_{g1}/K_{g2} ratios greater than 20 have been recorded in phenothiazine-nucleotide complexes, despite the exaggerated curvature visible in the binding plots[268].

The loss of isosbestic points is also a classic indicator of multicomponent systems. In the PtTMPyP4-nucleotide system, this might not necessarily be due to a 1:2 complex. For example, Sazanovich et al suggest, on the basis of fluorescence lifetime distribution analysis (Fig. 7.14), that there are four different types of complex formed between H_2TMPyP4 and GMP[222]. This is presumed to be due to the conformational freedom of the complex, and the presence of multiple binding geometries of similar affinity. Such a process may reveal itself in the ground-state absorption spectra.

The nucleotide titrations demonstrated some of the difficulties encountered with (relatively) weak interactions. In particular it is shown that complications can be avoiding by keeping the ligand (porphyrin) concentration fixed, thereby eliminating potential errors in the correction of data for dilution.

8.2 PtTMPyP4 and Polynucleotides

The interactions of PtTMPyP4 was examined in DNA ($[poly(dA\text{-}dT)]_2$, $[poly(dG\text{-}dC)]_2$, salmon sperm DNA) and RNA (poly(rA) and poly(rG)) polymers. The DNA polymers are in the classic double-stranded (ds) B structure (see Fig 1.6 on page 5). Poly(rA) and poly(rG) are the polymeric forms of AMP and GMP, so in principle are ideal comparisons with the mononucleotides. However, as discussed earlier, the absence of W-C base-pairing in the RNA homopolymers means they can form diverse and complex structures in solution. Poly(rA) forms a stacked single-stranded structure, while poly(rG) can adopt a number of morphologies including double-stranded and quadruplex forms[269]. As a result most studies on drug-DNA interactions focus on the double-stranded polymers, where the structure of the polymer and the binding sites are better defined.

The chiral nature of the polymers means that binding interactions can be monitored using CD spectroscopy, especially induced CD (ICD) where a chiral environment (DNA binding site) induces a CD signal in an otherwise achiral molecule (the porphyrin).

8.2.1 [poly(dA-dT)]$_2$

For titrations of a small molecule with DNA, concentrations are presented in the form P/D (phosphate/dye) ratio, analagous to the base/porphyrin ratio in this case. The inverse (D/P) is defined as r, or the binding ratio. These ratios relate the concentration of porphyrin to the concentration of available binding sites.

The addition of [poly(dA-dT)]$_2$ to PtTMPyP4 causes a bathochromic shift of 10 nm and a maximum hypochromism of 45% in the absorption spectrum (Fig. 8.7 on the following page). Isosbestic points were observed up to a P/D of 5 (Fig. 8.8 on the next page). Thereafter the absorbance showed a slight increase. The standard method for determining the binding affinities of small molecules to polynucleotides is by the method of McGhee and von Hippel (Eq. 8.6)[270], which accounts for neighbour exclusion effects, whereby binding of a molecule at one site may preclude binding to adjacent sites. In Eq. 8.6 r is the number of moles of bound porphyrin per total mole of base-pairs, C_f is the concentration of free porphyrin, and n is the exclusion parameter (the number of binding sites blocked).

$$\frac{r}{C_f} = K(1-nr)\left[\frac{1-nr}{1-nr+r}\right]^{n-1} \tag{8.6}$$

However it was not possible to fit the PtTMPyP4-[poly(dA-dT)]$_2$ system to this model, as suggested by the lack of a defined end-point in the titration.

Binding was then monitored using ICD spectroscopy, by performing titrations in two directions: the addition of porphyrin to [poly(dA-dT)]$_2$ (Fig. 8.9, page 131), and the addition of [poly(dA-dT)]$_2$ to porphyrin (Fig. 8.10, page 131). The changes in the spectrum shape in both cases confirm there are mixed binding modes. When there is a relatively low concentration of porphyrin relative to [poly(dA-dT)]$_2$ (low r, high P/D), the CD signal is dominated by a positive band at 405 nm. When there is a high porphyrin concentration relative to [poly(dA-dT)]$_2$ (high r, low P/D), the CD signal is bisignate (410 nm-/425 nm+). The CD spectrum appears to be a superposition of these two extremes, and it can be seen from Fig. 8.10 that the bisignate spectrum would become perfectly anti-symmetric if the positive CD is subtracted.

Spectroscopic data suggests a complicated binding association between PtTMPyP4 and [poly(dA-dT)]$_2$ with similar properties to those reported for the H_2TMPyP4-[poly(dA-dT)]$_2$ system. This includes the lack of a defined end-point in spectrophotometric titrations[186], and the change in the CD spectra with binding ratio. According to experiments from Kim and co-workers on H_2TMPyP4-[poly(dA-dT)]$_2$, the positive CD signal corresponds to minor-groove binding, while the bisignate signal is an exciton band arising from porphyrin self-stacking in the major groove[187].

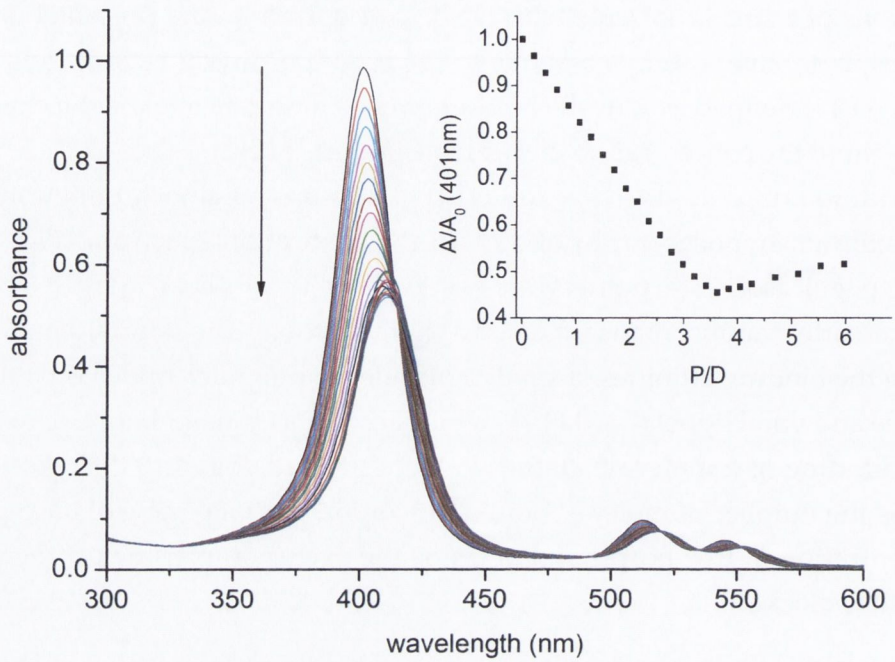

Figure 8.7: Absorption spectra of 5.7 μM PtTMPyP4 in increasing concentrations of [poly(dA-dT)]$_2$. Inset: change in absorbance of PtTMPyP4 as function of [poly(dA-dT)]$_2$ concentration

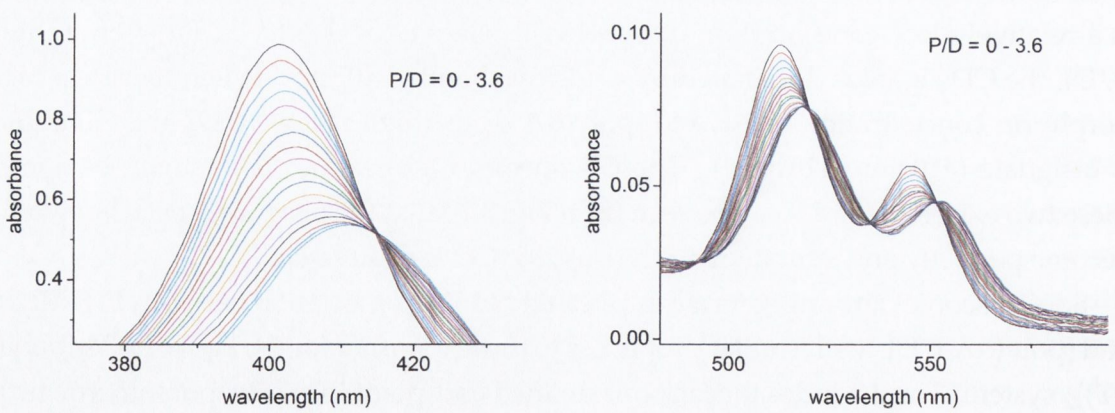

Figure 8.8: Isosbestic points in UV/vis spectra of PtTMPyP4 in increasing [poly(dA-dT)]$_2$ concentrations up to P/D=3.6 at LEFT: Soret band RIGHT: Q-band. 0.5 cm path-length

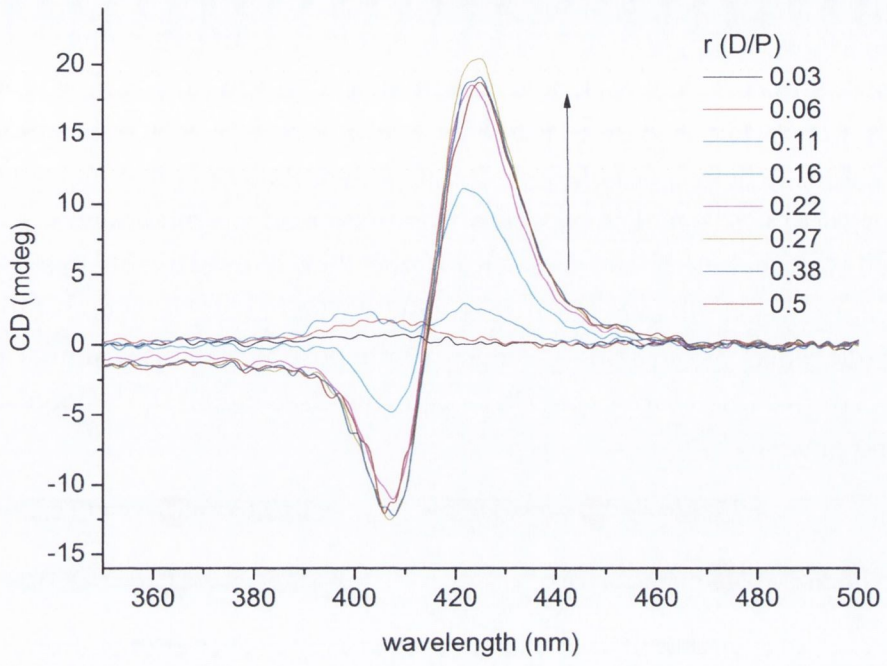

Figure 8.9: Induced CD spectra of 70 μM [poly(dA-dT)]$_2$ with increasing concentrations of PtTMPyP4 in 50 mM Na-phosphate buffer pH 7. 0.5 cm pathlength

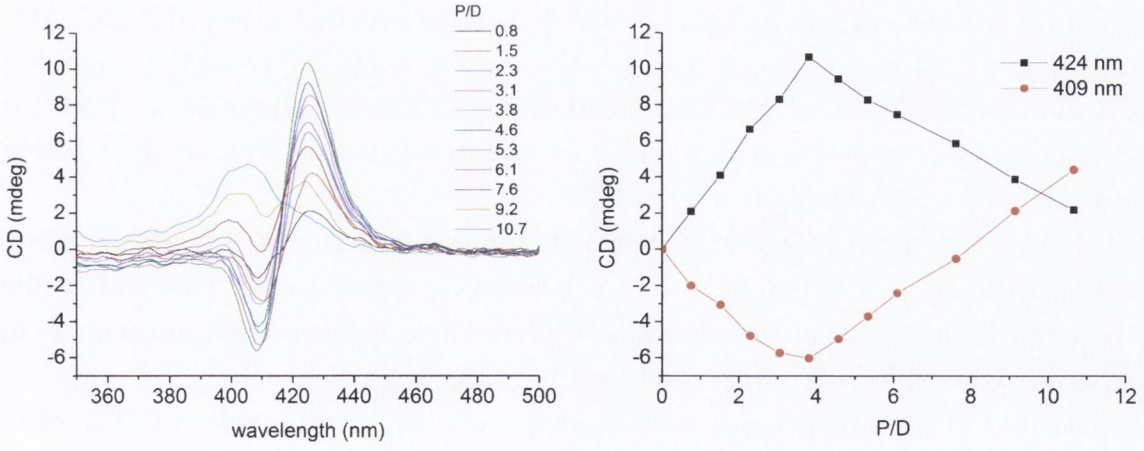

Figure 8.10: LEFT: Induced CD of 6 μM PtTMPyP4 in the presence of increasing concentrations of [poly(dA-dT)]$_2$ in 50 mM Na-phosphate buffer. RIGHT: Dependence of CD spectral extrema on [poly(dA-dT)]$_2$ concentration. 0.5 cm pathlength

Based on these assignments, binding of PtTMPyP4 to [poly(dA-dT)]$_2$ can be interpreted as follows: At low binding ratios PtTMPyP4 binds in the minor groove (and possibly also the major groove). As r increases the PtTMPyP4 molecules are forced to stack in the major groove. Conversely, when the [poly(dA-dT)]$_2$ is added to the PtTMPyP4, the porphyrins are conceivably occupying both sites, but as more sites become available the bound population relaxes preferentially to the minor groove.

The excitonic CD signal is expected to be reversed in 'moderately' stacked porphyrins[204]. However we do not see such a signal, though presumably this signal would be significantly weaker than in the 'extensively' stacked case. The shape of the excitonic signal should reflect the stacking geometry of the porphyrin, and is similar in shape to the CD spectra recorded for porphyrin J-aggregates (see Fig.8.11)[271], suggesting an offset stacking pattern.

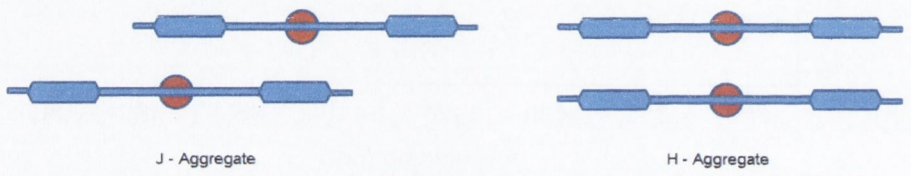

Figure 8.11: Common porphyrin J- and H- stacking patterns

8.2.2 [poly(dG-dC)]$_2$

Addition of [poly(dG-dC)]$_2$ to PtTMPyP4 causes a bathochromic shift and hypochromism (Fig. 8.12 on the facing page) which is more exaggerated than that observed in [poly(dA-dT)]$_2$ (Fig. 8.7, page 130). An association constant was calculated using the neighbour exclusion model (Eq. 8.6, Fig. 8.13 on the next page). The K value of 3.6 x 10^6 M^{-1} is commensurate with previous measurements on H_2TMPyP4-[poly(dG-dC)]$_2$[272] taking into account the ionic strength of the solutions.

Induced CD spectra (Fig. 8.14, page 134) shows a weak negative induced band, characteristic of intercalation between GC base-pairs, with a notable blue shift in the CD band with increased porphyrin concentration. There are also significant changes in the region where [poly(dG-dC)]$_2$ itself absorbs (<300 nm).

The shift in the CD spectrum with binding ratio was unexpected, as CD is selective only for the bound species. This shift is not present in the preceding literature on H_2TMPyP4-[poly(dG-dC)]$_2$[204], though it is shown in the titration of H_2TMPyP4 with [d(GCACGTGC)]$_2$[198]. Although it is not discussed in the latter paper, one possibility is that this shift is associated with a structural change in the GC polymer, and subsequent alteration of GC site environment.

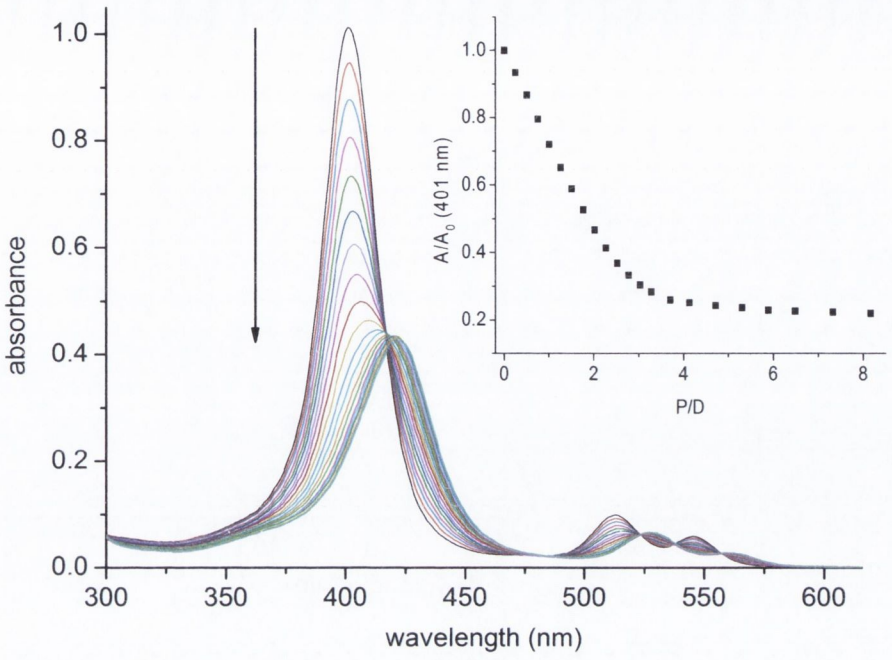

Figure 8.12: Absorption spectra of 5.8 μM PtTMPyP4 in increasing concentrations of [poly(dG-dC)]$_2$ in 50 mM Na-phosphate buffer. Inset: change in absorbance of PtTMPyP4 as function of [poly(dG-dC)]$_2$ concentration

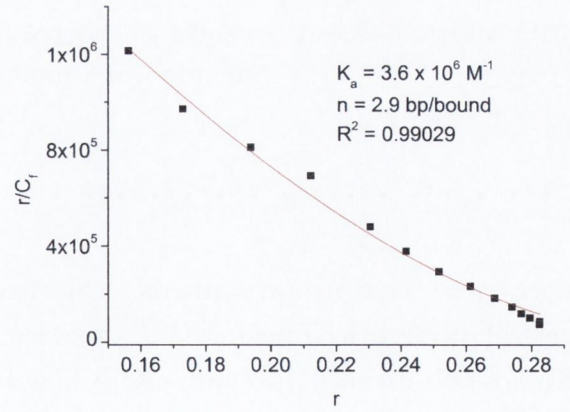

Figure 8.13: Binding plot for 5.8 μM PtTMPyP4 in increasing concentrations of [poly(dG-dC)]$_2$ by the McGhee-von-Hippel method

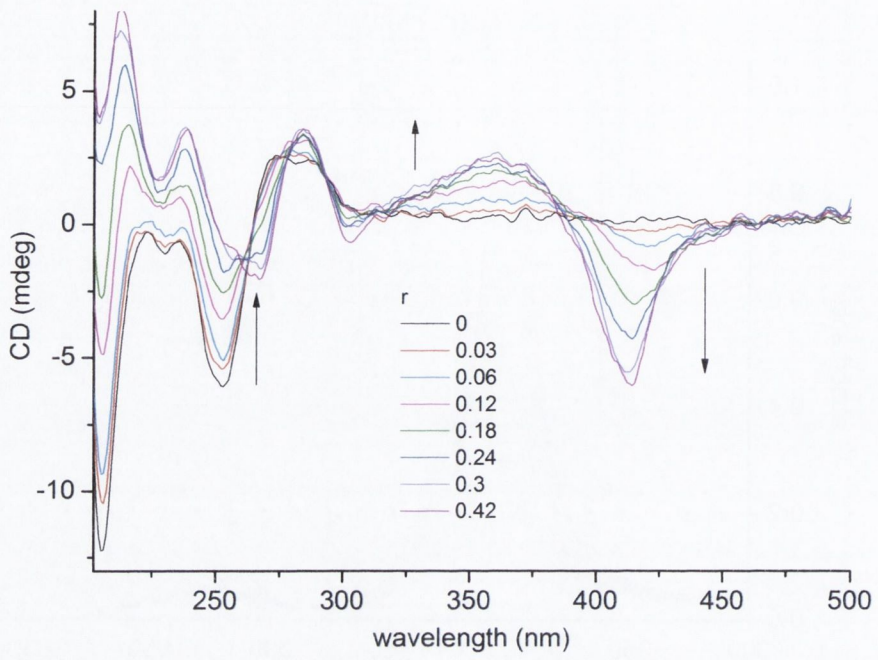

Figure 8.14: CD spectrum of 61 μM [poly(dG-dC)]$_2$ in the presence of increasing PtTMPyP4 concentrations in 50 mM Na-phosphate buffer. 0.5 cm pathlength

This type of theory has some precedence in the literature, with the unwinding of the GC helix proposed as an explanation for the emission properties of CuTMPyP4 in DNA[196]. In the particular case of a metalloporphyrin, further impediment may be presented by the large metal atom if the planarity of the porphyrin is compromised. The change in the CD spectrum of [poly(dG-dC)]$_2$ suggests this may be the case, and the shift in the ICD spectra may thus represent a transition from mainly partial/threading intercalation to a full intercalation.

8.2.3 DNA

Native DNA is a heterogeneous structure and contains a variety of binding sites. The effect of DNA on the spectral properties (shifts in the UV spectra and negative ICD) of PtTMPyP4 are similar to those observed in [poly(dG-dC)]$_2$ (Figs. 8.15 and 8.16 on the facing page). There are significant changes in the UV spectrum, and negative ICD in the Soret region. Thermal denaturation also shows stabilisation of the double-stranded helix by PtTMPyP4, a characteristic feature of intercalation (Fig. A.6 on page 212). There is very little evidence for groove-binding. This is not surprising as most planar TMPy prefer to intercalate into double-stranded natural DNA.

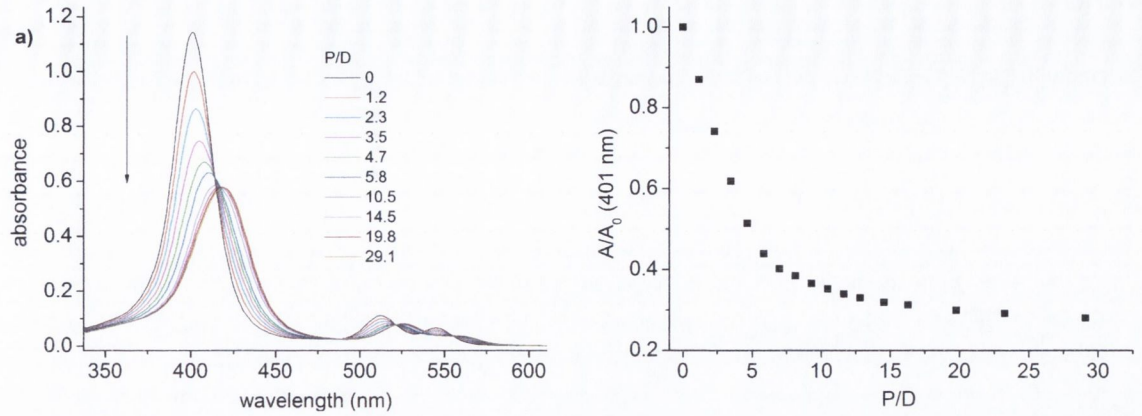

Figure 8.15: UV/vis spectra of 6.4 μM PtTMPyP4 in the presence of increasing concentrations of ds-DNA. In 50 mM Na-phosphate buffer pH 7

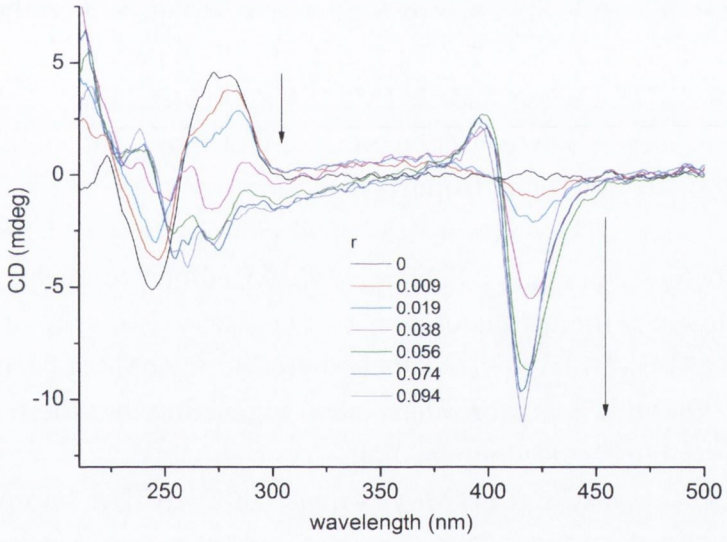

Figure 8.16: CD spectrum of 212 μM DNA (in phosphates) in the presence of increasing PtTMPyP4 concentrations. In 50 mM Na-phosphate buffer pH 7. 0.5 cm pathlength

8.2.4 Poly(rA) and Poly(rG)

The changes in the UV spectra indicate that PtTMPyP4 binds to both polymers (Fig. 8.17 on the following page). The poly(rA) data could not be fit to the neighbour exclusion model, though fits were obtained with poly(rG) with K$\sim 10^6$ M^{-1} (see Fig. A.5 on page 211)

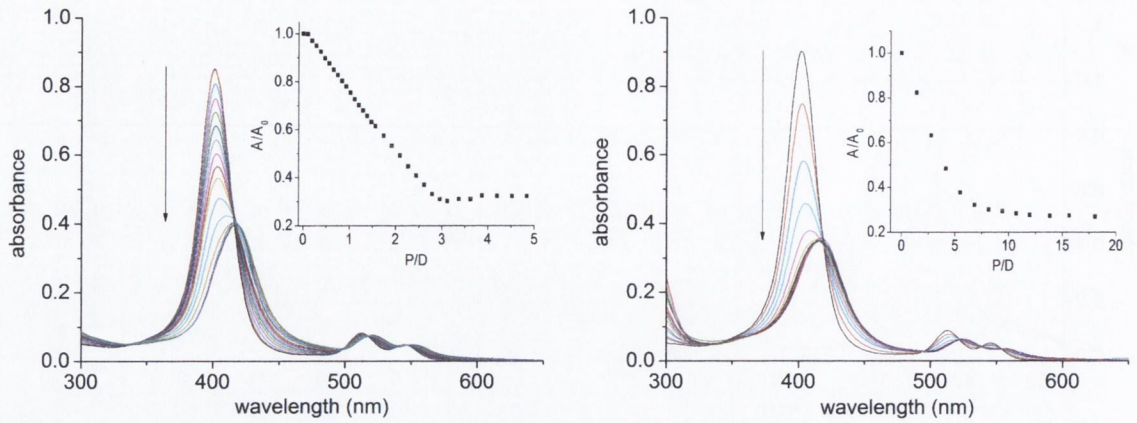

Figure 8.17: UV/vis titrations of PtTMPyP4 with LEFT: poly(rA) and RIGHT: poly(rG) in 50 mM Na-phosphate buffer pH 7. Inset shows change in Soret band absorption (401 nm) with increasing RNA concentration

Binding to poly(rA) results in a positive induced CD (Fig. 8.18 on the facing page), and a suppression of the poly(rA) CD (Fig. 8.19 on the next page).

A weak negative ICD is present for PtTMPyP4 in poly(rG) (Fig. 8.20 on page 138), suggesting an intercalation between G bases. The CD showed a shoulder at 295 nm, indicative of the four-stranded quadruplex structure.

The positive induced CD signal for the PtTMPyP4-poly(rA) systems was perplexing, as PtTMPyP4 shows a negative ICD in poly(dA), similar to the band observed in native DNA[216]. However there are substantial differences in ICD spectra for H_2TMPyP4, ZnTMPyP4 and CuTMPyP4 in poly(rA) and poly(dA)[273]. ZnTMPyP4 appears to bind to poly(rA) even though it is a poor intercalator, suggesting that there are alternative binding modes available besides intercalation.

The positive CD suggests that PtTMPyP4 does not intercalate into poly(rA) and is not oriented parallel to the A base. This may arise due to the short axial rise of poly(rA) which prevents intercalation. Instead the porphyrin may stack along the phosphate backbone. The loss of poly(rA) CD signal also suggests that PtTMPyP4 has a large effect on the structure of the polymer, and the possibility of extensive stacking interactions is suggested by the fact that PtTMPyP4-poly(rA) precipitated out of solution when left overnight.

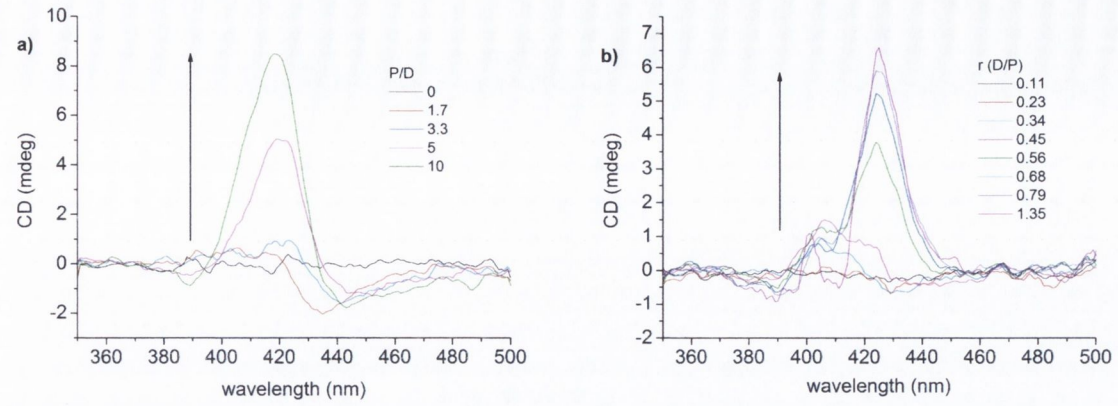

Figure 8.18: Induced CD spectra of (a) 6 μM PtTMPyP4 with increasing [poly(rA)] (b) 36 μM poly(rA) with increasing [PtTMPyP4]. Both in 50 mM Na-phosphate buffer. 0.5 cm pathlength

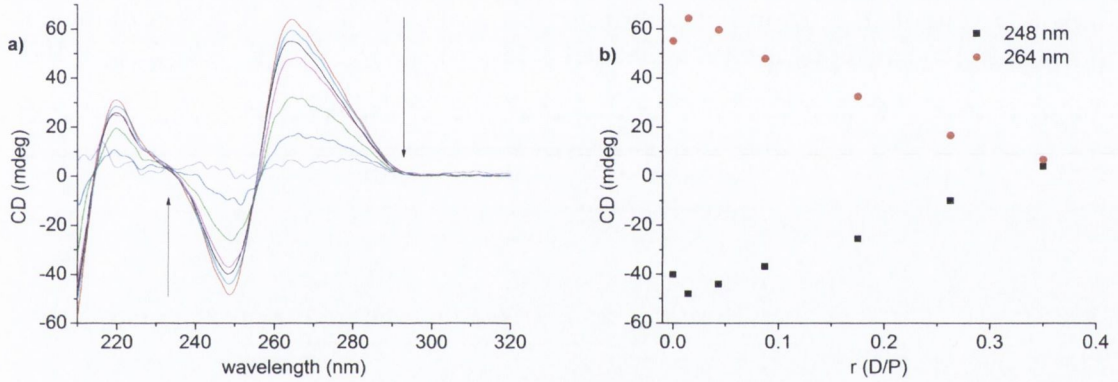

Figure 8.19: (a) CD spectra of 179 μM poly(rA) in presence of increasing [PtTMPyP4] (b) Change in CD max/min as function of binding ratio. 0.5 cm pathlength

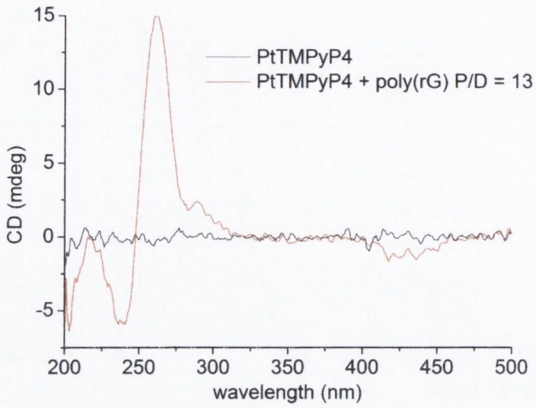

Figure 8.20: CD spectrum of 5.8 μM PtTMPyP4 in presence of poly(rG) in 50 mM Na-phosphate buffer pH 7. 0.5 cm pathlength

Table 8.2: Calculated ground-state binding parameters for PtTMPyP4-polynucleotide complexes in 50 mM phosphate buffer pH 7. H = $(A_{free\,max} - A_{bound})/A_{free\,max} \times 100$

	$\Delta\lambda$ (nm)	H(%)
$[poly(dA\text{-}dT)]_2$	10	45
$[poly(dG\text{-}dC)]_2$	21	54
ds-DNA	18	54
poly(rA)	15	54
poly(rG)	16	60

8.3 G-tetrad/G-quadruplex systems

8.3.1 Stacked GMP

Formation of G-tetrads was promoted by using high [GMP] (500 mM) with high buffer concentrations (500 mM). The mixtures were gently heated until a clear solution was formed and then cooled to room temperature. Formation of the G-tetrad was confirmed by CD and FTIR spectroscopy (Fig. 8.21 on the next page). The UV/vis spectrum of PtTMPyP4 shows a red shift of 20 nm, similar to those observed in an intercalation environment (e.g. $[poly(dG\text{-}dC)]_2$).

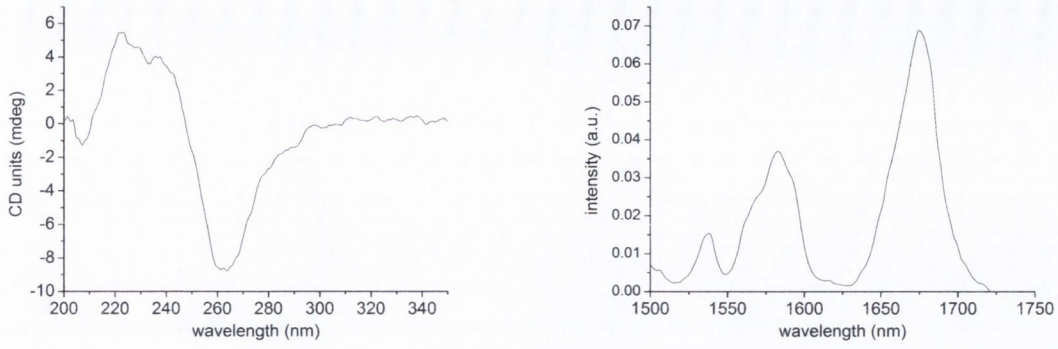

Figure 8.21: LEFT: CD and RIGHT: FTIR spectra of 540 mM GMP in 500 mM Na-phosphate buffer

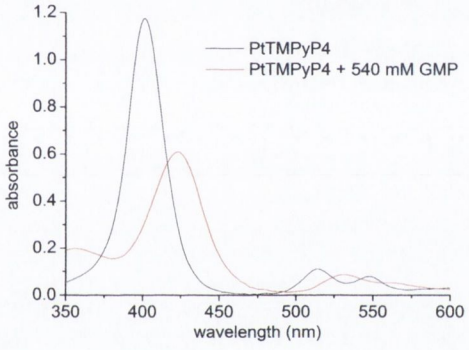

Figure 8.22: UV/vis spectrum of PtTMPyP4 in presence of 540 mM GMP in 500 mM Na-phosphate buffer

8.3.2 $[d(TGGGGT)]_4$

Solution studies on the $[d(TGGGGT)]_4$ systems were recorded using UV/vis and CD spectroscopy. Prior to measurements the d[TGGGGT] was annealed in the presence of 10 mM phosphate buffer and 100 mM NaCl (or KCl) salt up to a temperature of 65°C, and let cool slowly to room temperature in order to facilitate formation of the intermolecular parallel-stranded $[d(TGGGGT)]_4$ quadruplex.

UV titrations with PtTMPyP4 showed that saturation was achieved with a 1:1 ratio. With ZnTMPyP4, a larger ratio of $[d(TGGGGT)]_4$ is required for complete binding. CD confirms the formation of the quadruplex[237], but this signal (200-300 nm) is suppressed in the presence of PtTMPyP4 while it is mainly unaffected by ZnTMPyP4. We found little difference in the results when Na^+ was substituted with K^+.

Attempts were made to crystallise a $[d(TGGGGT)]_4$-porphyrin complex in the University of Reading. Crystallisations were performed by the sitting-drop method in the

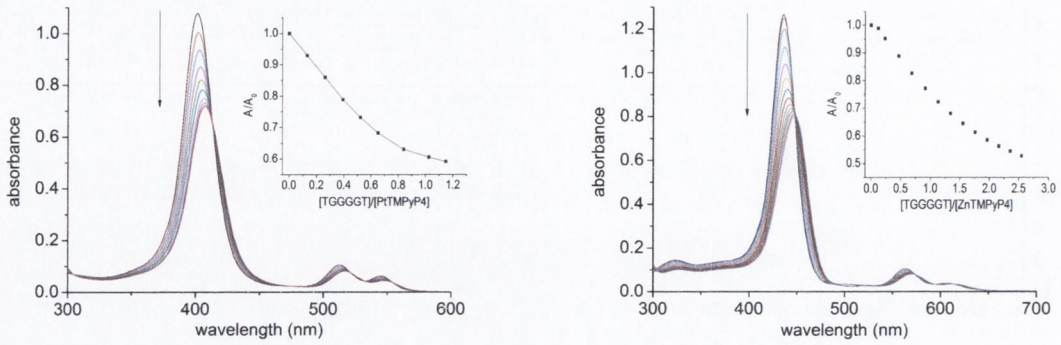

Figure 8.23: UV spectra of LEFT: PtTMPyP4-$[d(TGGGGT)]_4$ and RIGHT: ZnTMPyP4 in the presence of $[d(TGGGGT)]_4$ in 10 mM Na-phosphate buffer and 100 mM NaCl

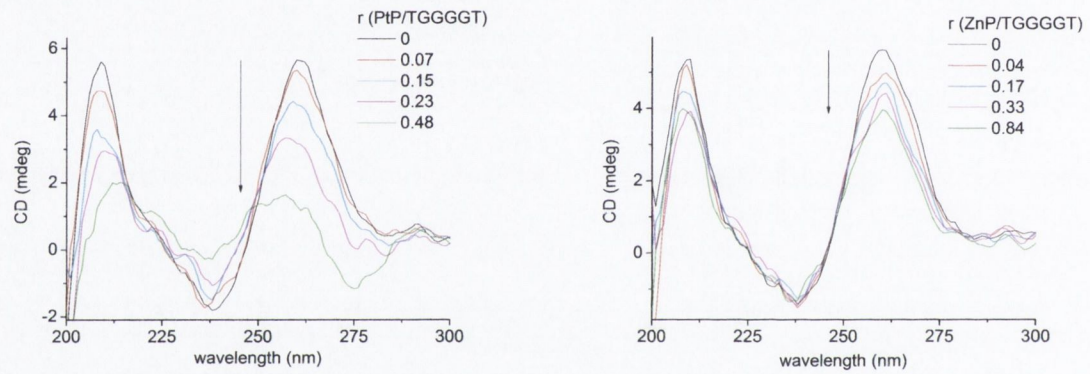

Figure 8.24: CD spectra of 14 μM (strand conc.) $[d(TGGGGT)]_4$ in the presence of LEFT: PtTMPyP4 and RIGHT: ZnTMPyP4 in 10 mM Na-phosphate buffer and 100 mM NaCl. 0.5 cm pathlength

presence of a metal salt, cacodylate buffer, and a polyamine. Initial crystallisation trials were performed on PtTMPyP4-$[d(TGGGGT)]_4$ using a Hampton Scientific mini-screen set, in order to eliminate the conditions in which crystallisation could not occur (ie where precipitation occured). It was noted that clear solutions were obtained with NaCl and KCl, and 4:1 KCl:$BaCl_2$ as the salts. Precipitation occurred with every solution containing cobalt hexamine as the polyamine, and pH 6.0 Na cacodylate as buffer, so these conditions were eliminated from future trays.

A number of test trays were then set up with PtTMPyP4 and ZnTMPyP4 with $[d(TGGGGT)]_4$. Variables included porphyrin concentration and the presence and concentration of mono- and divalent cations, including KCl, NaCl, $CaCl_2$, $BaCl_2$ and $SrCl_2$. Inspection of the test trays under an optical microscope revealed that precipitation was more widespread in the PtTMPyP4 solutions than ZnTMPyP4. After two weeks crys-

tals appeared to grow in the ZnTMPyP4-$SrCl_2$ trays under the conditions shown in Table 8.3.

Further optimisation trays were then set up with these conditions. The ZnTMPyP4-$SrCl_2$ crystals were mounted on the IO3 beamline at the Diamond synchrotron (Harwell, UK). However, these crystals only gave a featureless powder diffraction signal, and it appeared that the crystals were in fact amorphous or had melted in the X-Ray beam.

8.3.3 Discussion on G-Quadruplexes

Strong spectral shifts and induced CD suggest that PtTMPyP4 is stacked onto the G-tetrad formed from high GMP concentrations, though it is not clear whether a G-tetrad is stacked on both faces of the porphyrin. The more modest changes in $[d(TGGGGT)]_4$ suggest that PtTMPyP4 does not intercalate between tetrads in the four-stranded structure, consistent with current theory[249,253]. It may be end-binding, as H_2TMPyP4 is believed to do[249,274]. However, the loss of CD signal leads us to speculate that PtTMPyP4 may disrupt the quadruplex, and intercalate between GG steps in d(TGGGGT) single strands.

By contrast, ZnTMPyP4 is 5-coordinate so has less affinity for the single-stranded form, so may better stabilise the 4-stranded form. There are no reports of TMPy porphrins disrupting the quadruplex, though the four-stranded intermolecular structure would be entropically more unstable to dissociation than the intramolecular quadruplexes, and may have a greater tendency to dissociate if the strand concentration is low[275]. Incidentally, PtTMPyP4 has been reported to be a less efficient telomerase inhibitor than ZnTMPyP4[241]. Our results, although perfomed with a different DNA sequence, corroborate this.

A crystal structure was not obtained for a porphyrin-$[d(TGGGGT)]_4$ compound, although it can often take a long time for crystals to grow - during the session at Dia-

Table 8.3: Crystallisation conditions for ZnTMPyP4-$d[TG_4T]_4$ complex

stock conc.	species	drop conc.
12 mM	spermine	2.4 mM
5%	MPD	1%
40 mM	Na-cacodylate	8 mM
80 mM	$SrCl_2$	16 mM
2.1 mM	TGGGGT	0.21 mM
0.5 mM	ZnTMPyP4	0.05 mM

mond, five-year old crystals of acridine-[d(TGGGGT)]$_4$ complexes (Dr. Yu Gan) were found to give excellent diffraction signals. Our trials disproved the theory[276] that divalent ions necessarily cause precipitation. Our observation that PtTMPyP4 solutions precipitated more readily than ZnTMPyP4 suggests that there may have been some aggregation of the porphyrin. Although solution studies found little evidence for aggregation, the crystallisations were performed at significantly higher porphyin concentrations. PtTMPyP4 may be more readily forced to aggregate than ZnTMPyP4, due to its planar structure, and the known tendency for Pt(II) in general to dimerise[277].

8.4 Conclusions

PtTMPyP4 is shown to form a 1:1 stacked complex with AMP and GMP in the ground-state. 1:2 complex formation is believed to be possible but could not be confirmed from binding studies. Intercalation is favoured in GC polymers and in DNA, while a mixed stacking and groove-binding mode occurs in the presence of AT-DNA. These binding modes are similar to those observed with free base H_2TMPyP4. Binding with poly(rA) gave unexpected results, with the suggestion that the porphyrin does not stack parallel to the adenine bases. PtTMPyP4 stacks onto G-tetrad, but binds differently to [d(TGGGGT)]$_4$. A comparison with ZnTMPyP4 shows the effect of an axial ligand on quadruplex-binding properties.

Chapter 9

Emission Studies

The phosphorescence properties of PtTMPyP4 are studied in the presence of halides, dissolved oxygen, mononucleotides and polynucleotides, using steady-state and time-resolved emission spectroscopy. The data is correlated with ground-state data to explain the effect of binding on the excited triplet state, and on the photosensitising ability of PtTMPyP4. Excitation of all samples was performed in conditions of optical dilution ($A \leq 0.1$). For steady-state emission titrations the excitation wavelengths were typically chosen as the isosbestic points in the Q band region.

9.1 PtTMPyP4 and Halide Ions

Chloride ions are ubiquitous in biological solutions and commonly used in saline buffers for spectroscopic measurements. However they are known to quench the emission of PtTMPyP4[165,174], so their effect on the triplet state needs to be characterised before studying the interactions of PtTPMyP4 with nucleic acids.

The presence of 50 mM phosphate buffer alone has no effect on the absorption or emission of PtTMPyP4 (data not shown). The effect of halide ions (Cl^- and Br^-) was monitored using steady-state fluorimetry and single-photon counting (SPC). Titration of NaCl or NaBr into PtTMPyP4 results in quenching of emission intensity and lifetime (Fig. 9.1, page 145), but has no significant effects on the absorption spectra. The shape of the emission spectra is unchanged, and the lifetimes fit to monoexponential kinetics.

The steady-state and time-resolved data were fitted to the Stern-Volmer equations for pure dynamic quenching (Eqs 9.1 and 9.2 respectively), where k_q is the bimolecular rate constant for dynamic quenching, and τ_0 is the emission lifetime in the absence of quencher. The quantity Φ_0/Φ (also expressed as I_0/I) was determined by the ratio of integrated steady-state emission intensities for the unquenched and quenched porphyrin, respectively. Absolute values for Φ were not recorded.

$$\frac{\Phi_0}{\Phi} = 1 + k_q \tau_0 [X^-] \tag{9.1}$$

$$\frac{1}{\tau} = \frac{1}{\tau_0} + k_q [X^-] \tag{9.2}$$

Over the quenching range studied (up to $I_0/I \approx 10$), the Br^- plots are linear while those of Cl^- show downward curvature. Curvature is probably due to the increase in solution ionic strength as the [Cl^-] increases, resulting in decreased electrostatic attraction between fluorophore and quencher. Linear fitting was hence performed on the NaCl solution up to only 10 mM added salt (Fig. 9.2 on the facing page). With either halide, the Stern-Volmer fits yield identical k_q values for both steady-state and time-resolved measurements (see Table 9.1).

The lifetime and quantum yield are related by Eq. 9.3, and it follows that the rate constant for radiative decay (k_r) and the quantum yield of triplet state formation (Φ_{isc}) are constant. The latter observation confirms that quenching occurs from the triplet and not the singlet state. Stern-Volmer data, and the lack of change in UV/vis spectra, confirm that quenching occurs by a dynamic quenching mechanism. Br^- is therefore a very efficient quencher, as k_q approaches the limit for diffusion controlled quenching (10^9 - 10^{10} $dm^3\,mol^{-1}\,s^{-1}$)[146]. The k_q for Cl^- is an order of magnitude lower, and it should be mentioned that the concentration of Cl^- present as the PtTMPyP4 counterion ($\sim 2 \times 10^{-5}$ M) is too low to affect the emission significantly.

$$\Phi_r = \Phi_{isc} k_r \tau_0 \tag{9.3}$$

The iodide ion was also tested, but resulted in bleaching of the PtTMPyP4 solution followed by a visible aggregation and precipitation of the porphyrin. This is consistent with previous studies and is due to oxidation of I^- to I^{3-} by singlet oxygen generated by the porphyrin triplet state[278]. The large and polarisable I^{3-} then induces aggregation. Thiosulphate can inhibit the tri-iodide formation, but it was found that thiosulphate alone also quenched the PtTMPyP4 triplet state, so the iodide ion was not studied further.

Table 9.1: Quenching constants for Cl^- and Br^- in presence of PtTMPyP4 in 50 mM phosphate buffer pH 7

	NaCl		NaBr	
	lifetime	intensity	lifetime	intensity
k_q ($dm^3\,mol^{-1}\,s^{-1}$)	2.3×10^8	2.4×10^8	1.9×10^9	1.8×10^9
R^2	0.9996	0.9982	0.99869	0.999

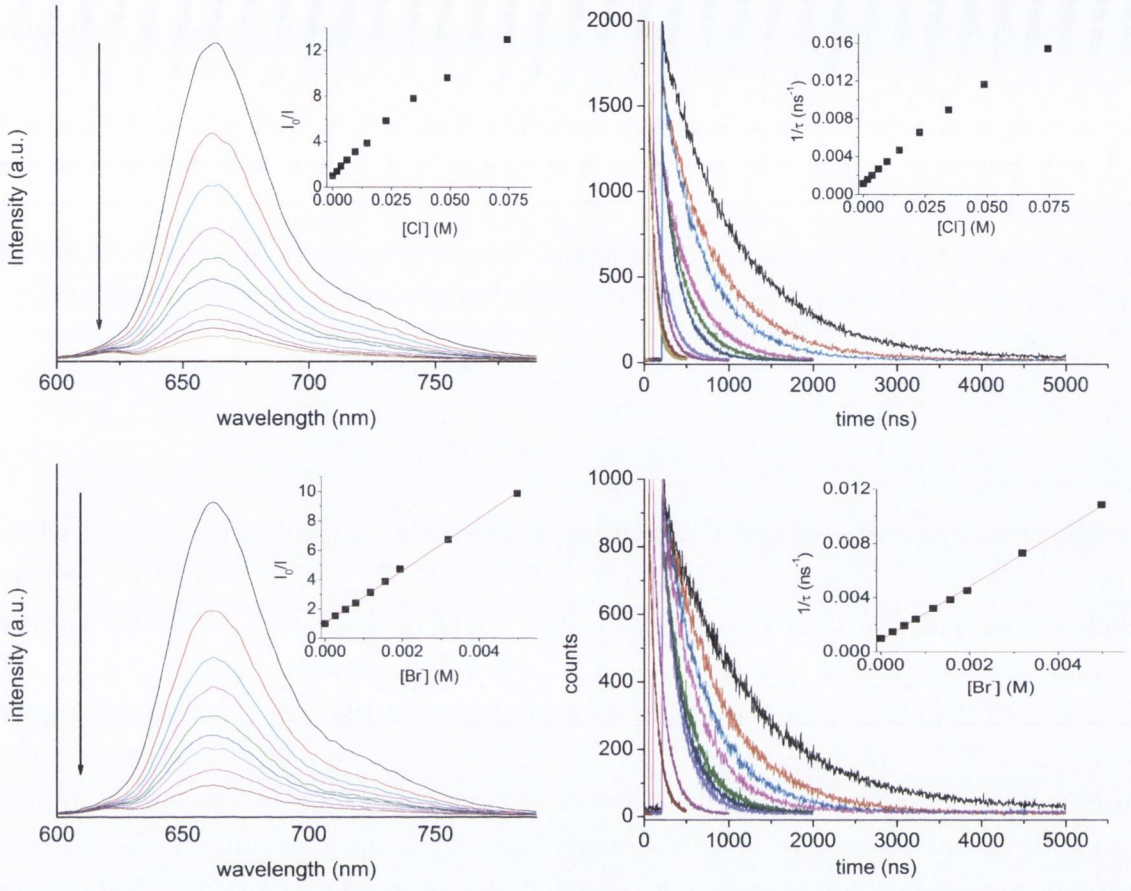

Figure 9.1: Steady-state (λ_{exc}= 513 nm) and time-resolved emission plots (λ_{exc}= 371 nm) for PtTMPyP4 in the presence of TOP: NaCl BOTTOM: NaBr. Inset are corresponding Stern-Volmer plots. Recorded in 50 mM Na-phosphate buffer (pH 7) in aerated solution

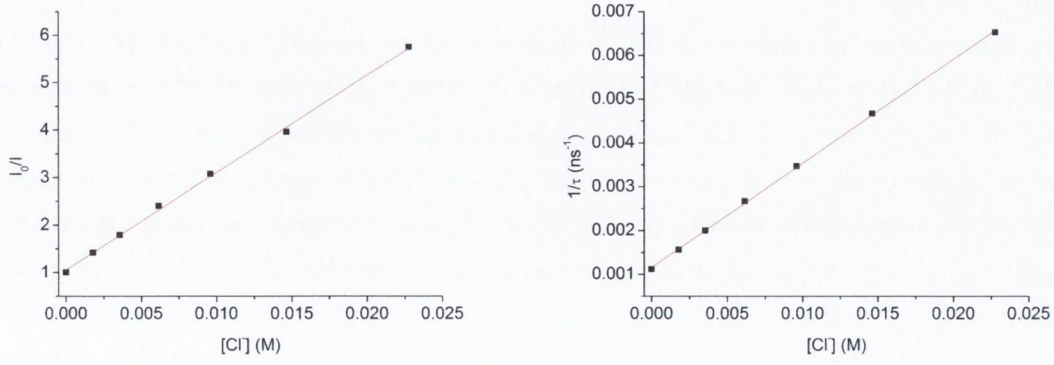

Figure 9.2: Linear Stern-Volmer plots for PtTMPyP4 in the presence of NaCl for LEFT: steady-state data RIGHT: time-resolved data

There are a number of possible mechanisms that could explain the phosphorescence quenching of PtTMPyP4 in the presence of halides. The first theory to address is that it is due to aggregation, as previously proposed by two research groups[165,174]. We have shown that this model is incorrect, by demonstrating that quenching proceeds via a dynamic mechanism, and that there is no self-association between porphyrins in the ground state.

The next to be considered is photoinduced electron transfer from the anionic halide to the cationic porphyrin. The likelihood of PET can be ascertained from the Gibbs free energy (Eq. 10.1).

$$\Delta G^O = F[E^O(X^-/X) - E^0(^3PtP^*/PtP^-)] \tag{9.4}$$

The reduction potential for PtTMPyP4 in its triplet state is quoted as 1.43 V[172], while the oxidation potentials of Cl^-/Cl and Br^-/Br are given as 2.60 V and 1.91 V, respectively (all vs SHE)[279]. Large positive ΔG values (+1.17 V for Cl^-, +0.48 V for Br^-) imply that direct photoinduced electron transfer is thermodynamically unfavourable.

The external heavy-atom effect has been invoked to explain both luminescence enhancement[280,281] and quenching[175,176,282]. The presence of a moderately heavy atom such as Br^- can increase intersystem crossing to the triplet state, but this is not important in Pt(II)TMPyP4 as the triplet is already populated with a very high yield. Instead, it might increase the rate of non-radiative $T_1 \rightarrow S_0$ intersystem crossing. There is already a significant heavy atom effect in this system from the Pt atom, though it has also been proposed that the presence of an internal heavy-atom effect actually enhances the external heavy-atom effect[177]. This process is suggested to involve a charge-transfer complex (exciplex) between fluorophore and quencher[176,177]. These examples show that halide quenching mechanisms are non-trivial, and arise due to an interplay of a number of processes.

The fluorescence quenching of zinc-tetra(4-sulfonatophenyl)porphyrin (ZnTPPS) by Cl^-, Br^- and I^- has been modelled using the Watkins mechanism[283–285]. In this model ion-pair formation occurs, followed by intersystem crossing from S_1 to T_1 and non-radiative decay back to the ground state (S_0). The relative quenching efficiencies of $I^->Br^->Cl^-$ can be attributed to a combination of the lower ionisation potentials, higher spin-orbit coupling constants, and larger ionic radii of the larger halides. This general model may apply to the PtTMPyP4 system also.

The fact that PtTMPyP4 is quenched by Cl^- is related to the relatively long emission lifetime of PtTMPyP4, which makes it susceptible to diffusional quenching. Cl^- can also quench phosphorescence from degassed PdTMPyP4 ($\tau > 100\mu s$)[165], whereas it does not quench the short-lived fluorescence of H_2TMPyP4 (τ c. 5 ns) or ZnTMPyP4

(τ c. 1 ns). It is conceivable that the triplet states of other porphyrins are quenched by Cl^-, although the lack of room temperature phosphorescence in most porphyrins means the triplet state is less readily observed by emission spectroscopy.

By far the most significant observation from these experiments is that the porphyrin is quenched by a physiological buffer salt. This has implications for the photosensitising ability of triplet emitters in physiological conditions, and also shows that care needs to be taken in the choice of 'innocent' buffer salts to use in photophysical measurements.

9.2 PtTMPyP4 and AMP

9.2.1 Deoxygenated Solution

The effects of the addition of AMP to N_2-purged solutions of PtTMPyP4 are shown in Fig. 9.3. There is an increase in phosphorescence intensity, which plateaus at Φ/Φ_0 = 1.5, while the emission λ_{max} also shifts from 668 nm to 675 nm. The maximum emission intensity is reached after the addition of less than 1 mM AMP, and does not increase further with higher AMP concentrations. The triplet lifetime of PtTMPyP4 lengthens from 6.4 μs to 10 μs in 10 mM AMP, where the PtTMPyP4 is expected to be fully bound.

The proportional increase of quantum yield and lifetime implies that Φ_{isc} and k_r are constant (see Eq. 9.3). As the phosphorescence quantum yield in deoxygenated aqueous solution is known (0.02)[165], k_r and k_{nr} can be calculated from Eqs 9.5 and 9.6.

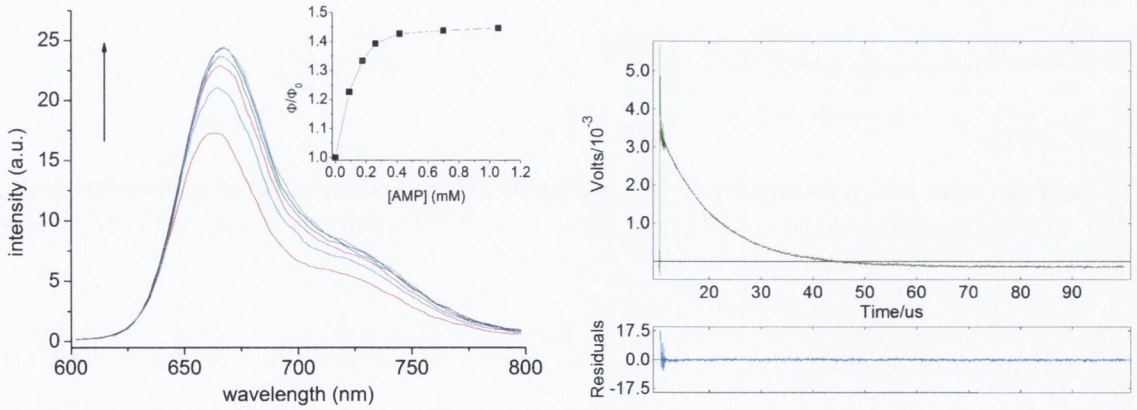

Figure 9.3: LEFT: Emission spectra of 6 μM PtTMPyP4 in deoxygenated solution in presence of increasing [AMP] λ_{exc}= 517 nm. RIGHT: Time-resolved emission decay of 6 μM PtTMPyP4 in 10 mM AMP, with monoexponential fit and residuals λ_{exc}= 355 nm. In 50 mM Na-phosphate buffer pH 7

$$k_r = \frac{\Phi_p \Phi_{isc}}{\tau_p} \tag{9.5}$$

$$k_{nr} = \frac{1 - \Phi_p \Phi_{isc}}{\tau_p} \tag{9.6}$$

The addition of AMP, and subsequent increase in quantum yield and lifetime, therefore correspond to a decrease in k_{nr}. This could be quantified from the kinetic data (Eq. 9.7), yielding an apparent drop in k_{nr} from 1.4 x 10^5 s^{-1} to 9.9 x 10^4 s^{-1}.

$$\tau_{\text{deox}} = \frac{1}{k_{\text{r}} + k_{\text{nr}}} \tag{9.7}$$

9.2.2 Aerated Solution

In aerated solution, the addition of AMP causes a significant increase in phosphorescence intensity, reaching a final value of $\Phi/\Phi_0 = 6$ after approx. 8 mM AMP has been added (Fig. 9.4). Notably, larger AMP concentrations are required to attain the maximum emission intensity than in deoxygenated solution.

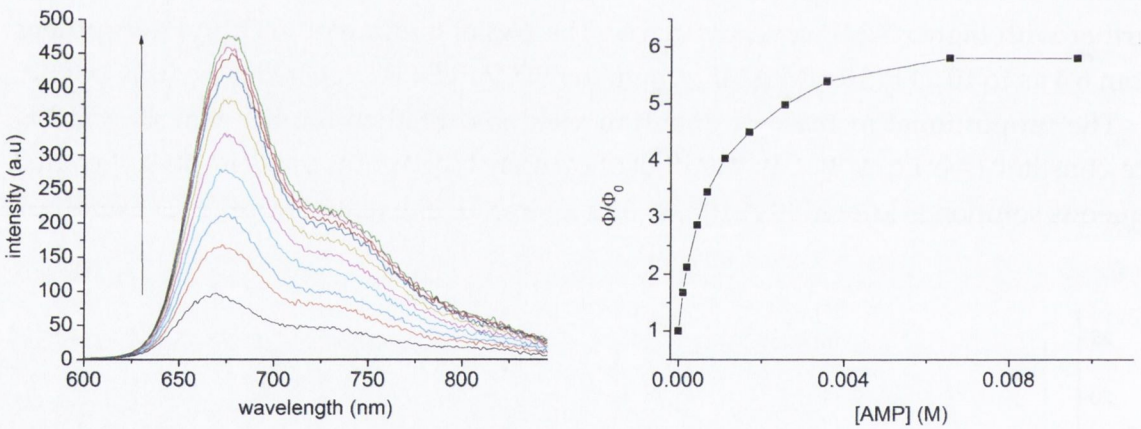

Figure 9.4: LEFT: Steady-state emission of PtTMPyP4-AMP complexes in aerated solution. LEFT: Dependence of emission intensity on AMP concentration. [PtTMPyP4] = 6 μM in 50 mM phosphate buffer pH 7. λ_{exc}= 517 nm

The phosphorescence lifetime increases from 1 μs for free PtTMPyP4 to 6 μs for PtTMPyP4 in 10 mM AMP. This is in direct proportion to the changes seen by steady-state measurements. In aerated solution, the change in photophysical parameters accounts for both non-radiative decay (k_{nr}) and quenching by molecular oxygen (Eq. 9.8).

$$\tau_{aer} = \frac{1}{k_r + k_{nr} + k_q[O_2]} \tag{9.8}$$

With knowledge of k_{nr} (Eq. 9.7), k_q (quenching constant for free PtTMPyP4) and k'_q (quenching constant for PtTMPyP4-AMP complex) can be calculated from Eqs 9.9 and 9.10, respectively.

$$k_q[O_2] = \frac{1}{\tau_{P,aer.}} - \frac{1}{\tau_{P,deox.}} \tag{9.9}$$

$$k'_q[O_2] = \frac{1}{\tau_{PA,aer.}} - \frac{1}{\tau_{PA,deox.}} \tag{9.10}$$

The concentration of dissolved oxygen for an air-equilibrated solution was taken to be 2.9×10^{-4} M at 20°C[286], yielding an apparent reduction in k_q from 3×10^9 dm^3 mol^{-1} s^{-1} for free PtTMPyP4 to 2.9×10^8 dm^3 mol^{-1} s^{-1} in the π-stacked complex.

Lifetime titrations were subsequently performed for PtTMPyP4 with various AMP concentrations. Both time-resolved emission and SPC were used. At [AMP] $<\sim 0.5$ mM, the kinetics fit better to a biexponential rather than a monoexponential model (Table 9.2 on the following page). The first component is a constant component of 770 ± 80 ns, which decreases in contribution as more AMP is added. The second component increases in both its value and contribution. An average lifetime was calculated from the relative amplitudes and shown to be proportional to the phosphorescence quantum yield (Fig. 9.5).

At concentrations greater than ~0.5 mM (where >50% of the PtTMPyP4 molecules are expected to be bound in the ground state) the decays could be adequately fitted to monoexponential kinetics, whether recorded by time-resolved emission or SPC (see Fig. 9.6 and Table 9.3 on the next page).

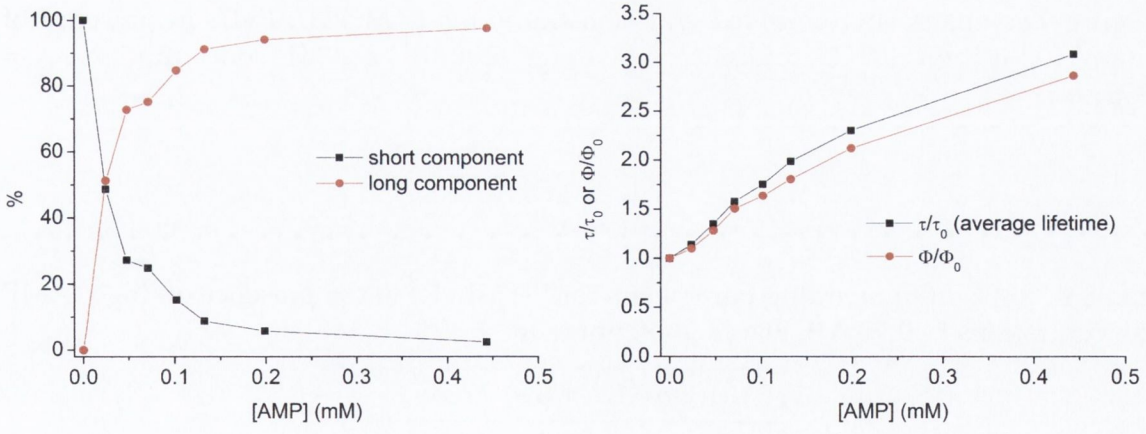

Figure 9.5: Photophysical data for 6 μM PtTMPyP4 in presence of low AMP(<0.5 mM) showing LEFT: dependence of % contribution for lifetime components on the AMP concentration RIGHT: comparison of average emission lifetime with steady-state emission. In 50 mM phosphate buffer pH 7

Table 9.2: SPC lifetime fitting parameters for PtTMPyP4 in presence of 'low' AMP concentrations (> 0.5 mM). Errors in lifetimes are ± 10%

AMP (mM)	τ_1 (ns)	% (Aτ)	τ_2 (ns)	%	χ^2	τ_{ave} (ns)	τ/τ_0	Φ/Φ_0
0	1000	100	-	0	-	1000	1	1
0.024	840	49	1420	51	1.086	1140	1.14	1.10
0.048	770	27	1570	73	1.08	1350	1.35	1.28
0.071	850	25	1820	75	1.075	1580	1.58	1.51
0.10	780	15	1930	85	1.07	1750	1.75	1.64
0.13	690	9	2110	91	1.01	1990	1.99	1.81
0.20	710	6	2400	94	0.975	2300	2.30	2.12
0.44	750	2	3140	98	0.991	3080	3.08	2.87

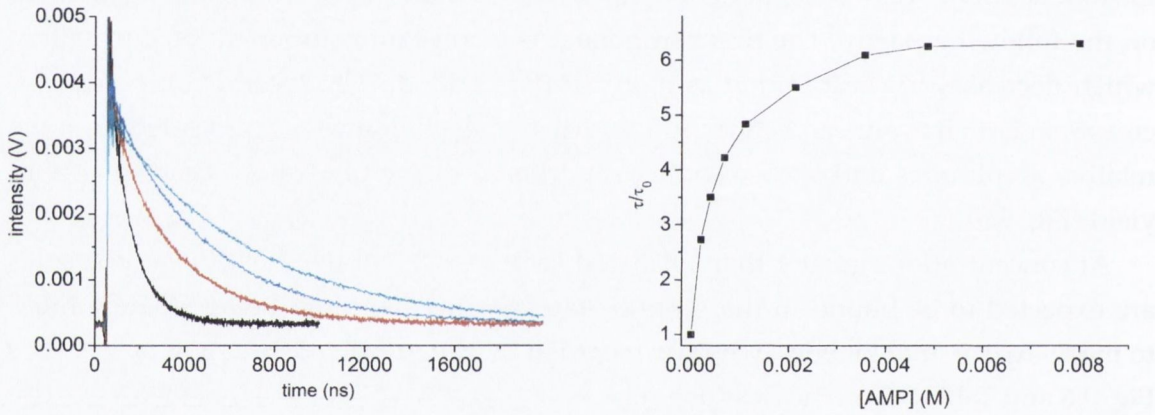

Figure 9.6: LEFT: Time-resolved emission traces for 6 μM PtTMPyP4 in presence of 'high' [AMP]. RIGHT: Dependence of average lifetime on AMP concentration λ_{exc}= 355 nm

Table 9.3: SPC lifetime fitting parameters for PtTMPyP4 in the presence of 'high' AMP concentrations (> 0.5 mM). Errors in lifetimes are ± 10%

[AMP](mM)	τ (ns)	red. χ^2
0.68	3620	0.945
1.1	4180	1.035
1.7	4770	0.972
2.6	5560	1.064
3.6	5720	1.111
4.0	6200	0.966

9.2.3 Association Constants

The results from the phosphorescence titrations were analysed in an effort to find values for K_g (ground-state association constant) and K_e (excited-state association constant).

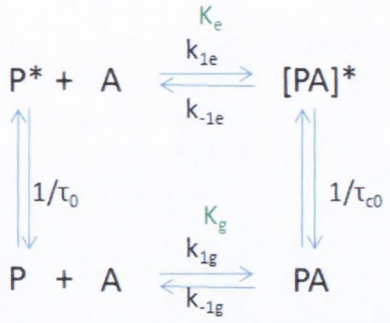

Figure 9.7: Scheme showing 1:1 ground- and excited-state association for PtTMPyP4-AMP system

The analysis was performed using Eq. 9.11 and Eq. 9.12[287]. As shown in Fig. 9.7, k_{xx} denotes the relevant rate constant for association and dissociation. Φ_0,τ_0 and Φ_{c0},τ_{c0} are the photophysical parameters for free and bound porphyrin, respectively.

$$\frac{\frac{\Phi}{\Phi_0} - 1}{[AMP]} = -\frac{\epsilon_c}{\epsilon} K_g \frac{\Phi}{\Phi_0} + \frac{\epsilon_c}{\epsilon} K_g \frac{\Phi_c 0}{\Phi_0} \tag{9.11}$$

when $k_{-1e}\tau_{c0}, k_{1e}\tau_0[Q] \ll 1$

$$\frac{\frac{\Phi}{\Phi_0} - 1}{[AMP]} = -\frac{\tau_0}{\tau_{c0}} K_e \frac{\Phi}{\Phi_0} + \frac{\tau_0}{\tau_{c0}} K_e \frac{\Phi_c 0}{\Phi_0} \tag{9.12}$$

when $k_{-1e}\tau_{c0}, k_{1e}\tau_0[Q] \gg 1$

A consequence of fitting to these equations is that the fitted slope can represent either K_g or K_e, depending on the excited-state lifetimes. For the deoxygenated solution, if τ_0 = 6.4 μs, and k_{fe} = 2 x 10^9 $dm^3\,mol^{-1}\,s^{-1}$ [179] then $k_{fe}\tau_0[Q]$ will be > 1 when [AMP] > ~80 μM. In aerated solution, the threshold is [AMP] > 0.5 mM. This implies that excited-state binding may be monitored using the phosphorescence data.

Titrations on the deoxygenated solutions were repeated a number of times. Reproducibility in the binding plots was poor despite good linearity in the fitting (Fig. 9.8 on the following page). This may be related to the small number of data points plotted, or difficulties in deoxygenating the solution. Significantly larger binding constants (approx. 30,000 M^{-1}) were recorded from these data than from spectrophotometry, sug-

gesting that this is an excited-state value (K_e). There was also curvature when an extended [AMP] range was plotted, an indicator of excited-state binding[287].

In aerated solution a value of approx. $8000\,M^{-1}$ was obtained (Fig. 9.9), which is close to the K_g values ($\sim 6000\,M^{-1}$) calculated by spectrophotometry.

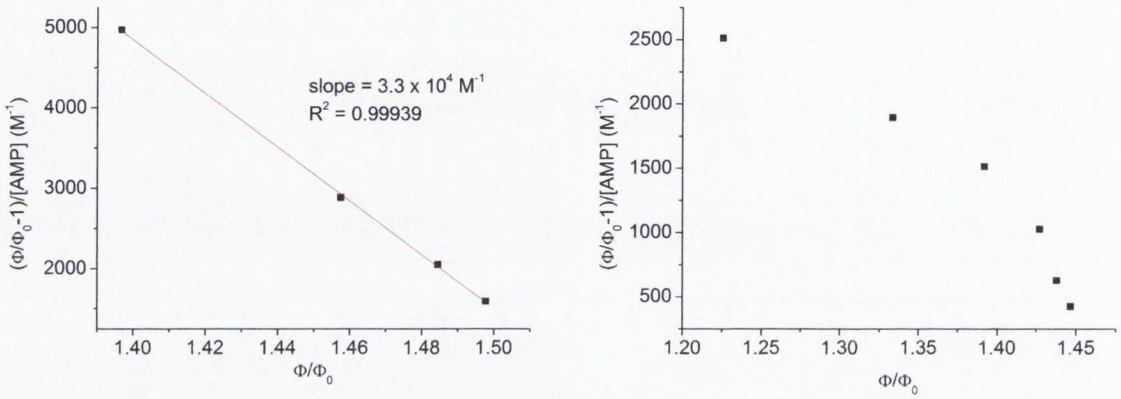

Figure 9.8: Plots of equation 9.12 for binding of AMP to PtTMPyP4 in deoxygenated solution LEFT: linear fit over large AMP concentration ranges RIGHT: plot over large AMP concentration ranges

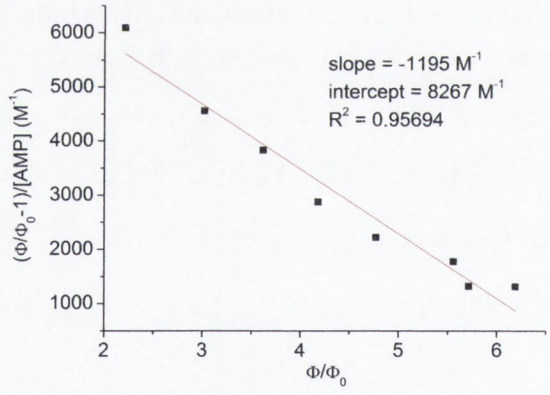

Figure 9.9: Fit to equation 9.11 for binding of AMP to PtTMPyP4 in aerated solution

The apparently large excited-state binding constant was considered with reference to Eq. 9.13, where $\Delta\tilde{\nu}$ is the average of spectral shifts (in cm^{-1}) between absorption and emission maxima of the free and bound porphyrin[287].

$$log_{10}\left(\frac{K_e}{K_g}\right) = \frac{0.65}{T}\Delta\tilde{\nu} \tag{9.13}$$

With $\Delta\tilde{\nu} = 180\,cm^{-1}$ the K_e/K_g ratio is 8. This agrees with the K values calculated above (Fig. 9.8), and stronger association in the excited state than the ground state.

However Eq. 9.13 is derived from fluorescence spectra, and there may be changes in the S_1–T_1 energy gap that need to be accounted for.

9.2.4 Anion Quenching

A small number of anion-quenching experiments were performed on the PtTMPyP4-AMP complex. NaCl was titrated into solutions of fully bound PtTMPyP4 ([AMP] = 10 mM). Quenching of emission fits to Stern-Volmer kinetics with an approximate k_q of 1.5×10^6 $dm^3\,mol^{-1}\,s^{-1}$ (Fig. 9.10). The absorption spectra was unchanged throughout the titration, showing that there was no significant decrease in the concentrations of bound complex concentration as the ionic strength was increased. Stern-Volmer kinetics clearly deviated from linearity due to salt effects. However, the notable result here is that the reduction in k_q for Cl^- (100-fold) in the complex is an order of magnitude larger than the reduction in k_q for O_2 (10-fold). This has implications for the mechanism of quenching of the halide ion relative to that of oxygen.

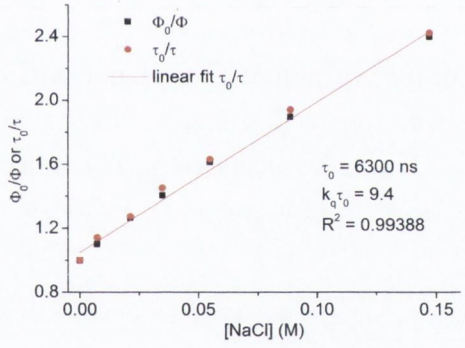

Figure 9.10: Stern-Volmer plot for quenching of PtTMPyP4-AMP complex by Cl^-. In 50 mM Na-phosphate buffer (pH 7) in aerated solution

9.2.5 Discussion on PtTMPyP4-AMP

The photophysical measurements in aerated and deoxygenated solution show that the formation of the PtTMPyP4-AMP complex causes a reduction in both k_{nr} and $k_q[O_2]$. The formation of π-stacked complexes between PtTMPyP4 and AMP decreases the ability of dissolved molecular oxygen to quench the excited triplet state of PtTMPyP4, due to exclusion of solvent from contact with the porphyrin. This has been documented for porphyrins associated with DNA polymers[215], where the intercalation environment

affords protection to both faces of the porphyrin. In a 1:1 complex only one face is protected, allowing quenching to occur at the vacant face. This model may present an argument in favour of a 1:2 complex, though protection from dissolved oxygen has been reported in other 1:1 porphyrin-nucleotide systems[162] implying that binding on only one face is sufficient to lower the oxygen quenching constant.

There are a number of potential influences on k_{nr} in the PtTMPyP4-AMP complex. The first is the ICT state that is reported to explain similar behaviour in the fluorescence of H_2TMPyP4[159,222]. However, the influence of the CT state may be affected by the nature of the central metal atom. The fluorescence of ZnTMPyP4, for example, is only slightly affected by binding to AMP.

A more likely explanation is that the decrease in k_{nr} is due to the greater rigidity of the porphyrin in the PtTMPyP4-AMP complex. Solid-substrate phosphorescence experiments on PdTMPyP4 show that the lifetime extends from 500 μs to 1000 μs in the presence of ct-DNA, an observation attributed to increased rigidity[221], while PtTMPyP4 immobilised in mesoporous substrates also has a lifetime considerably longer than that in solution[166–169].

The results of the emission titration experiments were noteworthy in that simple biexponential kinetics (corresponding to lifetimes of free and bound porphyrins) were not observed. There are a number of potential explanations for this. The first is that the complex can dissociate within the excited-state emission lifetime, which is clearly a consideration when dealing with long-lived emitters. The rate of formation (k_1) was estimated as 1.9×10^9 dm^3 mol^{-1} s^{-1}[179], allowing a dissociation rate (k_{-1}) to be calculated from Eq. 9.14.

$$K_a = \frac{k_1}{k_{-1}} \tag{9.14}$$

The calculated k_{-1} value of approx. 4×10^5 s^{-1} equates to a natural dissociation lifetime of 2.5 μs. As this is of same magnitude as the rate of excited-state decay, the monoexponential decay observed for the PtTMPyP4-AMP solutions may be explained by averaging of the lifetimes of bound and unbound forms. In cases where biexponential decay does occur (at [AMP] < 0.5 mM), the variable long component may be interpreted as a weighted average lifetime of free and bound species.

Second, the data may be considered in the context of the work of Sazanovich et al, who observed fluorescence lifetime distributions for H_2TMPyP4-AMP rather than discrete components, due to the perceived heterogeneity in the structure of the complex (see Fig. 7.14, page 116)[222]. This distribution of complexes may result in an apparent monoexponential decay if the lifetime distribution is narrow. However a larger distribution of lifetimes would be expected in PtTMPyP4-AMP ($\tau_{bound}/\tau_{free} = 6$) than in

H_2TMPyP4-AMP ($\tau_{bound}/\tau_{free} = 2$), meaning that such a distribution would be less likely in the PtTMPyP4-nucleotide system.

Our experiments on deoxygenated solutions have also highlighted the potential to observe kinetics from the excited-state complex (exciplex), which provides a significant complication in the interpretation of the photophysical data.

The 100-fold decrease in quenching constant for Cl^- in the PtTMPyP4-AMP complex shows that the triplet state is very well protected from chloride quenching when associated with DNA. This implies that the photosensitising ability of PtTMPyP4 in DNA would be inhibited only slightly by saline conditions. It is also notable that the shielding afforded from Cl^- in the complex is larger than that for O_2, where there is only a 10-fold decrease in k_q in the latter. A possible reason for this is that chloride is negatively charged, and would be attracted less to a PtTMPyP4-AMP complex than the free tetracationic porphyrin.

9.3 PtTMPyP4 and GMP

9.3.1 Steady-State

Addition of GMP to PtTMPyP4 results in phosphorescence quenching in both aerated and deoxygenated solution (Fig. 9.11), in contrast to the enhancement observed with AMP. Quenching is less dramatic in aerated solution as the porphyrin is already efficiently quenched by oxygen.

The results are presented in both intensity and Stern-Volmer forms (Fig. 9.12 on the next page). Final Φ_0/Φ values of 4 and 21 were recorded in aerated and deoxygenated

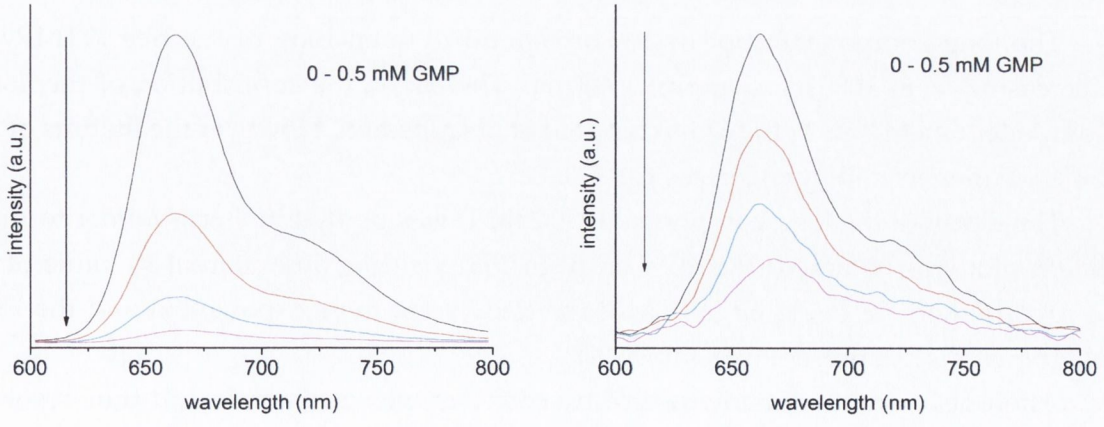

Figure 9.11: Emission spectra of 5 μM PtTMPyP4 with increasing concentrations of GMP in LEFT: deoxygenated and RIGHT: aerated solution. λ_{exc}= 517 nm

solutions, respectively, when data was plotted in Stern-Volmer form. These values were reached after the addition of approx 0.2–0.4 mM GMP. Thereafter the intensity did not decrease further, suggesting that an emissive complex had been formed.

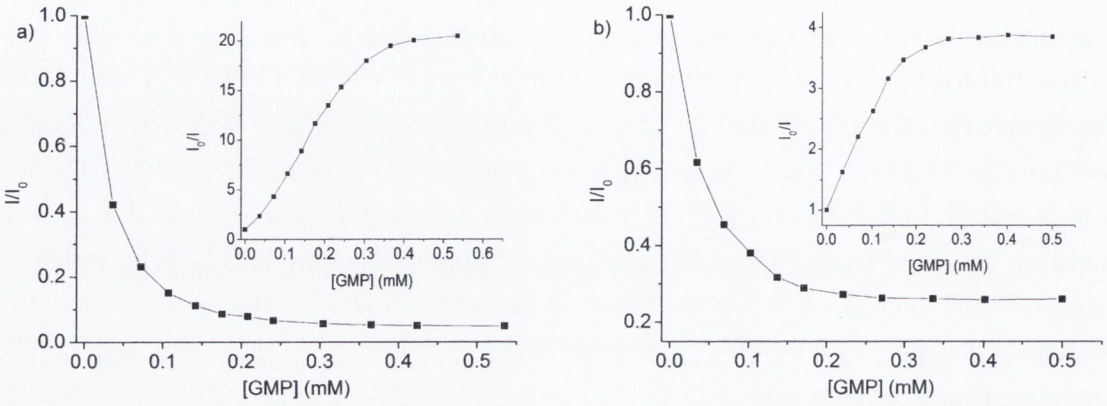

Figure 9.12: Steady-state emission quenching plots in I/I_0 and Stern-Volmer form (inset) for titration of PtTMPyP4 with GMP in (a) deoxygenated solution (b) air-equilibrated solution

9.3.2 Time-Resolved

SPC titrations were performed on aerated solutions over the same range of concentrations used in the steady-state measurements (Fig. 9.13a). The presence of low concentrations of GMP ($< \sim 2$ mM) results in biexponential decay kinetics (Table 9.4 on the facing page). A 'short' component of 67 ± 7 ns grows in relative contribution with increasing [GMP]. After ~ 0.2 mM GMP has been added, the contribution and magnitude of this component start to gradually decrease (Fig. 9.13b).

The long component appears to correspond to quenching of the free PtTMPyP4, decreasing from 1000 ns to approx. 400 ns. Thereafter, the contribution of the 'long' component increased as the 67 ns component disappeared. However the lifetime of the long component did not decrease further.

The decay of the long component (0–0.2 mM) was plotted in Stern-Volmer form. A linear plot was obtained (Fig. 9.14 on page 158) yielding an apparent k_q value of 3.7 x 10^9 $dm^3\,mol^{-1}\,s^{-1}$. At large [GMP] the decays are monoexponential and the 75 ns component is not present (see Table 9.4).

Attempts were then made to directly correlate the steady-state and time-resolved data, as disparities between these two measurements are often an indicator for static quenching. Furthermore, when emission occurs from the triplet state, the relationship between phosphorescence quantum yield and lifetime can infer if quenching of the

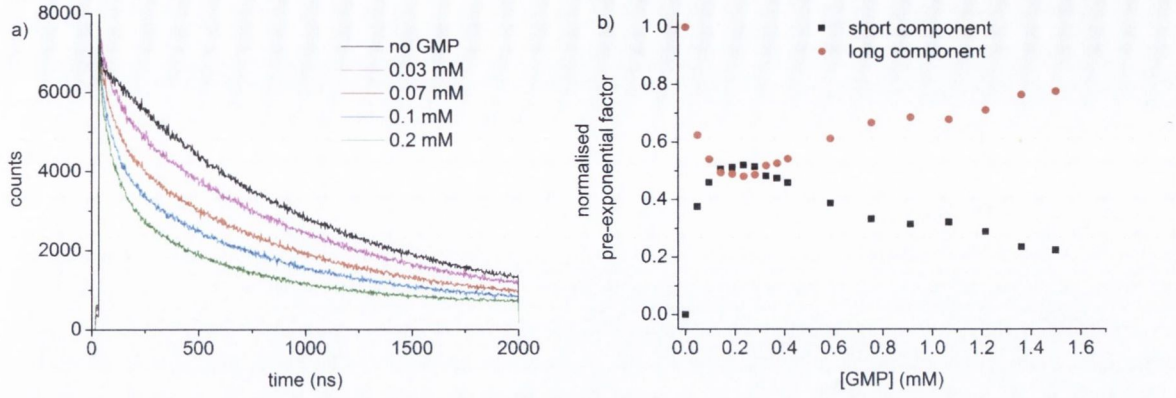

Figure 9.13: (a) SPC decays for PtTMPyP4-GMP (b) Contributions of long and short component with GMP concentrations. [PtTMPyP4] = 5 μM in 50 mM phosphate buffer

Table 9.4: Lifetime fitting parameters for PtTMPyP4 in the presence of low GMP concentrations in aerated solution in 50 mM Na-phosphate buffer pH 7. Errors in lifetimes are $\pm$ 10%

[GMP](mM)	τ_1 (ns)	%	τ_2 (ns)	%	τ_0/τ †	τ_0/τ ‡
0			997	100	1	1
0.034	76	2	970	98	1.3	1.1
0.068	75	4	850	96	1.7	1.2
0.10	72	6	750	93	2.1	1.4
0.14	69	8	730	92	2.2	1.4
0.17	71	10	630	90	2.8	1.7
0.20	70	11	570	89	3.2	1.9
0.23	73	13	550	87	3.4	2.1
0.27	68	13	490	87	3.6	2.3
0.30	67	13	470	87	3.8	2.4
0.33	69	13	460	86	3.8	2.5
0.36	66	14	440	86	4.0	2.6
0.40	64	13	420	86	4.2	2.7
0.43	68	14	410	86	4.2	2.8
0.59	66	9	440	91	3.4	2.5
0.75	59	6	470	94	3.2	2.4
0.91	57	6	450	94	3.2	2.4
1.5	70	4	470	96	2.8	2.3
10			440		2.2	2.2

†from Eq. 9.16.‡ from Eq. 9.15

singlet (S_1) state is occurring. In order to do this the two decay components had to be consolidated into an effective 'average' lifetime. This was calculated using both the intensity (Eq. 9.15) and amplitude (Eq. 9.16) averages[288]. Neither parameter scaled with

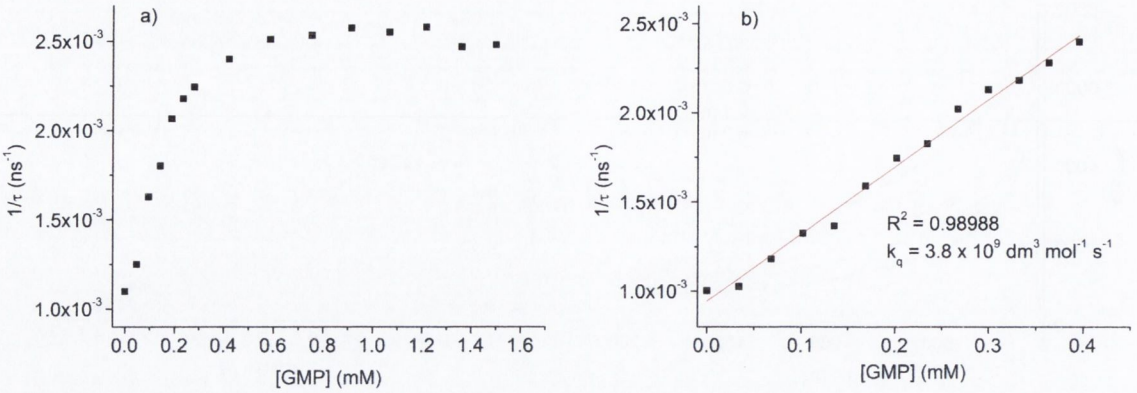

Figure 9.14: (a) Stern-Volmer plot for long component in titration of PtTMPyP4 with GMP (b) fit to linear portion of plot with calculated quenching constant

the steady-state data, although the closest agreement was found with the amplitude average (Fig. 9.15)

$$\langle \tau \rangle_f = \frac{\Sigma a_i \tau_i^2}{\Sigma a_i \tau_i} \tag{9.15}$$

$$\langle \tau \rangle_a = \frac{\Sigma a_i \tau_i}{\Sigma a_i} \tag{9.16}$$

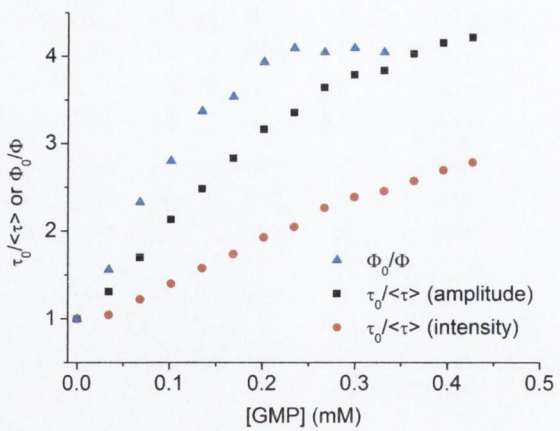

Figure 9.15: Average emission lifetimes for PtTMPyP4-GMP complexes in aerated solution

Table 9.5: Calculated photophysical parameters for PtTMPyP4 and nucleotide complexes. Errors in lifetimes are ± 10%.

	τ_{aer} (μs)	τ_{deox} (μs)	k_r (s^{-1})	k_{nr} (s^{-1})	k_q ($dm^3\,mol^{-1}\,s^{-1}$) O_2	Cl^-
PtTMPyP4	1.0	6.4	1300	1.4×10^5	3×10^9	2.4×10^8
PtTMPyP4-AMP	6.0	10	1300	9.9×10^4	2.9×10^8	1.5×10^6
PtTMPyP4-GMP	0.44		1300	2.3×10^6		
PtTMPyP4-GMP †	0.067		1300	1.3×10^7		

† <0.5 mM GMP

9.3.3 Discussion on PtTMPyP4-GMP

The quenching observed in the PtTMPyP4:GMP complex is most likely due to photoinduced electron transfer, given that a similar process occurs in H_2TMPyP4-GMP. As the Pt(II) atom is relatively inert oxidatively, the electron transfer almost certainly occurs to the porphyrin ligand and not to the metal, and probably occurs at the *N*-methylpyridyl group as previously proposed (Fig. 9.16)[170].

Figure 9.16: Suggested electron transfer mechanism in TMPy[170]

As mentioned earlier, the likelihood of an electron transfer can be predicted from the thermodynamic parameters (Eqn. 10.1 on page 193). Electron transfer is favoured if guanine has an oxidation potential less than 1.43 V[172]. A recent determination for the oxidation potential of dGMP is 1.31 V[289], yielding a ΔG of -0.12 V. However, there has been debate about the most accurate redox potential for guanine, mainly due to the rapid deprotonation of the guanine radical cation[290].

Literature values therefore show substantial variation, and high values of 1.53 V[291], 1.47 V[292], or 1.58 V[290], suggest triplet quenching may not be facile. It has been reported that an electron transfer ($k_{et} \sim 10^6\ s^{-1}$) occurs from GMP to triplet-excited H_2TMPyP4 despite a positive ΔG value of approximately 0.3 eV[224], so thermodynamic data should be interpreted with some discretion.

For photoinduced electron transfer, quenching of S_1 will always be energetically more favourable than T_1, and S_1 quenching should reveal itself in the emission measurements (see Eq. 9.3). For Pt(II) porphyrins the S_1-T_1 splitting is relatively low, im-

plying that S_1 should be very short-lived, and that the redox potentials of S_1 and T_1 would be similar. These properties suggest that S_1 quenching is unlikely in this system.

In the case of quenching by halides, the quantum yield and lifetime were quenched to the same extent. However there is a disparity for the PtTMPyP4-GMP system. This probably arises out of the need to calculate an effective lifetime from biexponential kinetics. The intensity average lifetime (Eq. 9.15) is often cited as the true average lifetime[293]. When a short component exists this can result in an understatement of the contributions from the short component, due to the squaring of the lifetime in the calculation[149]. As a result, static quenching can be overstated, and it has been suggested that the amplitude average (Eq. 9.16) is usually the most appropriate to use in order to evaluate the presence of static quenching[288]. Some disparity still exists even with the amplitude average (Fig. 9.15, page 158). However it is worth mentioning that disagreements have also been reported between steady-state and lifetime data for the singlet-state quenching of H_2TMPyP4 by GMP[181,182]. This may have a number of causes, including the assumption of discrete lifetimes in the Stern-Volmer plot, and the complex quenching processes that may be occurring in this system (e.g dynamic quenching, emissive complex formation).

In the analogous H_2TMPyP4-nucleotide system, photophysical changes occur over the same concentration ranges in both porphyrin-AMP and porphyrin-GMP systems[181]. However this is not true for PtTMPyP4, where emission changes level off at much lower nucleotide concentrations in PtTMPyP4-GMP than PtTMPyP4-AMP (see Fig. 9.17 on the next page). We had initially theorised that this was due to formation of 1:1 and 1:2 ground-state complexes. This appeared logical as the oxygen shielding effect would increase if a second nucleotide bound, while the electron transfer should only occur with the first bound GMP molecule. However, our ground-state binding studies failed to show evidence for significant 1:2 association over the concentration ranges studied, so we were persuaded to adopt a 1:1 ground-state model more commensurate with the previous literature[179–183].

An alternative explanation was sought. The most significant difference in the photophysics of H_2TMPyP4 and PtTMPyP4 is the luminescence lifetime. The implication of the longer lifetime of PtTMPyP4 is that it can be quenched by GMP molecules that are either bound ('static' quenching) or unbound (dynamic quenching). The lifetime thus drops quite abruptly. The grow-in of the short (67 ns) component is consistent with it being a PtTMPyP4-GMP complex. A forward rate constant for electron transfer to the PtTMPyP4 in the complex can then be estimated as $1.4 \times 10^7\ s^{-1}$. If the 440 ns lifetime is also a PtTMPyP4-GMP complex, that equates to a rate constant of $2.2 \times 10^6\ s^{-1}$. These compare with an average rate constant of $1.7 \times 10^9\ s^{-1}$ (up to as large as $10^{10}\ s^{-1}$) and $10^6\ s^{-1}$ for the S_1 and T_1 quenching, respectively, in the H_2TMPyP4-GMP com-

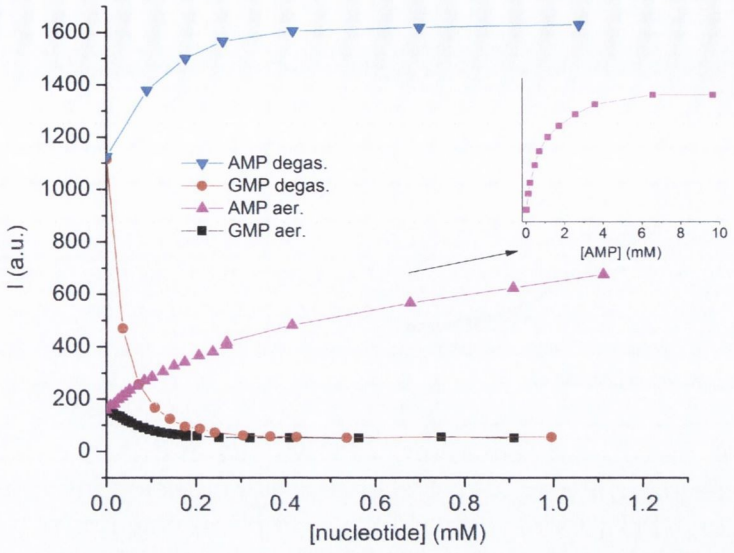

Figure 9.17: Comparison of the emission changes observed in all PtTMPyP4-nucleotide systems. [PtTMPyP4] = 6 μM in 50 mM phosphate buffer. Inset shows emission of PtTMPyP4-AMP extended to larger AMP concentrations (aerated solution)

plex. These data imply that the triplet is more readily reduced in PtTMPyP4 than in H_2TMPyP4. By comparison the PtTMPyP4 singlet state may be too short-lived to be effectively quenched. The apparent presence of two quenched lifetimes implies that multiple excited-state processes are occurring, possibly arising from different types of PtTMPyP4-GMP complex. As mentioned previously, four distinct lifetimes ranging from 100 ps to 6 ns have been recorded for H_2TMPyP4-GMP (Fig. 7.14, page 116), and geometric factors may have similar effects on emission lifetime in the PtTMPy4 system. The PtTMPyP4-GMP system is investigated further in the following chapter before conclusions are presented.

9.4 PtTMPyP4 and Polynucleotides

9.4.1 [poly(dA-dT)]$_2$

The addition of [poly(dA-dT)]$_2$ to buffered PtTMPyP4 (air-equilibrated) results in a substantial increase in phosphorescence intensity up to $\Phi/\Phi_0 = 13$, but without a shift in emission λ_{max} (Fig. 9.18 on the following page). Above P/D = 4 the intensity drops slightly with further additions. Notably this is the same P/D value where changes are observed in the UV and CD spectra.

Phosphorescence lifetimes were recorded using time-resolved emission, and unlike

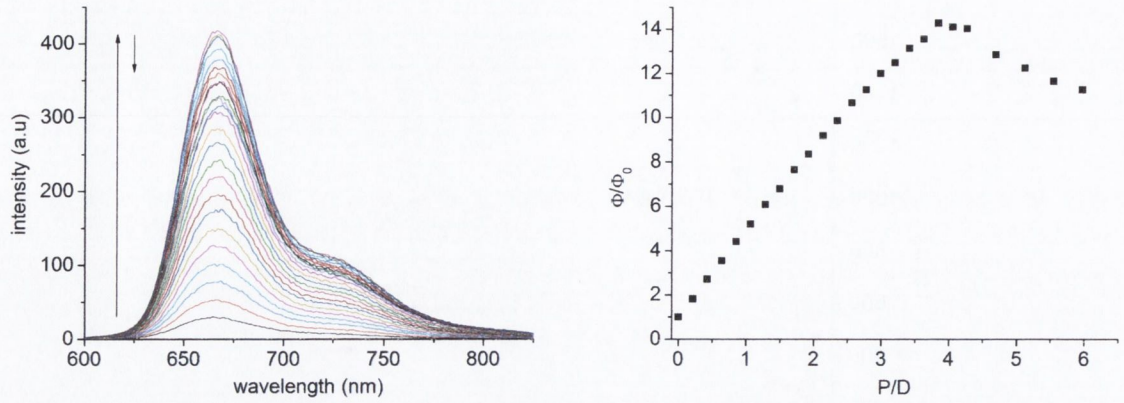

Figure 9.18: LEFT: Steady-state emission of PtTMPyP4 in presence of increasing concentrations of [poly(dA-dT)]$_2$. RIGHT: Dependence of emission intensity on [poly(dA-dT)]$_2$ concentration. [PtTMPyP4] = 6 μM in 50 mM phosphate buffer (pH 7) in aerated solution. λ_{exc}= 519 nm

in the PtTMPyP4-AMP complex, the decay traces show a clear biexponential process (Fig. 9.19 and Table 9.6 on the next page). The two components are a short component of approx. 1 μs (presumably unbound PtTMPyP4), and a longer component of approx. 13 μs (bound PtTMPyP4), which vary in contribution as the polynucleotide concentration increases.

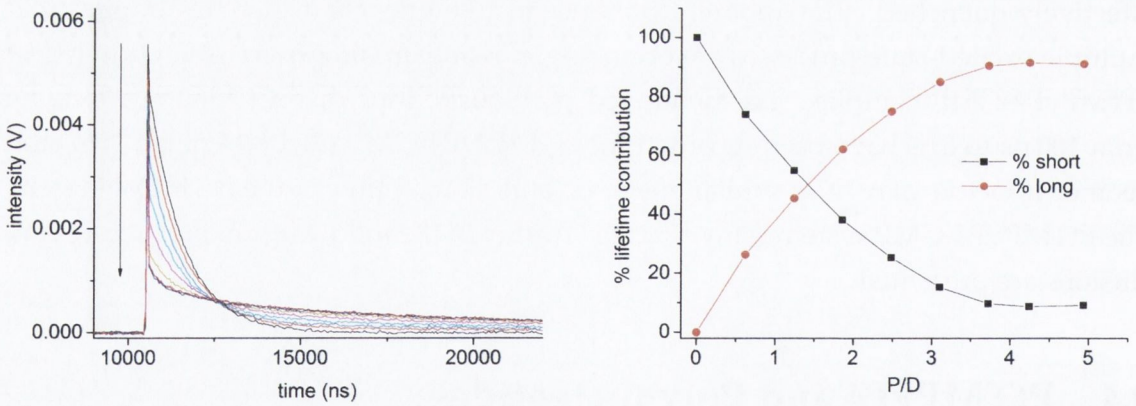

Figure 9.19: Time-resolved emission of PtTMPyP4 in presence of increasing concentrations of [poly(dA-dT)]$_2$. [PtTMPyP4] = 6 μM in 50 mM phosphate buffer (pH 7) in aerated solution λ_{exc} = 355 nm

Table 9.6: Lifetime fitting parameters for PtTMPyP4 in the presence of [poly(dA-dT)]$_2$. Errors in lifetimes are ± 10%

P/D	τ_1 (ns)	% (Aτ)	τ_2 (ns)	%	τ_{ave} (ns)	τ/τ_0
0	1010	100			1010	1
0.6	991	74	12200	26	3940	3.9
1.2	964	55	13000	45	6400	6.3
1.9	995	38	12900	62	8350	8.3
2.5	1030	25	13100	75	10100	10
3.1	1120	15	13100	85	11300	11.2
3.7	1260	10	13300	90	12200	12.0
4.2	1180	9	13200	91	12100	12.0
4.9	1250	9	12600	91	11600	11.5

9.4.2 [poly(dG-dC)]$_2$

The addition of [poly(dG-dC)]$_2$ to PtTMPyP4 results in a pronounced red-shift of emission λ_{max} (670 nm – 689 nm), corresponding to lowering of the $^3\pi\pi^*$ state due to intercalation between GC sites. An increase in quantum yield of up to $\Phi/\Phi_0 = 6$ (Fig. 9.20) is observed, in contrast to the quenching recorded for PtTMPy4-GMP.

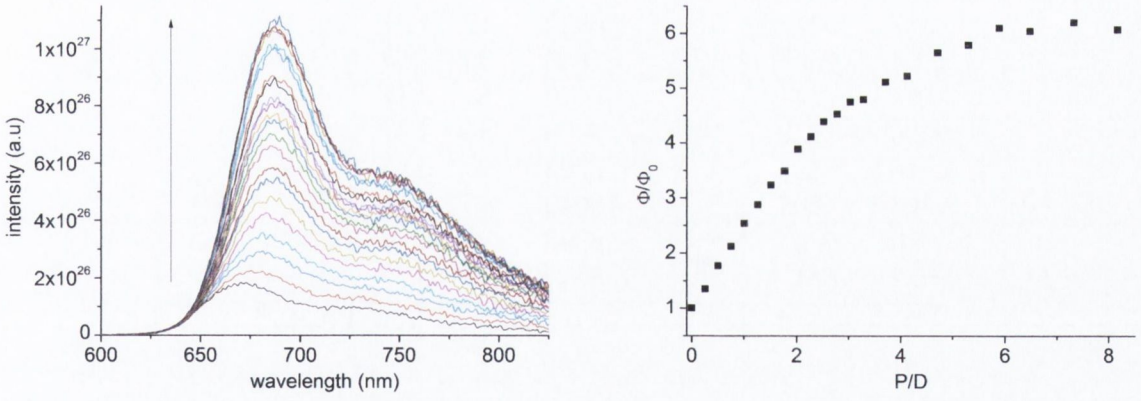

Figure 9.20: LEFT: Emission spectra of 6 μM PtTMPyP4 in presence of increasing concentrations of [poly(dG-dC)]$_2$. RIGHT: Dependence of emission intensity on [poly(dG-dC)]$_2$ concentration. λ_{exc} = 523 nm. In 50 mM Na-phosphate (pH 7) in aerated solution

Time-resolved emission titrations fit to biexponential kinetics with a lifetime of 1 μs and a second component of 7.5 μs (Fig. 9.21 and Table 9.7 on the following page). The contributions from these components scaled with the changes in UV and emission spectra, implying that they represent the free and bound forms. Average lifetimes had the best agreement with quantum yields when calculated as amplitude averages from Eq. 9.16 (Table 9.7).

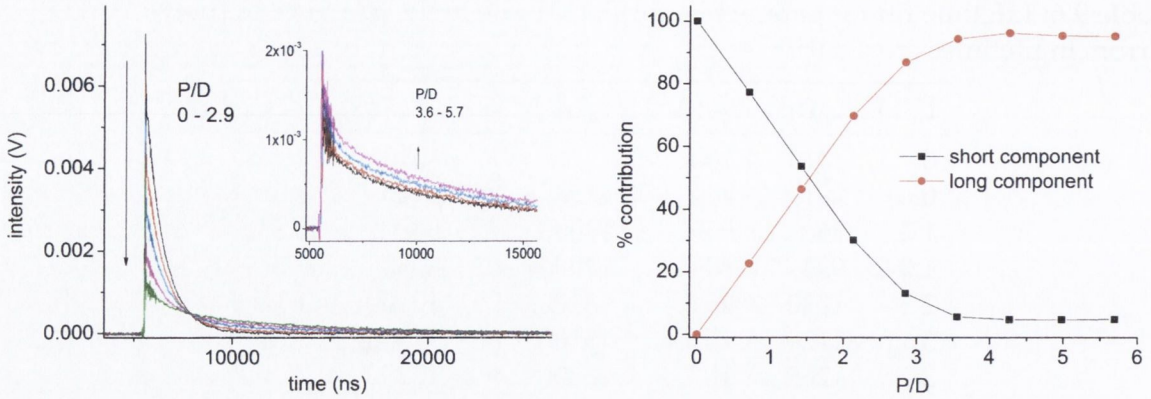

Figure 9.21: LEFT: Time-resolved emission decay of 8.3 μM PtTMPyP4 in increasing [poly(dG-dC)]$_2$ concentrations up to P/D = 2.9. Inset shows traces at higher [poly(dG-dC)]$_2$ concentrations. RIGHT: Contribution of lifetime components as function of P/D. In 50 mM Na-phosphate buffer (pH 7) in aerated solution, λ_{exc} = 355 nm

Table 9.7: Lifetime fitting parameters for PtTMPyP4 in the presence of [poly(dG-dC)]$_2$ in 50 mM Na-phosphate buffer (pH 7) in aerated solution, λ_{exc} = 355 nm

P/D	τ_1 (ns)	% (Aτ)	τ_2 (ns)	%	τ/τ_0†	τ/τ_0‡
0	931	100	-			
0.7	934	81	6920	19	1.27	2.22
1.4	966	61	7640	39	1.58	3.87
2.1	974	41	7740	59	2.17	5.36
2.8	1080	14	8200	86	4.6	7.75
3.6	815	5	7700	95	5.63	7.86
4.3	680	5	8040	95	5.48	8.22
5.0	634	5	8390	95	5.76	8.62
5.7	661	5	8590	95	5.91	8.83

†calculated from Eq. 9.16 ‡calculated from Eq. 9.15

9.4.3 DNA

Addition of double-stranded salmon DNA initially causes an increase in intensity up to Φ/Φ_0 = 4, followed by an emission red-shift at higher P/D once the intensity had levelled off (Fig. 9.22 on the next page). At low P/D values the porphyrin may be forced to bind at any available site, but as more sites become available the porphyrin has a preference for G-C sites, hence the red-shift observed at high P/D ratios.

Emission lifetimes fit to biexponential decay, corresponding to a short component of 1 μs and a longer component of 6 μs, corresponding to free and bound forms, respectively. Similar data was recorded by SPC (Fig. A.7 on page 212)

The increase in the emission intensity is not as large as that reported by Nyarko et al[174]. This is almost certainly because their data was recorded in the presence of Cl^-, whereby a large enhancement would be expected as the bound porphyrin becomes protected from Cl^-.

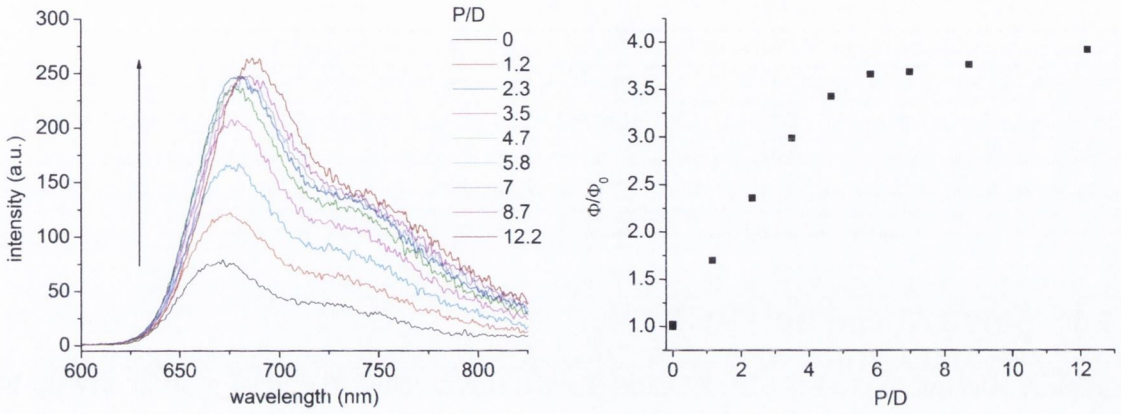

Figure 9.22: LEFT: Emission spectra of PtTMPyP4 in presence of increasing concentrations of ds-DNA. RIGHT: Dependence of emission intensity on DNA concentration. In 50 mM Na-phosphate buffer (pH 7) in aerated solution, $\lambda_{exc} = 521$ nm

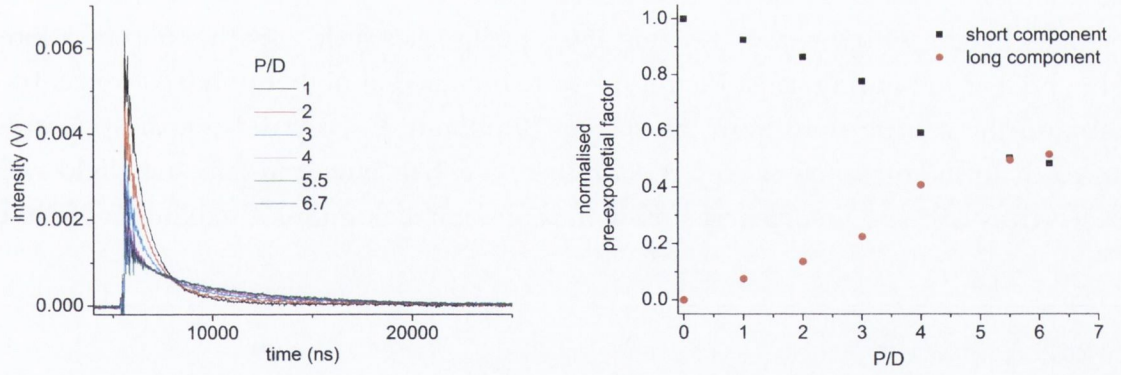

Figure 9.23: LEFT: Time-resolved emission decays for PtTMPyP4 in increasing concentrations of DNA. RIGHT: Contribution of lifetime components as function of P/D. In 50 mM Na-phosphate buffer (pH 7) in aerated solution, $\lambda_{exc} = 355$ nm

Table 9.8: Lifetime fitting parameters for PtTMPyP4 in the presence of salmon DNA in 50 mM Na-phosphate buffer (pH 7) in aerated solution, λ_{exc} = 355 nm

P/D	τ_1 (ns)	% (Aτ)	τ_2 (ns)	%	τ/τ_0†	τ/τ_0‡
0	930	100	-			
1	1040	93	6100	7	1.4	2.7
2	1030	86	5910	14	1.7	3.4
3	1100	78	6510	22	2.3	4.5
4	1050	59	5610	41	2.9	4.6
5.5	1110	50	6260	50	3.7	5.5
6.2	900	48	5560	52	3.3	4.9

†calculated from Eq. 9.16 ‡calculated from Eq. 9.15

9.4.4 poly(rA) and poly(rG)

Addition of poly(rA) to PtTMPyP4 causes a steady increase in emission intensity up to a maximum Φ/Φ_0 of 13 after a P/D of 4-5, similar to what was observed in [poly(dA-dT)]$_2$. However there was also a red-shift in λ_{max} from 668 nm to 673 nm. This is achieved after a small addition of poly(rA) (P/D = 0.2) and λ_{max} is constant with further addition.

Time-resolved emission data fits to biexponential kinetics with a component of 1 μs and another of 13 μs, similar to those recorded for PtTMPyP4-[poly(dA-dT)]$_2$ (Fig A.8 on page 213). As with previous systems, the contributions scale with the concentrations of bound and unbound forms. Poorer fits were obtained at higher poly(rA) concentration, and the contribution from the shorter ('unbound') decay did not disappear as expected. In the presence of poly(rG) a four-fold enhancement in emission yield was observed, as well as a notable red-shift in the emission maximum. A maximum lifetime

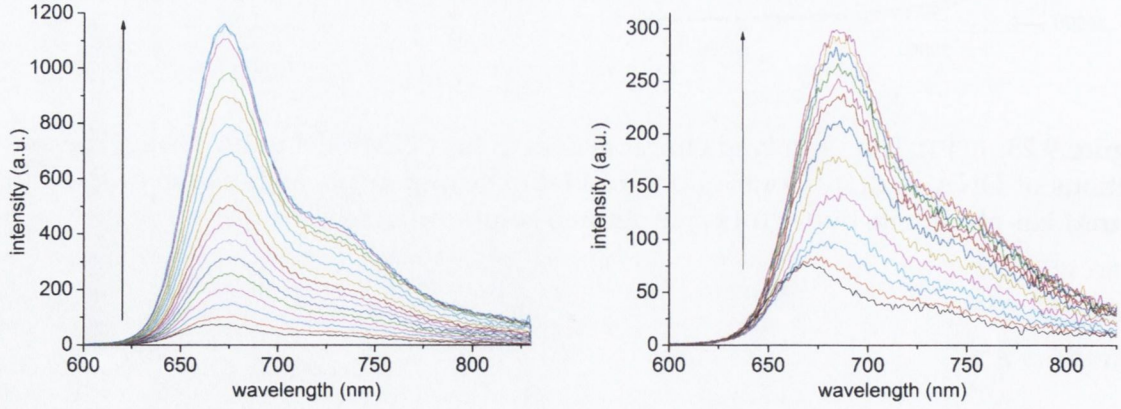

Figure 9.24: Phosphorescence spectra of 5 μM PtTMPyP4 in presence of LEFT: poly(rA) RIGHT: poly(rG). In 50 mM Na-phosphate buffer (pH 7) in aerated solution λ_{exc} = 518 nm

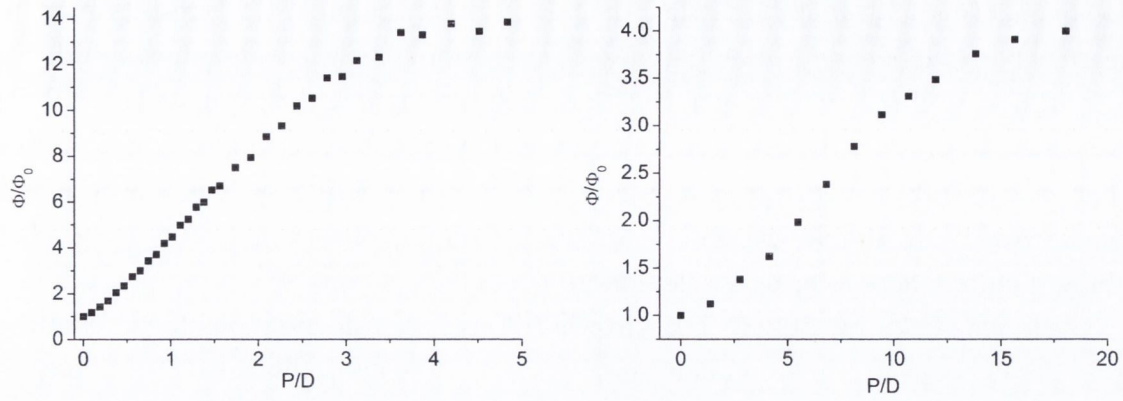

Figure 9.25: Dependence of phosphorescence intensity on P/D ratio for PtTMPyP4 in LEFT: poly(rA) RIGHT: poly(rG). In 50 mM Na-phosphate buffer (pH 7) in aerated solution.

of 6.5 μs was recorded (data not shown). However, when the experiment was repeated lifetimes as low as 3 μs were recorded, suggesting that the poly(rG) was existing in different conformations in solution.

9.5 Discussion on Polynucleotides

Enhancement in emission is observed for PtTMPyP4 in all polymers studied (Table 9.9) It was proposed in the previous chapter that PtTMPyP4 binds to [poly(dA-dT)]$_2$ by mixed modes in the major and minor grooves. Based on this model, we suggest that the increase in phosphorescence in [poly(dA-dT)]$_2$ is due to the self-stacked major-groove bound porphyrin, while the drop in phosphorescence at high P/D is observed when the bound population is redistributed to the minor groove. This would suggest that the porphyrin triplet state is slightly more susceptible to non-radiative processes (such as quenching by oxygen) in the minor groove.

Self-stacking of the porphyrins might be expected to result in quenching of emission, due to the self exchange between electronically coupled chromophores[160,161,294].

Table 9.9: Emission properties of PtTMPyP4-polynucleotide complexes

polymer	Φ/Φ_0 max	$\Delta\lambda_{max}$
[poly(dA-dT)]$_2$	13	0
[poly(dG-dC)]$_2$	6	+21
ds-DNA	4	+21
poly(rA)	13	+5
poly(rG)	4	+18

However, it is notable that the binding of H_2TMPyP4 to [poly(dA-dT)]$_2$ results in an increase of both singlet and triplet lifetimes[189], even though CD data also shows evidence for porphyrin-porphyrin interactions. This suggests that any stacking of H_2TMPyP4 or PtTMPyP4 in [poly(dA-dT)]$_2$ is very different to that observed in other porphyrins where excited-state quenching is observed[161,294]. In the TMPy systems the coupling may be very weak, or may depend on the type of aggregated species formed (e.g. H or J dimer/aggregate or long-range assembly).

The mode of binding of PtTMPyP4 to poly(rA) is uncertain, but notable for resulting in similar changes in emission quantum yield to that seen in [poly(dA-dT)]$_2$. It may be surmised that PtTMPyP4 is bound in a similar manner in poly(rA), and is protected from oxygen quencher to the same extent.

It is interesting that the phosphorescence of PtTMPyP4 is enhanced in G-containing polymer sequences ([poly(dG-dC)]$_2$, DNA, poly(rG)), compared to the quenching observed for PtTMPyP4-GMP. Slower rate constants have been recorded for H_2TMPyP4-[poly(dG-dC)]$_2$ than H_2TMPyP4-GMP, which has been proposed to be due to an unfavourable donor-acceptor orientation when the porphyrin is intercalated in the polymer[224]. This argument is reasonable considering the large size of the TMPy molecule, and the possibility that it does not intercalate fully between the GC steps.

In some cases the GC polymer system is reported to be more reducing than the GMP mononucleotide, and in the case of thionine, more efficient electron transfer is recorded with [poly(dG-dC)]$_2$ than with GMP[148]. This trend is opposite to that observed with H_2TMPyP4, suggesting that the decrease in efficiency is due to geometric rather than thermodynamic reasons. It therefore makes sense that electron transfer to PtTMPyP4 may be less efficient in [poly(dG-dC)]$_2$ than in GMP. In fact, the emission enhancement actually means that it is not immediately obvious if electron transfer is occurring at all. However the lifetime (7.5 μs) is shorter than that recorded in [poly(dA-dT)]$_2$ (13 μs), even though intercalation is expected to provide more protection from quenchers and impose the most conformational restriction on the porphyrin. It may similarly be noted that enhancement is greater in poly(rA) than in poly(rG). We therefore suggest that an additional (but relatively inefficient) decay pathway exists in the presence of G in the polymer, the effect of which is over-compensated by the reduction in other non-radiative processes.

Alternatively, electron transfer may occur with different efficiencies in different sites. Kruk et al rationalised that the long-lived fluorescence of H_2TMPyP4 in a hexamer sequence arose from bound, but unquenched, porphyrin[190]. The most natural explanation would be for a CG vs GC preference, but the authors show evidence that this is not the case. Considering that there is only one long lifetime component in PtTMPyP4-[poly(dG-dC)]$_2$, the model of Kruk et al is not deemed appropriate in the PtTMPyP4

system, and we suggest that all bound porphyrins have approximately similar triplet-state properties.

9.6 Conclusions

The triplet excited state of PtTMPyp4 is a sensitive luminescence probe for a number of species in its local environment. Bimolecular quenching is especially important with Cl^- and O_2. However the binding sites of AMP or DNA provides protection from these quenchers. This may alter the efficiency of singlet oxygen generation, but should preserve the ability of the porphyrin to react by a type 1 (electron transfer) mechanism. Quenching of PtTMPyP4 phosphorescence in GMP shows that photoinduced electron transfer takes place from the triplet state, although this process is apparently less efficient in DNA polymers.

Chapter 10

Transient Absorption Spectroscopy

PtTMPyP4 and its nucleic-acid complexes were also studied using transient absorption spectroscopy. The primary aims of these experiments were to characterise the excited state of PtTMPyP4, and to investigate the photoinduced electron transfer reported in the previous chapter. Experiments were performed using nanosecond transient UV/vis/NIR (Trinity College) and femtosecond/picosecond transient UV/vis and mid-IR (Rutherford Appleton Laboratories).

10.1 Nanosecond Transient Absorption Spectroscopy

10.1.1 PtTMPyP4

Samples for nanosecond TA were prepared to 5–10 μM PtTMPyP4 in 1 cm cuvettes, giving an absorbance at the pump wavelength (355 nm) of c. 0.1–0.2. Transient difference spectra were recorded point-by-point at 10 nm intervals.

The transient absorption spectrum of PtTMPyP4 in the UV/vis region was recorded in aerated solution (Fig. 10.1). A depletion occurs at the Soret band, and an intense transient is present around 450 nm. There is a broad and weak absorption across the visible region from 500 nm to 700 nm, with small Q-band bleaches at 513 nm and 545 nm.

The transient and bleach fit to mono-exponential lifetimes of $1.0 \pm 0.1\mu$s, similar to the phosphorescence lifetime recorded from emission spectroscopy. This confirms that the transient spectrum shows the PtTMPyP4 triplet state, and also that appreciable triplet-triplet annihilation does not occur under the chosen experimental conditions. Transient absorption persists into the near-IR, with a local maximum absorbance at 980 nm. Again, the lifetime of the near-IR transient is in agreement with the phosphorescence decay (Fig. 10.2 on the following page). The T-T spectrum of PtTMPyP4 in both the UV/vis and near-IR regions are similar to those recorded for other TMPy derivatives[231].

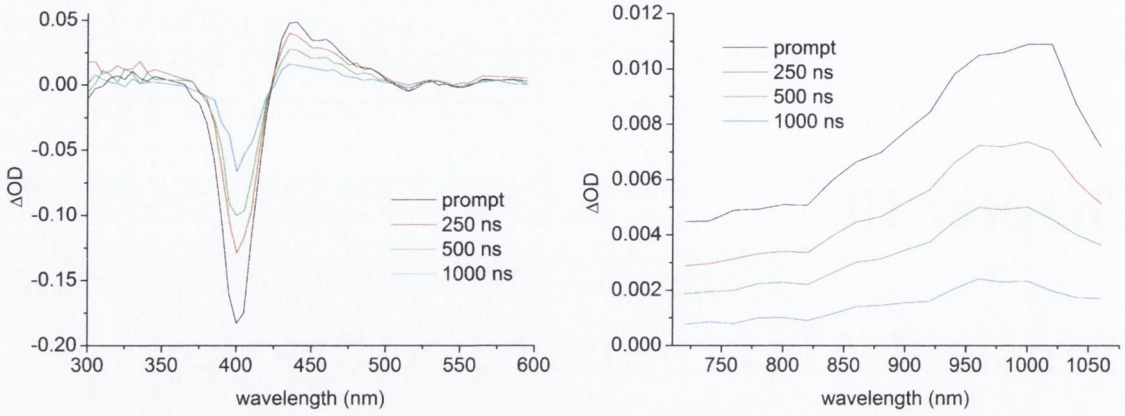

Figure 10.1: Transient absorption spectra of air-equilibrated 6 μM PtTMPyP4 recorded in UV/vis and NIR spectral ranges. Recorded point-by-point. In 50 mM Na-phosphate buffer pH 7 in H_2O, λ_{pump} = 355 nm

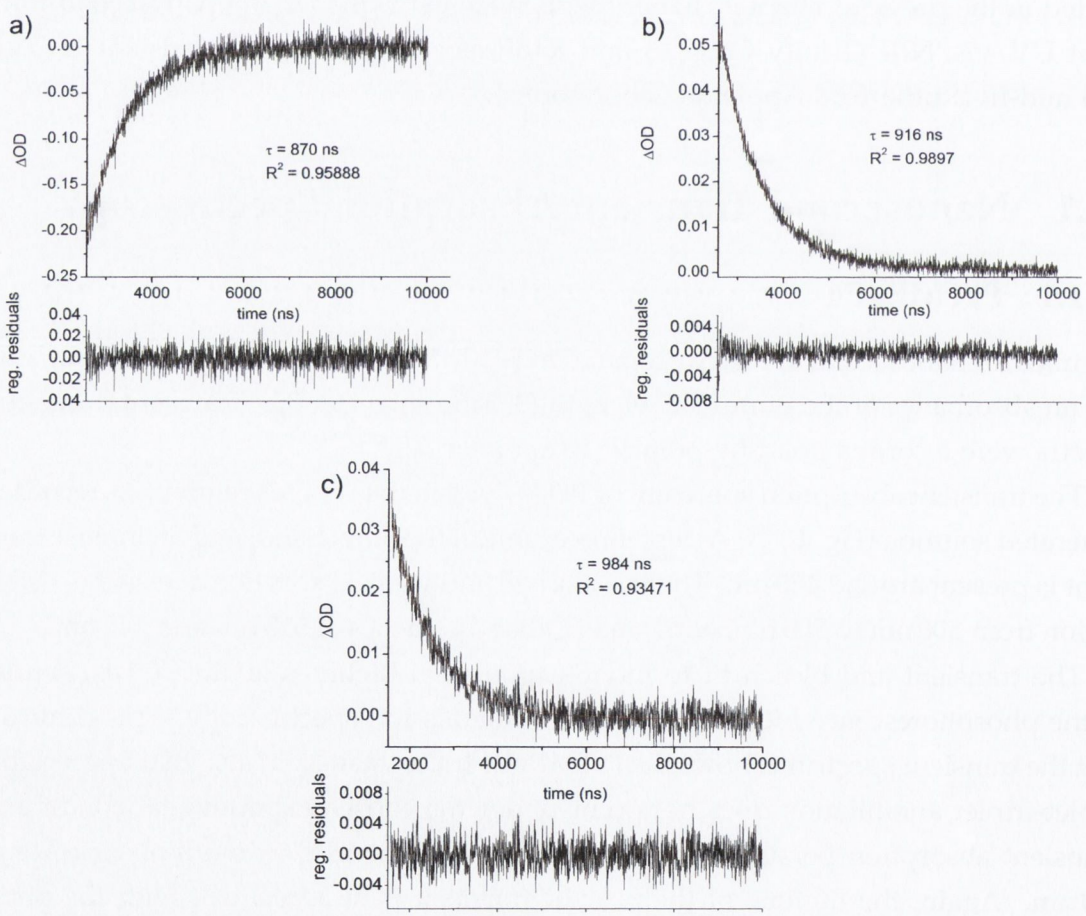

Figure 10.2: Kinetic fits to transient absorption spectrum of PtTMPyP4 at (a) 400 nm, (b) 440 nm and (c) 980 nm. In aerated 50 mM Na-phosphate pH 7 in H_2O

10.1.2 PtTMPyP4 and Mononucleotides

The UV/vis transient spectra of PtTMPyP4 in the presence of high mononucleotide concentrations (10 mM) show red-shifted Soret bleaches, and also show T-T absorptions at 450 nm (Fig. 10.3 on the next page). The T-T absorption are red-shifted by c. 10 nm (520 cm^{-1}) relative to the free base (435 nm–445 nm). By comparing the prompt spectra (after 20 ns) of PtTMPyP4-AMP and PtTMPyP4-GMP, it can be shown that the yields of triplet state formation are comparable, implying there is little difference in the quantum yield of intersystem crossing between either complex.

Kinetic fits to bleach and transient (Fig. 10.5, page 175) are monoexponential, and agree with those recorded by time-resolved emission spectroscopy. The lifetime of PtTMPyP4-AMP in deoxygenated solution (10 ± 1 μs, data not shown) also agrees with the emission lifetime. There was no noticeable difference in lifetimes when PtTMPyP4-GMP was deoxygenated (N_2 purging), consistent with the short lifetime of the complex and shielding effect in the complex ($\tau \leq 1/k_q[O_2]$).

In the near-IR (Fig. 10.4 on the following page), there is a clear red-shift of the transient band with respect to unbound PtTMPyP4 from 980 nm to 1010 nm ($\Delta\lambda$ = 30 nm, $\Delta\nu$ = 303 cm^{-1}). Lifetimes of the transient are the same as those recorded in the UV/vis.

It is notable that the spectra of PtTMPyP4-AMP and PtTMPyP4-GMP were very similar in both UV/vis and NIR. The porphyrin radical anion is expected to absorb around 750 nm[226–229], while the guanine radical cation has a broad and weak absorption around 500 nm[295]. We do not see evidence for either of these species in the PtTMPyP4-GMP spectra, implying that charge recombination occurs very rapidly (i.e. within the time response of the apparatus).

The PtTMPyP4-GMP system was investigated in more detail, considering the complex phosphorescence kinetics observed in the previous chapter. Bleach and transient kinetics were recorded for PtTMPyP4 at a range of GMP concentrations (see Fig. 10.6 on page 176). At the low concentrations biexponential decay was observed, with a similar long and short component to that seen by SPC. Kinetics were similar (lifetimes and contribution) whether recorded at bleach or transient wavelengths (Table 10.1 on page 176). These results show that both transient species arise from quenched PtTMPyP4 triplet states.

Experiments were also performed in deoxygenated solution. The long component is shown to increase in lifetime, while the short component shows little change (Fig. 10.7, page 177 and Table 10.2, page 176). The quenching of the long-lived state in oxygen is consistent with it being a triplet state. Stern-Volmer plots to the long-lived component yield $k_q = 4.0 \pm 0.4 \times 10^9$ $dm^3\,mol^{-1}\,s^{-1}$, the same value recorded in aerated solution by SPC (section 9.3.2).

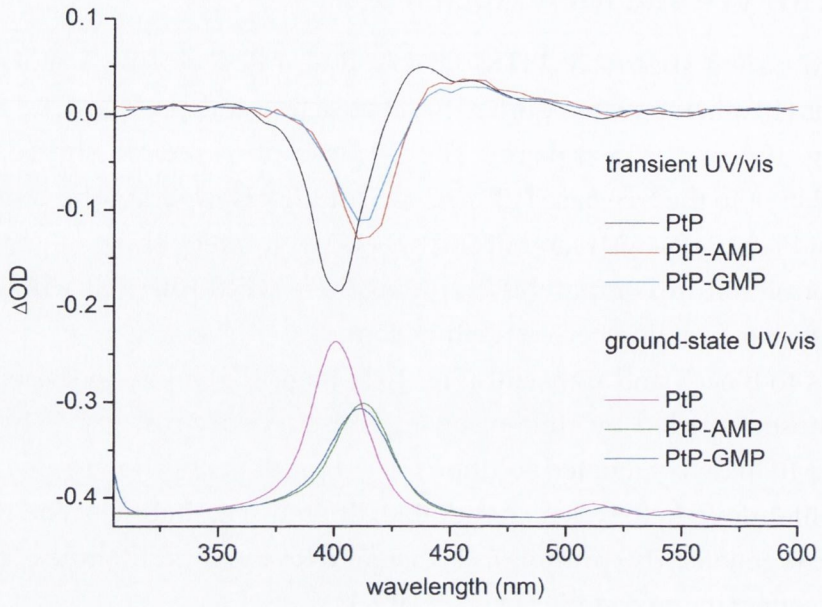

Figure 10.3: Transient UV/vis absorption spectra of 6 μM PtTMPyP4 and 10 mM nucleotide. Also shown are the corresponding ground-state spectra. In aerated 50 mM Na-phosphate buffer pH 7 in H_2O, λ_{pump} = 355 nm. Prompt = 20 ns after laser pulse

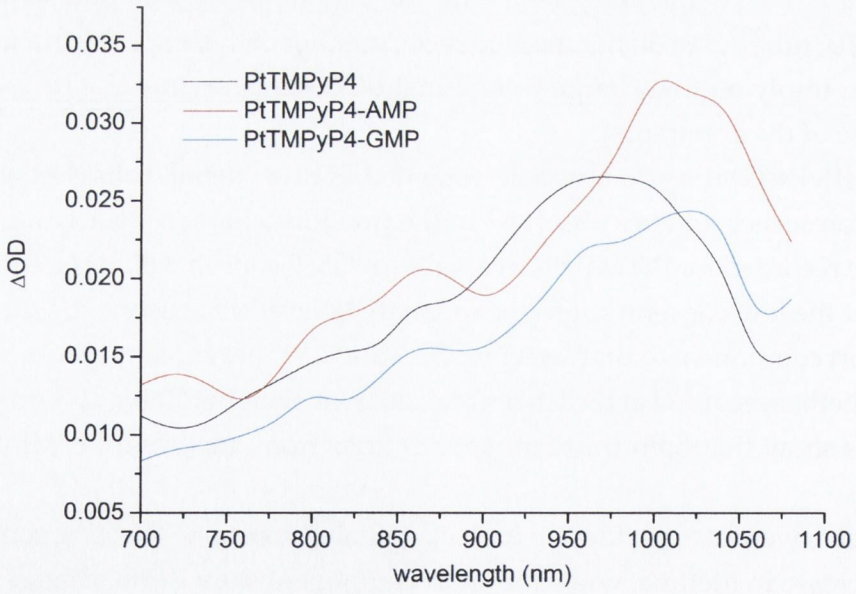

Figure 10.4: Transient UV/vis absorption spectra of 6 μM PtTMPyP4 and 10 mM AMP or GMP. Also shown is the spectrum of free PtTMPyP4. In aerated 50 mM Na-phosphate buffer pH 7 in H_2O, λ_{pump} = 355 nm. Prompt = 20 ns after laser pulse

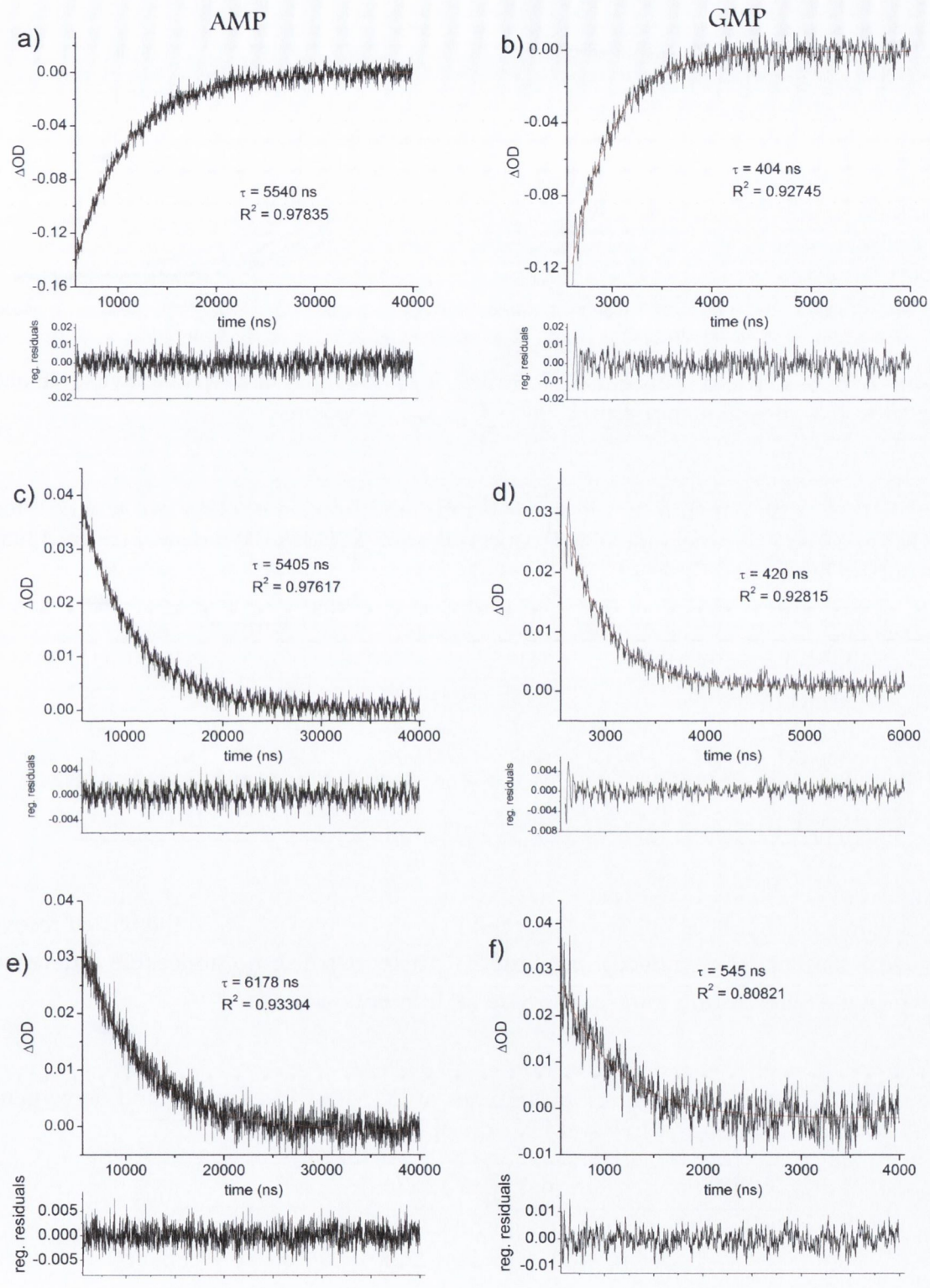

Figure 10.5: Kinetic fits to transient spectra of PtTMPyP4-AMP at (a) 410 nm, (c) 460 nm and (e) 1020 nm and PtTMPyP4-GMP at (b) 410 nm, (d) 460 nm and (f) 1020 nm. In aerated 50 mM Na-phosphate buffer pH 7 in H_2O. Note longer lifetimes for PtTMPyP4-AMP complex compared to PtTMPyP4-GMP

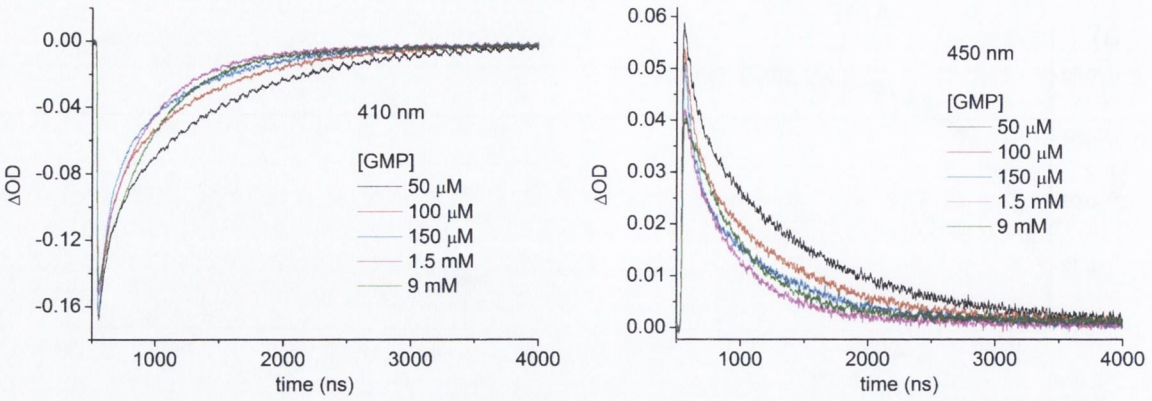

Figure 10.6: Bleach and transient kinetic traces for PtTMPyP4-GMP. [PtTMPyP4] = 6 μM in 50 mM Na-phosphate buffer pH 7 in H_2O, λ_{pump} = 355 nm

Table 10.1: Comparison of bleach (410 nm) and transient (450 nm) kinetics for PtTMPyP4-GMP as function of GMP concentration. [PtTMPyP4] = 6 μM in 50 mM Na-phosphate buffer pH 7 in H_2O

	410 nm				450 nm			
[GMP]	τ_1 (ns)	%	τ_2 (ns)	%	τ_1 (ns)	%	τ_2 (ns)	%
50 μM	86	31	893	69	87	28	935	72
100 μM	80	46	753	54	83	40	780	60
150 μM	77	52	667	48	79	46	691	54
1.5 mM	73	21	436	79	79	19	444	81
9 mM			437				450	

A component of 80 $\pm$ 7 ns was observed in both the transient and the bleach recovery, with similar relative decay amplitudes. There was also no noticeable difference between the Soret-region transient spectra at different delays.

Table 10.2: Comparison of transient lifetimes of PtTMPyP4 in aerated and deoxygentated solution. λ = 450 nm. In 50 mM Na-phosphate pH 7 in H_2O

[GMP]		τ_1 (ns)	%	τ_2 (ns)	%	R^2
50 μM	aer.	100 $\pm$ 1	38	853 $\pm$ 3	62	0.99909
	deox.	109 $\pm$ 1	35	2208 $\pm$ 18	65	0.99888
100 μM	aer.	77 $\pm$ 1	38	652 $\pm$ 3	62	0.99849
	deox.	88 $\pm$ 1	41	1410 $\pm$ 7	59	0.99892
200 μM	aer.	85 $\pm$ 1	48	501 $\pm$ 4	52	0.99709
	deox.	89 $\pm$ 1	55	868 $\pm$ 6	45	0.99465

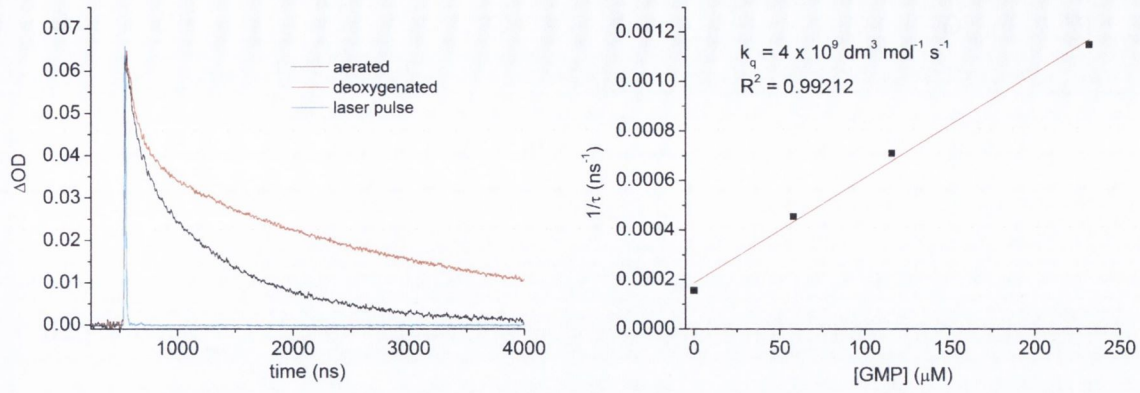

Figure 10.7: LEFT: Transient decay and instrument profile for PtTMPyP4 in the presence of 50 μM GMP in aerated and deoxygenated solution. RIGHT: Stern-Volmer fit to the long-lived component in deoxygenated solution. In 50 mM Na-phosphate buffer pH 7 in H_2O

10.1.3 Discussion on ns-TA

The shifts in the UV/vis and near-IR spectra observed in the presence of either AMP and GMP are attributed to perturbation of the PtTMPyP4 triplet state on forming the complex with the nucleotides. Steady-state and time-resolved phosphorescence measurements in the previous chapter showed that the electron transfer from guanine is occurring primarily, if not solely, via the T_1 state of PtTMPyP4. The similar T-T absorption intensity for equivalent PtTMPyP4-AMP and PtTMPyP4-GMP complexes recorded in this chapter confirms that the yield of intersystem crossing is not appreciably affected, and that quenching occurs from the triplet state. The failure to observe redox photoproducts by ns-TA suggests that there is efficient charge recombination.

The complex formed between PtTMPyP4 and GMP is relatively strong ($K = 5300\,M^{-1}$). As discussed in the previous chapter (Section 9.2.5), an estimate of the lifetime of the complex is 2.5 μs, which means cage escape will be inefficient if the rate of reverse electron transfer is higher than approx $10^6\,s^{-1}$.

The efficiency of the reverse electron transfer is an interesting result as charge recombination with a triplet state requires a forbidden spin-flip (Fig. 10.8 on the next page), which typically retards the charge recombination[296]. It may be possible that the considerable heavy atom effect in this system facilitates efficient spin conversion. Similar observations have been made in our group recently regarding the photo-oxidation of guanine by chromium polypyridyl complexes[297].

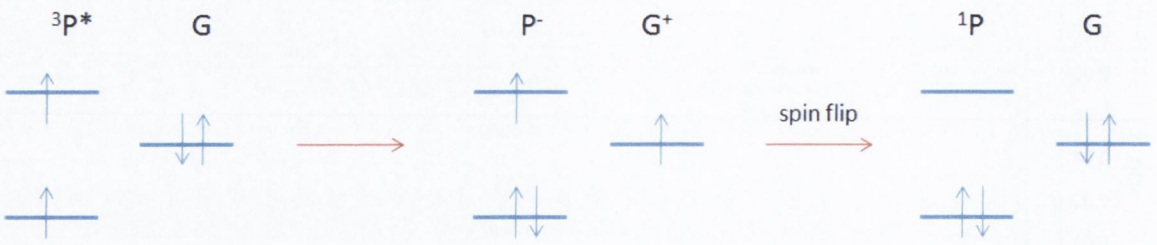

Figure 10.8: Spin-forbidden charge recombination in PtTMPyP4-GMP redox pair

10.2 Picosecond and Femtosecond Transient Absorption Spectroscopy

As nanosecond TA did not yield data on the reverse electron transfer, it was desirable to investigate these systems further using ultrafast techniques. It was also noted that there were significant gaps in the literature on this subject, with no reported ultrafast studies on PtTMPyP4, very few on H_2TMPyP4[225], and very few reports in general on TRIR spectroscopy of porphyrins[235].

Preliminary experiments were subsequently performed on porphyrin and porphyrin-mononucleotide systems at the Rutherford Appleton Laboratories using ps-TRIR (PIRATE) and fs-UV/vis and fs-TRIR (ULTRA). Both PtTMPyP4 and H_2TMPyP4 systems were studied. Spectra on the ULTRA apparatus were recorded by Prof. Kelly and Dr. Wojdyla with the RAL team.

The main electronic transitions with their relevant experimental parameters are shown in Figure 10.9 on the facing page. 400 nm laser excitation populates the S_2 state in both porphyrins. Due to the probability of rapid internal conversion from upper excited states to S_1 (Kasha's rule), the prominent absorptions are likely to arise from the S_1 state. The heavy-atom effect in Pt(II) porphyrins means that intersystem crossing may conceivably occur also from S_2. While the lifetime of S_1 in H_2TMPyP4 is c. 5 ns, the S_1 lifetime of PtTMPyP4 is unknown, but is likely to be quite short-lived (ps timescale)[150].

Samples for these experiments were prepared in demountable liquid IR cells, as was done for the the cytosine studies. Due to the short optical pathlengths used (56 μm), the porphyrin concentrations were in the mM range, considerably higher than those used for absorption and emission studies in the preceding two chapters.

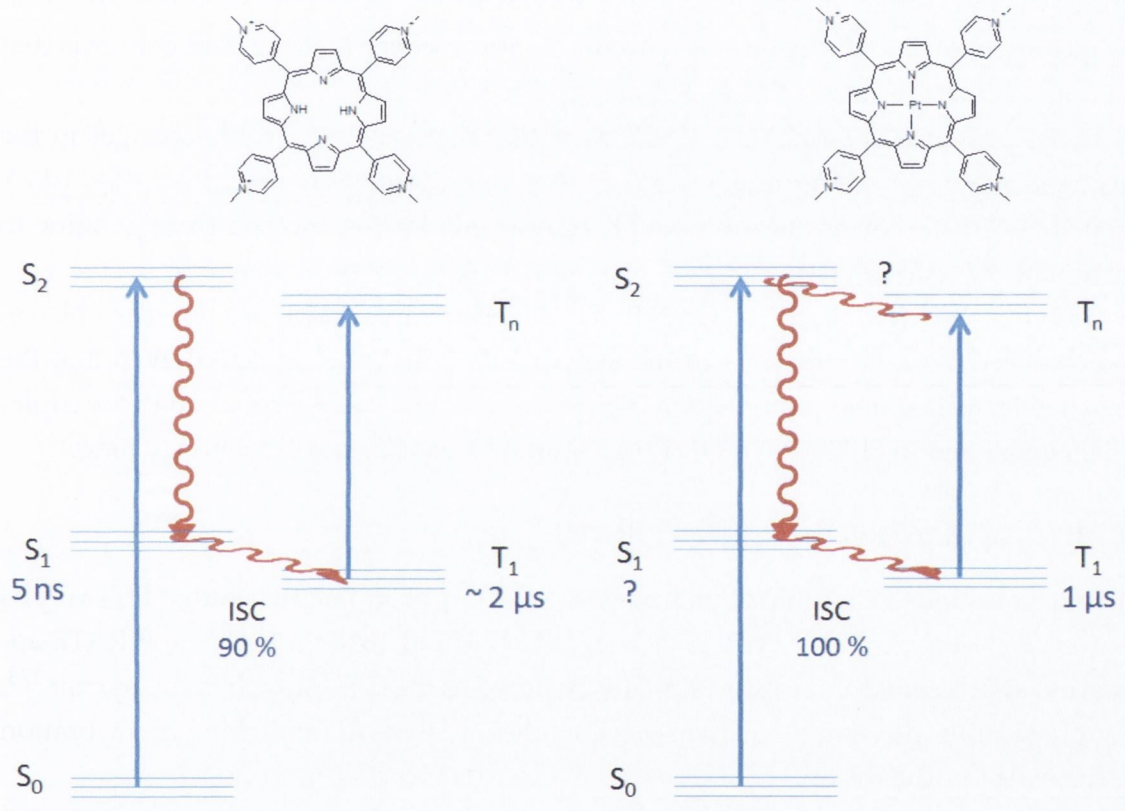

Figure 10.9: The relevant excited-state decay pathways in H_2TMPyP4 and PtTMPyP4 following 400 nm laser excitation in air-equilibrated solution

10.2.1 H_2TMPyP4 and H_2TMPyP4-GMP

10.2.1.1 UV/vis 400 nm Excitation – ULTRA

TA data is presented for times ≥ 4 ps. Earlier timed delays were also recorded but showed the effects of group velocity dispersion (also known as 'chirping', see chapter 13) so were removed.

The transient spectra of H_2TMPyP4 (Fig. 10.10 on the next page) show a strong transient band around 450 nm, and a broad weak transient in the 500-700 nm region. Kinetic fitting was performed at long delays, and lifetimes of c. 5 ns were found (Fig. 10.11 on the facing page). This is consistent with the S_1 fluorescence lifetime, and confirms that the initial spectrum shows the $S_1 \rightarrow S_n$ absorption spectrum.

In the presence of GMP (Fig. 10.12, page 182) there are no notable changes in the spectrum shape. However much shorter lifetimes (<200 ps) were recorded (Fig. 10.13, page 182). This is consistent with the photoinduced electron transfer from guanine to the S_1 state of H_2TMPyP4.

Both the H_2TMPyP4 and H_2TMPyP4-GMP spectra are notable for the lack of baseline recovery over the timescale of the experiment. This is as expected given that the long-lived triplet state is populated in high yields (see Fig. 8.22). Even though the triplet is also quenched in H_2TMPyP4-GMP, its lifetime (1.2 μs[224]) is still relatively long.

10.2.1.2 TRIR 267 nm Excitation – PIRATE

During a previous visit to RAL, members of the Kelly group observed that H_2TMPyP4 showed an intense transient and bleach signal at around 1640 cm^{-1} on the PIRATE apparatus. This bleach band is provisionally assigned as the C=N stretch in the pyrrole[173], though possible alternative assignments include C-C aromatic stretching or a vibration on the *meso* pyridyl group.

We repeated the experiment with H_2TMPyP4 and low GMP concentrations (10 mM) on the PIRATE system (Fig. 10.14, page 183). This experiment was performed at 267 nm where both GMP and H_2TMPyP4 absorb. The porphyrin bleach and transient are seen at 1640 cm^{-1}. Tracking of the fast transient decays is observed, which is indicative of vibrational cooling of the ground-state.

The porphyrin transient and bleach absorptions were decoupled by using Voigtian fitting analysis (Fig 10.15a, page 184). The peak width and shape were determined from the fitted ground-state spectrum (Fig. 10.15c), and kinetics were then calculated from the areas under the fitted Voigtian functions. Biexponential decay was observed, with a short component that is possibly due to vibrational cooling (Fig. 10.15b,d). The long component is provisionally assigned to the quenching of the porphyrin singlet state by GMP, as it is of similar magnitude to the lifetimes recorded by TA.

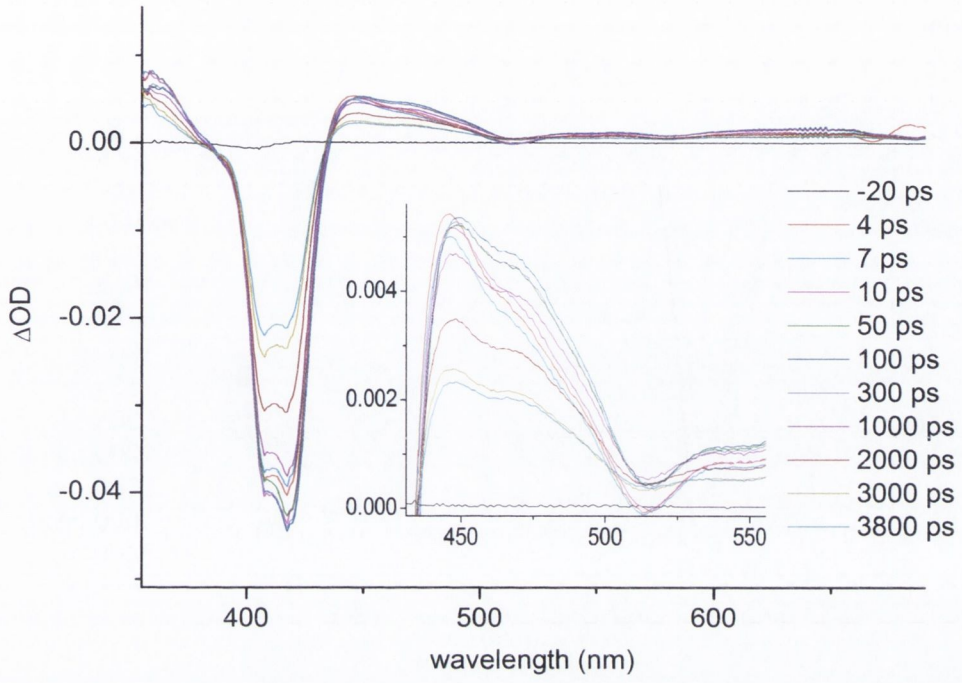

Figure 10.10: TA spectrum of ~0.5 mM H_2TMPyP4 on ULTRA. Some decays removed for clarity. In 50 mM Na-phosphate pH 7 in H_2O $\lambda_{pump} = 400$ nm

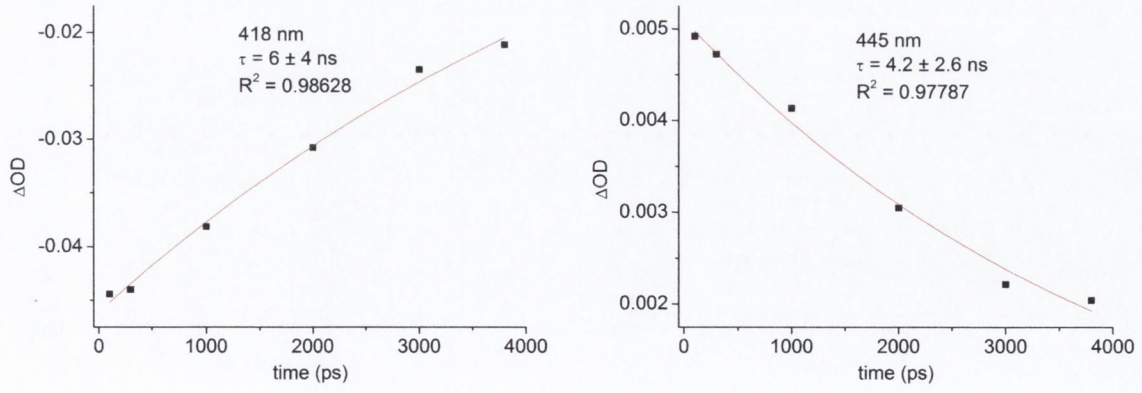

Figure 10.11: Kinetic fits to bleach and transient maxima of H_2TMPyP4. In 50 mM Na-phosphate pH 7 in H_2O $\lambda_{pump} = 400$ nm (ULTRA)

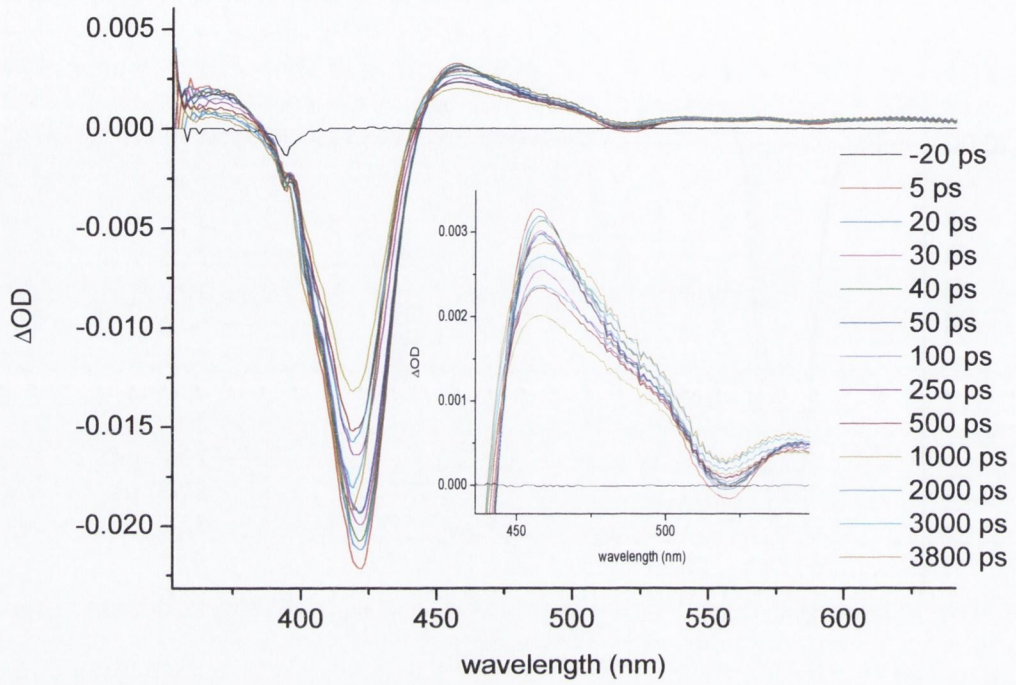

Figure 10.12: TA spectrum of ~0.5 mM H_2TMPyP4 in 10 mM GMP on ULTRA. Some decays removed for clarity. In 50 mM Na-phosphate pH 7 in H_2O $\lambda_{pump} = 400$ nm

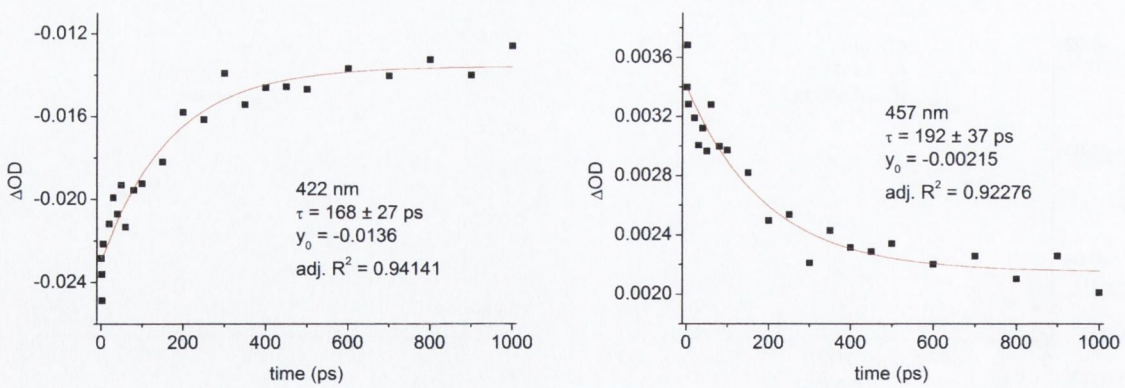

Figure 10.13: Kinetic fits to bleach and transient maxima of ~0.5 mM H_2TMPyP4 in 10 mM GMP on ULTRA. In 50 mM Na-phosphate pH 7 in H_2O $\lambda_{pump} = 400$ nm

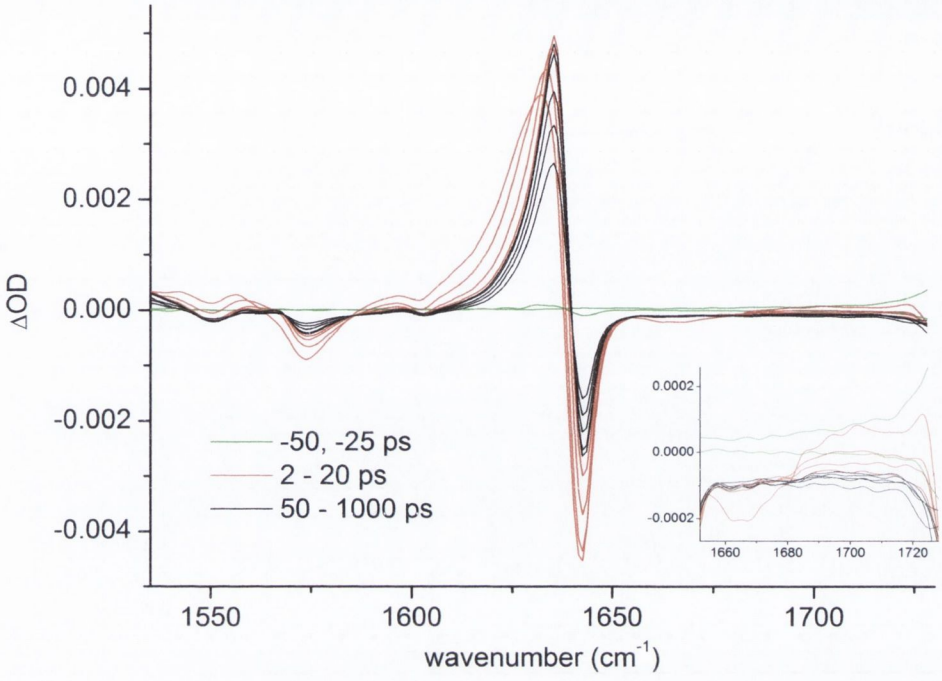

Figure 10.14: TRIR spectrum of 10 mM H_2TMPyP4 and 10 mM GMP. In 50 mM Na-phosphate pH 7 in D_2O, λ_{pump} = 266 nm, 25 μM spacer (PIRATE)

An expanded view of the 1580 cm^{-1} region (Fig. 10.16 on the next page) shows a bleach that is absent for the free porphyrin, and is likely to be due to the ring vibrations of guanine. Again, biexponential decay is observed, with a short component that matches the vibrational cooling lifetime of GMP[109]. The longer-lived decay may be related to the stacking interaction between the H_2TMPyP4 and GMP. There is also an apparent small absorption around 1700 cm^{-1}, the region where the guanine radical cation is believed to absorb[127,298]. However this feature occurs in a region close to the edge of the IR window, and may not be reliable.

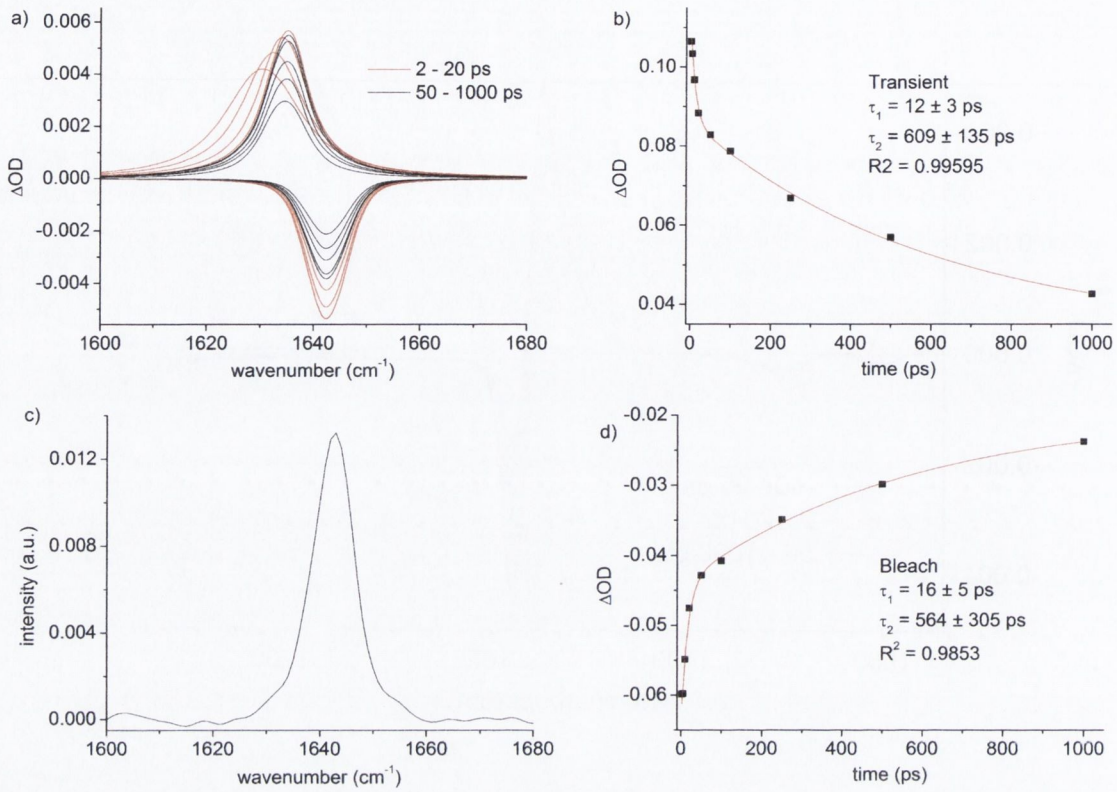

Figure 10.15: Fitted data for H_2TMPyP4-GMP system on PIRATE (a) Voigtian fits to bleach and transient at c. 1640 cm^{-1} (b) and (d) Biexponential fits calculated from areas of Voigtian curves (c) FTIR of 1640 cm^{-1} region of H_2TMPyP4-GMP in 50 mM Na-phosphate pH 7 in D_2O

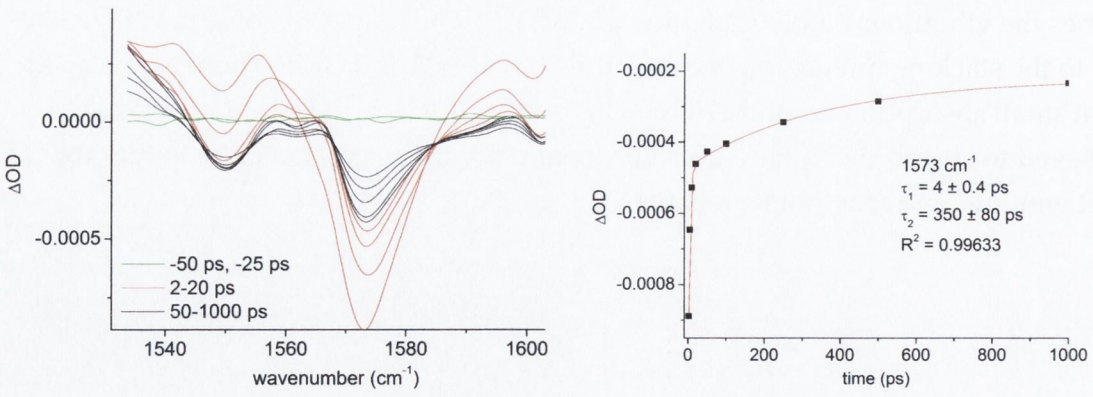

Figure 10.16: LEFT: Guanine ring bleach region for H_2TMPyP4-GMP and RIGHT: Corresponding biexponential fit. In 50 mM Na-phosphate pH 7 in D_2O. $\lambda_{pump} = 267$ nm

10.2.1.3 TRIR 400 nm Excitation – ULTRA

Later experiments were performed on ULTRA over a wider spectral region, and with 400 nm excitation (Fig. 10.17). The data does not afford any improvement in kinetics over what was recorded on PIRATE, but the main observation is the presence of a transient feature at 1515 cm^{-1}. This feature grows in with an apparent rise-time of 30 ps when fitted to an exponential model.

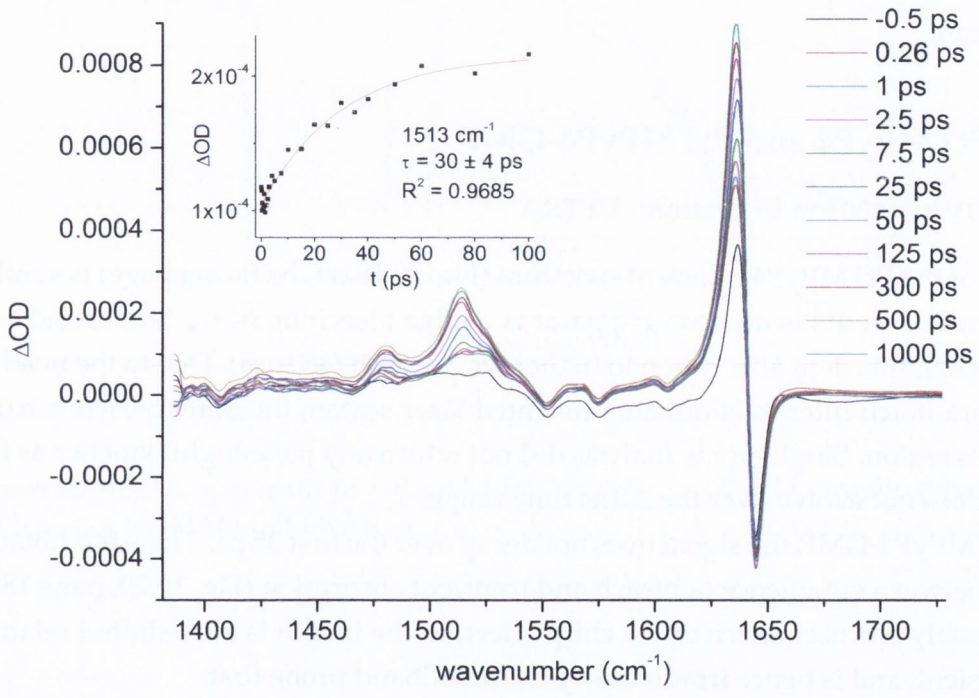

Figure 10.17: TRIR spectrum of ~0.5 mM H_2TMPyP4 in 10 mM GMP. In 50 mM Na-phosphate pH 7 in D_2O, λ_{pump} = 400 nm, (ULTRA)

10.2.1.4 Discussion on H_2TMPyP4 and H_2TMPyP4-GMP Complexes

The photophysics of H_2TMPyP4 and H_2TMPyP4-GMP complexes have been well characterised [155,181,182,188,222–224], so the transient data on these systems may be interpreted with some confidence.

The quenching of the transient lifetime in the presence of GMP corresponds to the rate of forward electron transfer, as it accounts for the disappearance of the S_1-S_n absorption. In certain studies, the bleach recovery has been used to collect information on

the reverse electron transfer, as the acceptor radical is re-oxidised to the ground state species[299]. However it is not clear in this system if the bleach recovery is a measure of the reverse transfer, as the kinetics of bleach and recovery are very similar, and reverse transfer may be occurring at a faster rate.

The most notable result from these experiments was that there was still no direct evidence for the photo-oxidation of guanine by H_2TMPyP4. Notably rapid reverse transfer rates in excess of $10^{12}\,s^{-1}$ have been reported for substituted acridine-TMPy derivatives[232,233], although there may still be a better chance of observing photoproducts if the ultrafast experiments were performed using a detector with good sensitivity above 700 nm.

10.2.2 PtTMPyP4 and PtTMPyP4-GMP

10.2.2.1 UV/vis 400 nm Excitation - ULTRA

The shape of the PtTMPyP4 transient spectrum (Fig. 10.18 on the facing page) is similar to that recorded on the nanosecond apparatus, with a bleaching of the Soret band and an overlapping transient absorption to higher wavelength (450 nm). Due to the need to use a 400 nm notch filter to eliminate unwanted laser scatter, the Soret bleach is truncated in this region. Single-point analysis did not return any meaningful kinetics as the spectrum does not evolve over the 3.8 ns time range.

For PtTMPyP4-GMP, the signal does not decay over the first 35 ps. There is a notable time shift between emergence of bleach and transient absorption (Fig. 10.20, page 188). This is possibly a consequence of the chirp effect, as the bleach is blue-shifted relative to the transient, and is hence irradiated by the broadband probe first.

At longer delays (up to 3800 ps), the signal actually grew in rather than decayed. This was also observed on some other samples such as H_2TMPyP4-AMP. We believe it is due to drift of the pump beam at long delay times.

10.2.2.2 TRIR 400 nm Excitation - ULTRA

PtTMPyP4 was initially examined on the PIRATE system, and experiments subsequently repeated on ULTRA (Fig. 10.21, page 189). There are two notable features in the spectrum, the transient/bleach region around $1640\,cm^{-1}$ and the transient at $1517\,cm^{-1}$. Both these features are similar to those observed in H_2TMPyP4.

The bleach and transient grow in over the first picoseconds after the excitation pulse. However it can be seen (Fig. 10.22 on page 189) that the $1515\,cm^{-1}$ transient does not appear until 1.5–2 ps after the formation of the $1640\,cm^{-1}$ transient/bleach. This suggests they may be due to different species. These features do not recover within the 1 ns

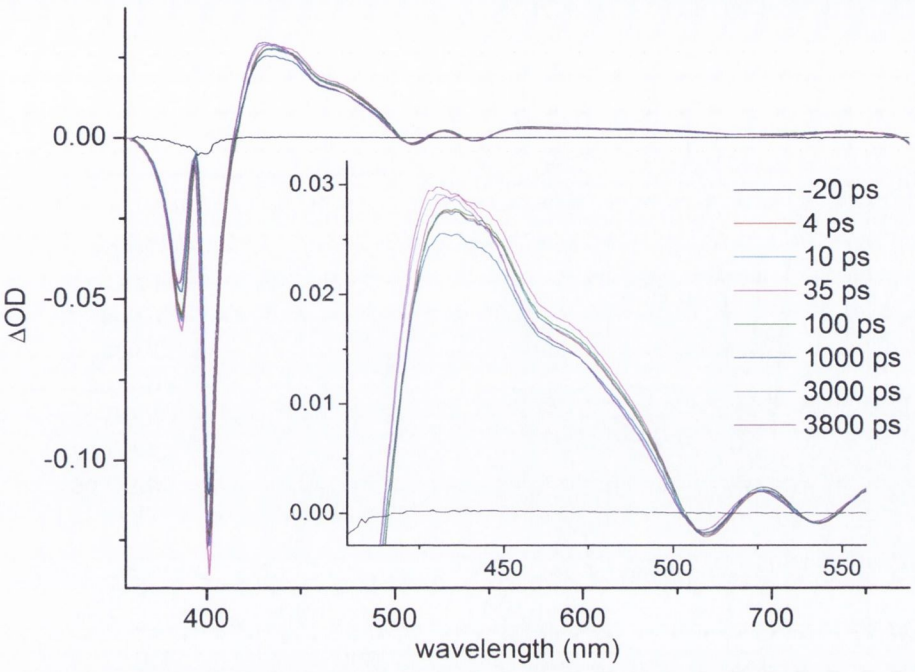

Figure 10.18: TA spectrum of ~0.5 mM PtTMPyP4. In 50 mM Na-phosphate pH 7 in H_2O, λ_{pump} = 400 nm (ULTRA)

timescale of the experiment.

The bleach and transient bands are not affected by the presence of GMP (Figs. 10.23 and 10.24 on page 190). However a new bleach feature appears at 1580 cm^{-1} in the region where the GMP ring absorbs. Kinetics could be fit in this region to a biexponential model (Fig. 10.25). The lifetimes of 4.0 ps and 0.4 ps closely match those previously recorded for the S_1 ($^1\pi\pi^*$) and S_0 vibrational cooling lifetimes respectively[5,109]. However, as can be seen from Fig. 10.19, this bleach attains a constant absorbance value and does not recovery on the 1 ns timescale.

There is also a weak transient absorption at 1700 cm^{-1} that is absent in the spectrum of free PtTMPyP4. This is the region of the guanine radical cation, but as mentioned earlier, the signal is quite weak and cannot be assigned with certainty.

Interestingly the guanine carbonyl bleach, expected around 1650 cm^{-1}, is not observed in the TRIR spectra. This suggests that the ring and carbonyl modes of GMP are affected differently by the presence of PtTMPyP4.

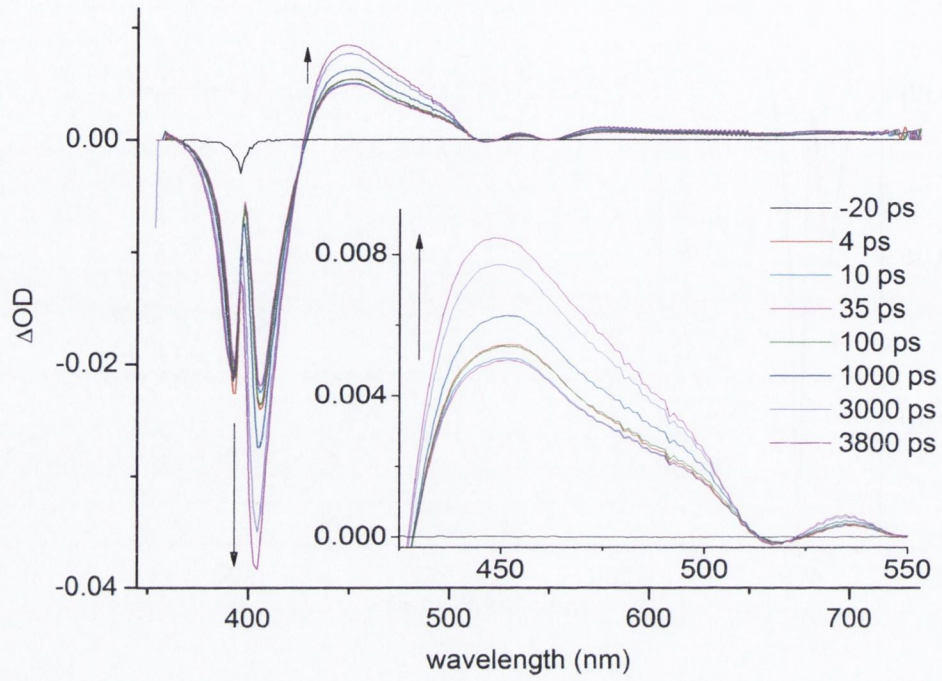

Figure 10.19: TA spectrum of ~0.5 mM PtTMPyP4 and 10 mM GMP. In 50 mM Na-phosphate pH 7 in H_2O, λ_{pump} = 400 nm (ULTRA)

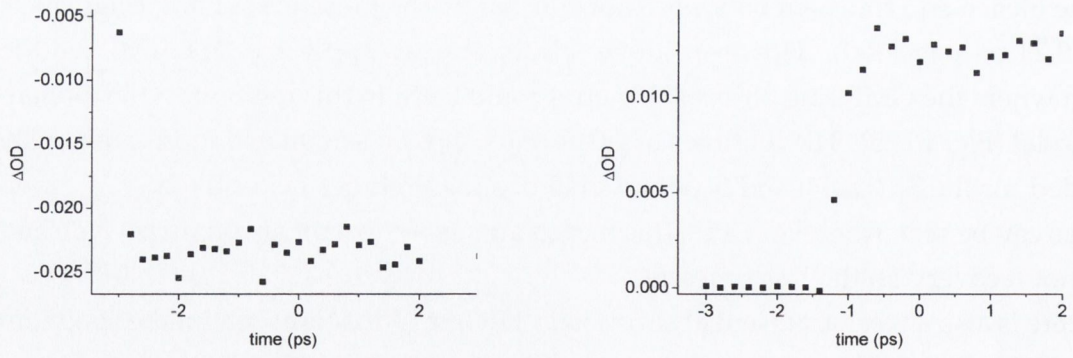

Figure 10.20: Evolution of LEFT: bleach (400 nm) and RIGHT: transient (440 nm) signals in PtTMPyP4-GMP over first few picoseconds. In 50 mM Na-phosphate pH 7 in H_2O. λ_{pump} = 400 nm (ULTRA)

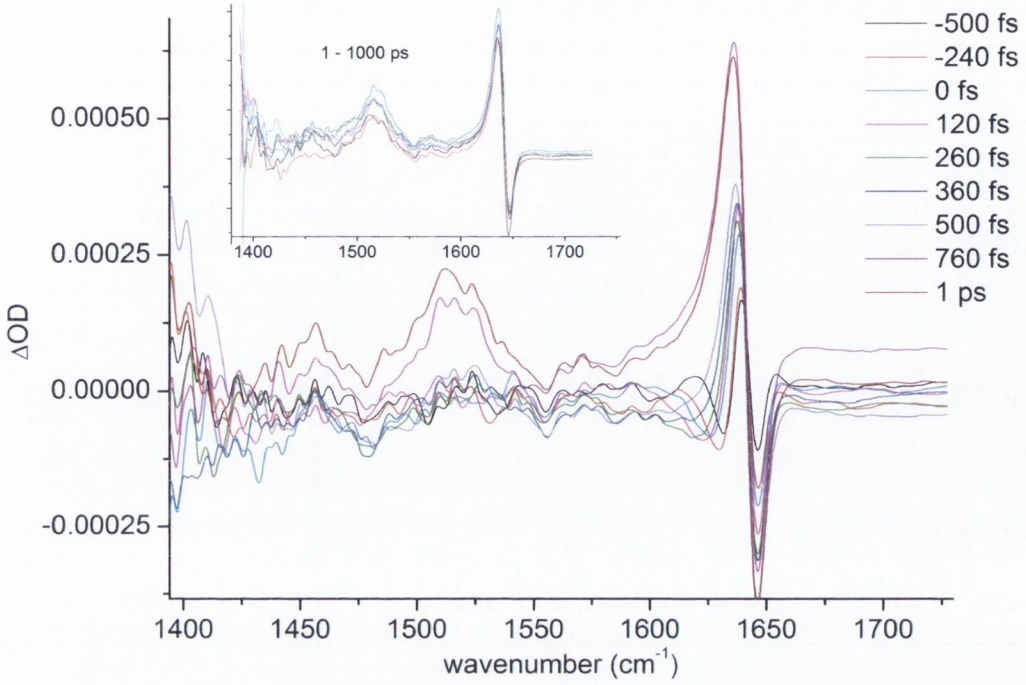

Figure 10.21: TRIR spectrum of ~0.5 mM PtTMPyP4. In 50 mM Na-phosphate pH 7 in D_2O, λ_{pump} = 400 nm (ULTRA)

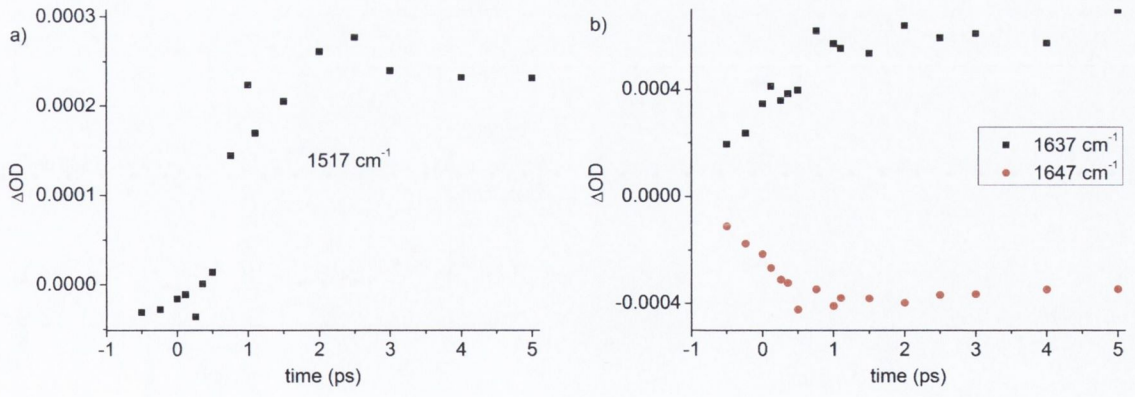

Figure 10.22: Evolution of (a) bleach at 1517 cm^{-1} and (b) bleach and transient in 1640 cm^{-1} region of ~0.5 mM PtTMPyP4. In 50 mM Na-phosphate pH 7 in D_2O, λ_{pump} = 400 nm (ULTRA)

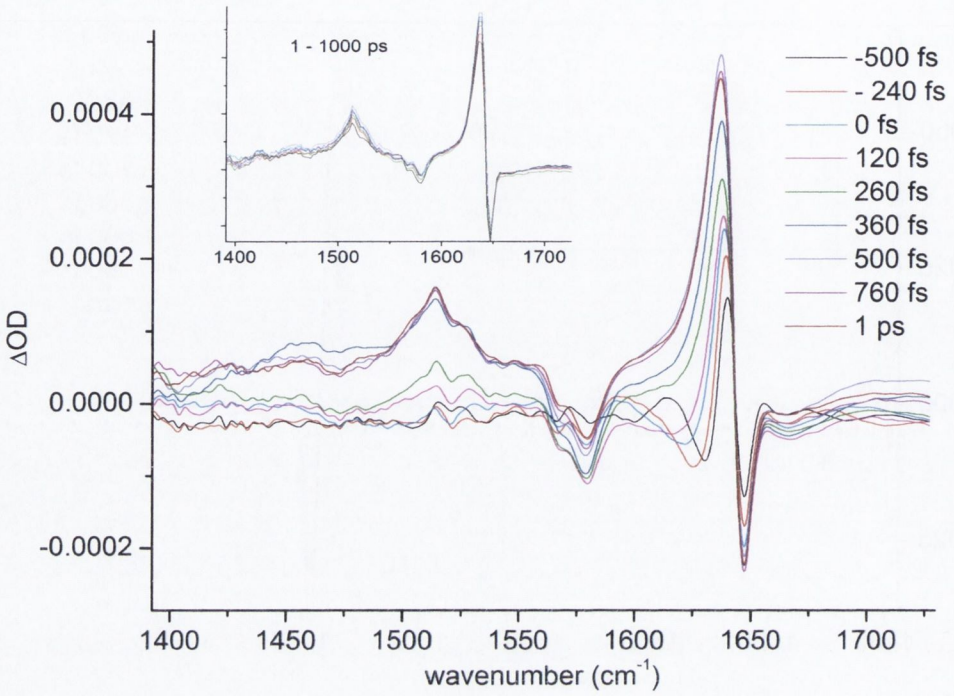

Figure 10.23: TRIR spectrum of ~0.5 mM PtTMPyP4 and 10 mM GMP. In 50 mM Na-phosphate pH 7 in D_2O, λ_{pump} = 400 nm (ULTRA)

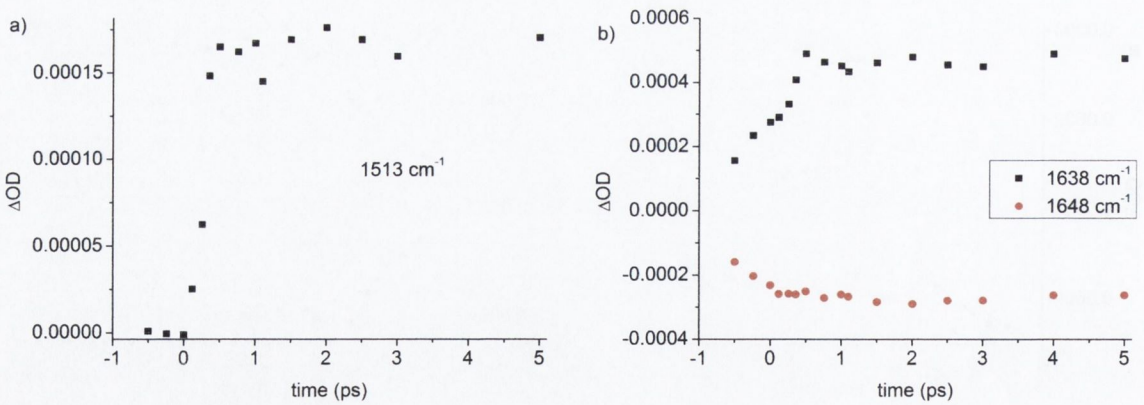

Figure 10.24: Evolution of (a) bleach at 1513 cm^{-1} and (b) bleach and transient in 1640 cm^{-1} region of ~0.5 mM PtTMPyP4 in 10 mM GMP. In 50 mM Na-phosphate pH 7 in D_2O, λ_{pump} = 400 nm (ULTRA)

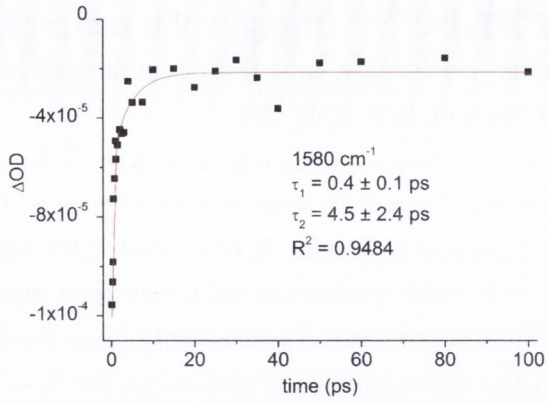

Figure 10.25: Kinetic fit to guanine bleach region in ~0.5 mM PtTMPyP4 in 10 mM GMP following 400 nm excitation. In 50 mM Na-phosphate pH 7 in D_2O (ULTRA)

10.2.2.3 Discussion on Intersystem Crossing in PtTMPyP4

In principle, the $S_1 \rightarrow T_1$ intersystem crossing should be observable as a change from S-S to T-T absorption, in either the UV/vis or IR regions. However, the intense S-S and T-T absorptions of many porphyrins overlap in the visible region. As a result it can be difficult to distinguish one species from the other, and certainly difficult to get sufficient absorption differences and hence reliable kinetics for the transition.

The ultrafast spectra on PtTMPyP4, whether recorded by UV/vis or IR, demonstrate lack of decay over the first few nanoseconds. The transient observed at the longest delays (i.e. after 3800 ps) would therefore be expected to be the triplet state. In the UV/vis this transient is recorded immediately after the laser pulse, which suggests that either the triplet is formed very rapidly (c. 1 ps), or the S_1 and T_1 state have very similar absorption spectra. Previous reports have indeed shown only very small differences between absorption spectra of S_1 and T_1 states of metalloporphyrins[150].

In the TRIR, we speculated that the feature at 1515 cm^{-1} in PtTMPyP4 may be due to the triplet state. The evidence in support of this is the fact that the growth of the 1515 cm^{-1} transient is delayed relative to the bleaching at 1643 cm^{-1}, and the fact that the transient feature at 1638 cm^{-1} changes shape with time. The fact that it does not decay over the 4 ns timescale is consistent with it being relatively long-lived. The presence of this band in H_2TMPyP4 argues against this model somewhat, as the formation of the triplet in H_2TMPyP4 should be relatively slow (rise time c. 5 ns).

The second explanation is that the 1515 cm^{-1} transient is a feature common to both S_1 and T_1 states. This model reconciles the data from H_2TMPyP4 and PtTMPyP4, namely the rapid formation (within 30 ps) of the transient in the former. A final possibility is that the IR characteristics correspond to an intramolecular CT state, that is

believed to occur in H_2TMPyP4[159,222]. However this is expected to be suppressed in the presence of a π-stacked nucleotide, and there has never been any suggestion that this state is accessible in the metalloporphyrins.

A c. 1 ps lifetime for the S_1 state equates favourably with $S_1 \rightarrow T_1$ intersystem crossing of other Pt(II) porphyrins. Upper lifetime limits of 8 ps and 15 ps have been placed on the S_1 states of Pt(II) protoporphyrin IX dimethyl ester and Pt(II) octaethylporphyrin, respectively[300,301]. A value as short as 500 fs has been reported in Pt tetraphenyltetrabenzo porphyrins[302]. In some cases the similarity been the S_1 and T_1 spectra have been noted[301,302], reiterating the subtleties of observing the $S_1 \rightarrow T_1$ transition by TA.

10.2.2.4 Discussion on Electron Transfer in PtTMPyP4-GMP

The ultrafast UV/vis spectra do not provide much information on the electron transfer between PtTMPyP4 and GMP, which is presumably because the electron transfer is expected to occur at much longer timescales.

However the presence of guanine bleach features on the TRIR of PtTMPyP4-GMP was intriguing, since guanine should not be excited at 400 nm (Fig. 10.23, page 190). We therefore considered that depopulation of the guanine ground-state was due to photooxidation of guanine, yielding the radical cation at 1700 cm^{-1}. The bleach would then be expected to recover at the reverse electron transfer rate. However we have found that the removal of the GMP ground-state occurs within the instrument response, while we expect the electron transfer to occur on the nanosecond scale. Also, there is no evidence for any photoreduction of PtTMPyP4 from the TRIR.

Alternatively the presence of the G ring bleach may be due to a different interaction with the PtTMPyP4 excited state than its ground state. This may include a stronger stacking interaction in the excited state, as implied from the large K_e values (30,000 M^{-1}) calculated for PtTMPyP4-AMP in the previous chapter. Such an interaction would be expected to suppress the ring mode but not affect the carbonyl to the same extent, and this would be consistent with the absence of a carbonyl bleach in the TRIR.

It is difficult to reconcile the ultrafast and nanosecond experiments, as the nanosecond data shows quenching on a timescale from 10s-100s of nanoseconds, which may be too slow to observe by ultrafast spectroscopy. Based on the kinetics for the PtTMPyP4-GMP system and the dependence on GMP concentration observed in this and the previous chapter, the following kinetic scheme is proposed (Fig. 10.26 on the next page).

A notable implication of this model is that the electron transfer in the PG_2 complex would be less efficient than in PG. This may occur if the porphyrin and GMP are oriented in such a way in the PG_2 molecule that electron transfer is less favourable than

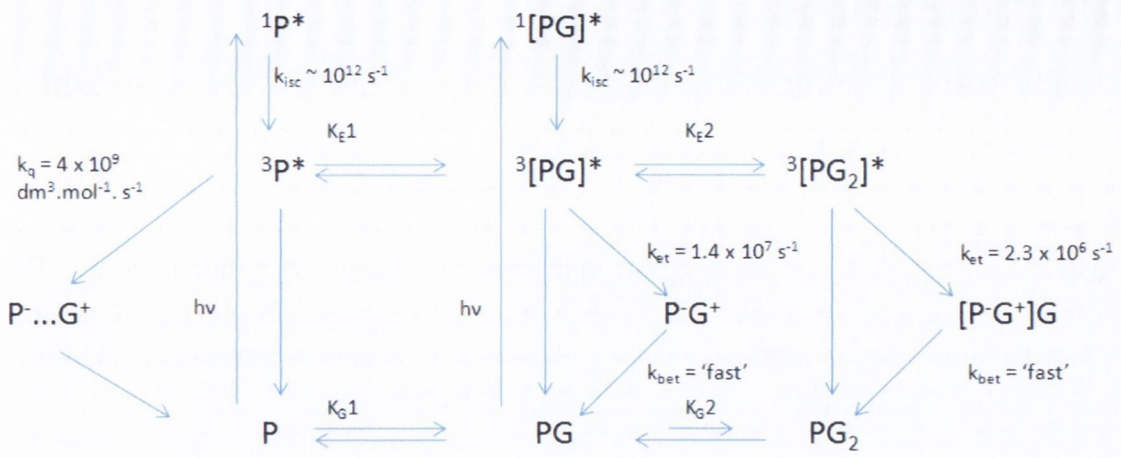

Figure 10.26: Proposed photophysical scheme for association of PtTMPyP4 with GMP in ground and excited states

in PG. Another possibility is that the presence of one stacked GMP anion lowers the reduction potential of the PtTMPyP4 triplet state. This is consistent with the reduction in quenching efficiency when the porphyrin is bound to polymeric G sequences such as $[poly(dG\text{-}dC)]_2$, DNA, poly(rG) or TGGGGT. A precedent from the literature is methylene blue, which was quenched less efficiently by poly(rG) than GMP, where the dye was sandwiched between two G moieties in the former[303]. Chirvony and coworkers have also suggested on a number of occasions that electron transfer processes in TMPy-nucleic acid systems are very sensitive to orientation[189,222,224].

The photophysical measurements suggest that forward transfer is relatively slow and the back transfer relatively fast. An approximate driving force for the recombination can be estimated from Eq. 10.1

$$\Delta G_{reverse} = -[E_{00,T} + \Delta G_{forward}] \tag{10.1}$$

When $E_{00,T}$ is 1.86 eV (from phosphorescence max at 666 nm), and $\Delta G_{forward}$ is 0.12 eV, then $\Delta G_{reverse}$= 1.74 eV. This is highly exergonic, and although it is placed in the Marcus inverted region, a large rate constant may be expected. The efficiency of reverse transfer is supported by previous experiments suggesting that PtTMPyP4 is primarily a type 2 photo-oxidant, and a less effective type 1 photo-oxidant than H_2TMPyP4[170].

10.3 Conclusions

The triplet state of PtTMPyP4 has been characterised in the UV/vis and near-IR on the nanosecond apparatus. Kinetics on the PtTMPyP4-GMP system corroborate the emission results and lead to the conclusion that multiple excited-state complexes exist, namely a 1:1 and a 1:2 complex. Direct and unambiguous evidence for an electron transfer is not found however, suggesting the reverse transfer is quite efficient. TRIR spectroscopy showed a number of features in the excited states of both H_2TMPyP4 and PtTMPyP4, with some evidence for $S_1 \rightarrow T_1$ intersystem crossing occurring in PtTMPyP4 on a picosecond timescale

Chapter 11

Photosensitised Oxidation - Conclusions and Future Work

11.1 Conclusions

PtTMPyP4 showed strong binding affinities with all nucleic-acid structures studied. With mononucleotides, a 1:1 association stoichiometry dominates, though our study revealed some of the difficulties inherent in determining the type of complex formed. The interaction with polynucleotides is similar to that observed for H_2TMPyP4, showing the classic preference for intercalation at GC sites in [poly(dG-dC)]$_2$ and double-stranded natural DNA. Multi-mode groove-binding is observed in [poly(dA-dT)]$_2$, with some evidence for self-stacking interactions at appropriate binding ratios. PtTMPyP4 also binds strongly to RNA homopolymers poly(rA) and poly(rG), but variability in the structures of these polymers means that binding modes are not assigned with certainty.

Strong affinity is found for quadruplex-forming sequences including stacked GMP and [d(TGGGGT)]$_4$, and different binding profiles are observed for four-coordinate PtTMPyP4 and five-coordinate ZnTMPyP4. The possibility exists that the PtTMPyP4 may actually disrupt, rather than stabilise, the quadruplex structure in [d(TGGGGT)]$_4$. Unfortunately a crystal structure of the porphyrin-quadruplex has not been obtained so far.

Although PtTMPyP4 is comparable to H_2TMPyP4 in many of its ground-state properties, the longer lifetime of the luminescent state means that quite different excited-state processes can be observed. The $^3(\pi\pi)^*$ phosphorescence of PtTMPyP4 is a revealing probe for its environment, being sensitive to the presence of dissolved oxygen, halide salts, and binding sites in nucleic acids. Dynamic quenching by chloride is shown to be a particularly significant observation considering the ubiquity of chloride in physiological solution, and the importance of triplet lifetime in singlet-oxygen

generation. Binding of PtTMPyP4 to mononucleotides and polynucleotides is shown to protect the chromophore from dissolved oxygen, with possible implications for the ability of the porphyrin to generate singlet oxygen.

The nucleotide studies, in particular, exemplifies the use of emission spectroscopy to distinguish different excited-state mechanism, with large enhancement in AMP compared to quenching in GMP. The latter case is the first report of photoinduced (type 1) electron transfer from a metal derivative of H_2TMPyP4 to guanine. The sensitivity of the triplet state reveals a complicated quenching process, with evidence for dynamic quenching by unbound GMP, and two complexes (assigned as PG and PG_2) depending on the GMP concentration. The proposal follows that binding is different in ground and excited state complexes. This possibility has not been considered in the previous literature, probably because excited-state binding is not readily studied when the exited-state emission lifetimes are short (*i.e.* on the ns scale).

Studies on G-rich polymers show that the electron transfer is relatively inefficient in the G-rich polymers, and does not prevent an enhancement in emission of the bound porphyrin. This suggests that the electron transfer is sensitive to the mutual orientation of donor and acceptor, and that optimal electron transfer geometry cannot be achieved in the crowded intercalation environment, similar to conclusions drawn previously about the analogous H_2TMPyP4 systems. The absence of any absorption of electron transfer photoproducts by transient spectroscopy suggests a rapid charge recombination, despite a spin-forbidden transition.

For the first time, a TRIR study of TMPy porphyrins has been reported. Distinctive marker bands are observed for both H_2TMPyP4 and PtTMPyP4, and based on these the lifetime of the S_1 $^1(\pi\pi)^*$ state of PtTMPyP4 is estimated as *ca.* 1 ps. The ultrafast IR and UV/vis data on both H_2TMPyP4 and PtTMPyP4 systems reveal features that could be interpreted as evidence for electron transfer, although they are ambiguous at present.

The relative inefficiency of the electron transfer, the apparent efficiency of the reverse transfer, and the sensitivity of the excited state to competing quenchers, all suggest that PtTMPyP4 will not be a potent type 1 photosensitiser.

The main photophysical processes in PtTMPyP4, as recorded in this work, are presented in Fig. 11.1.

11.2 Future Work

Further insight into the electron transfer may be gained by studying, for example, GTP (guanosine triphosphate) and G-containing dinucleotides (e.g. GpG, ApG, CpG etc.). In these systems binding affinities and donor-acceptor orientations can be altered. In the case of GpG, this may show the effect of having a guanine moiety stacked at either

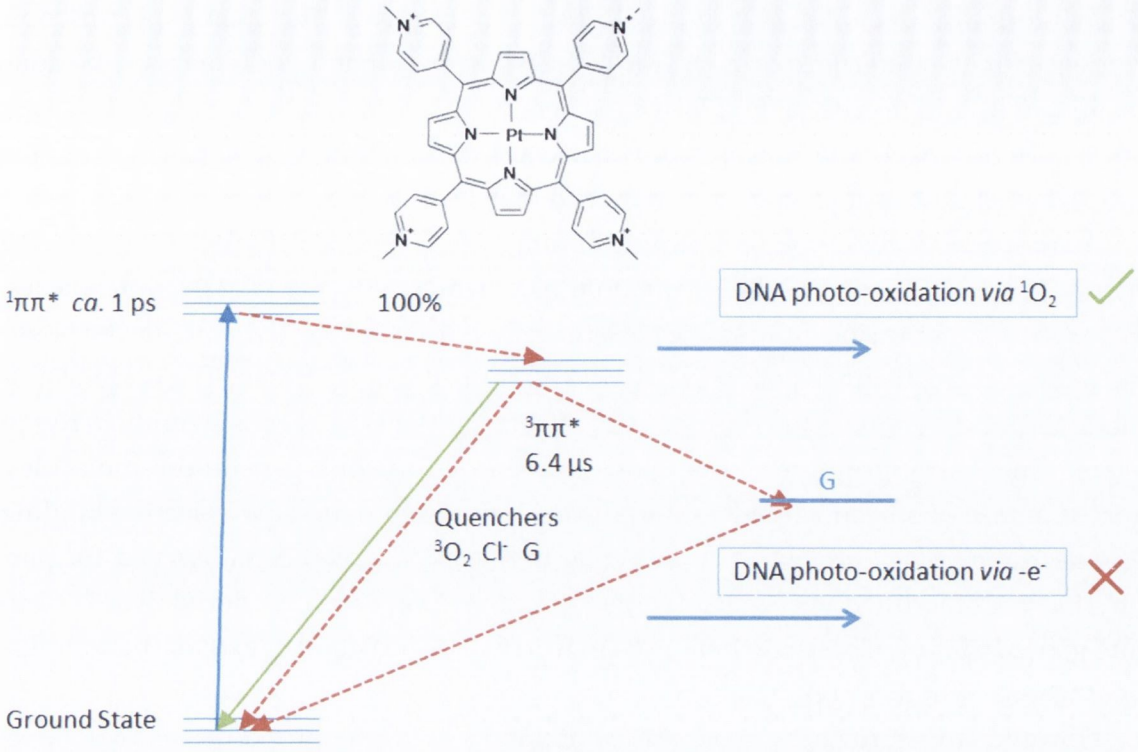

Figure 11.1: Summary of main conclusions from photophysical study of photosensitised oxidation by PtTMPyP4

face, and complement the studies already done on mono- and polynucleotide systems. It would be also interesting to repeat the experiments on GC systems in D_2O, as this may tell if electron transfer proceeds by a proton-coupled mechanism.

Further work is needed on the photosensitising ability of PtTMPyP4. Previous literature suggests that PtTMPyP4 acts by a type 2 mechanism, with little evidence for type 1 processes. In particular the formation and decay of singlet oxygen could be monitored in free and bound systems using near-IR luminescence (see e.g. Fig A.11 on page 214). This would allow us to test whether binding to DNA inhibits the ability to generate singlet oxygen. For other TMPy porphyrins, intercalation of the sensitiser into DNA results in similar yields of singlet oxygen formation, but with a longer rise time. Our preliminary comparisons of the photosensitised (λ_{exc} = 400 nm) degradation of guanine in D_2O and H_2O showed it was more efficient in the former, suggesting a type 2 process is occurring (see Fig. A.12 on page 215).

TRIR is a technique that has been used sparingly on porphyrin systems. However it is now known that they show strong characteristic features in the IR, and TRIR would

be an informative technique for future studies on porphyrins. The lack of spectroscopic evidence for electron transfer in H_2TMPyP4-GMP shows that work remains to be done on this subject. In the case of H_2TMPyP4, where there is little doubt that a type 1 process takes place, an ideal experiment would be to conduct the ultrafast spectroscopy into the near-IR where the reduced porphyrin radical may be detected.

A complete study of the quadruplex-binding properties of PtTMPyP4 requires the study of bimolecular (e.g. $G_4T_4G_4$) and unimolecular (e.g. $AG_3(T_2AG_3)_3$) quadruplexes. These structures may be more stable structures than $[d(TGGGGT)]_4$, so it may be possible to investigate the theory that PtTMPyP4 disrupts the quadruplex. The understanding of the binding modes of telomerase inhibitors has developed considerably in recent years. The TMPy porphyrins may now be regarded as 'first generation' molecules, and attention has been turned to porphyrin derivatives that show selective binding to quadruplex over duplex DNA. Selective interactions have been observed for porphyrins with modified *meso*-substituents[304], and for porphyrazine derivatives[305]. Future generations of telomerase inhibitors may in fact be designed to exploit the complex interactions with the loop regions[254].

However, much remains to be learned about excited-state properties of TMPy porphyrin in the presence of the quadruplex[253,306], in particular the specific nature of guanine photo-oxidation in the presence of G-quartets[307,308], and the efficiencies of singlet oxygen generation and diffusion in the quadruplex. Selective oxidation of telomeric guanines may be beneficial, as it would protect other vital sequences in the gene from damage[309]. This may occur if stacked guanines act as a 'thermodynamic sink', whereby the migrating positive hole in oxidised DNA is ultimately trapped at G-rich sequences[310]. Photo-oxidation would become important if photosensitising ability is built into a selective telomerase inhibitor, as it opens up opportunities for site-specific photo-oxidation at G-rich regions.

There are also fundamental questions remaining regarding the structure of PtTMPyP4. While it is assumed to be planar, there is the possibility that the structure is distorted as for other heavy metal (e.g. Hg, Cd) metalloporphyrins[151]. Crystal structure data, or DFT calculations, may help in addressing this issue. It is significant question, for example, when comparing the behaviour of H_2TMPyP4 and PtTMPyP4 in sterically restrictive intercalation environments.

Chapter 12

Concluding Remarks - Part One & Part Two

Photochemical damage of nucleic acids can occur by a number of mechanisms, and can occur from direct UV excitation or through an intermediate sensitiser molecule. We have demonstrated that the photophysical processes involved occur over orders of magnitude of timescales.

In part one, a dark state was studied in cytosine-rich nucleic acids that had lifetimes from 33 – 90 ps. Given that DNA nucleobases deposit most of the excited-state energy in under 1 ps, the presence of such a relatively long-lived state suggests that it may have a role to play in the formation of harmful photoproducts.

While very short-lived singlet states were studied in part one, part two was focussed on the much longer-lived triplet state of the PtTMPyP4 porphyrin. Here the photo-oxidation of guanine occurs over 10s to 100s of nanoseconds, while the generation of singlet oxygen would be likely on the microsecond scale. Just as cytosine can protect itself from photo-damage by ultrafast relaxation, so guanine can protect itself from type 1 photo-oxidation by PtTMPyP4, by means of efficient reverse electron transfer.

Given the different time domains studied here, it is clear that specific techniques are required in each case. For example, the excited states of cytosine are too short-lived and too weakly fluorescent to be studied by conventional emission techniques, while the phosphorescent state of PtTMPyP4 makes it readily observable.

It is also notable that direct and photosensitised excitation are of interest for different reasons. Direct UV excitation is an unavoidable natural phenomenon that DNA must protect itself from. By contrast, photosensitised reactions are more likely to be deliberately initiated to destroy harmful or unwanted tissue, notably avoiding the UV region and using visible or near-IR excitation instead.

Chapter 13

Materials and Methods

13.1 Time-Resolved Infrared – PIRATE

The PIRATE (Picosecond Infrared Absorption and Transient Excitation) apparatus[311] is located in the Lasers for Science Facility in the Rutherford Appleton Laboratories (see Fig. 13.1). Samples for IR measurements (FTIR and TRIR) were prepared in buffered (25 mM NaH_2PO_4, 25 mM Na_2HPO_4, pH 7) D_2O solution. Samples of c. 40 μL volume were dropped between two CaF_2 (25 mm dia.) windows (Crystan Ltd., UK), separated by a Teflon spacer of known pathlength (typically 56 μM), in a demountable liquid cell (Harrick Scientific Products Inc., New York). The sample was excited with 267 nm, 200 fs pulses with c. 2 μJ of energy at 0.5 kHz repetition rate, generated from the third harmonic of part of the output from a 1 kHz, 800 nm, 200 fs, 1 mJ regenerative amplifier (Spectra Physics Tsunami/Spitfire) and probed with 150 cm^{-1} FWHM broadband infrared pulses generated by difference–frequency mixing the signal and idler outputs of a BaB_2O_4 optical parametric amplifier, pumped with some residual 800 nm, in $AgGaS_2$ at 1 kHz. The spot size was 200 μm and 150 μm diameter for the pump and the probe beam, respectively. The sample was raster scanned in x- and y- directions at an approximate rate of 100 mm/ms. The difference signal (pump-on minus pump-off) was normalized on a shot-by-shot basis and typically accumulated for four successive rounds of 30 s data integration for a single time delay. The infrared beams were dispersed by 150 l/mm, 4000 nm blaze, gold grating monochromators and imaged onto a 64 element HgCdTe (MCT) array. The data were collected in a number of 150 cm^{-1} spectral windows using the delay line for optical delays between 2 ps and 1.5 ns.

The difference signal was calibrated using water vapour absorption lines present in the probe spectrum (Fig. 13.2). Corroborating data was obtained by matching bleaches in the TRIR to the FTIR spectrum. As the MCT detector array pixels are linear with respect to wavelength, calibration was performed in wavelength units before final con-

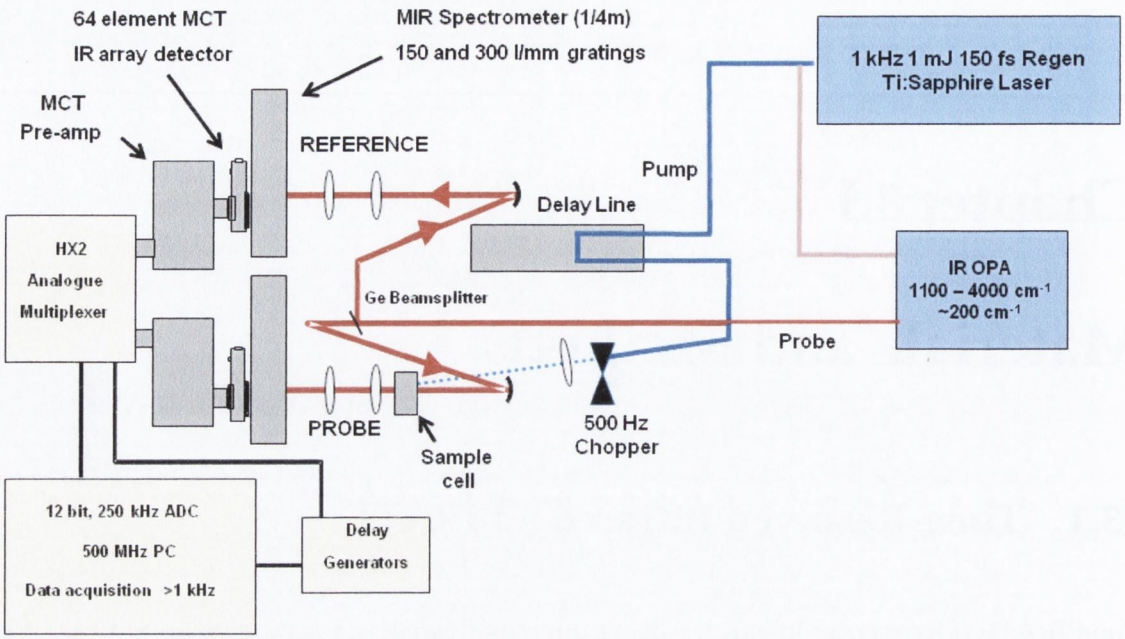

Figure 13.1: PIRATE apparatus

version to wavenumbers. Spectral windows were interleaved ('stitched') after calibration, preferably at isosbestic points in the difference spectrum. Scaling, where necessary, was performed using overlapping transients recorded at the same delay time.

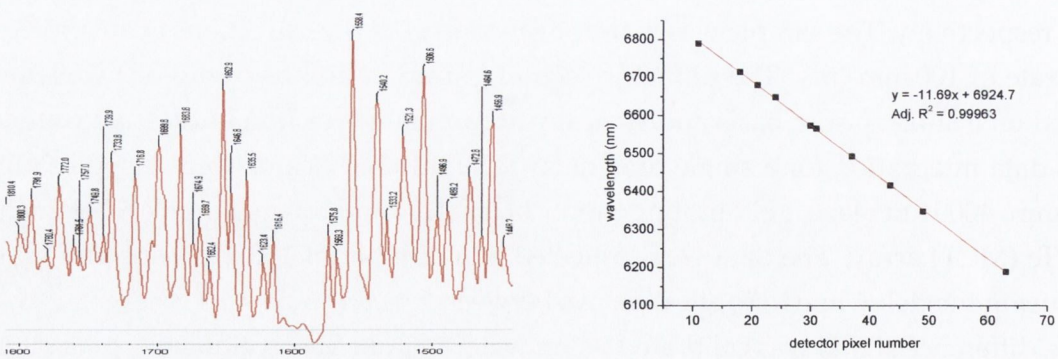

Figure 13.2: LEFT: Spectrum of water vapour used to calibrate PIRATE data. RIGHT: Example of a calibration plot, linear in wavelength

13.2 Time-Resolved Infrared and UV/vis Absorption – ULTRA

The ULTRA apparatus[312] is located in the Lasers for Science Facility at the Rutherford Appleton Laboratories. Samples were prepared as described in Section 13.1. Briefly, the time-resolved IR (TRIR) spectrometer comprises of a 10 kHz repetition rate titanium sapphire dual output amplifier (Thales), producing two synchronised 0.8 mJ outputs with 40 fs and 2 ps pulse durations, both at 800 nm. Optical parametric amplifiers (Light Conversion, TOPAS) and third harmonic generation of the 800 nm crystals created the mid-infrared radiation and 266 nm femtosecond UV pump pulses used for direct DNA excitation, while the second harmonic created the 400 nm pump used in the photosensitiser experiments. The pump pulses at the sample were at magic angle with energy of 1.5 microjoules. The IR probe beam was split to form the reference and probe beams, and were passed through spectrographs onto MCT array detectors (IR Associates). The 266 nm pump pulses were focussed (c. 100 μm spot sizes) and overlapped with the probe beam (c. 50 μm spot size) in the sample cell. High speed data acquisition systems (Quantum Detectors) allowed 10 kHz acquisition and processing of the probe and reference pulses to generate a pump-on pump-off infrared absorption difference signal. The sample was raster scanned in x- and y- directions at an approximate rate of 100 mm/ms. The difference signal in TRIR mode was calibrated using the characteristic cis-stilbene absorption lines[313]. The difference signal in UV/vis TA mode was calibrated against a selection of five visible-light filters.

Early spectra recorded on ULTRA were uncorrected for group dispersion, also known as 'chirping' (see Fig. 13.4). This was caused by the slower speed of blue light in the broadband visible probe, which resulting in red light lagging a few femtoseconds be-

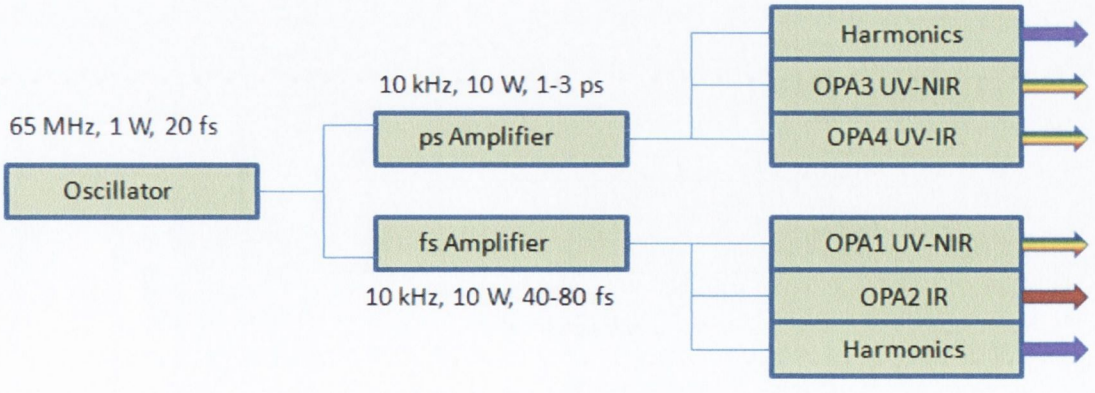

Figure 13.3: Generation of multipurpose pump-probe beams in the ULTRA apparatus

hind blue light. As a result, early spectra (<4 ps) could not be included in some data.

13.3 Nanosecond Transient Absorption Spectroscopy

Transient absorption spectra and kinetics, and phosphorescence lifetimes, were recorded on an Edinburgh Instruments FP920 kinetic absorption spectrometer. The pump excitation source was the 355 nm emission from a water-cooled, frequency trebled Nd:YAG laser (Spectron), with 10 ns pulse width, operating at 10 Hz. Pulse energy was ca. 20 mJ. The probe source was a 450 W air-cooled pulsed Xenon lamp. A Cerzy-Turner monochromator was used with both 1800 g/mm, 500 nm (UV/vis) and 600 g/mm, 1000 nm (Near-IR) blazed gratings. Signals in the UV/vis and near-IR ranges were recorded on R955 and R5108 photomultiplier tubes, respectively (both Hamamatsu Photonics), with a Tektronix 100 MHz two-channel oscilloscope. A 600 nm long pass filter (Andover Corp.) was used for phosphorescence lifetime and near-IR transient absorption measurements to eliminate second order laser light and triplet-triplet absorption, respectively.

13.4 Nanosecond Time-Correlated Single Photon Counting

Fluorescence lifetimes were recorded on a JobinYvon Horiba Fluorolog®TCSPC. Excitation sources was a 370 nm NanoLED (pulse width c. 1 ns, pulse repetition 10 kHz -

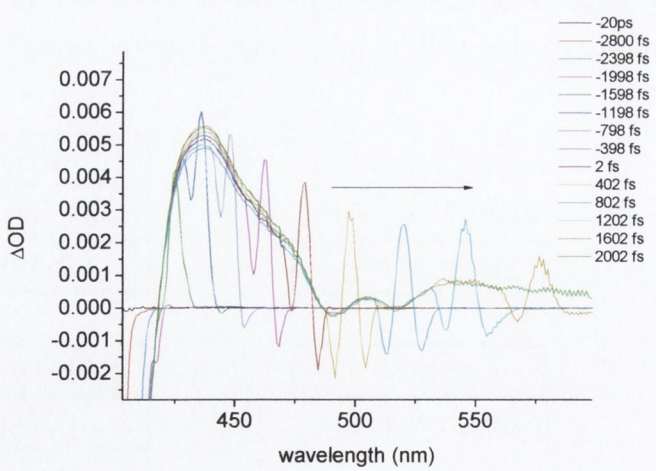

Figure 13.4: Example of the chirp effect at short time delays on ULTRA. Sample is PtTMPyP4 with GMP

1 MHz)) passed through a UG1 Schott filter onto an R928 PMT. Fluorescence lifetimes (Section 9.1) were also recorded on an Edinburgh Instruments FL920 TCSPC spectrometer, with excitation from a 371 nm pulsed diode laser (Hamamatsu Photonics) onto a Peltier-cooled red-sensitive R2658P PMT (Hamamatsu Photonics). Correction for instrument response, where necessary, was made by recording the scatter signal at identical excitation/emission wavelength with a solution of colloidal silica (Ludox®).

13.5 FTIR

FTIR spectra were recorded on a Perkin-Elmer 2000FTIR (TCD) spectrometer or a N_2 purged Nicolet Avatar FTIR spectrometer (RAL). Samples were prepared as described earlier (Section 13.1).

13.6 UV/vis Absorption Spectroscopy

UV-vis spectra were recorded on a Cary 50 scan, Shimadzu UVPC2401 spectrophotometer, or a Perkin-Elmer Lambda1050 spectrophotometer (RAL). Melting curves were recorded on a Perkin-Elmer Lambda35 UV/vis spectrophotometer coupled to a PTP 1 Peltier temperature controller.

13.7 Circular Dichroism

Circular dichroism spectra were recorded on a JASCO J810 spectropolarimeter. Spectra were typically accumulated at least 8 times.

13.8 Steady-State Emission Spectroscopy

Emission spectra were recorded on a Perkin-Elmer LS55 fluorimeter operating in phosphorescence mode for decays in the microsecond region. Delay time was set to 0, and gate time set to 200-400 μs. Correction of photomultiplier response (Fig. 13.5) was made using a solution of 4-dimethylamino-4'-nitrostilbene (DMANS) in orthodichlorobenzene (ODCB)[293].

13.9 X-Ray Crystallography

Crystallisation trials were set up using the sitting-drop method in 6 x 4 crystallisation trays (Figs 13.6 and 13.7), and afterwards left in a 4°C cold room.

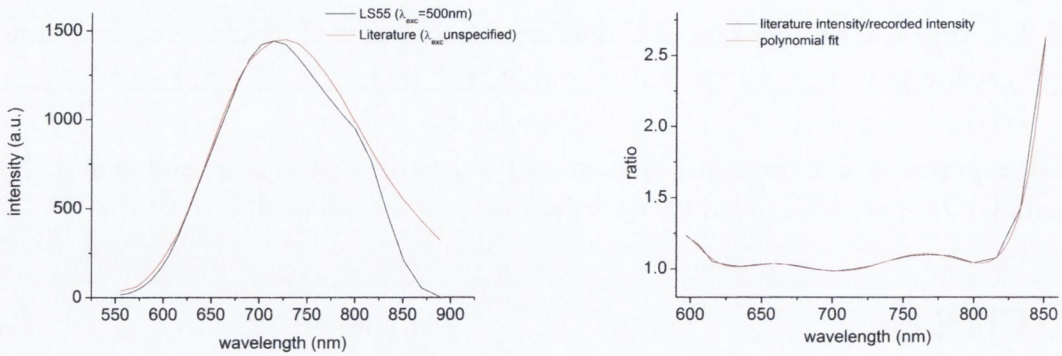

Figure 13.5: LEFT: Comparison of DMANS fluorescence spectrum from experiment and literature. RIGHT: Polynomial correction curve

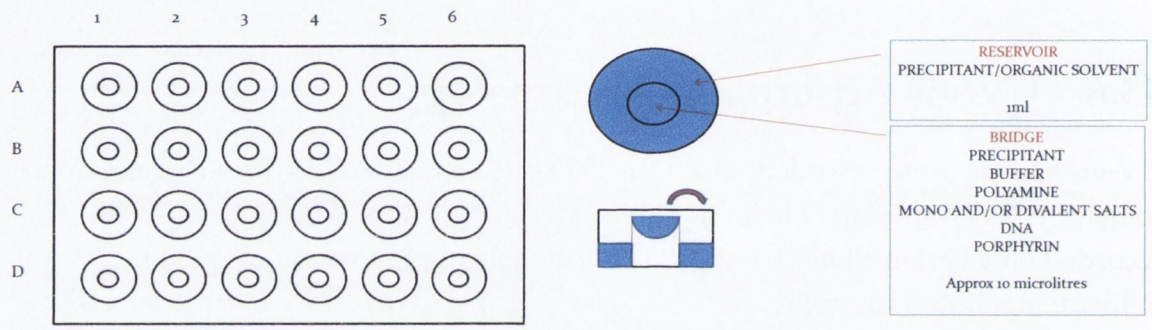

Figure 13.6: Preparation of crystallography trays by sitting-drop method

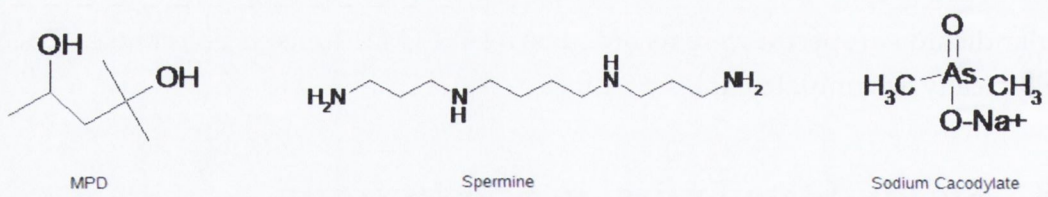

Figure 13.7: Structures of reagents used in crystallography trials

Samples were mounted on the IO3 beamline at the Diamond Synchrotron (Harwell, Oxfordshire,UK)

13.10 Data Analysis

Data analysis and non-linear fitting was performed using OriginPro 8.0/8.5. Lorentzian and Voigtian curve-fitting was performed using Fityk peak-fitting software. Exponen-

tial decay fitting and deconvolution on Edinburgh Instrument and JobinYvon spectrometers were made using EI commercial software and Decay Analysis Software v6.3, respectively. Exponential fitting was performed based on the following decay model

$$I(t) = I_0 + A_1 exp\left[\frac{-t}{\tau_1}\right] + A_2 exp\left[\frac{-t}{\tau_2}\right] + \ldots \quad (13.1)$$

Due to instrument delay, kinetic traces on the SPC or ns flash were not zeroed with respect to time. When these traces were analysed in OriginPro a correction was made for the delay.

$$I(t) = I_0 + A_1 exp\left[\frac{-(t-t_0)}{\tau_1}\right] + A_2 exp\left[\frac{-(t-t_0)}{\tau_2}\right] + \ldots \quad (13.2)$$

The addition of the time shift does not affect calculated lifetimes, but does affect the relative contributions in multi-exponential systems. In purpose-built commercial software this time shift is automatically accounted for. Best fit to the exponential model was made using the iterative Marquardt-Levenbug algorithm.

13.11 Computational Methods

Gas-phase ground state IR spectra were calculated using Gaussian 094[116] at the Hartree-Fock (HF) level with the 6-311++G(d,p) basis set and using a scaling factor of 0.9 for the frequencies[314]. Solvent was incorporated into the calculations using the default Polarizable Contimuum model (PCM)[315]. Excited state geometries were calculated using Configuration Interaction Singles (CIS)

13.12 Materials

Pt(II)TMPyP4 was purchased from Frontier Scientific as the tetrachloride salt. Unless stated, synthetic RNA and DNA mononucleotides and polynucleotides were purchased from Sigma-Aldrich and used without further purification. d(CpC) was purchased from ATDBio (Southampton, UK). 1-methylcytosine was purchased from Synchem, Germany and recrystallized according to the method of Hosmane and Leonard[316]. Oligonucleotide d(TGGGGT) was purchased in HPLC-purified form from both Sigma-Genosys and ATDBio. Oligonucleotides d(CCCTAACCCTAACCCTAACCCTAA) and d(CCCCCTTTCCCCCTTTCCCCCTTTCCCCC) were synthesised in HPLC-purified form by Sigma-Genosys and desalted on Nap-5 columns. Extinction coefficients for reagents are listed in Table 13.1.

Table 13.1: Extinction coefficients

species	ϵ ($dm^3\,mol^{-1}\,cm^{-1}$)	λ
PtTMPyP4	17200	402
H_2TMPyP4	22600	423
ZnTMPyP4	18000	437
1-MeCyt	7400	260
5′GMP	11800	260
5′AMP	15400	260
5′CMP	7200	260
5′dCMP	7400	260
d(CpC)	7300	260
poly(rC)	6200	269
poly(rA)	9800	258
poly(rG)	9400	253
[poly(dG-dC)]$_2$	8400	254
[poly(dA-dT)]$_2$	6600	262
d(TGGGGT)	9750	260
d$(C_3TA_2)_4$	6200	269
d$(C_5T_3)_3C_5$	6200	269

Appendix

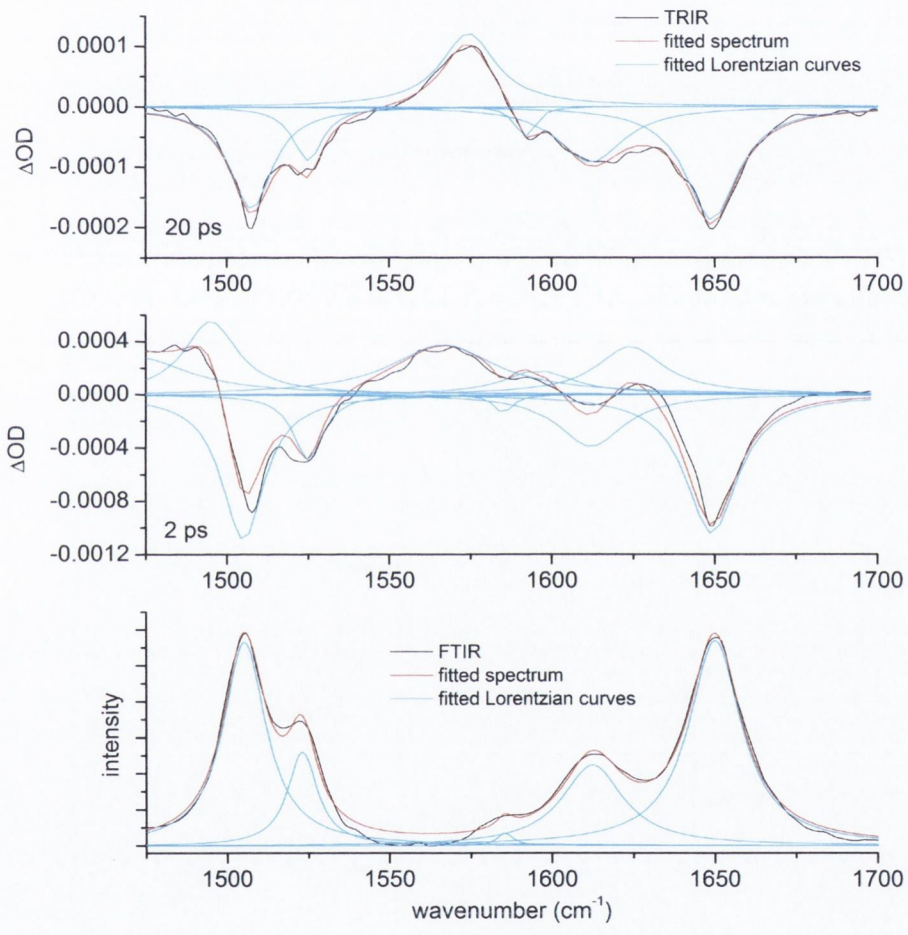

Figure A.1: FTIR and TRIR (2 ps, 20 ps) of 10 mM dCMP in buffered D_2O fit to sum of overlapping Lorentzian peaks. Data from PIRATE

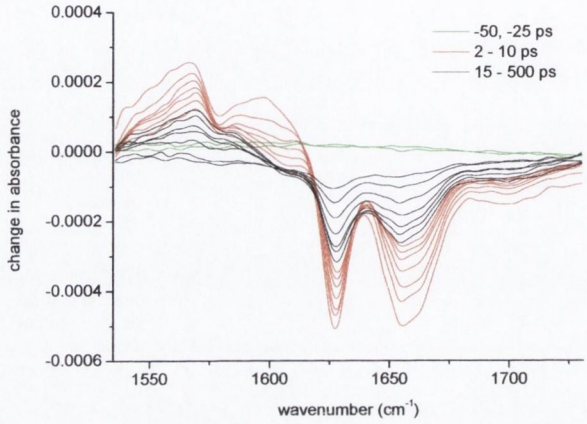

Figure A.2: TRIR spectra of 10 mM $d(C_3TA_2)_4$ in 50 mM Na-phosphate pH 7 in D_2O on PIRATE. Delays at (ps) -50, -25, 2, 3, 4, 5, 6.5, 10, 15, 20, 35, 50, 100, 250, 500

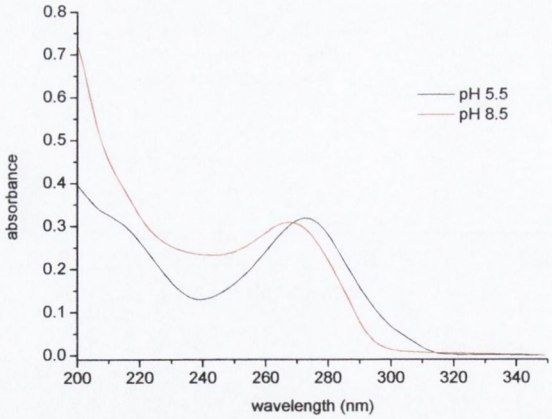

Figure A.3: UV spectra of 10 mM $(C_5T_3)_3C_5$ at pH 5.5 and pH 8.5

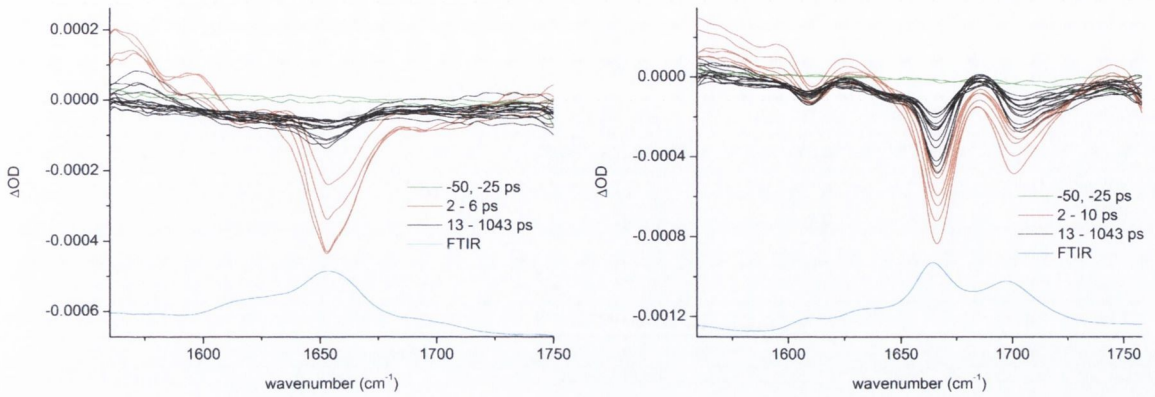

Figure A.4: ps-TRIR spectra of 10 mM $d(C_5T_3)_3C_5$ in D_2O recorded on PIRATE LEFT: pH 8.5 (50 mM Na_2HPO_4). Delays (ps) -50, -25, 2, 2.5, 4, 6, 13, 20, 37, 67, 99, 133, 177, 212, 258, 310, 371, 447, 546, 696, 1043. RIGHT:pH 5.5 (50 mM NaH_2PO_4). Delays (ps) -50, -25, 2, 2.5, 4, 6, 8, 10, 13, 20, 37, 57, 99, 177, 212, 258, 310, 371, 445, 546, 696, 1043

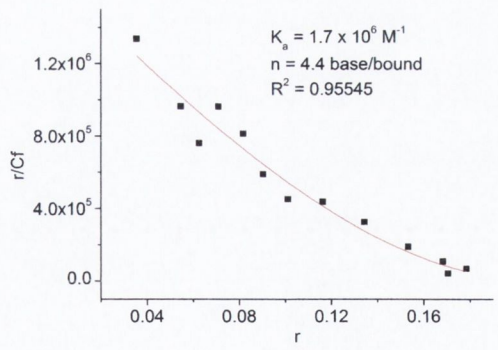

Figure A.5: Binding plot for PtTMPyP4 with poly(rG) in 50 mM Na-phosphate fit to method of McGhee and von Hippel

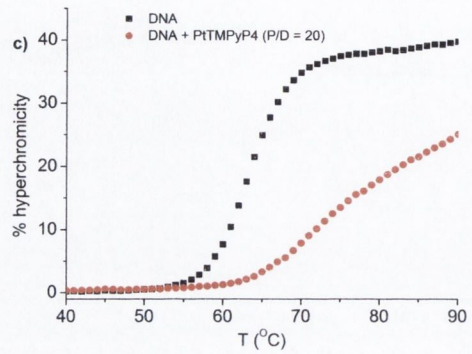

Figure A.6: Thermal denaturation of double-stranded salmon DNA in the presence of PtTMPyP4

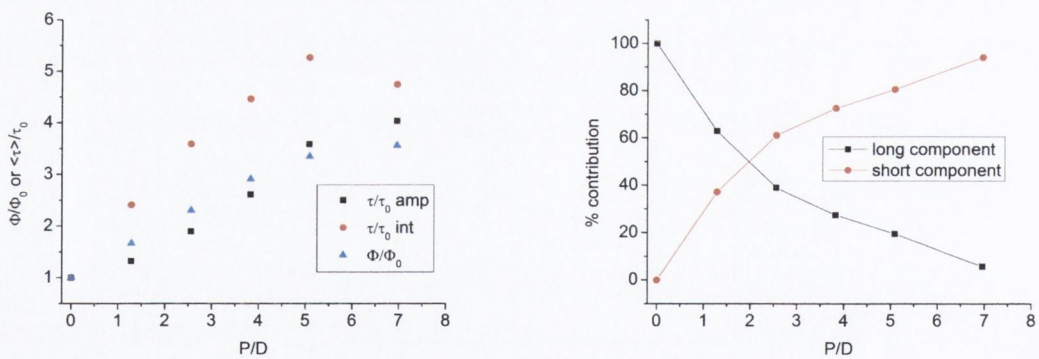

Figure A.7: LEFT Relative contributions of short and long components in PtTMPyP4 as function of P/D ratio. RIGHT: Comparison of steady-state quantum yield and average lifetimes ('amp' from Eq. 9.16, 'int' from Eq. 9.15). Recorded in 50 mM Na-phosphate buffer in aerated solution. λ_{exc} = 521 nm (steady-state), 371 nm (SPC)

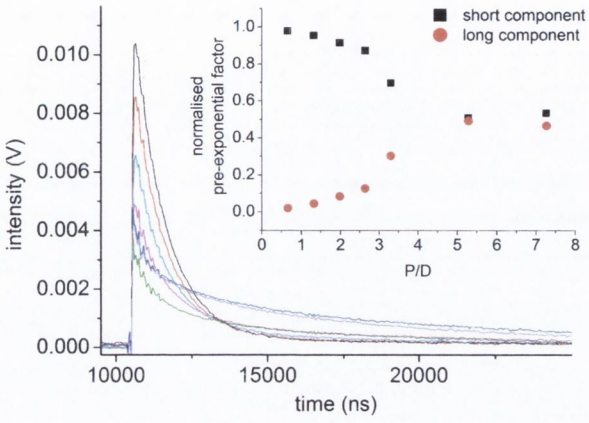

Figure A.8: Time-resolved emission decays of PtTMPyP4 in poly(rA)

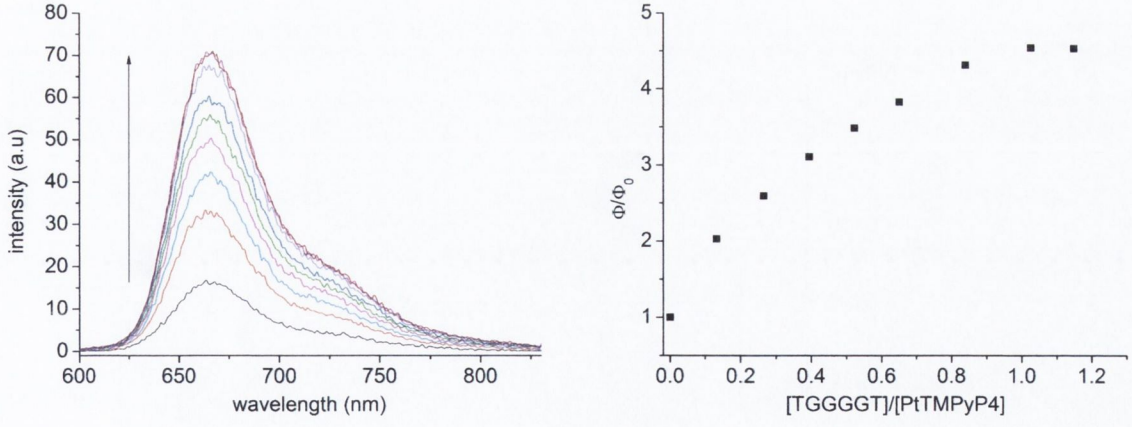

Figure A.9: Emission spectra of PtTMPyP4 in presence of TGGGGT in 100 mM Na-phosphate buffer pH 7

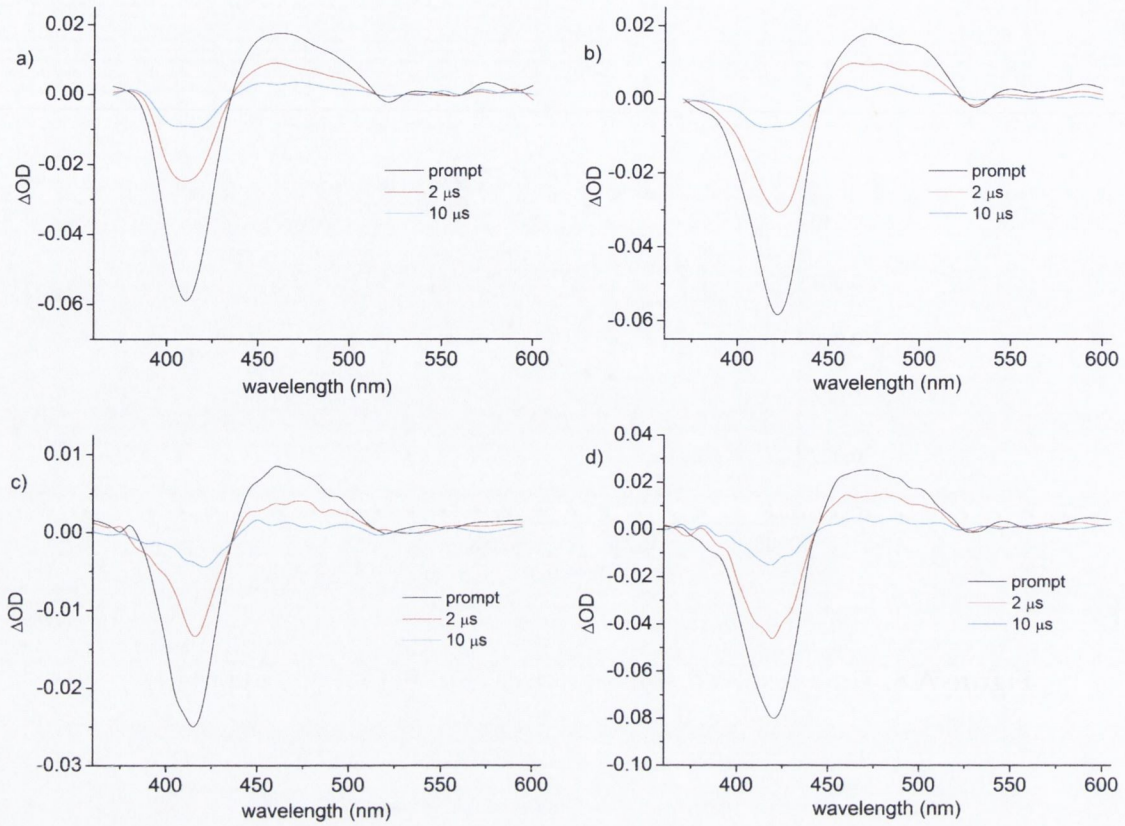

Figure A.10: Nanosecond transient UV/vis spectra of PtTMPyP4 in presence of (a) $[poly(dA\text{-}dT)]_2$, (b) $[poly(dG\text{-}dC)]_2$, (c) poly(rA), (d) DNA. In 50 mM PBS pH 7, λ_{pump} = 355 nm

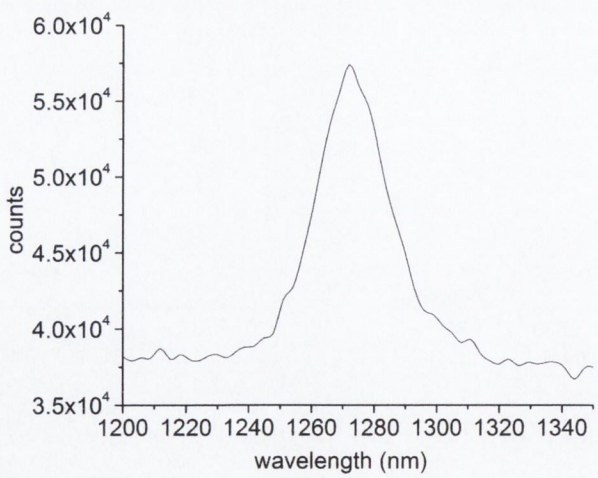

Figure A.11: Luminescence of singlet oxygen sensitised from ^{3}PtTMPyP4* in D_2O. λ_{exc} = 400 nm

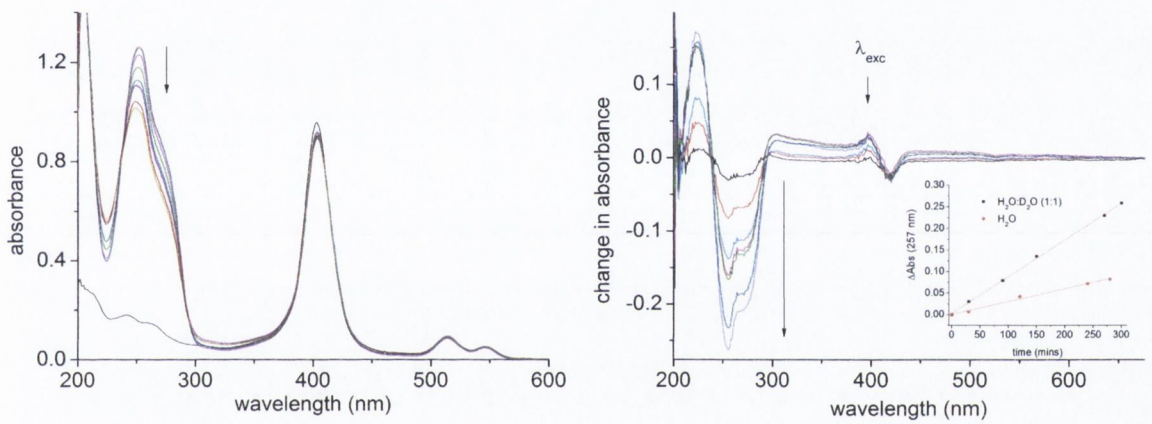

Figure A.12: LEFT: Effect of 400 nm irradiation on UV/vis spectrum of 6 μM PtTMPy4 with 80 μM GMP in 1:1 H_2O:D_2O in 50 mM Na-phosphate buffer. RIGHT: Change in spectra with increased 400 nm exposure time. Inset: change in G absorption at 257 nm with time in H_2O and 1:1 H_2O:D_2O solutions. Light source is 450 nm Xe-lamp passed through monochromator (15 nm band pass)

Bibliography

[1] Middleton, C. T.; de La Harpe, K.; Su, C.; Law, Y. K.; Crespo-Hernandez, C. E.; Kohler, B. *Ann. Rev. Phys. Chem.* **2009**, *60*, 217–239.

[2] *Wikipedia (online)*, <http://en.wikipedia.org/wiki/DNA> accessed Oct 2010.

[3] *Nucleic Acids in Chemistry and Biology*, 3rd ed.; Blackburn, G. M., Gait, M. J., Loakes, D., Williams, D. M., Eds.; RSC Publishing, 2006.

[4] *UCSB (online)*, <http://www.chem.ucsb.edu/~kalju/chem110L> accessed Oct 2010.

[5] Pecourt, J. M. L.; Peon, J.; Kohler, B. *J. Am. Chem. Soc.* **2000**, *122*, 9348–9349.

[6] Crespo-Hernandez, C. E.; Cohen, B.; Hare, P. M.; Kohler, B. *Chem. Rev.* **2004**, *104*, 1977–2019.

[7] Gustavsson, T.; Improta, R.; Markovitsi, D. *J. Phys. Chem. Lett.* **2010**, *1*, 2025–2030.

[8] Markovitsi, D.; Gustavsson, T.; Talbot, F. *Photochem. Photobiol. Sci.* **2007**, *6*, 717–724.

[9] Smets, J.; Adamowicz, L.; Maes, G. *J. Phys. Chem.* **1996**, *100*, 6434–6444.

[10] Podolyan, Y.; Gorb, L.; Leszczynski, J. *Int. J. Mol. Sci.* **2003**, *4*, 410–421.

[11] Aleman, C. *Chem. Phys.* **1999**, *244*, 151–162.

[12] Aleman, C. *Chem. Phys. Lett.* **1999**, *302*, 461–470.

[13] Gorb, L.; Leszczynski, J. *Int. J. Quantum Chem.* **1998**, *70*, 855–862.

[14] Shishkin, O.; Gorb, L.; Leszczynski, J. *J. Phys. Chem. B* **2000**, *104*, 5357–5361.

[15] Kwiatkowski, J. S.; Leszczynski, J. *J. Phys. Chem.* **1996**, *100*, 941–953.

[16] Shukla, M.; Leszczynski, J. *J. Phys. Chem. A* **2002**, *106*, 11338–11346.

[17] Malone, R. J.; Miller, A. M.; Kohler, B. *Photochem. Photobiol.* **2003**, *77*, 158–164.

[18] Mitchell, D. L. In *CRC Handbook of Organic Photochemistry and Photobiology*; Horspool, W., Lenci, F., Eds., 2nd ed.; CRC Press, 2004; pp 140–1 – 140–8.

[19] Douki, T.; Cadet, J. *Biochemistry* **2001**, *40*, 2495–2501.

[20] Friedel, M. G.; Cichan, M. K.; Carell, T. In *CRC Handbook of Organic Photochemistry and Photobiology*; Horspool, W., Lenci, F., Eds., 2nd ed.; CRC Press, 2004; pp 141–1 – 141–22.

[21] Douki, T.; Reynaud-Angelin, A.; Cadet, J.; Sage, E. *Biochemistry* **2003**, *42*, 9221–9226.

[22] Lan, Z.; Fabiano, E.; Thiel, W. *J. Phys. Chem. B* **2009**, *113*, 3548–3555.

[23] Cadet, J.; Vigny, P. In *Bioorganic Photochemistry*; Morrison, H., Ed.; John Wiley & Sons: New York, 1990; Vol. 1, pp 1–272.

[24] Ismail, N.; Blancafort, L.; Olivucci, M.; Kohler, B.; Robb, M. A. *J. Am. Chem. Soc.* **2002**, *124*, 6818–6819.

[25] Quinn, S.; Doorley, G. W.; Watson, G. W.; Cowan, A. J.; George, M. W.; Parker, A. W.; Ronayne, K. L.; Towrie, M.; Kelly, J. M. *Chem. Commun.* **2007**, 2130–2132.

[26] Sharonov, A.; Gustavsson, T.; Carre, V.; Renault, E.; Markovitsi, D. *Chem. Phys. Lett.* **2003**, *380*, 173–180.

[27] Hare, P. M.; Crespo-Hernandez, C. E.; Kohler, B. *Proc. Natl. Acad. Sci. U. S. A.* **2007**, *104*, 435–440.

[28] Onidas, D.; Markovitsi, D.; Marguet, S.; Sharonov, A.; Gustavsson, T. *J. Phys. Chem. B* **2002**, *106*, 11367–11374.

[29] Pecourt, J. M. L.; Peon, J.; Kohler, B. *J. Am. Chem. Soc.* **2001**, *123*, 10370–10378.

[30] Peon, J.; Zewail, A. H. *Chem. Phys. Lett.* **2001**, *348*, 255–262.

[31] Sharonov, A.; Gustavsson, T.; Marguet, S.; Markovitsi, D. *Photochem. Photobiol. Sci.* **2003**, *2*, 362–364.

[32] Blancafort, L.; Cohen, B.; Hare, P.; Kohler, B.; Robb, M. A. *J. Phys. Chem. A* **2005**, *109*, 4431–4436.

[33] Middleton, C. T.; Cohen, B.; Kohler, B. *J. Phys. Chem. A* **2007**, *111*, 10460–10467.

[34] Kang, H.; Lee, K. T.; Jung, B.; Ko, Y. J.; Kim, S. K. *J. Am. Chem. Soc.* **2002**, *124*, 12958–12959.

[35] Ullrich, S.; Schultz, T.; Zgierski, M. Z.; Stolow, A. *Phys. Chem. Chem. Phys.* **2004**, *6*, 2796–2801.

[36] Canuel, C.; Mons, M.; Piuzzi, F.; Tardivel, B.; Dimicoli, I.; Elhanine, M. *J. Chem. Phys.* **2005**, *122*, 074316(1–6).

[37] Kosma, K.; Schroeter, C.; Samoylova, E.; Hertel, I. V.; Schultz, T. *J. Am. Chem. Soc.* **2009**, *131*, 16939–16943.

[38] Fogarasi, G. *J. Phys. Chem. A* **2002**, *106*, 1381–1390.

[39] Tomic, K.; Tatchen, J.; Marian, C. M. *J. Phys. Chem. A* **2005**, *109*, 8410–8418.

[40] Hare, P. M.; Crespo-Hernandez, C. E.; Kohler, B. *J. Phys. Chem. B* **2006**, *110*, 18641–18650.

[41] Merchan, M.; Serrano-Andres, L. *J. Am. Chem. Soc.* **2003**, *125*, 8108–8109.

[42] Blancafort, L.; Robb, M. A. *J. Phys. Chem. A* **2004**, *108*, 10609–10614.

[43] Matsika, S. *J. Phys. Chem. A* **2004**, *108*, 7584–7590.

[44] Sobolewski, A. L.; Domcke, W. *Phys. Chem. Chem. Phys.* **2004**, *6*, 2763–2771.

[45] Zgierski, M. Z.; Patchkovskii, S.; Lim, E. C. *J. Chem. Phys.* **2005**, *123*, 081101(1–4).

[46] Zgierski, M. Z.; Patchkovskii, S.; Fujiwara, T.; Lim, E. C. *J. Phys. Chem. A* **2005**, *109*, 9384–9387.

[47] Merchan, M.; Gonzalez-Luque, R.; Climent, T.; Serrano-Andres, L.; Rodriguez, E.; Reguero, M.; Pelaez, D. *J. Phys. Chem. B* **2006**, *110*, 26471–26476.

[48] Blancafort, L. *Photochem. Photobiol.* **2007**, *83*, 603–610.

[49] Kistler, K. A.; Matsika, S. *J. Phys. Chem. A* **2007**, *111*, 2650–2661.

[50] Kistler, K. A.; Matsika, S. *J. Chem. Phys.* **2008**, *128*, 215102(1–14).

[51] Hudock, H. R.; Martinez, T. J. *ChemPhysChem* **2008**, *9*, 2486–2490.

[52] Blancafort, L.; Migani, A. *J. Photochem. Photobiol. A* **2007**, *190*, 283–289.

[53] Santoro, F.; Barone, V.; Gustavsson, T.; Improta, R. *J. Am. Chem. Soc.* **2006**, *128*, 16312–16322.

[54] So, R.; Alavi, S. *J. Comput. Chem.* **2007**, *28*, 1776–1782.

[55] Improta, R.; Barone, V. *Theor Chem. Acc.* **2008**, *120*, 491–497.

[56] Johnson, W. C.; Itzkowitz, M. S.; Tinoco, I. *Biopolymers* **1972**, *11*, 225–&.

[57] Powell, J. T.; Richards, E. G.; Gratzer, W. B. *Biopolymers* **1972**, *11*, 235–250.

[58] Lee, C. H.; Ezra, F. S.; Kondo, N. S.; Sarma, R. H.; Danyluk, S. S. *Biochemistry* **1976**, *15*, 3627–3638.

[59] Chan, S. I.; Bangerter, B. W.; Peter, H. H. *Proc. Natl. Acad. Sci. U. S. A.* **1966**, *55*, 720–727.

[60] Chan, S. I.; Nelson, J. H. *J. Am. Chem. Soc.* **1969**, *91*, 168–183.

[61] Bangerter, B. W.; Chan, S. I. *J. Am. Chem. Soc.* **1969**, *91*, 3910–3921.

[62] Ts'o, P. O. P.; Kondo, N. S.; P, S. M.; Hollis, D. P. *Biochemistry* **1969**, *8*, 997–1029.

[63] Brahms, J.; Maurizot, J.; Michelson, A. M. *J. Mol. Biol.* **1967**, *25*, 481–495.

[64] Adler, A. J.; Grossman, L.; Fasman, G. D. *Biochemistry* **1968**, *7*, 3836–3843.

[65] Warshaw, M. M.; Cantor, C. R. *Biopolymers* **1970**, *9*, 1079–1103.

[66] Norberg, J.; Nilsson, L. *Biophys. J.* **1995**, *69*, 2277–2285.

[67] Hingerty, B.; Broyde, S. *Nucleic Acids Res.* **1978**, *5*, 127–137.

[68] Broyde, S.; Wartell, R. M.; Stellman, S. D.; Hingerty, B. *Biopolymers* **1978**, *17*, 1485–1506.

[69] Norberg, J.; Nilsson, L. *Chem. Phys. Lett.* **2004**, *393*, 282–283.

[70] Zarudnaya, M.; Samijlenko, S.; Potyahaylo, A.; Hovorun, D. *Nucleosides, Nucleotides Nucleic Acids* **2002**, *21*, 125–137.

[71] Langridge, R.; Rich, A. *Nature* **1963**, *198*, 725–728.

[72] Hartman, K. A.; Rich, A. *J. Am. Chem. Soc.* **1965**, *87*, 2033–2039.

[73] Chou, C. H.; Thomas, G. J. *Biopolymers* **1977**, *16*, 765–789.

[74] Broido, M. S.; Kearns, D. R. *J. Am. Chem. Soc.* **1982**, *104*, 5207–5216.

[75] Bell, A. F.; Hecht, L.; Barron, L. D. *J. Am. Chem. Soc.* **1997**, *119*, 6006–6013.

[76] Guo, K.; Pourpak, A.; Beetz-Rogers, K.; Gokhale, V.; Sun, D.; Hurley, L. H. *J. Am. Chem. Soc.* **2007**, *129*, 10220–10228.

[77] Catasti, P.; Chen, X.; Deaven, L.; Moyzis, R.; Bradbury, E.; Gupta, G. *J. Mol. Biol.* **1997**, *272*, 369–382.

[78] Gehring, K.; Leroy, J. L.; Gueron, M. *Nature* **1993**, *363*, 561–565.

[79] Kang, C.; Berger, I.; Lockshin, C.; Ratliff, R.; Moyzis, R.; Rich, A. *Proc. Natl. Acad. Sci. U. S. A.* **1994**, *91*, 11636–11640.

[80] Chen, L. Q.; Cai, L.; Zhang, X. H.; Rich, A. *Biochemistry* **1994**, *33*, 13540–13546.

[81] Mergny, J. L.; Lacroix, L.; Han, X. G.; Leroy, J. L.; Helene, C. *J. Am. Chem. Soc.* **1995**, *117*, 8887–8898.

[82] Collin, D.; Gehring, K. *J. Am. Chem. Soc.* **1998**, *120*, 4069–4072.

[83] Fenna, C. P.; Wilkinson, V. J.; Arnold, J. R. P.; Cosstick, R.; Fisher, J. *Chem. Commun.* **2008**, 3567–3569.

[84] Cohen, B.; Larson, M. H.; Kohler, B. *Chem. Phys.* **2008**, *350*, 165 – 174.

[85] Roca-Sanjuan, D.; Olaso-Gonzalez, G.; Gonzalez-Ramirez, I.; Serrano-Andres, L.; Merchan, M. *J. Am. Chem. Soc.* **2008**, *130*, 10768–10779.

[86] Crespo-Hernandez, C. E.; Kohler, B. *J. Phys. Chem. B* **2004**, *108*, 11182–11188.

[87] Takaya, T.; Su, C.; de La Harpe, K.; Crespo-Hernandez, C. E.; Kohler, B. *Proc. Natl. Acad. Sci. U. S. A.* **2008**, *105*, 10285–10290.

[88] Crespo-Hernandez, C. E.; Cohen, B.; Kohler, B. *Nature* **2005**, *436*, 1141–1144.

[89] Markovitsi, D.; Talbot, F.; Gustavsson, T.; Onidas, D.; Lazzarotto, E.; Marguet, S. *Nature* **2006**, *441*, E7.

[90] Buchvarov, I.; Wang, Q.; Raytchev, M.; Trifonov, A.; Fiebig, T. *Proc. Natl. Acad. Sci. U. S. A.* **2007**, *104*, 4794–4797.

[91] Groenhof, G.; Schaefer, L. V.; Boggio-Pasqua, M.; Goette, M.; Grubmueller, H.; Robb, M. A. *J. Am. Chem. Soc.* **2007**, *129*, 6812–6819.

[92] Miannay, F.-A.; Banyasz, A.; Gustavsson, T.; Markovitsi, D. *J. Am. Chem. Soc.* **2007**, *129*, 14574–14575.

[93] Doorley, G. W.; McGovern, D. A.; George, M. W.; Towrie, M.; Parker, A. W.; Kelly, J. M.; Quinn, S. J. *Angew. Chem., Int. Ed.* **2009**, *48*, 123–127.

[94] Crespo-Hernandez, C. E.; de La Harpe, K.; Kohler, B. *J. Am. Chem. Soc.* **2008**, *130*, 10844–10845.

[95] de La Harpe, K.; Crespo-Hernandez, C. E.; Kohler, B. *J. Am. Chem. Soc.* **2009**, *131*, 17557–17559.

[96] Eisinger, J.; Gueron, M.; Shulman, R.; Yamane, T. *Proc. Natl. Acad. Sci. U. S. A.* **1966**, *55*, 1015–1020.

[97] Vigny, P.; Favre, A. *Photochem. Photobiol.* **1974**, *20*, 345–349.

[98] Favre, A. *FEBS Lett.* **1972**, *22*, 280–282.

[99] Kononov, A. I.; Bakulev, V. M.; Rapoport, V. L. *J. Photochem. Photobiol. B* **1993**, *19*, 139–144.

[100] Plessow, R.; Brockhinke, A.; Eimer, W.; Kohse-Hoinghaus, K. *J. Phys. Chem. B* **2000**, *104*, 3695–3704.

[101] Hare, P. M.; Middleton, C. T.; Mertel, K. I.; Herbert, J. M.; Kohler, B. *Chem. Phys.* **2008**, *347*, 383 – 392.

[102] Schreier, W. J.; Schrader, T. E.; Koller, F. O.; Gilch, P.; Crespo-Hernandez, C. E.; Swaminathan, V. N.; Carell, T.; Zinth, W.; Kohler, B. *Science* **2007**, *315*, 625–629.

[103] Schreier, W. J.; Kubon, J.; Regner, N.; Haiser, K.; Schrader, T. E.; Zinth, W.; Clivio, P.; Gilch, P. *J. Am. Chem. Soc.* **2009**, *131*, 5038–5039.

[104] Mouret, S.; Philippe, C.; Gracia-Chantegrel, J.; Banyasz, A.; Karpati, S.; Markovitsi, D.; Douki, T. *Org. Biomol. Chem.* **2010**, *8*, 1706–1711.

[105] McCullagh, M.; Hariharan, M.; Lewis, F. D.; Markovitsi, D.; Douki, T.; Schatz, G. C. *J. Phys. Chem. B* **2010**, *114*, 5215–5221.

[106] Olaso-Gonzalez, G.; Roca-Sanjuan, D.; Serrano-Andres, L.; Merchan, M. *J. Chem. Phys.* **2006**, *125*, 231102.

[107] Nachtigallova, D.; Hobza, P.; Ritze, H.-H. *Phys. Chem. Chem. Phys.* **2008**, *10*, 5689–5697.

[108] Kuimova, M. K.; Dyer, J.; George, M. W.; Grills, D. C.; Kelly, J. M.; Matousek, P.; Parker, A. W.; Sun, X. Z.; Towrie, M.; Whelan, A. M. *Chem. Commun.* **2005**, 1182–1184.

[109] McGovern, D. A.; Quinn, S.; Doorley, G. W.; Whelan, A. M.; Ronayne, K. L.; Towrie, M.; Parker, A. W.; Kelly, J. M. *Chem. Commun.* **2007**, 5158–5160.

[110] Towrie, M.; Doorley, G. W.; George, M. W.; Parker, A. W.; Quinn, S. J.; Kelly, J. M. *Analyst* **2009**, *134*, 1265–1273.

[111] McGovern, D. A.; Doorley, G. W.; Whelan, A. M.; Parker, A. W.; Towrie, M.; Kelly, J. M.; Quinn, S. J. *Photochem. Photobiol. Sci.* **2009**, *8*, 542–548.

[112] Robb, M. A. *Personal Communication*.

[113] Santoro, F.; Barone, V.; Improta, R. *J. Am. Chem. Soc.* **2009**, *131*, 15232–15245.

[114] Hocquet, A.; Leulliot, N.; Ghomi, M. *J. Phys. Chem. B* **2000**, *104*, 4560–4568.

[115] Emanuele, E.; Zakrzewska, K.; Markovitsi, D.; Lavery, R.; Millie, P. *J. Phys. Chem. B* **2005**, *109*, 16109–16118.

[116] Frisch, M. J. et al. *Gaussian 09, Revision A.1*, 2009.

[117] Leulliot, N.; Ghomi, M.; Jobic, H.; Bouloussa, O.; Baumruk, V.; Coulombeau, C. *J. Phys. Chem. B* **1999**, *103*, 10934–10944.

[118] Szczesniak, M.; Szczepaniak, K.; Kwiatkowski, J. S.; Kubulat, K.; Person, W. B. *J. Am. Chem. Soc.* **1988**, *110*, 8319–8330.

[119] Lee, C.; Cho, M. *J. Chem. Phys.* **2006**, *125*, 114509.

[120] Sambrano, J. R.; de Souza, A. R.; Queralt, J. J.; Andres, J. *Chem. Phys. Lett.* **2000**, *317*, 437–443.

[121] Kistler, K. A.; Matsika, S. *J. Phys. Chem. A* **2009**, *113*, 12396–12403.

[122] Miannay, F.-A.; Banyasz, A.; Gustavsson, T.; Markovitsi, D. *J. Phys. Chem. C* **2009**, *113*, 11760–11765.

[123] Banyay, M.; Sarkar, M.; Graslund, A. *Biophys. Chem.* **2003**, *104*, 477–488.

[124] Maevsky, A. A.; Sukhorukov, B. I. *Nucleic Acids Res.* **1980**, *8*, 3029–3042.

[125] Doorley, G. W. Ph.D. thesis, Trinity College Dublin, 2009.

[126] de La Harpe, K.; Crespo-Hernandez, C. E.; Kohler, B. *ChemPhysChem* **2009**, *10*, 1421–1425.

[127] Kuimova, M. K.; Cowan, A. J.; Matousek, P.; Parker, A. W.; Sun, X. Z.; Towrie, M.; George, M. W. *Proc. Natl. Acad. Sci. U. S. A.* **2006**, *103*, 2150–2153.

[128] Li, W.; Wu, P.; Ohmichi, T.; Sugimoto, N. *FEBS Lett.* **2002**, *526*, 77–81.

[129] Kaushik, M.; Suehl, N.; Marky, L. A. *Biophys. Chem.* **2007**, *126*, 154–164.

[130] Taillandier, E.; Liquier, J. In *Handbook of Vibrational Spectroscopy*; Chalmers, J. M., Griffiths, R. P., Eds.; Wiley, Chichester, 2002; pp 3465–3480.

[131] Volker, J.; Klump, H. H.; Breslauer, K. J. *Biopolymers* **2007**, *86*, 136–147.

[132] Kawai, K.; Fujitsuka, M.; Majima, T. *Chem. Commun.* **2005**, 1476–1477.

[133] Shukla, M. K.; Leszczynski, J. *J. Phys. Chem. A* **2002**, *106*, 4709–4717.

[134] Cohen, B. *Personal Communication.*

[135] Kumar, N.; Nielsen, J. T.; Maiti, S.; Petersen, M. *Angew. Chem. Int. Ed.* **2007**, *46*, 9220–9222.

[136] Lacroix, L.; Mergny, J.; Leroy, J.; Helene, C. *Biochemistry* **1996**, *35*, 8715–8722.

[137] Snoussi, K.; Nonin-Lecomte, S.; Leroy, J. *J. Mol. Biol.* **2001**, *309*, 139–153.

[138] Egli, M.; Lubini, P.; Bolli, M.; Dobler, M.; Leumann, C. *J. Am. Chem. Soc.* **1993**, *115*, 5855–5856.

[139] Krummel, A.; Mukherjee, P.; Zanni, M. *J. Phys. Chem. B* **2003**, *107*, 9165–9169.

[140] Hunt, N. T. *Chem. Soc. Rev.* **2009**, *38*, 1837–1848.

[141] Cadet, J.; Douki, T.; Gasparutto, D.; Ravanat, J. *Mutat. Res., Fundam. Mol. Mech. Mutagen.* **2003**, *531*, 5–23.

[142] Hirakawa, K.; Kawanishi, S.; Hirano, T.; Segawa, H. *J. Photochem. Photobiol. B* **2007**, *87*, 209–217.

[143] Hirakawa, K.; Kawanishi, S.; Matsumoto, J.; Shiragami, T.; Yasuda, M. *J. Photochem. Photobiol. B* **2006**, *82*, 37–44.

[144] Rehm, D.; Weller, A. *Isr. J. Chem.* **1970**, *8*, 259–271.

[145] Turro, N. J.; Ramamurthy, V.; Scaiano, J. C. *Principles of Molecular Photochemistry: An Introduction*; University Science Books, Sausalito, California, 2009.

[146] Valeur, B. *Molecular Fluorescence : Principles and Applications*; Weinheim ; Chichester : Wiley-VCH, 2002.

[147] Marcus, R. A. *J. Chem. Phys.* **1956**, *24*, 966–978.

[148] Reid, G. D.; Whittaker, D. J.; Day, M. A.; Turton, D. A.; Kayser, V.; Kelly, J. M.; Beddard, G. S. *J. Am. Chem. Soc.* **2002**, *124*, 5518–5527.

[149] Webber, S. E. *Photochem. Photobiol.* **1997**, *65*, 33–38.

[150] Kalyanasundaram, K. *Photochemistry of Polypyridine and Porphyrin Complexes*; Academic Press: London, 1992.

[151] Horvath, O.; Huszank, R.; Valicsek, Z.; Lendvay, G. *Coord. Chem. Rev.* **2006**, *250*, 1792–1803.

[152] Borek, C.; Hanson, K.; Djurovich, P. I.; Thompson, M. E.; Aznavour, K.; Bau, R.; Sun, Y.; Forrest, S. R.; Brooks, J.; Michalski, L.; Brown, J. *Angew. Chem., Int. Ed.* **2007**, *46*, 1109–1112.

[153] Galievsky, V. A.; Chirvony, V. S.; Kruglik, S. G.; Ermolenkov, V. V.; Orlovich, V. A.; Otto, C.; Mojzes, P.; Turpin, P.-Y. *J. Phys. Chem.* **1996**, *100*, 12649–12659.

[154] Kruglik, S. G.; Galievsky, V. A.; Chirvony, V. S.; Apanasevich, P. A.; Ermolenkov, V. V.; Orlovich, V. A.; Chinsky, L.; Turpin, P.-Y. *J. Phys. Chem.* **1995**, *99*, 5732–5741.

[155] Murphy, M. J. Ph.D. thesis, Trinity College Dublin, 1985.

[156] Praseuth, D.; Gaudemer, A.; Verlhac, J.; Kraljic, I.; Sisssoeff, I.; Guille, E. *Photochem. Photobiol.* **1986**, *44*, 717–724.

[157] Kano, K.; Minamizono, H.; Kitae, T.; Negi, S. *J. Phys. Chem. A* **1997**, *101*, 6118–6124.

[158] Kano, K.; Fukuda, K.; Wakami, H.; Nishiyabu, R.; Pasternack, R. *J. Am. Chem. Soc.* **2000**, *122*, 7494–7502.

[159] Vergeldt, F. J.; Koehorst, R. B. M.; Vanhoek, A.; Schaafsma, T. J. *J. Phys. Chem.* **1995**, *99*, 4397–4405.

[160] Ricchelli, F. *J. Photochem. Photobiol. B* **1995**, *29*, 109–118.

[161] Lang, K.; Anzenbacher, P.; Kapusta, P.; Kral, V.; Kubat, P.; Wagnerova, D. *J. Photochem. Photobiol. B* **2000**, *57*, 51–59.

[162] Kubat, P.; Lang, K.; Kral, V.; Anzenbacher, P. *J. Phys. Chem. B* **2002**, *106*, 6784–6792.

[163] Fiel, R.; Datta-Gupta, N.; Mark, E.; Howard, J. *Cancer Res.* **1981**, *41*, 3543–3545.

[164] Tabata, M.; Nakajima, K.; Nyarko, E. *J. Inorg. Biochem.* **2000**, *78*, 383–389.

[165] Blinova, I. A.; Vasil'ev, V. V. *Russ. J. Phys. Chem.* **1995**, *69*, 995–999.

[166] Zhang, H.; Sun, Y.; Ye, K.; Zhang, P.; Wang, Y. *J. Mat. Chem.* **2005**, *15*, 3181–3186.

[167] Borisov, S. M.; Vasile'ev, V. V. *J. Anal. Chem.* **2004**, *59*, 155–159.

[168] Vasil'ev, V. V.; Borisov, S. M. *Sens. Actuators, B* **2002**, *82*, 272–276.

[169] Vasil'ev, V. V.; Borisov, S. M.; Molinari, A. *J. Porphyrins Phthalocyanines* **2003**, *7*, 780–786.

[170] Kasturi, C.; Platz, M. S. *Photochem. Photobiol.* **1992**, *56*, 427–429.

[171] Laster, B. H.; Dixon, D. W.; Novick, S.; Feldman, J. P.; Seror, V.; Goldbart, Z. I.; Kalef-Ezra, J. A. *Brachytherapy* **2009**, *8*, 324–330.

[172] Vasil'ev, V. V.; Blinova, I. A.; Golovina, I. V.; Borisov, S. M. *J. Appl. Spectrosc.* **1999**, *66*, 583–587.

[173] Van Caemelbecke, E.; Derbin, A.; Hambright, P.; Garcia, R.; Doukkali, A.; Saoiabi, A.; Ohkubo, K.; Fukuzumi, S.; Kadish, K. *Inorg. Chem.* **2005**, *44*, 3789–3798.

[174] Nyarko, E.; Hanada, N.; Habib, A.; Tabata, M. *Inorg. Chim. Acta* **2004**, *357*, 739 – 745.

[175] Hofeldt, R. H.; Sahai, R.; Lin, S. H. *J. Chem. Phys.* **1970**, *53*, 4512–4518.

[176] Sahai, R.; Hofeldt, R. H.; Lin, S. H. *Trans. Faraday Soc.* **1971**, *67*, 1690–1697.

[177] McGlynn, S. P.; Daigre, G. W.; Chrisodoyleas, N.; Reynolds, M. J. *J. Phys. Chem.* **1962**, *66*, 2499–2505.

[178] McGlynn, S. P.; Sunseri, R.; Christodoyleas, N. *J. Chem. Phys.* **1962**, *37*, 1818–&.

[179] Pasternack, R. F.; Gibbs, E. J.; Gaudemer, A.; Antebi, A.; Bassner, S.; Depoy, L.; Turner, D. H.; Williams, A.; Laplace, F.; Lansard, M. H.; Merienne, C.; PerreeFauvet, M. *J. Am. Chem. Soc.* **1985**, *107*, 8179–8186.

[180] Tabata, M.; Sakai, M.; Yoshioka, K.; Kodoma, H. *Anal. Sci.* **1990**, *6*, 651–656.

[181] Belin, C. M.Sc. thesis, Trinity College Dublin.

[182] Jasuja, R.; Jameson, D. M.; Nishijo, C. K.; Larsen, R. W. *J. Phys. Chem. B* **1997**, *101*, 1444–1450.

[183] Sirish, M.; Schneider, H. J. *Chem. Commun.* **2000**, 23–24.

[184] Jasuja, R.; Hazlett, T. L.; Helms, M. K.; Lee, S. H.; Jameson, D. M.; Larsen, R. W. *Chem. Phys. Lett.* **2001**, *350*, 515–521.

[185] Sirish, M.; Schneider, H. *J. Am. Chem. Soc.* **2000**, *122*, 5881–5882.

[186] Pasternack, R. F.; Gibbs, E. J.; Villafranca, J. J. *Biochemistry* **1983**, *22*, 2406–2414.

[187] Jin, B.; Ahn, J. E.; Ko, J. H.; Wang, W.; Han, S. W.; Kim, S. K. *J. Phys. Chem. B* **2008**, *112*, 15875–15882.

[188] Kelly, J. M.; Murphy, M. J.; McConnell, D. J.; Ohuigin, C. *Nucleic Acids Res.* **1985**, *13*, 167–184.

[189] Kruk, N. N.; Dzhagarov, B. M.; Galievsky, V. A.; Chirvony, V. S.; Turpin, P. Y. *J. Photochem. Photobiol. B* **1998**, *42*, 181–190.

[190] Kruk, N. N.; Shishporenok, S. I.; Korotky, A. A.; Galievsky, V. A.; Chirvony, V. S.; Turpin, P.-Y. *J. Photochem. Photobiol. B* **1998**, *45*, 67–74.

[191] Marzilli, L. G.; Banville, D. L.; Zon, G.; Wilson, W. D. *J. Am. Chem. Soc.* **1986**, *108*, 4188–4192.

[192] Pasternack, R. F.; Gurrieri, S.; Lauceri, R.; Purrello, R. *Inorg. Chim. Acta* **1996**, *246*, 7–12.

[193] Lipscomb, L.; Zhou, F.; Presnell, S.; Woo, R.; Peek, M.; Plaskon, R.; Williams, L. *Biochemistry* **1996**, *35*, 2818–2823.

[194] Fiel, R. J.; Howard, J. C.; Mark, E. H.; Dattagupta, N. *Nucleic Acids Res.* **1979**, *6*, 3093–3118.

[195] Fiel, R. J.; Munson, B. R. *Nucleic Acids Res.* **1980**, *8*, 2835–2842.

[196] Hudson, B. P.; Sou, J.; Berger, D. J.; McMillin, D. R. *J. Am. Chem. Soc.* **1992**, *114*, 8997–9002.

[197] Pasternack, R. F.; Gibbs, E. J.; Villafranca, J. J. *Biochemistry* **1983**, *22*, 5409–5417.

[198] Guliaev, A.; Leontis, N. *Biochemistry* **1999**, *38*, 15425–15437.

[199] Yun, B.; Jeon, S.; Cho, T.; Yi, S.; Sehlstedt, U.; Kim, S. *Biophys. Chem.* **1998**, *70*, 1–10.

[200] McKinnie, R. E.; Choi, J. D.; Bell, J. W.; Gibbs, E. J.; Pasternack, R. F. *J. Inorg. Biochem.* **1988**, *32*, 207–224.

[201] Pasternack, R. F.; Sidney, D.; Hunt, P. A.; Snowden, E. A.; Gibbs, E. J. *Nucleic Acids Res.* **1986**, *14*, 3927–3943.

[202] Strickland, J.; Marzilli, L.; Wilson, W.; Zon, G. *Inorg. Chem.* **1989**, *28*, 4191–4198.

[203] Ford, K.; Pearl, L.; Neidle, S. *Nucleic Acids Res.* **1987**, *15*, 6553–6562.

[204] Lee, S.; Lee, Y.; Lee, H.; Lee, J.; Kim, D.; Kim, S. *Biophys. J.* **2002**, *83*, 371–381.

[205] Lee, Y.; Kim, J.; Cho, T.; Song, R.; Kim, S. *J. Am. Chem. Soc.* **2003**, *125*, 8106–8107.

[206] Park, T.; Shin, J.; Han, S.; Son, J.; Kim, S. *J. Phys. Chem. B* **2004**, *108*, 17106–17111.

[207] Jin, B.; Lee, H.; Lee, Y.; Ko, J.; Kim, C.; Kim, S. *J. Am. Chem. Soc.* **2005**, *127*, 2417–2424.

[208] Jin, B.; Shin, J. S.; Bae, C. H.; Kim, J.-M.; Kim, S. K. *Biochim. Biophys. Acta, Gen. Subj.* **2006**, *1760*, 993–1000.

[209] Park, T.; Kim, J.; Han, S.; Lee, D.; Kim, S. *Biochim. Biophys. Acta, Gen. Subj.* **2005**, *1726*, 287–292.

[210] Pasternack, R. F.; Garrity, P.; Ehrlich, B.; Davis, C. B.; Gibbs, E. J.; Orloff, G.; Giartosio, A.; Turano, C. *Nucleic Acids Res.* **1986**, *14*, 5919–5931.

[211] Geacintov, N.; Ibanez, V.; Rougee, M.; Bensasson, R. *Biochemistry* **1987**, *26*, 3087–3092.

[212] Borissevitch, I. E.; Gandini, S. C. *J. Photochem. Photobiol., B* **1998**, *43*, 112 – 120.

[213] Thomas, K.; McMillin, D. *J. Phys. Chem. B* **2001**, *105*, 12628–12633.

[214] Chirvony, V. S.; Galievsky, V. A.; Terehkov, S. N.; Dzhagarov, B. M.; Ermolenkov, V.; Turpin, P.-Y. *Biospectroscopy* **1999**, *5*, 302–312.

[215] Brun, A. M.; Harriman, A. *J. Am. Chem. Soc.* **1994**, *116*, 10383–10393.

[216] Pasternack, R. F.; Brigandi, R. A.; Abrams, M. J.; Williams, A. P.; Gibbs, E. J. *Inorg. Chem.* **1990**, *29*, 4483–4486.

[217] Terekhov, S. N.; Chirvony, V. S.; Turpin, P.-Y. *J. Appl. Spectrosc.* **2005**, *72*, 585–593.

[218] Kruglik, S. G.; Ermolenkov, V. V.; Shvedko, A. G.; Orlovich, V. A.; Galievsky, V. A.; Chirvony, V. S.; Otto, C.; Turpin, P.-Y. *Chem. Phys. Lett.* **1997**, *270*, 293–298.

[219] Gandini, S. C. M.; Borissevitch, I. E.; Perussi, J. R.; Imasato, H.; Tabak, M. *J. Lumin.* **1998**, *78*, 53 – 61.

[220] Mojzes, P.; Kruglik, S. G.; Baumruk, V.; Turpin, P.-Y. *J. Phys. Chem. B* **2003**, *107*, 7532–7535.

[221] Guo, L.; Dong, W.; Tong, X.; Dong, C.; Shuang, S. *Talanta* **2006**, *70*, 630 – 636.

[222] Sazanovich, I. V.; Petrov, E. P.; Chirvony, V. S. *Opt. Spectrosc.* **2006**, *100*, 209–218.

[223] Chirvony, V. S.; Galievsky, V. A.; Kruk, N. N.; Dzhagarov, B. M.; Turpin, P.-Y. *J. Photochem. Photobiol. B* **1997**, *40*, 154–162.

[224] Chirvony, V. *J. Porphyrins Phthalocyanines* **2003**, *7*, 766–774.

[225] Sazanovich, I. V.; Chirvony, V. S. *Quantum Electron.* **2005**, *35*, 756–760.

[226] Neta, P. *J. Phys. Chem.* **1981**, *85*, 3678–3684.

[227] Mosseri, S.; Nahor, G. S.; Neta, P.; Hambright, P. *J. Chem. Soc., Faraday Trans.* **1991**, *87*, 2567–2572.

[228] Harriman, A. *J. Chem. Soc., Faraday Trans. 2* **1981**, *77*, 1281–1291.

[229] Baral, S.; Hambright, P.; Neta, P. *J. Phys. Chem.* **1984**, *88*, 1595–1600.

[230] Le Nouen, D.; Marko, J.; Vermeersch, G.; Febvay-Ebvagarot, N.; Lablavhe-Combier, A.; Perree-Fauvet, M.; Gaudemer, A. *Photochem. Photobiol.* **1989**, *49*, 7–18.

[231] Kalyanasundaram, K.; Neumannspallart, M. *J. Phys. Chem.* **1982**, *86*, 5163–5169.

[232] Steenkeste, K.; Enescu, M.; Tfibel, F.; Perree-Fauvet, M.; Fontaine-Aupart, M. P. *J. Phys. Chem. B* **2004**, *108*, 12215–12221.

[233] Steenkeste, K.; Tfibel, F.; Perree-Fauvet, M.; Briandet, R.; Fontaine-Aupart, M.-P. *J. Phys. Chem. A* **2010**, *114*, 3334–3339.

[234] Wei, S.; Zhou, J.; Feng, Y.; Wang, X.; Zhang, B.; Huang, D.; Shen, J. *Spectrosc. Lett.* **2007**, *40*, 129–137.

[235] Gabrielsson, A.; Hartl, F.; Zhang, H.; Smith, J.; Towrie, M.; Vlcek, A.; Perutz, R. *J. Am. Chem. Soc.* **2006**, *128*, 4253–4266.

[236] Davis, J. *Angew. Chem., Int. Ed.* **2004**, *43*, 668–698.

[237] Paramasivan, S.; Rujan, I.; Bolton, P. H. *Methods* **2007**, *43*, 324 – 331.

[238] Simonsson, T. *Biol. Chem.* **2001**, *382*, 621–628.

[239] Sun, D.; Hurley, L. H. *J. Med. Chem.* **2009**, *52*, 2863–2874.

[240] Hurley, L. H.; Wheelhouse, R. T.; Sun, D.; Kerwin, S. M.; Salazar, M.; Fedoroff, O. Y.; Han, F. X.; Han, H.; Izbicka, E.; Hoff, D. D. V. *Pharmacol. Ther.* **2000**, *85*, 141 – 158.

[241] Shi, D.; Wheelhouse, R.; Sun, D.; Hurley, L. *J. Med. Chem.* **2001**, *44*, 4509–4523.

[242] Freyer, M. W.; Buscaglia, R.; Kaplan, K.; Cashman, D.; Hurley, L. H.; Lewis, E. A. *Biophys. J.* **2007**, *92*, 2007 – 2015.

[243] Han, F. X. G.; Wheelhouse, R. T.; Hurley, L. H. *J. Am. Chem. Soc.* **1999**, *121*, 3561–3570.

[244] Haq, I.; Trent, J. O.; Chowdhry, B. Z.; Jenkins, T. C. *J. Am. Chem. Soc.* **1999**, *121*, 1768–1779.

[245] Izbicka, E.; Wheelhouse, R. T.; Raymond, E.; Davidson, K. K.; Lawrence, R. A.; Sun, D. Y.; Windle, B. E.; Hurley, L. H.; Von Hoff, D. D. *Cancer Res.* **1999**, *59*, 639–644.

[246] Seenisamy, J.; Bashyam, S.; Gokhale, V.; Vankayalapati, H.; Sun, D.; Siddiqui-Jain, A.; Streiner, N.; Shin-ya, K.; White, E.; Wilson, W. D.; Hurley, L. H. *J. Am. Chem. Soc.* **2005**, *127*, 2944–2959.

[247] Wheelhouse, R. T.; Sun, D. K.; Han, H. Y.; Han, F. X. G.; Hurley, L. H. *J. Am. Chem. Soc.* **1998**, *120*, 3261–3262.

[248] Keating, L.; Szalai, V. *Biochemistry* **2004**, *43*, 15891–15900.

[249] Wei, C. Y.; Jia, G. Q.; Yuan, J. L.; Feng, Z. C.; Li, C. *Biochemistry* **2006**, *45*, 6681–6691.

[250] Mita, H.; Ohyama, T.; Tanaka, Y.; Yamamoto, Y. *Biochemistry* **2006**, *45*, 6765–6772.

[251] Yamashita, T.; Uno, T.; Ishikawa, Y. *Bioorg. Med. Chem.* **2005**, *13*, 2423 – 2430.

[252] Evans, S. E.; Mendez, M. A.; Turner, K. B.; Keating, L. R.; Grimes, R. T.; Melchoir, S.; Szalai, V. A. *J. Biol. Inorg. Chem.* **2007**, *12*, 1235–1249.

[253] Wei, C.; Wang, L.; Jia, G.; Zhou, J.; Han, G.; Li, C. *Biophys. Chem.* **2009**, *143*, 79 – 84.

[254] Parkinson, G. N.; Ghosh, R.; Neidle, S. *Biochemistry* **2007**, *46*, 2390–2397.

[255] Parkinson, G.; Lee, M.; Neidle, S. *Nature* **2002**, *417*, 876–880.

[256] Horvath, M.; Schultz, S. *J. Mol. Biol.* **2001**, *310*, 367–377.

[257] Haider, S.; Parkinson, G.; Neidle, S. *J. Mol. Biol.* **2002**, *320*, 189–200.

[258] Phillips, K.; Dauter, Z.; Murchie, A.; Lilley, D.; Luisi, B. *J. Mol. Biol.* **1997**, *273*, 171–182.

[259] Caceres, C.; Wright, G.; Gouyette, C.; Parkinson, G.; Subirana, J. *Nucleic Acids Res.* **2004**, *32*, 1097–1102.

[260] Creze, C.; Rinaldi, B.; Haser, R.; Bouvet, P.; Gouet, P. *Acta Crystallogr., Sect. D: Biol. Crystallogr.* **2007**, *63*, 682–688.

[261] Lee, M. P. H.; Parkinson, G. N.; Hazel, P.; Neidle, S. *J. Am. Chem. Soc.* **2007**, *129*, 10106–10107.

[262] Benesi, H. A.; Hildebrand, J. H. *J. Am. Chem. Soc.* **1949**, *71*, 2703–2707.

[263] Foster, R. *Organic Charge-Transfer Complexes*; London : Academic Press, 1969.

[264] Tuite, E. Ph.D. thesis, Trinity College Dublin, 1992.

[265] Brodkorb, A.; Mesmaeker, A. K. D.; Rutherford, T. J.; Keene, F. R. *Eur. J. Inorg Chem.* **2001**, 2151–2160.

[266] Deranleau, D. A. *J. Am. Chem. Soc.* **1969**, *91*, 4044–4049.

[267] Deranleau, D. A. *J. Am. Chem. Soc.* **1969**, *91*, 4050–4054.

[268] Tuite, E.; Kelly, J. M. *Biopolymers* **1995**, *35*, 419–433.

[269] Petrovic, A. G.; Polavarupa, P. L. *J. Phys. Chem. B* **2008**, *112*, 2245–2254.

[270] McGhee, J. D.; von Hippel, P. H. *J. Mol. Biol.* **1974**, *86*, 469–489.

[271] Maiti, N. C.; Mazumdar, S.; Periasamy, N. *J. Phys. Chem. B* **1998**, *102*, 1528–1538.

[272] Strickland, J.; Marzilli, L.; Gay, K.; Wilson, W. *Biochemistry* **1988**, *27*, 8870–8878.

[273] Bustamante, C.; Gurrieri, S.; Pasternack, R. F.; Purrello, R.; Rizzarelli, E. *Biopolymers* **1994**, *34*, 1099–1104.

[274] Erra, E.; Petraccone, L.; Esposito, V.; Randazzo, A.; Mayol, L.; Ladbury, J.; Barone, G.; Giancola, C. *Nucleosides, Nucleotides Nucleic Acids* **2005**, *24*, 753–756.

[275] Merkina, E.; Fox, K. *Biophys. J.* **2005**, *89*, 365–373.

[276] Neidle, S. *Methods* **2007**, *43*, 245.

[277] Housecroft, C. E.; Sharpe, A. G. *Inorganic Chemistry*, 1st ed.; Prentice Hall, 2002.

[278] Mosinger, J.; Janosková, M.; Lang, K.; Kubát, P. *J. Photochem. Photobiol., A* **2006**, *181*, 283 – 289.

[279] Hurley, J.; Linschitz, H.; Treinin, A. *J. Phys. Chem.* **1988**, *92*, 5151–5159.

[280] Wirz, D. R.; Wilson, D. L.; Schenk, G. H. *Anal. Chem.* **1974**, *46*, 896–900.

[281] White, W.; Seybold, P. G. *J. Phys. Chem.* **1977**, *81*, 2035–2040.

[282] Tomita, G.; Kim, S. S. *Nature* **1965**, *207*, 975–976.

[283] Lebold, T. P.; Yeow, E. K. L.; Steer, R. P. *Photochem. Photobiol. Sci.* **2004**, *3*, 160–166.

[284] Watkins, A. R. *J. Phys. Chem.* **1974**, *78*, 2555–2558.

[285] Watkins, A. R. *J. Phys. Chem.* **1974**, *78*, 1885–1890.

[286] Murov, S. L.; Carmichael, I.; Hug, G. L. *Handbook of Photochemistry*, 2nd ed.; New York: Marcel Dekker, 1993.

[287] Badea, M.; Georghiou, S. *Photochem. Photobiol.* **1976**, *24*, 417–423.

[288] Sillen, A.; Engelborghs, Y. *Photochem. Photobiol.* **1998**, *67*, 475–486.

[289] Fukuzumi, S.; Miyao, H.; Ohkubo, K.; Suenobu, T. *J. Phys. Chem. A* **2005**, *109*, 3285–3294.

[290] Steenken, S.; Jovanovic, S. V. *J. Am. Chem. Soc.* **1997**, *119*, 617–618.

[291] Kittler, L.; Lober, G.; Gollmick, F.; Berg, H. *Bioelectrochem. Bioenerg.* **1980**, *7*, 503–511.

[292] Seidel, C. A. M.; Schulz, A.; Sauer, M. H. M. *J. Phys. Chem.* **1996**, *100*, 5541–5553.

[293] Lakowicz, J. R. *Principles of Fluorescence Spectroscopy*, 2nd ed.; Kluwer Academic/Plenum Publishers, 1999.

[294] Prochazkova, K.; Zelinger, Z.; Lang, K.; Kubat, P. *J. Phys. Org. Chem.* **2004**, *17*, 890–897.

[295] Ohkubo, Y. K., K; Fukuzumi, S. *Chem. Commun.* **2006**, , 2504–2506.

[296] Verhoeven, J. W. *J. Photochem. Photobiol., C* **2006**, *7*, 40–60.

[297] Wojdyla, M.; Smith, J. A.; Vasudevan, S.; Quinn, S. J.; Kelly, J. M. *Photochem. Photobiol. Sci.* **2010**, *9*, 1196–1202.

[298] Parker, A. W.; Lin, C. Y.; George, M. W.; Towrie, M.; Kuimova, M. K. *J. Phys. Chem. B* **2010**, *114*, 3660–3667.

[299] Reid, G. D.; Whittaker, D. J.; Day, M. A.; Creely, C. M.; Tuite, E. M.; Kelly, J. M.; Beddard, G. S. *J. Am. Chem. Soc.* **2001**, *123*, 6953–6954.

[300] Kobayashi, T.; Straub, K. D.; Rentzepis, P. M. *Photochem. Photobiol.* **1979**, *29*, 925–931.

[301] Ponterini, G.; Serpone, N.; Bergkamp, M. A.; Netzel, T. L. *J. Am. Chem. Soc.* **1983**, *105*, 4639–4645.

[302] Rajapakse, G. V. N. Ph.D. thesis, Bowling Green State University, Ohio, 2008.

[303] Enescu, M.; Lindqvist, L. *Photochem. Photobiol.* **1995**, *62*, 55–59.

[304] Dixon, I. M.; Lopez, F.; Tejera, A. M.; Esteve, J.-P.; Blasco, M. A.; Pratviel, G.; Meunier, B. *J. Am. Chem. Soc.* **2007**, *129*, 1502–1503.

[305] Goncalves, D. P. N.; Rodriguez, R.; Balasubramanian, S.; Sanders, J. K. M. *Chem. Commun.* **2006**, 4685–4687.

[306] Zhang, H.-J.; Wang, X.-F.; Wang, P.; Ai, X.-C.; Zhang, J.-P. *Photochem. Photobiol. Sci.* **2008**, *7*, 948–955.

[307] Delaney, S.; Barton, J. *Biochemistry* **2003**, *42*, 14159–14165.

[308] Pothukuchy, A.; Mazzitelli, C. L.; Rodriguez, M. L.; Tuesuwan, B.; Salazar, M.; Brodbelt, J. S.; Kerwin, S. M. *Biochemistry* **2005**, *44*, 2163–2172.

[309] Friedman, K. A.; Heller, A. *J. Phys. Chem. B* **2001**, *105*, 11859–11865.

[310] Saito, I.; Nakamura, T.; Nakatani, K.; Yoshioka, Y.; Yamaguchi, K.; Sugiyama, H. *J. Am. Chem. Soc.* **1998**, *120*, 12686–12687.

[311] Towrie, M.; Grills, D. C.; Dyer, J.; Weinstein, J. A.; Matousek, P.; Barton, R.; Bailey, P. D.; Subramaniam, N.; Kwok, W. M.; Ma, C. S.; Phillips, D.; Parker, A. W.; George, M. W. *Appl. Spectrosc.* **2003**, *57*, 367–380.

[312] Greetham, G. M.; Burgos, P.; Cao, Q.; Clark, I. P.; Codd, P. S.; Farrow, R. C.; George, M. W.; Kogimtzis, M.; Matousek, P. A. W., P; Pollard, M. R.; Robinson, D. A.; J, X. X.; Towrie, M. *Appl. Spectrosc.* **2010**, *64*, 1311–1319.

[313] Brackman, D. S.; Plesch, P. H. *J. Chem. Soc.* **1952**, 2188–2190.

[314] Irikura, K. K.; Johnson, R. D.; Kacker, R. N. *J. Phys. Chem. A* **2005**, *109*, 8430–8437.

[315] Tomasi, J.; Mennucci, B.; Cammi, R. *Chem. Rev.* **2005**, *105*, 2999–3093.

[316] Hosmane, R. S.; Leonard, N. J. *Sythesis-Stuttgart* **1981**, 118–119.